

**Synthesis of Nanostructured Carbon and
Silicon Carbon Heterostructured Thin Films by
Plasma Enhanced Chemical Vapour Deposition
techniques for Energy based Applications**

THESIS SUBMITTED FOR THE DEGREE OF
Ph. D. (SCIENCE)
in PHYSICS
to the
JADAVPUR UNIVERSITY
2024

By
SUCHARITA SAHA
(Index No.: 193/18/Phys./26)
(Registration No. SOPHY1119318)

Energy Research Unit
School of Materials Sciences
Indian Association for the Cultivation of Science
Jadavpur, Kolkata-700032, India



इंडियन एसोसियेशन फर दि कल्पितेशन आफ साइंस
इंडियन एसोसियेशन फर दि कालितिभेशन अव सायेन्स
INDIAN ASSOCIATION FOR THE CULTIVATION OF SCIENCE

Certificate from the Supervisor

This is to certify that the thesis entitled "Synthesis of Nanostructured Carbon and Silicon Carbon Heterostructured Thin Films by Plasma Enhanced Chemical Vapour Deposition Techniques for Energy based Applications." Submitted by Smt. Sucharita Saha who got her name registered on 20.09.2018 [Registration No. SOPHY1119318, Index No.: 193/18/Phys./26] for the award of Ph. D. (Science) degree of Jadavpur University, is absolutely based upon her own work under the supervision of Prof. Debajyoti Das and that neither this thesis nor any part of it has been submitted for either any degree / diploma or any other academic award anywhere before.

Debajyoti Das
30/8/2024

(Prof. Debajyoti Das)

(Signature of the Supervisor date with official seal)

Dr. Debajyoti Das
Sr. Professor •
Energy Research Unit
Indian Association for the Cultivation of Sciences
Jadavpur, Kolkata - 700 032

Declaration

I hereby declare that the work entitled "Synthesis of Nanostructured Carbon and Silicon Carbon Heterostructured Thin Films by Plasma Enhanced Chemical Vapour Deposition techniques for Energy based Applications" submitted to the Jadavpur University, Kolkata is a record of original work by me under the guidance of Prof. Debajyoti Das, Senior Professor, Energy Research Unit, School of Materials Sciences, I.A.C.S, Kolkata. This work has not performed the basis for the award of any other degree.

Sucharita Saha 30/8/2024

(Sucharita Saha)

Mobile: 9433892312/ 8240212012

Email: sucharitasaha205@gmail.com

Index No.: 193/18/Phys./26

Registration No: **SOPHY1119318**

Date of Registration: 20.09.2018

Dedicated to my Family

Acknowledgement

The completion of this Ph.D. thesis marks a significant milestone in my academic journey, and it would not have been possible without the support, guidance, and encouragement of many individuals.

*First of all, I am deeply grateful to my thesis supervisor **Prof. Debajyoti Das**, Energy Research Unit, Indian Association for the Cultivation of Science, for his active guidance, stimulating initiation and whole-hearted support in accomplishing the present research work. His energy, remarkable endurance, and meticulous attention to every detail have consistently inspired me. I am grateful for his invaluable research lessons. He taught me the importance of patience and diligence, consistently encouraging me to strive for excellence through dedicated effort. He imparted to me the understanding that scientific research demands perseverance, endurance, and a dedicated pursuit of knowledge. I am deeply grateful to him for offering me numerous research opportunities in his laboratory and for providing the encouragement essential for the successful completion of my Ph.D. program.*

*I want to acknowledge **the Department of Science and Technology (DST), Govt. of India** for the financial assistance in the form of Research Fellowship (INSPIRE), to continue the research work. I extend my sincere gratitude to the **Indian Association for the Cultivation of Science (IACS)** for offering the necessary opportunities and administrative support that facilitated the completion of my research work. I am obliged to the faculty members and staff of **Jadavpur University** for allowing me to be registered as a Ph. D student and providing me the assistance in official procedure of thesis submission. I owe my gratitude to the faculty members in my Research Advisory Committee for mentoring my research activities through meetings.*

I want to thank my seniors in the lab, Amit Banerjee, Debjit Kar, and Praloy Mondal, for generously sharing their insights and knowledge with me at the onset of my research career. I am thankful to all my lab-mates, Subhashis Samanta, Ajay Roy, Laxmikanta Karmarkar, Pronay Makal, Prami Nandi, Amaresh Dey, Chandralina Patra, Payel Sahu, Sukalyan Shyam, and Brijmohan Paramanik for their limitless support, encouragement and the unforgettable moments we shared in the lab.

I am extremely grateful to Mr. Tapas Dutta, for his unconditional support throughout my research tenure. I want to thank Mr. Sutapes Datta, Mr. Indranath Bhowmik, Dr. Manas Ghosh, Mr. Dinabandhu Prasad and Mr. Dipankar Majumdar for their technical support.

This thesis would not have been complete without the tremendous efforts, continuous support and unconditional faith in me by my parents..... my mother 'Sarmila Saha', my father 'Satyabrata Saha' and my brother 'Subhajit Saha'. I dedicate the thesis to them. I would like to thank my mother-in-law 'Mithu Sarkar' and father-in-law 'Amarendranath Sarkar' for their support and hard work during my thesis writing.

I cannot acknowledge enough the efforts of my dear husband 'Kalyan Sarkar', who stood by me through every difficult phase of my life. His guidance and understanding throughout my journey of this thesis completion has made it easier and celebration worthy.

Finally, I would like to express my gratitude to all my teachers and other mentors whose guidance and support have significantly shaped who I am today.

IACS, Kolkata.
August 2024

Sucharita Saha
(Sucharita Saha) 30/8/2024

Table of Contents

Abstract.....	iv
List of Figures	v-ix
List of Tables	x
List of publications	xi
Conference and Symposium	xii
Brief introduction to the author and energy research unit	xiii
Chapter 1: Motivation and General Introduction	1–26
1.1 Motivation.....	2
1.2 Plan of execution.....	7
1.3 Overview of carbon.....	8
1.3.1 Use of elemental carbon in everyday life.....	8
1.3.2 Environment and carbon.....	9
1.3.3 Types of carbon bonding and hybridization.....	9
1.3.4 Allotropes of carbon.....	11
1.4 Carbon-Silicon heterostructures.....	19
1.5 Framework of the thesis	21
1.6 References	22
Chapter 2: Thin film deposition techniques.....	27–48
2.1 Introduction.....	28
2.2 Physical vapour deposition (PVD).....	28
• Vacuum thermal evaporation	29
• Sputtering.....	30
• Ion Beam Deposition (IBD).....	33
• Pulsed laser deposition (PLD).....	34
2.3 Chemical vapour deposition (CVD).....	35
• Thermal chemical vapour deposition (Thermal CVD).....	36
• Plasma enhanced chemical vapour deposition (PECVD).....	37
➢ Capacitively coupled plasma enhanced CVD (CC PECVD).....	38
➢ Inductively coupled plasma enhanced CVD (ICP CVD).....	39
➢ Microwave plasma enhanced CVD (MP CVD).....	41
2.4 Plasma physics and chemistry in PECVD.....	43
2.5 Role of ions.....	43
2.6 Growth mechanism of thin film deposition.....	45
2.7 References.....	47
Chapter 3: Thin film characterization techniques.....	49–69
3.1 Introduction.....	50
3.2 Optical properties.....	50
• UV-Vis NIR optical spectroscopy.....	50
3.3 Physical properties.....	53

• Profilometer.....	53
3.4 Structural Properties.....	54
• X-ray diffraction (XRD).....	54
• Raman spectroscopy.....	57
• Transmission electron microscopy (TEM).....	59
• Field emission scanning electron microscopy (FESEM).....	60
• Atomic force microscopy (AFM).....	62
3.5 Compositional properties.....	64
• X-ray photoelectron spectroscopy (XPS).....	64
3.6 Electrical properties.....	66
• Temperature dependent dark conductivity.....	66
3.7 Measurement of solar cell I-V characteristics.....	67
3.8 References.....	69

SECTION A: Carbon Nanostructures (DLC): Growth and Characterization 70–147

• A.1: DLC films by ICP CVD.....	73–129
➤ Introduction.....	74
➤ Experimental.....	74
A.1.1: Chapter 4: Intrinsic DLC films	77–94
4.1 Results.....	78
4.1.1 Effect of variation of CH ₄ flow rate.....	78
4.1.2 Effect of negative substrate bias.....	83
4.2 Discussion.....	91
4.3 Summary and conclusion.....	94
A.1.2: Chapter 5: Boron doped DLC films.....	95–129
➤ Introduction.....	96
➤ Experimental.....	97
5.1: Effect of changing B ₂ H ₆ /CH ₄ on B-DLC properties.....	98
5.1.1 Results and discussion.....	99
5.1.2 Conclusion.....	111
5.2: Effect of substrate bias variation on B-DLC.....	112
5.2.1 Results and discussion.....	113
5.2.2 Conclusion.....	129
• A.2: DLC films by CCP CVD.....	131–147
➤ Introduction.....	132
➤ Experimental.....	133
A.2.1: Chapter 6: Optimization of intrinsic DLC films.....	135–147
6.1 Results and discussion.....	136
6.1.1 Optimization of pressure.....	136
6.1.2 Optimization of H ₂ /CH ₄ flow rate ratio.....	143
6.2 Conclusion.....	147

SECTION B: Carbon-Silicon Heterostructures: Applications in Si based devices148–157

• B.1:	
Chapter 7: Application of DLC films as ARC in silicon solar cells.....	150–157
7.1 Introduction.....	151
7.2 Experimental.....	152
7.3 Results and discussion.....	153
7.3.1 Antireflection properties.....	153
7.3.1.1 ARC theory.....	153
7.3.1.2 Surface reflectivity and optical constants.....	153
7.3.1.3 Application in <i>p-i-n</i> single junction nc-Si:H based solar cells.....	155
7.4 Conclusion.....	157
References.....	158
Chapter 8: Summary, conclusion and future outlook.....	169–177
8.1 Summary.....	170
8.2 Conclusion.....	173
8.3 Future outlook.....	174
8.4 Front pages of published peer-review papers	175

Abstract

Title: Synthesis of Nanostructured Carbon and Silicon Carbon Heterostructured Thin Films by Plasma Enhanced Chemical Vapour Deposition techniques for Energy based Applications.

Author: Sucharita Saha (Index No.: 193/18/Phys./26, Registration No.: SOPHY1119318)

The primary aim of this study is to develop and optimize diamond-like carbon (DLC) films and doped DLC films enriched with nanodiamond components on cost-effective glass substrates without involving the conventional pre-treatment with diamond powders. The films are synthesized using CH₄ precursors diluted with Ar and H₂ in a high-density plasma environment at low pressure (~ 30-40 mTorr) and low power (250 W) and at a relatively low temperature (450 °C). This unique approach of fabrication of DLC films is possible only by employing two types of plasma enhanced chemical vapour deposition systems (PECVD): inductively coupled plasma CVD (ICP CVD) and capacitively coupled plasma CVD (CCP CVD). Operating at radio frequencies (13.56 MHz), both types of PECVDs enable the ignition and sustenance of high-density plasma at low pressures and low powers respectively by their own specialized techniques. Initially, an optimization of the flow rates of CH₄ was carried out with other parameters fixed at 900 W of RF power, 30 mTorr pressure and 450 °C substrate temperatures in order to obtain DLC films with good nanocrystalline phases and high optical band gap. Later, the effect of applying negative bias voltages to the substrate and its variation on the crystalline qualities was studied. The next work deals with the investigation on the consequences of boron dopant incorporation in intrinsic DLC thin film through an increased flow rate ratio of B₂H₆/CH₄ in ICP-CVD. The optimized B doped DLC films were found to possess sufficient electrical conductivity as compared to its intrinsic counterpart, while maintaining considerable nano-crystallinity. Later, an effort was made to improve the boron doping effect and subsequent electrical conductivity at room temperature without the addition of further dopant input, only by increasing the bias voltage application to the substrate. This technique was fruitful in not only improving the electrical conductivity, but also helped in enhancing the crystallinity sufficiently. The next work is based on the optimization of transparent and crystalline DLC films in CCP CVD at a low RF power of 250 W by the variation of pressure and flow rates of CH₄ and H₂. Further, its application as an antireflective coating on glass-based Si solar cells to enhance its efficiency has been demonstrated.

Debjyoti Das
30/8/2024

Dr. Debjyoti Das
Sr. Professor
Energy Research Unit
Indian Association for the Cultivation of Science
Jadavpur, Kolkata - 700 032

Sucharita Saha
30/8/2024

List of Figures

Figure No.	Caption	Page
Fig. 1.1	(a) Electronic configuration of C in the ground and hybridized states..... (b) Orbital orientation of the three different hybridized states.....	10
Fig. 1.2	Different allotropes of carbon.....	11
Fig. 1.3	Atomic set up in graphite crystal structure.....	12
Fig. 1.4	Diamond structure.....	13
Fig. 1.5	Nanodiamond core with outer graphitic shell.....	14
Fig. 1.6	Phase diagram of carbon materials with different contents of sp^3 , sp^2 and H..	15
Fig. 1.7	Electronic band diagram of (a) intrinsic, (b) p-type and (c) n-type semiconductor.....	17
Fig. 1.8	Different sizes of spherical fullerenes with different numbers of C atoms.....	18
Fig. 1.9	Types of CNTs.....	19
Fig. 2.1	Step by step process of Physical Vapour Deposition.....	28
Fig. 2.2	Schematic diagram of vacuum thermal vapour deposition system.....	30
Fig. 2.3	Schematic diagram of RF sputtering.....	31
Fig. 2.4	Magnetron sputtering system in our lab, used for depositing TCO layers.....	33
Fig. 2.5	Schematic diagram of PLD.....	34
Fig. 2.6	Schematic diagram of Thermal CVD.....	36
Fig. 2.7	Schematic diagram of RF CCP CVD system.....	39
Fig. 2.8	Schematic diagram of ICP CVD system used in our laboratory.....	40
Fig. 2.9	Photograph of the ICP-CVD system used in our laboratory, used for the growth of DLC and B-doped DLC thin films.....	41
Fig. 2.10	Schematic diagram of microwave CVD.....	42
Fig. 2.11	Step by step representation of the thin film deposition process.....	46
Fig. 3.1	Tauc's plot of a DLC thin film grown on glass.....	51
Fig. 3.2	Schematic diagram of UV-Vis NIR spectrophotometer.....	52
Fig. 3.3	Schematic of the profilometer.....	54
Fig. 3.4	Illustrating the Braggs Law.....	55
Fig. 3.5	Schematic arrangement of the XRD components.....	56
Fig. 3.6	Band diagram showing the fundamentals of Raman Scattering.....	57
Fig. 3.7	Schematic of the Raman microscope.....	58
Fig. 3.8	The schematic representation of the components of TEM.....	60
Fig. 3.9	The internal components of FESEM.....	61
Fig. 3.10	The interaction volume and signal emission.....	62
Fig. 3.11	Working principle of Atomic Force Microscope.....	63
Fig. 3.12	Interatomic variation of forces with sample to tip distance.....	64

Fig. 3.13	Electronic interactions at the core level of atomic orbitals.....	65
Fig. 3.14	Schematic of the working of an XPS instrument.....	65
Fig. 3.15	The arrangement of the electrodes on the thin film for electrical measurement.....	66
Fig. 3.16	I-V and P-V curve of a solar cell.....	68
Fig. A.1.1	Schematic diagram of the inductively coupled plasma chemical vapour deposition system.....	75
Fig. 4.1	(a) and (b) Deconvoluted Raman spectra of the films prepared at 900 W with varying CH ₄ flow rates from 5 to 50 sccm; (c) Variation of the Intensity ratios I _D /I _G and I _{Diag} /I _D with CH ₄ flow rate; (d) Variation of diamond peak and G peak positions with increasing CH ₄ flow rate; (e) Changes in the residual stress developed within the DLC films with increasing CH ₄ flow rate.....	79
Fig. 4.2	C 1s XPS spectrum of the sample grown with 25 sccm CH ₄	81
Fig. 4.3	(a) Transmission spectra of the samples prepared with varying the CH ₄ flow rate from 5 to 40 sccm, (b) corresponding Tauc's plot showing the optical band gaps of the samples; inset shows the variation of the optical band gaps (E _g) and the corresponding slopes of the tangents to the Tauc's plot.....	82
Fig. 4.4	The variation of RMS roughness of the samples prepared with CH ₄ flow rates changed from 5 to 40 sccm, and the inset shows the AFM image of the sample prepared with 25 sccm CH ₄	83
Fig. 4.5	(a–f) Deconvoluted spectra of films prepared with 25 sccm CH ₄ at varying negative bias; (g) The variation of the intensity ratios I _D /I _G and I _{Diag} /I _D with the increase in negative substrate bias voltage.....	84
Fig. 4.6	The XRD spectra of films prepared at 0 V, -40 V and -80 V dc substrate bias; Inset: Magnified portion of the peak appearing at $2\theta = 43.8^\circ$	86
Fig. 4.7	Deconvoluted C 1s XPS spectrum of the film prepared at -40 V bias.....	87
Fig. 4.8	(a) Transmission spectra of the samples prepared with different bias voltages varying from 0 to -100 V dc, (b) Corresponding Tauc's plot of the samples with the inset showing the variation of the band gap and slope of the Tauc's plot with the variation of the bias voltage.....	88
Fig. 4.9	The variation of RMS roughness of the samples prepared with 25 sccm CH ₄ flow rate at varied substrate bias from 0 to -100 V, and the inset shows the AFM image of the sample prepared at -40 V dc bias.....	89
Fig. 4.10	SEM micrographs of the DLC films prepared with (a) 25 sccm CH ₄ , without bias, (b) 40 sccm CH ₄ , without bias, (c) 25 sccm CH ₄ , with a substrate bias of -40 V dc, and (d) 25 sccm CH ₄ , with a substrate bias of -80 V dc.....	90
Fig. 4.11	(a) TEM micrographs of the optimized nanodiamond films prepared with -40.0 V dc substrate bias; (b) High-resolution image, showing the distinct <111> crystalline planes present in circular patches distributed all over; (c) inset shows	

the SAED image with the planes; (d) A 3D-shape of nanodiamond obtained in the matrix; (e) Distinct $<111>$ crystal planes observed with sharp 3 D ridges; (f) Crystal lattice and hexagonal shape with almost equal sides.....	91	
Fig. 4.12	Comparison of I_D/I_G values of DLC obtained in different works reported in the literature.....	93
Fig. 5.1.1	(a) Deconvoluted Raman spectra of the samples with r ($=B_2H_6/CH_4$) varying from 0 to 1% (Black vertical lines are to guide the eyes corresponding to the nearest deconvoluted satellite peaks); (b) Variation of the intensity ratios: I_D/I_G , I_{Dia}/I_D , and I_{Dia}/I_G with the changes in r ($=B_2H_6/CH_4$).....	101
Fig. 5.1.2	XRD patterns of the samples prepared with r varying from 0 to 1%.....	102
Fig. 5.1.3	(a) XPS wide range spectrum of the sample prepared at $r = 1\%$; High resolution (b) C 1s spectrum, and (c): B 1s spectrum of the sample.....	103
Fig. 5.1.4	(a) $\ln(\sigma)$ vs $1/T$ graph of the samples prepared with varying r , and (b) variation of room temperature conductivity (σ_{RT}) and the corresponding high-temperature activation energy (ΔE_H) with the increase in r from 0 to 1%.....	105
Fig. 5.1.5	(a) Variation of $\ln(\sigma)$ vs $(T)^{-1/4}$ with change in r ; (b) Variation of Mott parameter T_{OM} with r ; (c) Plot of $\ln(\sigma_{OM})$ vs $T_{OM}^{1/4}$, showing a linear relationship.....	106
Fig. 5.1.6	(a) Transmission spectra of the samples prepared by varying r from 0 to 1%, (b) corresponding Tauc's plots; and (c) variation of the optical band gaps concerning r (%).	107
Fig. 5.1.7	AFM images of the samples prepared at (a) $r = 0\%$, (b) 0.6%, and (c) 1%. (d) Changes of RMS roughness with r varying from 0 to 1%.....	109
Fig. 5.1.8	SEM micrographs of the samples prepared at $r = 0.08, 0.6$, and 1%.....	109
Fig. 5.1.9	High-resolution TEM images of the films prepared at $r =$ (a) 0%, (b) 0.08%, and (c) 1%, and (d-f) show the SAED patterns of the corresponding samples. The doped film prepared at $r = 0.08\%$ shows very prominent $<111>$, $<220>$, and $<311>$ planes of a diamond.....	110
Fig. 5.1.10	EDX spectra of the sample prepared at $r = 1\%$ showing the absolute elemental contents of C and B (obtained from the TEM)	110
Fig. 5.2.1	(a) Deconvolution in the Raman bands of several B-DLC films grown at several negative substrate bias voltages; The deconvoluted spectra of an intrinsic DLC film prepared at -80 V is given for comparison; (b) variations in the B-DLC films' corresponding intensity ratios: I_D/I_G , I_{Dia}/I_D and I_{Dia}/I_G ; (c) comparison of the different intensity ratios of the doped and intrinsic DLC film grown at -80 V dc bias.....	114
Fig. 5.2.2	Wide scan XPS response of DLC network grown at (a) -40 V, (b) -80 V, and (c) -120 V substrate dc bias. Deconvolution of C 1s peaks of films at (d) -40 V, (e) -80 V, and (f) -120 V.....	118

Fig. 5.2.3	The high-resolution XPS B 1s spectrum of each film grown at dc bias: (a) -40 V, (b) -80 V, and (c) -120 V.....	118
Fig. 5.2.4	(a) $\ln(\sigma)$ vs $1/T$ plots for the DLC films grown at various substrate biases, (b) The RT conductivity (σ) and activation energy (ΔE_H , ΔE_L) of the samples varying with substrate bias.....	120
Fig. 5.2.5	Variation of $\ln\sigma_0$ vs ΔE_H for the DLC films grown at different substrate biases varying from -40 to -120 V, where MNR is followed during -40 to -80 V and reverse MNR is obeyed beyond -80 V.....	121
Fig. 5.2.6	$\ln(\sigma)$ vs $1/T^{1/4}$ plot showing Mott's conductivity at the low-temperature region for the B-DLC samples grown at varying dc bias.....	122
Fig. 5.2.7	(a) Transmission profile of the B-DLC films deposited at different substrate biases; (b) Tauc's plot of the samples; and (c) changes in optical band gap with applied bias.....	124
Fig. 5.2.8	The AFM micrograph of B-DLC samples grown at different biases: (a) -40 V, (b) -80 V, (c) -120 V; and (d) changes in the films' RMS roughness with applied bias voltage.....	125
Fig. 5.2.9	The SEM micrographs of B-DLC films grown at a different bias: (a) -40 V, (b) -80 V and (c) -120 V.....	126
Fig. 5.2.10	(a) TEM micrograph of the B-DLC film corresponding to -80 V dc substrate bias; inset shows the SAED pattern with $<111>$, $<220>$ and $<311>$ planes, (b–c) high-resolution images of the sample showing the prominent $<111>$ crystalline planes of diamond; (d) EDX spectrum presenting the contents of B and C in the sample; (e) dark field HRTEM image; (f–g) elemental mapping signifying the presents of C and B.....	127
Fig. 6.1	Deconvoluted Raman spectra of the samples prepared at different deposition pressures varying from (a) 1 to 4 Torr and (b) 4 to 7 Torr; and (c) Variation of intensity ratios with the changes in pressure.....	137
Fig. 6.2	(a) Variation of D and G band positions, (b) variation of diamond peak position and its corresponding FWHM, and (c) the change in the stress generated within the DLC network with changes in deposition pressure from 1 to 7 Torr.....	138
Fig. 6.3	C 1s XPS spectra of the samples grown at (a) 1 Torr, (b) 4 Torr, and (c) 7 Torr.....	140
Fig. 6.4	(a) Transmittance spectra of the samples prepared at different pressures (1 to 7 Torr); (b) corresponding Tauc's plots and variation of optical band gap vs deposition pressure in the inset.....	141
Fig. 6.5	AFM micrographs of the films prepared at (a) 2 Torr; (b) 4 Torr; (c) 6 Torr; (d) The change of RMS roughness of the samples at different pressures.....	142

Fig. 6.6	(a) Deconvoluted Raman spectra of the samples prepared at different flow rate ratios of H ₂ /CH ₄ ; (b) The changing intensity ratios (I _D /I _G , I _{Diag} /I _D , and I _{Diag} /I _G) with H ₂ /CH ₄	143
Fig. 6.7	Contents of <i>sp</i> ³ C–C and <i>sp</i> ² C=C bonds at different H ₂ /CH ₄ ratios, derived from XPS analysis.....	144
Fig. 6.8	(a) Transmittance of the DLC films at varying H ₂ /CH ₄ ratios; (b) The corresponding Tauc plots and the change of the optical band gaps with the varying H ₂ /CH ₄ flow ratios are shown in the inset.....	145
Fig. 6.9	XRD pattern of DLC films grown at different H ₂ /CH ₄ ratios.....	146
Fig. 6.10	(a) SEM image of the DLC film grown at 4 Torr and H ₂ /CH ₄ ratio = 1; (a-i) enlarged image showing the nanocrystals; (b) TEM image showing the distribution of the nanocrystals in the network; (c) high-resolution image the marked hexagonal nanocrystal with distinct <111> crystalline planes and (d) SAED image of the film showing different crystalline planes of diamond.....	146
Fig. 7.1	Reflectance spectra of the DLC films grown at (a) different pressures, and (b) different H ₂ /CH ₄ flow rate ratios.....	154
Fig. 7.2	(a) A schematic diagram of <i>p-i-n</i> single junction nc-Si:H-based solar cell, with DLC as an ARC layer, (b) J–V characteristics of the cells, one without DLC layer and another with DLC layer, and inset is the tabulated cell parameters for both the case.....	156

List of Tables

Table No.	Title	
Table 4.1	The variation of the different components of the films grown at 25 sccm CH ₄ with increasing negative substrate bias voltage from 0 to -100 V.....	85
Table 5.1.1	Set of samples prepared by varying $r = (B_2H_6/CH_4)$ in %.....	99
Table 5.2.1	Table of the Raman component peaks.....	115
Table 5.2.2	Elemental percentage of the different bonds, present in the DLC films prepared at different dc bias voltages.....	119
Table 5.2.3	Comparative study of similar works reported in the literature.....	128
Table 6.1	Variation of different components from analysis of Raman spectra with the change in the flow rate ratio H ₂ /CH ₄ from 0.5 to 4.....	144
Table 7.1	Growth conditions of the individual layers of the single junction <i>p-i-n</i> Si solar cell.....	152
Table 7.2	R, <i>n</i> , and <i>k</i> values at $\lambda \sim 550$ nm of DLC films prepared at different growth conditions.....	155
Table 7.3	General characteristics of each layer of the <i>p-i-n</i> single junction nc-Si:H solar cell.....	156

List of Publications

1. **Sucharita Saha** and Debajyoti Das, Evolution of Nanocrystalline Diamond Thin Films by High-Density Low-Pressure in Planar Inductively Coupled Plasma CVD, *AIP Conference Proceedings* 2265 (2020) 030292.
2. **Sucharita Saha** and Debajyoti Das, Growth of diamond-like carbon films with significant nanocrystalline phases in a low-pressure high-density CH₄ plasma in ICP-CVD: Effect of negative dc substrate bias, *Applied Surface Science* 596 (2022) 153638.
3. **Sucharita Saha** and Debajyoti Das, Diamond-Like Carbon Thin Films from Low-Pressure and High-Density CH₄ Plasma, *IOP Conference Series: Materials Science and Engineering* 1221 (2022) 012037.
4. **Sucharita Saha** and Debajyoti Das, Preparation of boron doped diamond-like carbon films in a low-pressure high-density plasma in RF ICP-CVD, *Materials Today: Proceedings* 62 (2022) 5105–5109.
5. **Sucharita Saha** and Debajyoti Das, Growth of Boron-doped Diamond-like-Carbon films from a low-pressure high-density plasma in Inductively Coupled Chemical Vapour Deposition, *Thin Solid Films* 797 (2024) 140362.
6. Debajyoti Das and **Sucharita Saha**, Negative dc substrate bias influencing the low-temperature growth of B-doped DLCs in a low-pressure rf inductive plasma, *Diamond and Related Materials* 146 (2024) 111219.
7. **Sucharita Saha**, Kalyan Sarkar and Debajyoti Das, Growth of diamond-like carbon thin films with nanocrystalline phases in a low RF powered Capacitively Coupled PECVD and its applications as ARC layers in silicon solar cells (*Communicated*).
8. Kalyan Sarkar, **Sucharita Saha** and Debajyoti Das, Enhanced field emission characteristics of DLC-coated silicon nanowires with significant nanocrystallinity retained in the DLC structure (*Communicated*).

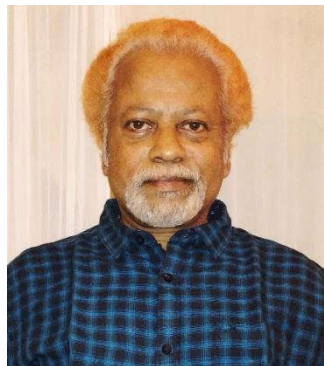
Conferences and Symposium

- ❖ 64th DAE Solid State Physics Symposium 2019 (**DAE SSPS 2019**) [18-22 Dec, 2019] ([Poster presentation](#))
- ❖ Second International E-Conference on Physics of Materials and Nanotechnology (**ICPN-2021**) [28-30 Oct, 2021] ([Poster presentation](#))
- ❖ International Conference on Emerging Trends in Material Science and Technology (**ICETMT 2022**) [10-11 Feb, 2022] ([Oral presentation](#))

Brief introduction to the author and Energy Research Unit



Sucharita Saha, is a Master of Science in Physics from the Department of Physics, Presidency University, Kolkata and right now a senior research fellow in the Energy Research Unit, School of Materials Sciences, Indian Association for the Cultivation of Science (IACS), Kolkata. Sucharita has co-authored three scientific journal publications and three conference proceedings publications presented in three national and international conferences during her tenure of Ph.D. Her current research interest includes development of intrinsic and doped diamond like carbon thin films along with their applications in Silicon based device applications, e.g as ARCs in solar cells and as enhancers of field emission effects of Silicon nanowires, as well as in other electronic applications. Alongside the pursuit of high academic goals, Sucharita is keenly interested in writing, drawing and different types of sport activities.



Energy Research Unit under the leadership of **Prof. Debajyoti Das**, Senior Professor at the School of Materials Sciences, Indian Association for the Cultivation of Science, is the premier research group with the thrust of development of materials and fabrication technology for Thin Film Silicon Solar Cells. Prof. Das has co-authored numerous highly cited scientific papers, owns several awards and patents and membership of learned bodies. His current research interests: Development of Nanomaterials for Energy Applications (Photovoltaic and Photocatalytic): (Silicon and Germanium Quantum-Dots, Nano-rods, Nano-tips & Superlattice structures; Carbon Nano-tubes, Nano-Diamond, DLC & Graphene; TCO films e.g., ITO, SnO_2 & doped ZnO_2 nanostructures, and also various composite nanostructures of TiO_2 and ZnO). The nano-materials developed by the Energy Research Unit are potential candidate for industrialization and the group proudly stands as the front runner in the path of R & D and industry collaborations for the Indian Prime Ministers ambitious call for 'make in India' initiative.

Chapter 1

Motivation and General Introduction

Chapter 1

1.1 Motivation:

Carbon, being one of the remarkable elements, has its presence in every corner on earth. Its unique property of being able to bond with itself and any other element to form oligomers, polymers and other functional groups has made it very important in life processes. This enables the production of the numerous structures that make carbon such a valuable commodity element, for example in fuels and chemicals. However, its tendency to form strong bonds with O, forming CO₂ in abundance, is hazardous to life, revealing its ‘dark side’ [1]. Therefore, it becomes crucial to understand and control the chemistry of the bonding property of Carbon for the wellbeing of nature and mankind.

Apart from its ability to form bonds, C can exist in different hybridization states of sp^3 , sp^2 and sp , allowing it to form different types of allotropes, like diamond, graphene, diamond like carbon (DLC), graphite, fullerenes, carbon nanotubes and more [1]. These, in nanostructured forms are useful in a varied fields of applications for the development of technology. Thus, Carbon-based materials that are amenable to nanoscale production and characterization have emerged as a cornerstone in the field of nanotechnology.

Diamond, an allotrope of carbon, is the hardest known material on earth and due to its excellent mechanical and chemical properties, it finds huge applications for the utility of mankind. Since, these are naturally formed at high temperatures (~1800 °C) and pressures (~10 GPa), artificial manufacturing of diamonds involves advanced techniques, which are both energetically and financially costly [2]. DLC thin films are an alternative to diamonds, which can be easily prepared in the laboratories at a much lower temperature and pressure, without involving such high expenses.

In addition to procuring superior properties like that of bulk diamond, even in its thin film configuration, diamond like carbon (DLC) thin films have the capability of possessing characteristics that can be tuned according to requirements in diverse fields of applications [3]. The properties inherited from diamond include high hardness, low friction co-efficient, high transparency, thermal conductivity and electrical resistivity. DLC films are endowed with adjustable properties like, optical band gap (1-4 eV) [4], refractive index (1.6-2.2) [5] and crystalline content within the network, making them suitable for applications in micro-electrodes, cathodes in lithium-ion batteries, field emission displays, and in opto-electronics [6,7]. Applications as protective coatings for moisture-resistant lubricants, batteries, water repellents as well as anti-reflection coatings (ARCs) for solar cells against radiation which degrades the efficiency of solar cells [8,9]. ARCs are described to be a type of coating applied

Chapter 1

on solar cells, lenses and other optical instruments, which enhances the device performance by reducing the reflection loss, thereby increasing transmission through it. DLCs having high transmittance and low reflectance are thus apt ARCs for increasing the efficiency of solar cells [10].

The typical growth techniques involved for DLC thin film deposition in the laboratories are rf magnetron sputtering [11,12], ion beam implantation [13] and various plasma enhanced chemical vapour deposition (PECVD) techniques like rf capacitively coupled PECVD [14] and microwave PECVD [15,16]. These processes usually involve high temperatures ($> \sim 900$ °C) [17] and high pressure (\sim several Torrs) plasmas from gaseous precursors like CH₄ and H₂ [15]. It is usually not desirable for the fabrication of DLC thin films at high temperatures, pressures or requiring higher power consumption, when their implementation in opto-electronic, micro and nano-electronic devices are concerned. This is because, the formation of DLCs at such intense conditions on the devices can damage their functionality. Further-more, when DLCs are to be deposited as ARCs on the top of an already fabricated solar cell, special care must be taken so that the solar cells remain intact. Needless to say, the maintenance of deposition conditions, (like high substrate temperature, power, pressures, etc) requiring high energy consumption incur a lot of expenses. These limit the utility of DLC films for industrial applications to a large extent. Hence, it has been very important to develop DLC films at moderate deposition conditions, consuming lower energy, so as to make these applicable for electronic and industrial requirements.

The use of microwave plasma CVD for DLC films has been adequately explored [18,19]. However, there are practical drawbacks involved with microwave operated CVD. Microwaves are hazardous towards health and needs proper shielding during deposition, incurring expense. Moreover, it is difficult to initiate the plasma and maintain its stability, within the microwave generated atmosphere. These challenges can be easily dealt with by using harmless RF operated CVD systems (ICP and CCP), where stable plasma can be sustained [20]. Considering the advantages of the ICP and CCP systems, in terms of lower frequency operation and uniform deposition via the generation and sustenance of highly dense plasma, the synthesis of DLC films in these processes are focussed. An important advantage of the ICP CVD system is that it is capable of maintaining stable and uniform plasma even at very low pressure (\sim 30-40 mTorr) [21]. However, CCP has a built-in benefit in terms of easier apparatus setup, lower energy usage, and a more homogeneous plasma that facilitates scaling up [22]. The work

Chapter 1

presented in this thesis mainly embodies the purpose of optimising the DLC deposition parameters in PECVD systems (ICP and CCP) at lower pressures and lower powers.

According to the literature reports, single crystal wafers of Si are used in almost all experiments as substrates for DLC film growth. In many instances, the preparation of DLC films involves a pre-treatment with diamond powders, typically achieved either by ultrasonic agitation of the substrates in a diamond powder solution or by mechanically polishing the substrate surface with diamond grit [23,24]. The single crystal nature of Si wafers facilitates the nucleation and subsequent epitaxial growth of DLC films. The pre-treatment techniques ensure that diamond particles adhere to the substrate surface, providing reactive sites that favor diamond growth. This process enhances nucleation density and promotes the oriented growth of crystalline films. However, the pre-treatment process, which includes the use of diamond powders, is complex and costly, as it requires a two-step procedure that demands careful handling during film preparation. Additionally, post-deposition annealing is sometimes performed to improve the crystalline quality of the DLC films [25,26]. Growing DLC films on glass substrates without any pre-treatment and through a single-step deposition technique remains a significant challenge.

Although intrinsic DLC films possess superior properties, making it suitable for numerous applications, low electrical conductivity along with wide band gap (~ 5.5 eV) [27] limits its utilisation in electronic devices. Moreover, the performance of conventional DLC degrades at high temperatures due to its low thermal resistance [28]. The sp^3 C-C bonds starts transforming to sp^2 C=C bonds, leading to graphitization at elevated temperatures [29]. Additionally, under extreme stress, DLC films become metastable [28]. These are all correlated to the physical properties, chemical composition, and structure of DLC film network.

To improve the electrical conductivity, thermal resistance and network stability, one of the most significant ways is doping DLC films [28]. Doping improves the natural stability of DLC films by inhibiting graphitization [30]. The integration of dopants into the carbon-carbon matrix introduces defect states between the bands. These defect states aid in the transport of charge carriers to the adjacent bands, thereby improving conductivity. Electrically conductive DLC films have a wide range of applications in high-speed micro-electronics and opto-electronics, including field emission flat panel displays [31,32].

Even though carbon shares electronic similarities with silicon, doping in carbon or diamond-like carbon (DLC) is more challenging than in silicon. This difficulty arises from carbon atoms' tendency to form graphitic and amorphous structures with sp^2 hybridized C=C

Chapter 1

bonds, in addition to the sp^3 hybridized tetrahedral C-C bonds [33–35]. Consequently, the enhancement in electrical conductivity of doped diamond films may not be as pronounced as that in doped silicon films with an identical dopant concentration. Nonetheless, by doping DLC films with nitrogen and phosphorus, n-type semiconductors can be formed. On the other hand, doping with B is an easy way to obtain *p*-type DLC films [36,37]. This is because B has an atomic radius, comparable to that of C, which makes it an effective dopant.

B, being a suitable single electron acceptor, plays an attractive role as dopant in DLCs. As the doping level in the DLC network increases, a transition takes place from a semiconductor to a metal and ultimately to a superconductor. When the doping concentration is low ($\leq 0.5\%$), the doped B atoms can substitute the C atoms in the lattice and bond with the neighbouring C in the sp^3 hybridized environment. Meanwhile, in the ground state, the holes bond with the three-fold degenerate states (binding energy = 0.38 eV) [38]. When the dopant concentration rises to $\sim 4\%$, B atoms place themselves in the neutral interstitial positions within the network [38]. At higher doping levels, the distance between the B atoms reduces to closer ranges (as that of Bohr radius), resulting in metallic conduction at room temperatures, of the order of $\sim 10^2 \Omega^{-1} \text{ cm}^{-1}$. It had been earlier reported by K. Thonke, that the B doping concentration in diamond for the metal-insulator transition is $\sim 2 \times 10^{20} \text{ cm}^{-3}$ [39]. At very high doping concentrations ($\sim 5 \times 10^{21} \text{ cm}^{-3}$), B doped diamond show superconductivity at temperatures $\sim (4 - 7 \text{ K})$ [40].

Boron-doped diamond-like carbon (DLC) films can be synthesized using various techniques, including plasma ion immersion technique [41], microwave plasma chemical vapor deposition (CVD) [42], pulsed laser deposition [43], electron cyclotron resonance (ECR) plasma CVD [44], plasma-enhanced CVD (PECVD) [45] and hot filament CVD [46]. In PECVD, boron doping is performed *in situ* at low deposition temperatures by introducing gaseous sources such as diborane (B_2H_6), trimethyl boron (TMB), and boron trioxide (B_2O_3) into a precursor gas mixture of hydrogen (H_2), argon (Ar), and hydrocarbons [47]. A key advantage of PECVD is its ability to produce thin films with a broad range of properties by adjusting the growth parameters [48].

In order to improve the nanocrystalline qualities of B doped DLC films, many have taken resort to substrate pre-treatments like, mechanical scratching and ultrasonication with diamond powders, just as for intrinsic DLCs [49,50], which incur a lot of inconveniences and expenses. Applying a negative bias voltage to the substrate offers a notable benefit for enhancing the crystallinity of boron-doped diamond-like carbon (B-doped DLC) films through a one-step process, eliminating the need for diamond powders. The bias voltage facilitates the

Chapter 1

initial nucleation on the substrates and assists in etching the amorphous layers of the developing films by attracting precursor ions to the substrates [51].

The primary objective of this study is to achieve transparent diamond-like carbon (DLC) films containing significant nanocrystalline phases on widely available and inexpensive glass substrates. The improvement of crystalline quality of the DLC films via the application of negative dc substrate bias has also been investigated. This is accomplished through a single-step deposition process using both (a) planar inductively coupled plasma-assisted chemical vapor deposition (Planar ICP-CVD) system at a low pressure and (b) capacitively coupled plasma-assisted chemical vapor deposition (CCP-CVD) at a low RF power, and at relatively low temperature, without the need for traditional diamond powder substrate pre-treatment. Adopting the same advantageous techniques and deposition parameters of the ICP CVD, the introduction of B as dopant in the DLC network and its effect on the crystalline qualities, optical transparency and electrical conductivity has been focussed. Our aim was to improve the electrical conductivity, maintaining optimal crystallinity and transparency in the B doped DLC network by the application of negative substrate bias.

The second part of the work is based on the utilization of DLC films in silicon-based device applications. Si is considered as the backbone of the semiconductor industry due to its versatile properties that are unique and environment friendly. It is easily available, being the second most abundant element on earth (after oxygen). Si, in its micro/ nano crystalline thin film forms is the active component in the next generation micro/nano electronics [52,53] and high-efficient low-cost solar cells [54]. Si thin films feature distinctive characteristics like high doping efficiency and carrier mobility along-with low optical band gap of 1.1 eV (which responds efficiently with the solar radiation). All these qualities of Si thin films, adjusted in different proportions and combinations makes them apt for their applications in electronic fields and solar cells.

One of the major challenges which hampers the efficiency of Si thin film based solar cells is the reflection loss of the incident solar light by the different layers of the cell. In order to reduce this loss, 1-D nano-structured Si like Si nanowires, nanopillars and nanocones are introduced as antireflective coatings (ARCs) on the top layer of the light facing surface of solar cells [55]. These help in trapping the sunlight by multiple reflections in between the 1-dimensional structures, thereby inducing higher absorption with increased surface area [56]. Their geometrically favoured structure facilitates easy omnidirectional flow of charge carriers, enhancing the solar cell efficiencies [57].

Chapter 1

The main motive of the work is to investigate the effect of DLC films as anti-reflection coatings on Si based solar cells.

1.2. Plan of Execution:

The optimization of both intrinsic and boron doped DLC thin films for achieving good crystalline properties, along with high transparency and electrical conductivity at low pressures, relatively low temperatures and low RF powers has been possible only by employing RF power driven PECVD techniques: (i) Inductively coupled plasma enhanced CVD (ICP CVD) unit and (ii) Capacitively coupled plasma enhanced CVD (CCP CVD) unit.

(a). Deposition achieved at low pressure by ICP CVD:

The growth processes in plasma occur predominantly in non-equilibrium conditions, characterized by a fluctuating competition between two contrasting reaction pathways: one enhancing film growth and the other leading to the etching away of the deposited layers. The key advantage of plasma-assisted growth is the high electron energy within the plasma, which enhances the excitation and dissociation of precursor molecules. When plasma is sustained at elevated deposition pressures, the growth rates of crystalline diamond thin films increase. Nonetheless, achieving film uniformity across large areas becomes difficult at high pressures [58]. Conversely, low pressure facilitates uniform deposition over extensive areas but results in lower growth rates due to the formation of a low-density plasma. The inductively coupled plasma (ICP) chemical vapor deposition (CVD) system emerges as a promising high-density plasma source, with an electron density of approximately 10^{12} cm^{-3} . This system maintains high deposition rates even at low pressures due to its high dissociation efficiency. Additionally, the low plasma sheath potential near the chamber walls reduces ion bombardment on substrates, thereby enhancing uniformity. The ICP-CVD system also ensures excellent uniformity of plasma parameters both axially and radially, promoting more consistent crystallization throughout the film network [21,59,60].

(b). Deposition achieved at low RF power operated CCP CVD:

Preparation of DLC films by CVD often requires a high power ($> = 500 \text{ W}$) for the generation of electric field for plasma initiation [18,61]. High power plasma initiation is a usual phenomenon for microwave CVD systems [18]. In a radio frequency driven CCP CVD, higher the power employed, higher is the potential drop across the electrode plates [20]. However, by

Chapter 1

obtaining a higher capacitance, via adjusting the distance between the two electrode plates within the plasma chamber, a strong electric field can also be generated even at a low power in CCP CVD.

1.3. Overview of carbon:

Carbon, represented as ‘C’ in the periodic table, is the key element of all life forms. It has an atomic number of 6 and weighs 12.01 atomic mass units. Being an insulator by nature, it possesses four electrons in its outer electronic orbit, enabling it to form strong covalent bonds with numerous other atoms. This tetravalency is the cornerstone of its capability to form diverse compounds, ranging from simple to complex molecules. Due to its versatile nature and unique properties, it is essential in biological processes, industrial applications and in environmental systems.

Carbon is the fourth most abundant (by mass) element in the universe. Its presence is found in sun, stars and in the atmosphere of almost all planets. On earth, it is widely available as carbonates in minerals (like limestone and dolomite) and in fossil fuels like coal, oil and natural gas.

Ever since the discovery of the importance of carbon in every sphere of life sustenance and advancement of new technologies, it has been a topic of huge interest among researchers. The discovery of the new compound of carbon, i.e., fullerene is attracting researchers from various fields like chemistry, physics and material sciences. The ability of carbon to be present in various forms, along with their individual fascinating properties and applications is the main reason of the growing research interest amongst the scientific community.

1.3.1. Use of elemental carbon in everyday life:

Carbon-based products permeate every aspect of daily life, from diamond jewellery to soot from chimneys. Some of the endless list of applications are shown below.

- Carbon is a necessary ingredient in the production of steel, where it is mixed with iron to create different kinds of steel.
- In automobile industry, the tyres are manufactured from the black carbon soot.
- Rubber, synthetic fibers, and plastics are made of carbon compounds.
- Vegetable chars are used to purify and decolorize foods and sugar.
- Activated charcoal is used as a cleanser for gases and water, along with a broad range of applications as material catalyst, etc.
- The use of graphite as large electrodes, in batteries as well as lubricants.

Chapter 1

- Diamond has been in use in considerable proportion in optical windows and space crafts.
- Micro-crystalline diamond coatings are inevitable in cutting devices.

1.3.2. Environment and carbon:

The carbon cycle is a fundamental phenomenon on earth, pertaining to the continuous exchange of Carbon in between the atmosphere, biosphere, hydrosphere and lithosphere. Since long, human activities, like excessive burning of fossil fuels and deforestation have had a serious impact on it. These have significantly increased the carbon level in the atmosphere, causing serious hazards like pollution, climate changes, effects of green-house gases, etc. In order to combat climate change, efforts must be made to reduce carbon emissions and improve carbon sequestration.

1.3.3. Types of carbon bonding and hybridization:

The electronic configuration of carbon is $1s^2, 2s^2, 2p^4$. This signifies the bonding state of the 6 electrons of carbon. The first two electrons are bonded to the innermost shell. The remaining 4 electrons in the outer shell contribute to its covalent nature. This tetravalency plays the key role in the forming the majority of compounds. The bonding in carbon is can be understood by the term ‘hybridization’.

Hybridization refers to the mixing of atomic orbitals with different energies, resulting in the formation of new hybrid orbitals with equal energies, which readily form covalent bonds with other atoms. With the suitable orbital orientation of electrons in the outer shell of carbon, three different hybridized states are formed: sp , sp^2 and sp^3 . The following Fig. 1.1(a) represents the electronic states of carbon in the ground state and excited hybridized states. When one s orbital of the outer shell ($2s$) combines with one p orbital (of the three $2p$), a new hybridized orbital energy state is formed, the sp hybridized state, with the other two p orbitals remaining unhybridized. It forms a linear structure with in between bond angle of 180° . The C atoms present in acetylene (C_2H_2) are sp hybridized. Here, the sp states of the two C atoms forms a sigma bond (σ), while the two unhybridized p states form pi (π) bonds with the corresponding p orbitals of the other C. The remaining sp orbital of each C bonds with H atom with a sigma bond. The sp^2 state is formed when one s and two p orbitals are mixed. The remaining one p orbital remains as it is. Thus, three sp^2 states are produced, ready to form covalent bonds with other atoms. These states lie in a plane, with the bond angle being 120° each. The p lies in a plane perpendicular to the sp^2 states. The C atoms in ethene (C_2H_4) are sp^2

Chapter 1

hybridized. Two sp^2 orbitals of the two C atoms approach each other head-to-head, forming sigma bonds, while the two p orbitals approach each other sideways, in a pi bond. The other two sp^2 orbitals of each C are sigma bonded with two H atoms. The combination of one s and three p orbitals is responsible for the formation of four sp^3 hybridization states. It forms a tetrahedral structure with a bond angle of 109.4° . The C in CH_4 is sp^3 hybridized with its 4 states bonding with H atoms in sigma bonds. Since sigma bonds are closer to the core of the atoms, they are stronger bonds with respect to the pi bonds, which are in the periphery. The orbital orientations of the different hybridized states of C are shown in [Fig. 1.1 \(b\)](#).

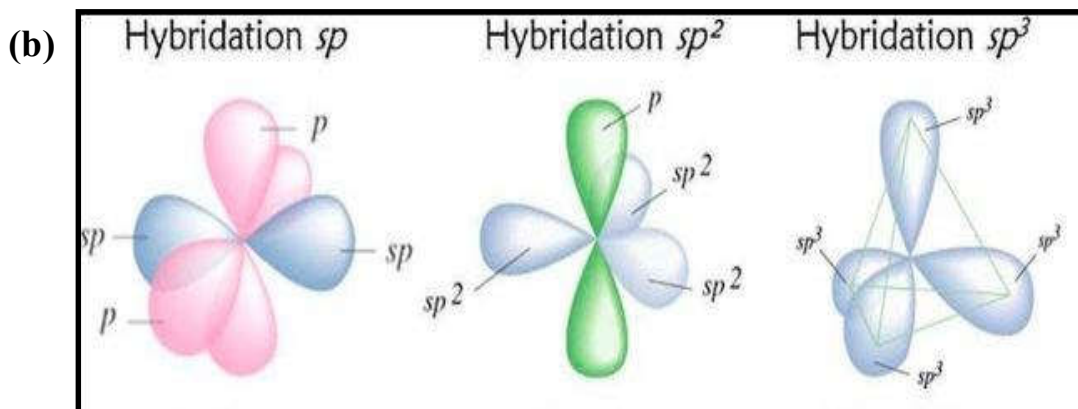
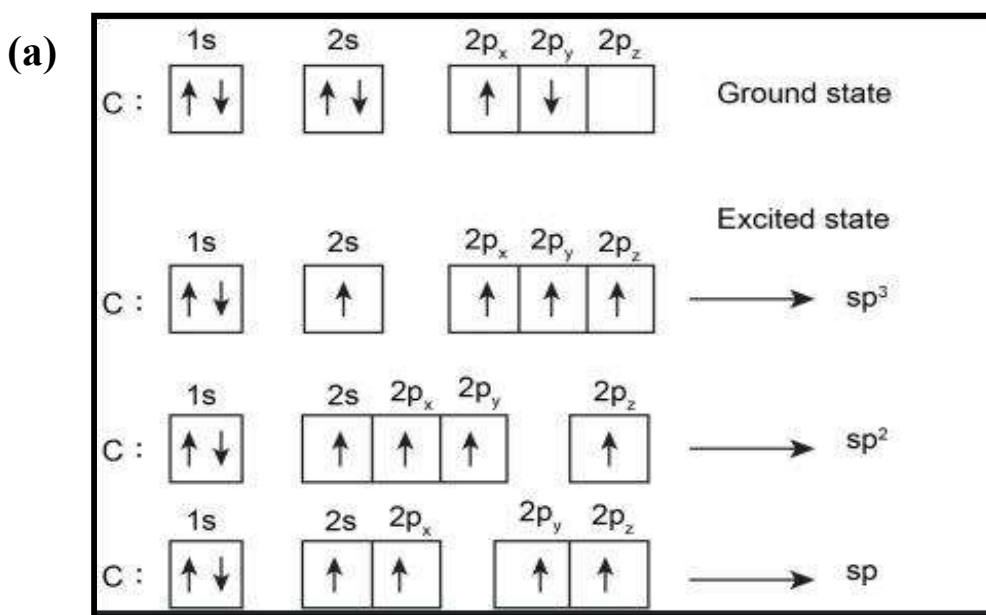


[Fig 1.1 \(a\): Electronic configuration of C in the ground and hybridized states; \(b\): Orbital orientation of the three different hybridized states.](#)

Chapter 1

1.3.4. Allotropes of carbon:

On virtue of the different states of hybridization, exhibited by carbon, it can form single (sp^3 state), double (sp^2 state) and triple (sp state) bonds with itself and other atoms. Combinations of different proportions of these hybridized C-C bonds give way to the generation of various types of forms of carbon compounds, which vary in physical and chemical properties, as well as in structural morphologies. These are termed as allotropes of carbon. These exist in any dimensional (like 0D, 1D, 2D and 3D) structures. [Fig. 1.2](#) illustrates the different types of allotropes of carbon in N-dimensional forms.

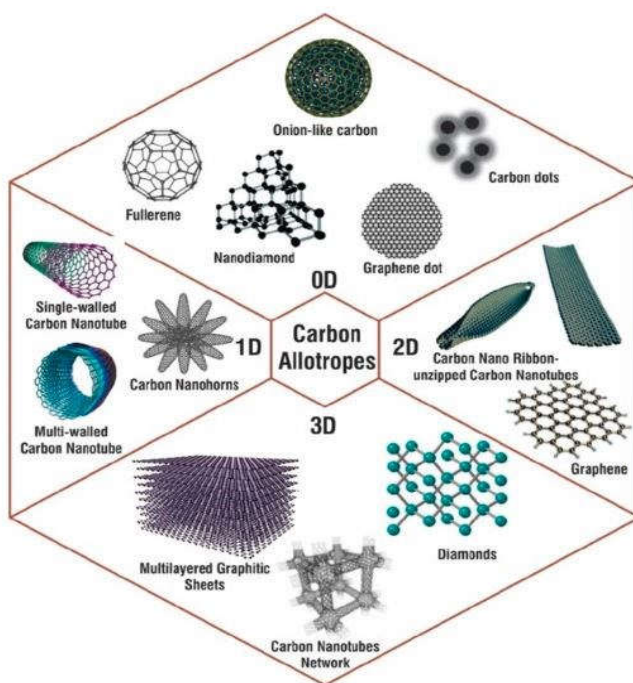


[Fig 1.2: Different allotropes of carbon \(adopted from \[62\]\).](#)

Diamonds, graphite, nanodiamonds, fullerenes, graphene, carbon nanotubes, diamond-like carbon and amorphous carbon are few of the numerous allotropes of carbon found in nature. The versatile nature of the different allotropes is exhibited by different properties. For instance, Diamond is the hardest known material on earth, whereas graphite is the softest. Similarly, Graphite's opaque nature contrasts sharply with the transparency of diamond. In addition to this extra-ordinary property, carbon also shows polymorphism. Some of the important allotropes are discussed further.

- **Graphite:**

Being one of the most common allotropes of carbon, graphite is mainly composed of sp^2 hybridized C=C bonds. The molecules are thus trigonal in shape. C atoms (sp^2 hybridized) are oriented in a six membered honeycomb shaped lattice, forming a planar structure. These planar

Chapter 1

layers are stacked one on the other with a weak van der Waals force supported by the pi (π) bonds, generating a crystalline network. The inter-planar distance is 0.335 nm, whereas the bond length of the C-C sigma (σ) bonds within the same plane is 0.141 nm. The bond energy of the in-plane σ bonds is 524 kJ/mole and that of the weak van der Waal (π) bonds is only 7 kJ/mole. Although the sp^2 C-C bonds within each plane is quite strong, it is the fragile nature of the van der Waal forces that contribute to the softness of graphite. It possesses a low specific gravity [63] and is a good conductor of heat and electricity [63,64]. It can withstand temperatures above 3600°C without losing its stiffness or strength [63]. In addition to being chemically inert and resistant to corrosion, it is highly lubricating in nature. Due to these versatile properties, graphite finds its place in widespread applications in technologically advanced and innovative fields and industries, like in electrodes, lithium-ion batteries, fibre optics, electronic devices, fuel cells, spintronics and water purification among many others [63].

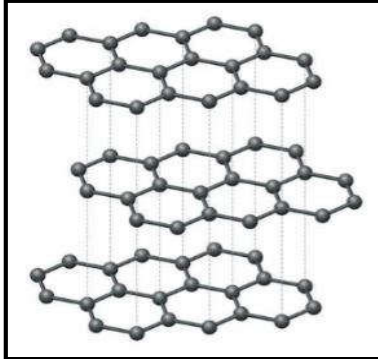


Fig. 1.3: Atomic set up in graphite crystal structure.

Graphite can be categorized as natural and synthetic. There are three types of natural graphites: (a) crystalline small flake graphite (or flake graphite); (b) amorphous graphite; and (c) crystalline vein or lump graphite [65]. All these types are different from each other in terms of physical properties, appearances, chemical composition and the formation process. Fig 1.3 shows the atomic orientation of graphite.

- **Graphene:**

Graphene is a rather newly discovered allotrope of carbon, which is actually a single atomic planar layer, constituting the graphite structure. Being the lightest and the thinnest known material on universe, it falls under the 2D category of the carbon allotropes. Because of its 2D nature, it has a huge surface area (theoretical surface area $\sim 2630 \text{ m}^2/\text{g}$), which in turn potentiates extra-ordinary properties. Its intrinsic carrier mobility has been described to be ultra-high, being $\sim (200,000 \text{ cm}^2 \text{ V}^{-1} \text{ s}^{-1})$. Its thermal conductivity is higher than that of metallic Cu ($5000 \text{ W m}^{-1} \text{ K}^{-1}$). It exhibits excellent mechanical properties along with extremely high

Chapter 1

Young's modulus (~ 1 TPA) [66]. Thus, graphene is the topic of research for the scientific community due to its extensive applications in high energy sensors, electronic devices, as electrodes, electrochemical capacitors, renewable energy sources, etc [67–69].

- **Diamonds:**

Diamond, the hardest allotrope of carbon, is composed of sp^3 hybridized C atoms bonded to each other via strong covalent sigma (σ) bonds. Each C atom is bonded to four other C atoms, with every bond angle equalling $109^\circ 28'$, forming a fully crystalline orientation in three dimensions. The unit cell in diamond forms a tetrahedral structure, which combines in a cubic symmetry. These strong bonds, (each of bond length 154 pm) is responsible for the extremely hard structure of diamond.

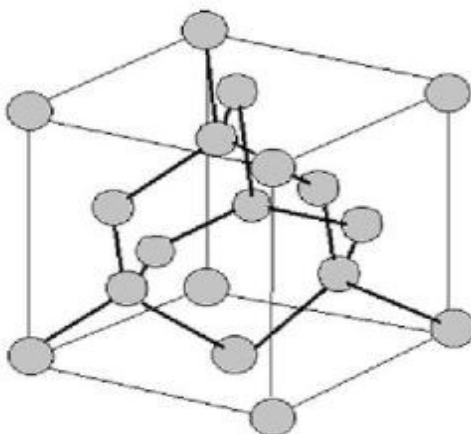


Fig. 1.4: Diamond structure.

Since all the valence electrons are covalently connected, leaving no free electrons, pure diamonds are insulators. The possession of high optical band gap with above 90 % optical transparency, very low co-efficient of friction and high thermal conductance and electrical resistance, besides being hard, chemically inert to environmental harshness makes diamonds widely applicable to scientific advancements and technology [70,71]. Diamond can be categorized as:

- ✓ Natural diamond: Originating deep within the earth's crust, at high temperatures and pressures, which is the only classical source of gem stones used in jewellery.
- ✓ Synthetic diamond: Grown for industrial purposes under high pressures artificially.
- ✓ Chemical vapour deposited (CVD) diamond: Prepared for research purpose, where optimization of the deposition conditions is done to lower down the pressure and temperatures, required for diamond growth, for exploring the avenues of applications.
- ✓ Diamond-like carbon (DLC): Grown at much lower temperature and pressures, these are involved in optical and optoelectronic purposes and coating industries.

Chapter 1

Important Properties of diamond:

1. Among solids, diamond possesses the highest thermal conductivity at room temperature ($2000 - 2200 \text{ W m}^{-1} \text{ K}^{-1}$) [72].
2. It is the hardest material on earth.
3. It is extremely rigid and strong, with the highest number density of atoms than any other material.
4. Possesses high optical transparency in the high frequency region, from UV to infra-red and an unusually high refractive index.
5. It exhibits high lubricity, with properties similar to Teflon.
6. It is chemically inert to almost all types of chemical reactions, even at high temperatures. It gets oxidized at temperatures as high as 900 K [72].

- **Nanodiamonds:**

These are small portions of diamond nanostructures of sizes ranging from 2-8 nm in size [62]. Typically, a layer of functional groups coats the surface of nanodiamonds (NDs), stabilizing the particle by minimizing dangling bonds. In the process, some of the sp^3 hybridized C-C bonds in the outer layer may get converted into amorphous soot, chains and graphitic patches with sp^2 hybridization, which increases the stability. Among other functional groups, oxygen containing groups are the majority, which passivates the surface bonds. NDs can have faceted or rounded shapes [73].

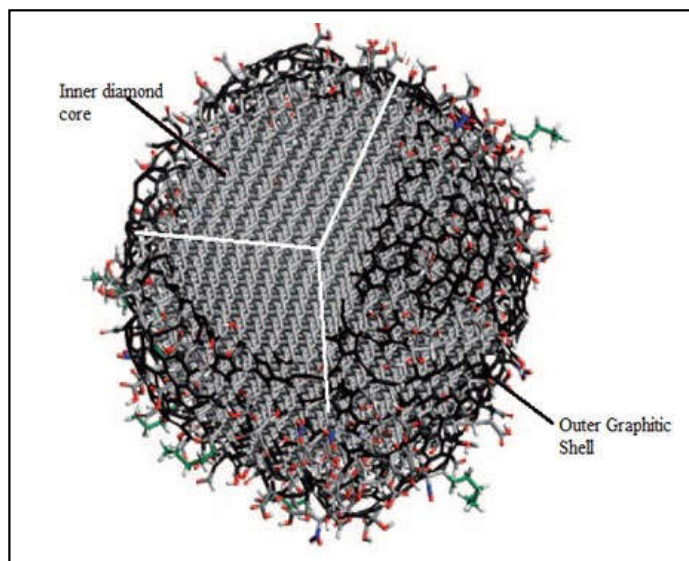


Fig. 1.5: Nanodiamond core with outer graphitic shell.

Some specific and unique properties of NDs and their recognition like physicochemical characteristics, biocompatibility, disaggregation, surface modification, fluorescence and

Chapter 1

optical dispersion have opened up new areas of advanced biomedical applications [74]. Their unique ability to load high amounts of drugs and to easily penetrate cellular membranes, have made NDs a very suitable candidate as drug delivery medium in biological systems [62]. Their active participation in bioimaging is due to their excellent optical properties, as well as their numerous sensing and therapeutic components.

- **Diamond like carbon:**

Any disordered structure or graphitization (conversion of sp^3 to sp^2 hybridization) of the perfect crystalline diamond gives rise to amorphous carbon. Since sp^3 C atoms form stronger sigma (σ) bonds whereas sp^2 C atoms involves pi (π) bonds, the proportion of sp^3 hybridized C-C bonds are related to ‘diamond-like’ and those related to the sp^2 C=C bonds are linked to ‘graphite-like’. Amorphous carbon thus consists of both diamond-like and graphite-like components. The percentage composition of these two types in the amorphous carbon, dictates the physical and chemical properties of the material [75,76]. The material with a significant amount of ‘diamond-like’ or sp^3 C-C bonds are referred to as Diamond-like carbon (DLC), which have similar properties to that of diamond [75].

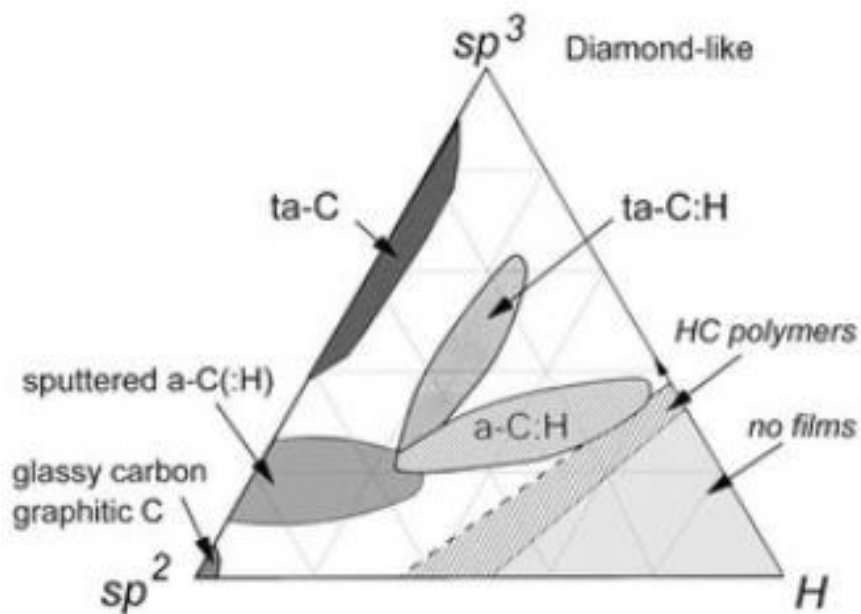


Fig.1.6: Phase diagram of carbon materials with different contents of sp^3 , sp^2 and H [77].

The sp^3 content can be adjusted according to the desired properties of the material. The carbon allotrope with ~85 % of sp^3 content is termed as tetrahedral amorphous carbon (ta: C). In many cases, hydrogen gets inevitably attached to the carbon matrix of the material, forming hydrogenated tetrahedral amorphous materials (ta: CH) or hydrogenated DLC (HDLC) or hydrogenated amorphous carbon (a: CH). HDLCs have 10-50 at.% hydrogen content, whereas

Chapter 1

ta: CH are composed of low hydrogen (20-30 at. %) [78]. The following is the phase diagram of different types of carbon materials with different proportions of sp^3 , sp^2 and H content (Fig. 1.6).

DLCs can be divided into two types, depending on their applications: mechanical grade DLC and optical grade DLCs. Hydrogen free DLCs, with higher hardness and density constitute the mechanical grade DLC. These have higher internal stress and higher frictional coefficients. Optical grade DLCs are hydrogenated ones, which have higher transmittance, higher optical band gaps, along with lower stress and smaller friction coefficients. These are not so hard [79].

Unlike diamonds, since the properties of DLC films can be adjusted according to the desired application requirements, DLCs are a topic of high interest among researchers. Moreover, possessing superior properties similar to diamonds, DLCs can be prepared at much lower temperatures and pressures compared to that required for the generation of diamonds (High Temperature High Pressure (HPHT): ~ 1800 °C and 10 GPa) [2]. The properties which make DLCs a potential participant in opto-electronic fields, nano/micro electronic devices, antireflective and protective coatings for lenses and solar cells, gas sensors, etc [6,7], includes extreme hardness and resistive to chemical reactions, high optical transparency, high thermal conductivity and electrical resistivity, low frictional coefficients and excellent field emission properties [80].

Doping of DLCs:

The high resistive character of DLCs seriously limits its applications in a wide range of nano/micro-electronic fields. With its other advantageous properties, improvement in its electrical conductivity would absolutely enhance DLCs as a potential candidate for a wide range of applications. This has been done by incorporating impurities (dopants) within the DLC lattice, which changes the electronic structure of the network. This is what is meant by the term ‘doping’. DLC films can be doped using acceptors (electron deficient atoms, having incomplete outer shells) like Boron and Nitrogen to form p-type DLCs. Electron donors (having extra electrons) like Phosphine and Iodine, when introduced within the network, forms n-type DLCs. The electronic band structure of intrinsic, p-type and n-type semiconductor is shown in the Fig 1.7.

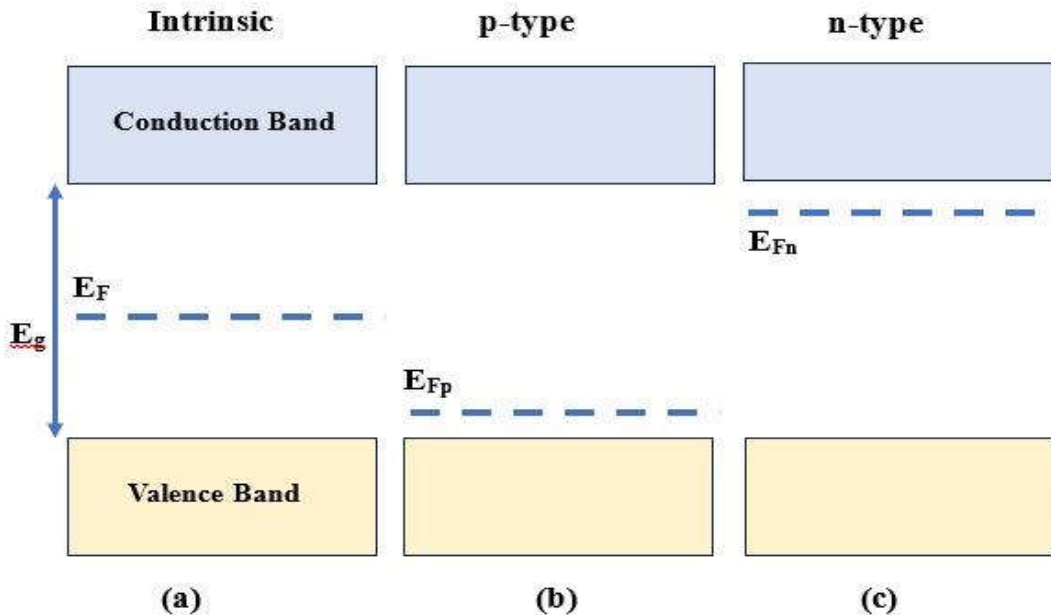


Fig 1.7: Electronic band diagram of (a) intrinsic, (b) p-type and (c) n-type semiconductor.

The electronic band gap E_g of DLC is high (~ 4 eV), which makes it almost impossible for the free electrons (present if any) to transit from the valence band (VB) to the conduction band (CB). For intrinsic DLC films, the Fermi energy level (E_F) is located at the middle of the VB and CB. When DLCs are doped with atoms having lesser number of valence electrons than C atoms (i.e, acceptors like B), impurity bands are formed closer to the VB. The fermi energy level for p-type (E_{Fp}) shifts towards the VB. With the electrons being promoted to E_{Fp} (acceptor state), holes are generated in the VB. In a p-type semiconductor, holes are the majority charge carriers, where conduction takes place by the transport of holes in the VB. In the n-type DLC, doped with atoms having excess of electrons than C (like P), an impurity state or donor level is formed near the CB edge. The Fermi level in n-type (E_{Fn}) shifts towards the donor state, near CB. Excess electrons present in E_{Fn} jumps to the CB, resulting in the transport of electrons (majority) through the CB itself. P-type doping of DLCs is technically easy to obtain. However, it is quite a challenge to achieve n-type doping of DLCs [81].

- **Fullerenes:**

Since the discovery of fullerenes by Kroto et. al. in 1985, it has opened up a new field of research in Chemistry and Material Sciences due to its potential for numerous applications for advancement in technologies and industries [82]. It is finite, stable and discrete in nature. It is composed of C atoms arranged in hollow sphere, ellipsoid or tube. The most common type of fullerene exists as C_{60} and termed as buckminster fullerene, where C atoms are arranged on

Chapter 1

the surface of a football in hexagonal and pentagonal shapes. Ellipsoidal fullerenes are elongated in shape, whereas tubular ones exist as cylinders. Other types of fullerenes include even numbered clusters of C atoms ranging from 30 to 100 (like C₃₀ to C₁₀₀) [83]. This family of C allotrope got its name ‘fullerene’ after R. B. Fuller, designer and builder of geodesic domes, having shapes resembling to that of this specific C clusters [84]. Fig. 1.8 shows the different types of spherical fullerenes.

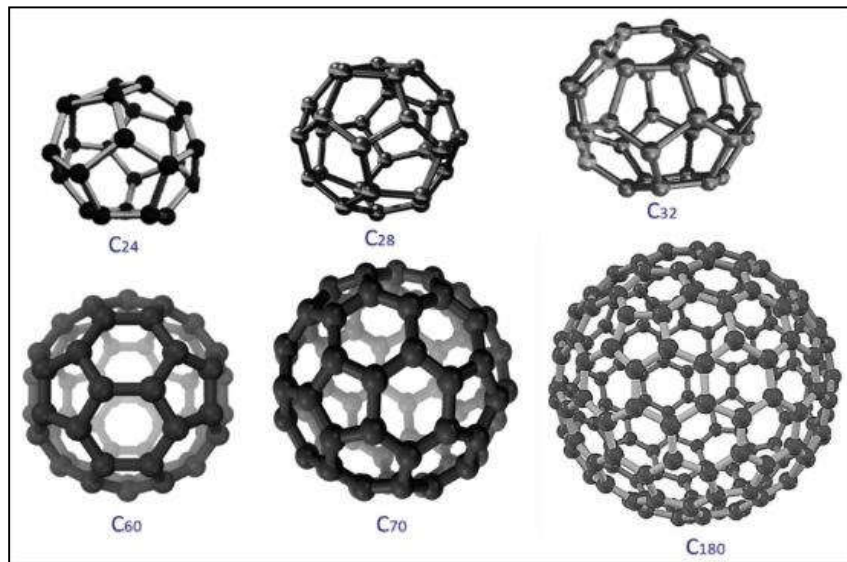


Fig. 1.8: Different sizes of spherical fullerenes with different numbers of C atoms [85].

The hollowed spheres of fullerenes, often termed as caged spheroids, vary in size, shape as well as properties depending on the number of C atoms present in the clusters. The closed cages are formed with C atoms arranged in combinations of pentagons and hexagons. While, exactly twelve pentagonal forms are required for a closed spherical cage formation, the number of hexagons of C atoms can vary with the formula C_{20+2n}, with n stands for the number of hexagons. The C atoms bond with each other in sp^3 and sp^2 hybridization states, whose proportions are dependent on the number C atoms present in the cluster. Till date, only five theoretically possible forms of fullerenes have been identified and characterized: C₆₀, C₇₀, C₇₆, C₇₈ and C₈₄ [86]. Fullerenes are distinct because of their electrical characteristics, durability, and excellent symmetry. Thus, they find huge applications in electronic industries, solar cells and also in drug delivery systems [87].

- **Carbon Nanotubes (CNTs):**

Carbon nanotubes (CNTs), being a member of the fullerene family, constitute another unique allotrope of carbon. The first discovery of CNTs was made by S. Iijima in the year 1991 [88]. These are formed when carbon sheets or graphene layers rolled up in a cylindrical shaped

Chapter 1

hollow tube. The name ‘CNT’ is derived from this shape of the allotrope. It is the dimensions, or specifically the radii and the rolling angle (chiral vector) of the CNTs that determine their structural, physical and chemical properties. The C atoms in the graphene sheets forming the CNTs are all sp^2 hybridized, interconnected to each other via sigma and pi bonds, generating honeycomb shaped structures. When a single layer of graphene sheet is rolled to form a single hollowed cylinder, a single walled CNT (SWCNT) is formed. The specific identification of SWCNTs was done by Iijima and Donald Brune in the year 1993. They termed this newly found structure as ‘Buckytubes’ [88,89]. This discovery created a revolution among the scientists in order to fully understand the excellent properties of SWCNTs and find its applications in various advanced technologies like nano-electronics and optics. When two or more layers of graphene get rolled over, forming concentric cylinders, multi walled CNTs (MWCNTs) are formed. Ideally, these nanotubes are of infinite length, with both ends capped by hemi-fullerenes, with no dangling bonds around. As the name suggests, the radii of the CNTs are in the range of a few to several nano-meters (less than 1 nm to ~ 70 nm) [88,90]. The fascinating electronic properties of CNTs have attracted a lot of scientists all over the world for various applications in nanotechnology. [Fig 1.9](#) shows the formation and types of CNTs.

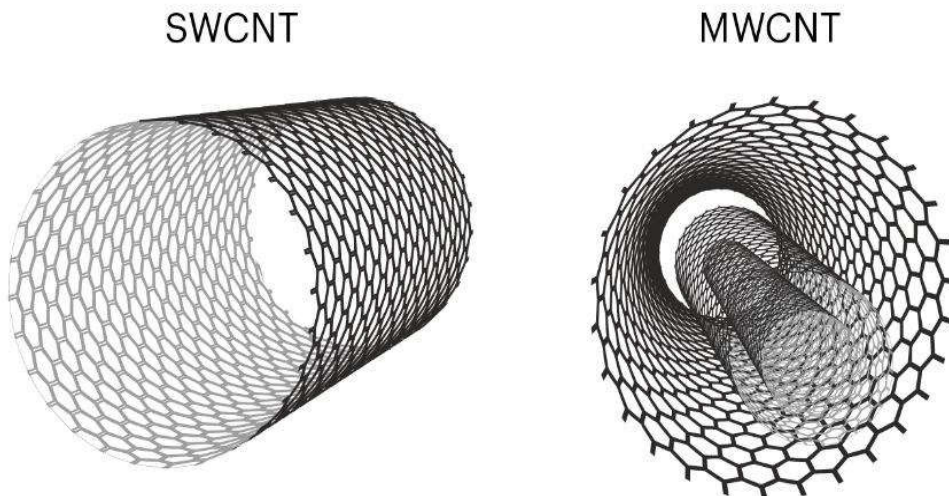


[Fig. 1.9: Types of CNTs.](#)

1.4. Carbon-Silicon heterostructures:

Silicon (Si) is one of the most active participants in the semiconducting industry, mainly due to its unique and attractive properties, abundant availability and non-toxic environment friendly nature. It is an element of group IV, having a face centred cubic structural unit cell, with its four valence electrons at the corners of a tetrahedron, just like that of Carbon. Its lattice

Chapter 1

spacing is 0.543 nm. Si has an indirect band gap of 1.1 eV, which can be modified by doping or by changing the growth parameters, like temperature and pressure.

The most significant application of silicon is in semiconductor solar power engineering, where it is utilized in the production of photovoltaic devices, specifically solar cells (SCs), which convert solar energy into electricity [91–94]. Currently, over 90% of the global production of solar modules (SMs) and solar batteries is based on silicon, which includes both monocrystalline and polycrystalline forms [94].

One effective method to enhance the performance of silicon solar cells is by reducing light reflection losses, which are primarily due to silicon's high refractive index [95]. A promising method for minimizing light reflection losses in silicon solar cells involves creating nano- and submicron-scale structures on their surfaces. To mitigate this issue, one-dimensional nanostructured silicon, such as silicon nanowires, nanopillars, and nanocones, is employed as antireflective coatings (ARCs) on the top layer of the solar cells [96]. These nanostructures enhance light trapping through multiple reflections within the one-dimensional structures, thereby increasing absorption due to the enlarged surface area [97]. Other options include porous Si layers [98,99], SiO_x films [99] and coatings of nanorods of SiO_2 , ITO [100] and ZnO [101,102]. However, such structures have low mechanical characters and require extra protection layers [100]. In these cases, DLCs are of particular interest, thanks to their optimal combination of optical and mechanical properties [103]. These can be effectively utilized to address challenges related to antireflection and protection in silicon solar cells (SCs) as well as silicon-based optical components in the infrared (IR) spectral region.

1.5. Framework of the thesis:

The main objective of the work presented in this thesis, is to develop transparent Diamond-like carbon (DLC) thin films with nanocrystalline phases in a single step ICP CVD process from gaseous precursors of CH₄ and Ar at a relatively low substrate temperature and a low pressure. Efforts had been made to obtain crystalline DLC matrix without using any pre-treatments like scratching and ultrasonication with nanodiamond powders or any post-treatments like thermal annealing. The effect of substrate bias application on the improvement of intrinsic DLC films was studied. In order to improve the electrical properties of DLC films, Boron doping was introduced and an optimisation was made to obtain good electrical conductivity at room temperature, while maintaining crystallinity. A comprehensive study on the effect of low power RF generated plasma by CCP CVD technique on the crystalline qualities of intrinsic DLC films was made. Later, its impact on the efficiency of Si solar cells as an anti-reflective coating was investigated. Thus, an overall view on the fabrication of DLCs along-with their extensive investigation on the structural, chemical, optical, and morphological properties has been outlined in this thesis. Their application as antireflective coatings for Si based solar cells has been covered here.

- After this introductory episode as described in this **chapter 1**, the reader is introduced to the various growth techniques of thin film deposition along with the related plasma mechanisms which are involved in the fabrication of DLC thin films in **chapter 2**.
- **Chapter 3** deals with the different characterisation techniques used to study the various properties of the as grown DLC thin films.
- In **chapter 4**, a detailed study on the optimisation of intrinsic DLC films with nanocrystalline phases at a relatively low temperature and low pressure has been made. The growth technique involved a high-density plasma of CH₄ and Ar gases ignited at a low pressure by radio frequency power driven ICP CVD. Optimization of different flow rates of the gaseous precursors has been carried out. Further, the effect of introducing negative substrate bias application and subsequent bias magnitude variation on the structural, chemical and optical properties of DLC has been analysed in detail.
- In **chapter 5**, the introduction of B as dopant within the DLC matrix under the previously optimised conditions of intrinsic DLC films, followed by the corresponding effect on the structural, optical and most importantly, electrical properties have been conducted. In the later part of this chapter, the effect of increasing the substrate bias magnitude on the

Chapter 1

crystalline quality, optical properties as well as on the electrical conductivities have been investigated thoroughly.

- The development of intrinsic crystalline DLC films in a different aspect of growing in a lower power high-density plasma in a CCP CVD has been explored in **chapter 6**. The effect of varying the pressure and flow rates of precursor gases (CH₄ and H₂) on the different properties of DLC film was studied.
- In **chapter 7**, the practical application of the optimized DLC film (as obtained from **chapter 6**) as antireflection coating on solar cells was carried out to investigate the change in the efficiency and performance of the Si solar cell.
- **Chapter 8** gives a final summary of the work that was intended to be done and how much of it has been accomplished, followed by a future outlook of the DLC films and its applications.

1.6. References

- [1] N.J. Coville, S.D. Mhlanga, E.N. Nxumalo, A. Shaikjee, S. Afr. J. Sci. 107 (2011) 1–15.
- [2] R.W. Luth, Y.N. Palyanov, H. Bureau, Rev. Mineral. Geochem. 88 (2022) 755–808.
- [3] W.S. Choi, B. Hong, Renew. Energy 33 (2008) 226–231.
- [4] A. Grill, Diam. Relat. Mater. 8 (1999) 428–434.
- [5] Q. Yang, S. He, R. Huang, M. Yu, C. Chen, S. Zheng, D. Yun, L. Zheng, Q. Cheng, Diam. Relat. Mater. 111 (2021) 108184.
- [6] H. Zanin, P.W. May, M.H.M.O. Hamanaka, E.J. Corat, ACS Appl. Mater. Interfaces. 5 (2013) 12238–12243.
- [7] H. Sheng, W. Xiong, S. Zheng, C. Chen, S. He, Q. Cheng, Carbon Lett. 31 (2020) 929–939.
- [8] R. Paul, S.N. Das, S. Dalui, R.N. Gayen, R.K. Roy, R. Bhar, A.K. Pal, J. Phys. D: Appl. Phys. 41 (2008) 055309.
- [9] A. Singha, A. Ghosh, A. Roy, N.R. Ray, J. Appl. Phys. 100 (2006) 44910–44914.
- [10] C.R. Lin, D.H. Wei, C.K. Chang, W.H. Liao, K.R. Peng, Jpn. J. Appl. Phys. 50 (2011) 035802.
- [11] D. Das, A. Banerjee, Applied Surface Science 345 (2015) 204–215.
- [12] M. Lubwama, B. Corcoran, K.V. Rajani, C.S. Wong, J.B. Kirabira, A. Sebbit, K.A. McDonnell, D. Dowling, K. Sayers, Surf. Coat. Technol. 232 (2013) 521–527.
- [13] F.C. Tai, S.C. Lee, C.H. Wei, S.L. Tyan, Mater. Trans. 47 (2006) 1847–1852.
- [14] D. Caschera, F. Federici, S. Kaciulis, L. Pandolfi, A. Cusmà, G. Padeletti, Mater. Sci. Eng. C. 27 (2007) 1328–1330.

Chapter 1

- [15] C. Rattanasatien, N. Tonanon, W. Bhanthumnavin, B. Paosawatyanyong, *J. Nanosci. Nanotechnol.* 12 (2012) 642–647.
- [16] J. Xu, H. Fan, H. Kousaka, N. Umehara, D. Diao, W. Liu, *Diam. Relat. Mater.* 16 (2007) 161–166.
- [17] Y. Fu, C.Q. Sun, H. Du, B. Yan, *Surf. Coat. Technol.* 160 (2002) 165–172.
- [18] W. Zhu, Z. Su, J. Guo, K. Li, K. Chen, W. Li, A. Yi, Z. Liao, Y. Luo, Y. Hu, Y. Xu, Q. Lin, X. Meng, *Diam. Relat. Mater.* 122 (2022) 108820.
- [19] Z. Seker, H. Ozdamar, M. Esen, R. Esen, H. Kavak, *Appl. Surf. Sci.* 314 (2014) 46–51.
- [20] J. Beckman, R. B. Jackman, J. S. Foord, *Diam. Relat. Mater.* 3 (1994) 602–607.
- [21] J. Hopwood, *Plasma Sources Sci. Technol.* 1 (1992) 109–116.
- [22] C. -C. Yen, Y. -C. Chang, H. -C. Tsai, W. -Y. Woon, *Carbon* 154 (2019) 420–427.
- [23] A.P. Mousinho, R.D. Mansano, M.C. Salvadori, *Surf. Coat. Technol.* 203 (2009) 1193–1198.
- [24] L. Yu, C.Q. Yun, Y. Huan, X. Ming, H.S. Long, *Appl. Mech. Mater.* 723 (2015) 502–506.
- [25] H. Li, T. Xu, C. Wang, J. Chen, H. Zhou, H. Liu, *Thin Solid Films* 515 (2006) 2153–2160.
- [26] Š. Meškinis, A. Čieglis, A. Vasiliauskas, K. Šlapikas, R. Gudaitis, I. Yaremcuk, V. Fitio, Y. Bobitski, S. Tamulevičius, *Nanoscale Res. Lett.* 11 (2016) 146.
- [27] C.J.H. Wort, R.S. Balmer, *Mater. Today* 11 (2008) 1–2.
- [28] W. Li, X.Y. Tan, Y.M. Park, D.C. Shin, D.W. Kim, T.G. Kim, *Front. Mater.* 7 (2020) 1–8.
- [29] J. Robertson, *Mater. Sci. Eng. R: Rep.* 37 (2002) 129–281.
- [30] W.H. Fang, S.D. Peyerimhoff, *Mol. Phys.* 93 (1998) 329–339.
- [31] J.C. Pu, S.F. Wang, C.L. Lin, J.C. Sung, *Thin Solid Films* 519 (2010) 521–526.
- [32] P. Avouris, Z.H. Chen, V. Perebeinos, *Nat. Nanotechnol.* 2 (2007) 605–612.
- [33] J. Huang, Y. Zeng, R. Tan, W. Wang, Y. Yang, N. Dai, W. Song, *Appl. Surf. Sci.* 270 (2013) 428–431.
- [34] D. Kar, D. Das, *J. Appl. Phys.* 120 (2016) 025102.
- [35] D. Das, S. Samanta, *Physica E* 128 (2021) 114615.
- [36] R. Kalish, *Carbon* 37 (1999) 781–785.
- [37] M.-A. Pinault, J. Barjon, T. Kociniewski, F. Jomard, J. Chevallier, *Physica B: Condensed Matter* 401–402 (2007) 51–56.
- [38] D. Wu, Y.C. Ma, Z.L. Wang, Q. Luo, C.Z. Gu, N.L. Wang, C.Y. Li, X.Y. Lu, Z.S. Jin, *Phys. Rev. B* 73 (2006).
- [39] K. Thonke, *Semicond. Sci. Technol.* 18 (2003) S20–S26.
- [40] E.A. Ekimov, V.A. Sidorov, E.D. Bauer, N.N. Mel’nik, N.J. Curro, J.D. Thompson, S.M. Stishov, *Nature* 428 (2004) 542–545.
- [41] X.M. He, K.C. Walter, M. Nastasi, *J. Phys. Condens. Matter.* 12 (2000) L183–L189.
- [42] M. Benabdesselam, P. Iacconi, F. Wrobel, A. Petitfils, J.E. Butler, *Diam. Relat. Mater.* 16 (2007) 805–808.

Chapter 1

- [43] M. Rusop, X.M. Tian, S.M. Mominuzzaman, T. Soga, T. Jimbo, M. Umeno, *Sol. Energy.* 78 (2005) 406–415.
- [44] G. Sepold, A. Stephen, S. Metev, *Diam. Relat. Mater.* 8 (1999) 1677–1681.
- [45] M. Nesladek, J.J. Mares, D. Tromson, C. Mer, P. Bergonzo, P. Hubik, J. Kristofik, *Sci. Technol. Adv. Mater.* 7 (2006) S41–S44.
- [46] A.F. Azevedo, R.C. Mendes de Barros, S.H.P. Serrano, N.G. Ferreira, *Surf. Coat. Technol.* 200 (2006) 5973–5977.
- [47] W. Mei, W. Weichen, H. Yujie, L. Musen, *Rare Met.* 31 (2012) 189–192.
- [48] J. Podder, M. Rusop, T. Soga, T. Jimbo, *Diam. Relat. Mater.* 14 (2005) 1799–1804.
- [49] Z. Ren, H. Qin, Y. Dong, G.L. Doll, C. Ye, *Wear* 203031 (2019) 436–437.
- [50] Z.Q. Ma, B.X. Liu, *Sol. Energy Mater. Sol. Cells* 69 (2001) 339–344.
- [51] A. Saravanan, B.R. Huang, K.J. Sankaran, C.L. Dong, N.H. Tai, I.N. Lin, *Appl. Phys. Lett.* 104 (2014) 181603.
- [52] M. Marinkovic, E. Hashem, K.Y. Chan, A. Gordijn, H. Stiebig, D. Knipp, *Appl. Phys. Lett.* 97 (2010) 073502.
- [53] K.Y. Chan, E. Bunte, D. Knipp, H. Stiebig, *Semicond. Sci. Technol.* 22 (2007) 1213.
- [54] S.Y. Myong, K. Sriprapha, S. Miyajima, M. Konagai, A. Yamada, *Appl. Phys. Lett.* 90 (2007) 263509.
- [55] J.-Y. Jung, H.-D. Um, S.-W. Jee, K.-T. Park, J.H. Bang, J.-H. Lee, *Sol. Energy Mater. Sol. Cells.* 112 (2013) 84–90.
- [56] K. Sarkar, D. Das, *Energy Fuels* 37 (2023) 16880–16892.
- [57] D. Banerjee, N.S. Das, K.K. Chattopadhyay, *Appl. Surf. Sci.* 261 (2012) 223–230.
- [58] H. Noda, H. Nagai, M. Shimakura, M. Hiramatsu, M. Nawata, *J. Vac. Sci. Technol. A* 16 (1998) 3170–3174.
- [59] G. Nogay, Z.M. Saleh, E. Özkol, R. Turan, *Mater. Sci. Eng. B* 196 (2015) 28–34.
- [60] D. Das, L. Karmakar, *Nanoscale.* 12 (2020) 15371–15382.
- [61] B. Paosawatyanyong, A. Muakngam, S. Thitianan, *AMR* 93–94 (2010) 699–702.
- [62] M. Gaur, C. Misra, A.B. Yadav, S. Swaroop, F.Ó. Maolmhuaidh, M. Bechelany, A. Barhoum, *Materials* 14 (2021) 5978.
- [63] A.D. Jara, A. Betemariam, G. Woldetinsae, J.Y. Kim, *Int. J. Min. Sci. Technol.* 29 (2019) 671–689.
- [64] W. Zheng, S.-C. Wong, *Compos. Sci. Technol.* 63 (2003) 225–235.
- [65] H. Li, Q. Feng, L. Ou, S. Long, M. Cui, X. Weng, *Int. J. Min. Sci. Technol.* 23 (2013) 855–861.
- [66] S.K. Tiwari, V. Kumar, A. Huczko, R. Oraon, A.D. Adhikari, G.C. Nayak, *Crit. Rev. Solid State Mater. Sci.* 41 (2016) 257–317.
- [67] V. Singh, D. Joung, L. Zhai, S. Das, S.I. Khondaker, S. Seal, *Prog. Mater. Sci.* 56 (2011) 1178–1271.
- [68] A. Tiwari, *Adv. Mater. Lett.* 3 (2012) 172–173.

Chapter 1

- [69] R. Oraon, A. De Adhikari, S.K. Tiwari, G.C. Nayak, RSC Adv. 5 (2015) 68334–68344.
- [70] J. C. Angus, Thin Solid Films 216 (1992) 126.
- [71] M. N. Yoder, Synthetic Diamond: Emerging CVD Science and Technology, First ed., K. E. Spear, J. P. Dismukes eds., John Wiley & Sons, (1994).
- [72] J.E. Field, Rep. Prog. Phys. 75 (2012) 126505.
- [73] S. Nafisi, Nanotechnology in cosmetics. In *Cosmetic Science and Technology*; Routledge: London, UK, 2017.
- [74] R. N. Rao, Nanomaterials in Chromatographic Sample Preparations; Elsevier: Amsterdam, The Netherlands, 2017.
- [75] A.C. Ferrai and J. Robertson, Phys. Rev. B 61 (2000) 14095.
- [76] A. Singha, A. Ghosh, A. Roy and N.R. Ray, J. App. Phys. 100 (2006) 44910.
- [77] J. Liu, T. Yang, H. Cao, Q. Deng, C. Pan, F. Wen, Nanotechnology Reviews 11 (2022) 2839–2856.
- [78] A. Banerjee and D. Das, Appl. Surf. Sci. 273 (2013) 806.
- [79] S. Flege, R. Hatada, W. Ensinger and K. Baba, J. Mater. Res. 27 (2012) 845.
- [80] P.W. May, Philos. Trans. R. Soc. A. 358 (2000) 473.
- [81] H. Yang, Y. Ma, Y. Dai, Funct. Diamond. 1 (2021) 150–159.
- [82] R.E. Smalley, Rev. Mod. Phys. 69 (1997) 723–730.
- [83] F. Diederich, R.L. Whetten, Act. Chem. Res. 25 (1992) 119-126.
- [84] R. Buckminster Fuller, W. Marlin, Garland Publishing, New York, (1984).
- [85] A. Kausar, I. Ahmad, M. Maaza, M.H. Eisa, Membranes 13 (2022) 27.
- [86] R.C. Haddon, Chem. Res. 25 (1992) 127–133.
- [87] P.S. Karthik, A.L. Himaja, S.P. Singh, Carbon. Lett. 15 (2014) 219–237.
- [88] S. Iijima, Nature 354 (1991) 56–58.
- [89] M. Monthioux, V.L. Kuznetsov, Carbon 44 (2006) 1621–1623.
- [90] J. Osterodt, A. Zett, F. Vögtle, Tetrahedron 52 (1996) 4949–4962.
- [91] R.B. Bergmann, Applied Physics A: Materials Science & Processing 69 (1999) 187–194.
- [92] W.A. Badawy, J. Adv. Res. 6 (2015) 123–132.
- [93] S. Sharma, K.K. Jain, A. Sharma, Mater. Sci. Appl. 6 (2015) 1145–1155.
- [94] J. Liu, Y. Yao, S. Xiao, X. Gu, J. Phys. D: Appl. Phys. 51 (2018) 123001.
- [95] B. Sha, A.N. Lukianov, M.G. Dusheiko, V.B. Lozinskii, A.N. Klyui, D.V. Korbutyak, S.E. Pritchin, NickolaiI. Klyui, Opt. Mater. 106 (2020) 109959.
- [96] J.-Y. Jung, H.-D. Um, S.-W. Jee, K.-T. Park, J.H. Bang, J.-H. Lee, Sol. Energy Mater. Sol. Cells. 112 (2013) 84–90.
- [97] K. Sarkar, D. Das, Energy Fuels 37 (2023) 16880–16892.

Chapter 1

- [98] V. Yerokhov, O. Ierokhova, 2016 International Conference on Electronics and Information Technology (EIT) (2016).
- [99] L. Remache, A. Mahdjoub, E. Fourmond, J. Dupuis, L. Lemiti, REPQJ 1 (2010) 191–195.
- [100] A.K. Sood, A.W. Sood, R.E. Welser, G.G. Pethuraja, Y.R. Puri, X. Yan, D.J. Poxson, J. Cho, E.F. Schubert, N.K. Dhar, D.L. Polla, P. Haldar, J.L. Harvey, MSA 03 (2012) 633–639.
- [101] N.P. Klochko, K.S. Klepikova, I.I. Tyukhov, Y.O. Myagchenko, E.E. Melnychuk, V.R. Kopach, G.S. Khrypunov, V.M. Lyubov, A.V. Kopach, Sol. Energy 120 (2015) 330–336.
- [102] N.P. Klochko, V.R. Kopach, I.I. Tyukhov, D.O. Zhadan, K.S. Klepikova, G.S. Khrypunov, S.I. Petrushenko, V.M. Lyubov, M.V. Kirichenko, S.V. Dukarov, A.L. Khrypunova, Sol. Energy 164 (2018) 149–159.
- [103] A. K., A. Varade, N.R. K., S. Dhan, C. M., B. N., P. Krishna, Diam. Relat. Mater. 78 (2017) 39–43.

Chapter 2

Thin Film Deposition Techniques

2.1. Introduction

Thin films are defined as a two-dimensional layer of atoms or molecules of elements extending infinitely in the two directions, while being restricted in one. The thickness of the films varies from few nm to several μm . The process of growing of the thin films in a controlled way thereby regulating its various properties like thickness, physical characteristics as well as its chemical composition has been termed as ‘deposition’. In this chapter, the deposition processes involved for the fabrication of nanostructured carbon thin films are to be discussed. There are various types of deposition processes that assist the formation of these films, which can be broadly categorized as physical and chemical techniques. Different types of deposition processes have their own advantages and disadvantages. Among these, the physical vapour deposition (PVD) from the physical processes and chemical vapour deposition (CVD) from the chemical processes are of utmost interest and beneficial, as far as their applications in electrical and optoelectronic fields is concerned.

The deposition techniques used for the synthesis of carbon (DLC) films presented in this thesis has been described in brief, along with the other important deposition methods.

2.2 Physical vapour deposition (PVD):

This type of deposition technique involves the vaporization of a material in the solid phase, followed by its subsequent reaction with other gaseous precursors present in the reactor chamber while getting transported over the substrates. The gaseous molecules formed after the chemical reactions are then deposited on the substrates, thereby going through a direct phase transition from gas to solid [1]. The step-by-step process is shown in Fig. 2.1.

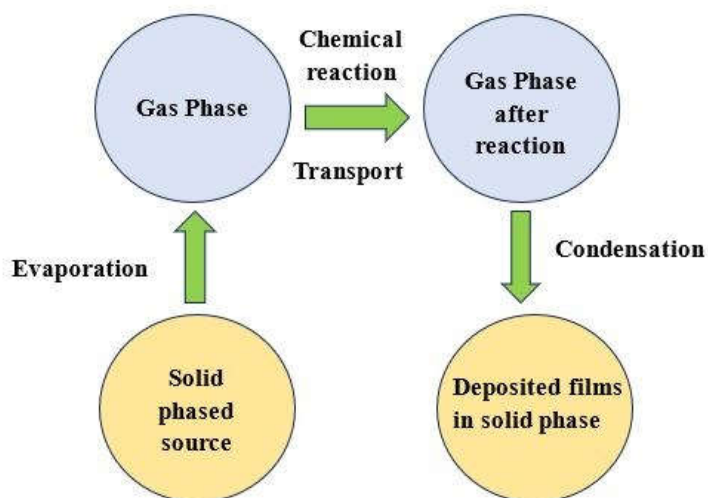


Fig. 2.1: Step by step process of Physical Vapour Deposition.

Chapter 2

The PVD process is advantageous in various ways. It is a simple and straightforward, being cost effective and involving clean, dry and top-quality techniques. Moreover, it is suitable for manufacturing integrated circuits (ICs). However, there are limitations, like, it is difficult to control the stoichiometric composition of the films formed. The PVD process is also not compatible for all types of materials, for instance, it is impossible to vaporize dielectric materials in a PVD set-up [2]. Some of the common PVD processes described here are: (a) vacuum thermal evaporation; (b) ion beam evaporation; (c) pulsed laser deposition and (b): sputter deposition.

- **Vacuum thermal evaporation:**

In this PVD process, the source material is heated to such a high temperature that it reaches its melting point and readily vaporizes into its gas phase [3]. The whole process is conducted in a high vacuum system ($10^{-5} - 10^{-7}$ Torr), so that the molecules of source element in the gaseous phase cannot come into interaction with any other molecules present in the atmosphere. The vacuum is created with the help of diffusion pump attached in support of the rotary pump. Usually, a boat made of Tungsten or Molybdenum (with high electrical resistance) is involved, within which the source material is placed. On increasing filament current to the range of 10-20 A, the source material starts melting, followed by instant vaporization. Deposition of this gaseous element takes place when a substrate is placed in the path of the vapour molecules by the method of condensation and adhesion to the substrates. A coating of the material is formed as a thin film on the substrates. The thickness of the film depends on the amount of source material and the duration of exposure of the substrate surface to the ejecting vapor molecules. This is controlled by a movable metal cover which can be used to block the path of the molecules and cover the substrates.

[Fig. 2.2](#) shows the schematic diagram of the thermal evaporation system. This system is advantageous as: (a) films of excellent purity are obtained, (b) it does not hamper the layers of film already formed on the surface (thus, it is widely applicable for forming electrode layers on already formed films), (c) it is cost effective and does not involve any complications. However, several disadvantages had made this technique unsuitable: (a) only source materials with lower melting points must be used; (b) dielectric materials cannot be used as they cannot be vaporized; (c) only a limited amount of source, depending on the capability of the filament current, can be taken within the crucible and (d) poor adhesion of the film on the substrate. These restricts the formation of good quality films on any type of substrate. Nevertheless, this method has been used for the deposition of Aluminium

Chapter 2

electrodes for electrical conductivity measurements of the DLC films, presented in this work.

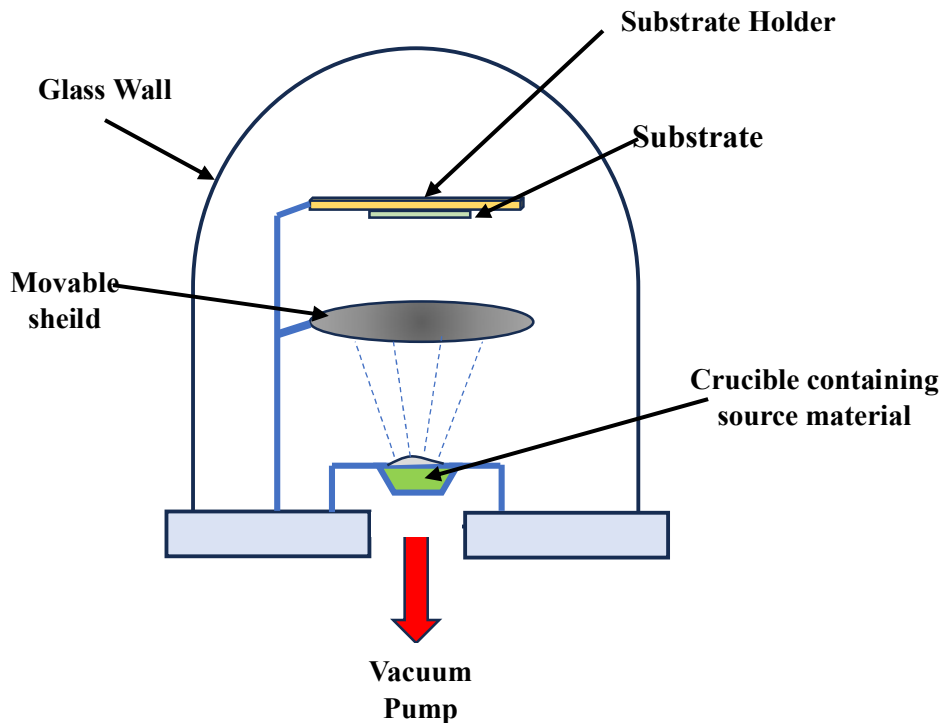


Fig. 2.2: Schematic diagram of vacuum thermal vapour deposition system.

- **Sputtering:**

One of the most important PVD processes, the sputtering is used to form thin films of different materials for a wide range of applications. In this method, the source target is sputtered or etched by energetic ions of noble gases, ejecting atoms from the target surface into the gas phase, followed by deposition on the substrate. The process is conducted in high vacuum environments, where there is no disturbance from the other molecules of air or atmosphere.

A source target material is set at position just perpendicular to the placement of the substrates, within the vacuum chamber. Inert gas, mostly Ar is inserted into the chamber [4]. A DC or RF voltage is applied across the target (anode) and the substrate, due to which a plasma state of Ar^+ is formed. The energy of the Ar^+ ions is controlled by the pressure (within 1-10 mTorr), temperature and the gas flow rate inserted by the throttle valve, temperature controller and mass flow controllers respectively. The energetic Ar^+ ions with strikes the target of the source material with high momentum, thereby ejecting atoms of the source into the plasma state. These ejected atoms get condensed on the substrate, which is the grounded electrode, forming thin films. The

Chapter 2

thickness as well as the structure of the thin films thus formed, depends on the sputtering time. Types of sputtering includes:

➤ DC sputtering:

Here DC negative voltage is applied to the target, such that the Ar^+ ions are attracted to the target, causing ejection of target molecules into the plasma, followed by deposition on the substrate surface. However, since the target (insulator) is neutral, after a certain time, there is accumulation of Ar^+ ions on the target, resulting in a state when Ar^+ ions are no longer attracted towards the target. Thus, there is a gradual decrease in the deposition rate and finally the process comes to an end. In case of metal targets, the DC voltage application does not cause any problem, since the Ar^+ ions get neutralized by the free electrons of metals. This deposition type is thus suitable only for metal targets. Nevertheless, the lower deposition rate due to the formation of lesser Ar^+ ions by DC voltage is a major drawback of the process.

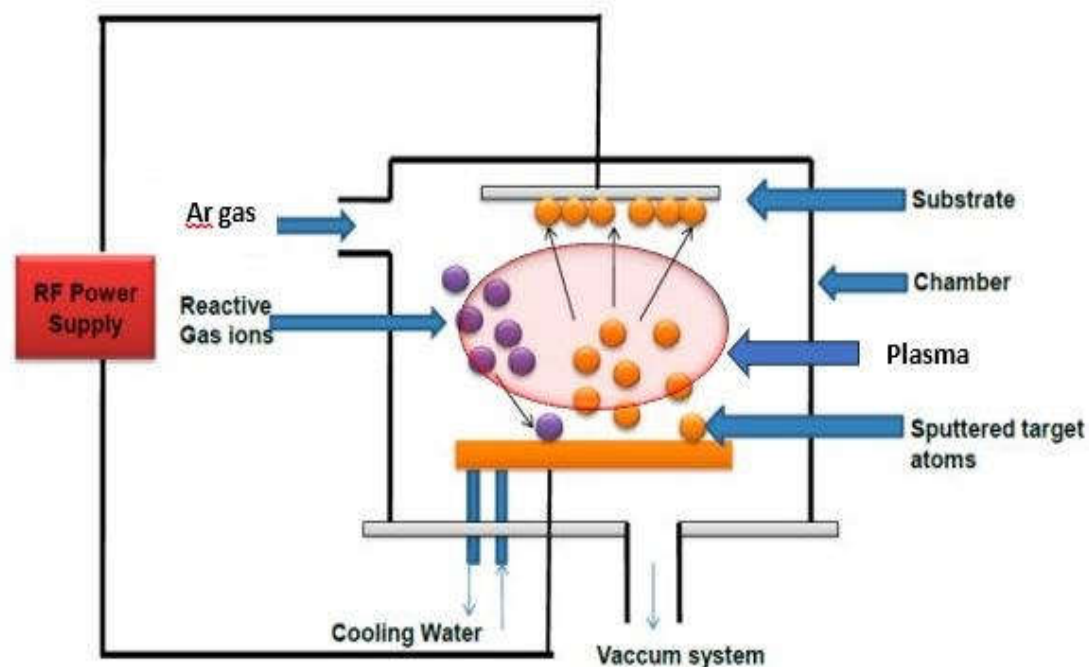


Fig. 2.3: Schematic diagram of RF sputtering.

➤ RF sputtering:

To overcome the above problem formed due to the DC voltage application, an alternative to the DC voltage; i.e., radio frequency generated AC voltage is employed. Here, both the two electrodes, the target and the substrate holder act as cathode and anode alternatively, thereby electrons and holes oscillate in between the electrodes at a radio frequency. Thus, there is no accumulation of Ar^+ ions on the target, facilitating

Chapter 2

continuous film deposition. Moreover, due to the frequent movement of charge carriers within the plasma, increased collisions with Ar molecules generates higher amounts of Ar^+ ions. This increases the sputtering and deposition rate [5–7].

➤ **Magnetron sputtering:**

To further increase the deposition rate, another additional feature is incorporated within the rf sputtering unit. A magnetic field is applied at the target by attaching magnets at the base of the target material, in addition to the electric field by the RF source. This gives extra momentum to the Ar^+ ions so that they strike the target with high energy, ejecting more and more target atoms. These readily gets deposited on the substrate, thereby increasing the deposition rate. However, there is no chance that the Ar^+ ions sputter the deposited film on the substrate surface, since they are confined in the region of mutually perpendicular electric and magnetic fields (i.e., near the target). As a result, the magnetron sputtering system is the most effective sputtering, helpful in obtaining uniform thin films with high deposition rates. A water cooling set up is fitted beneath the sputtering target, circulating chilled water that keeps the target temperature low and prevents it from getting damaged or broken due to the extreme heat generated during sputtering. The major advantages of the sputtering system are pointed as:

- (a). Any type of material (metals to insulators, etc) can be used as target and its thin films can be formed.
- (b). The deposited films can be etched and cleaned if required by just reversing the potentials.
- (c). Films are uniformly deposited; by changing the target size or area, uniform films deposited over large areas can be obtained.
- (d). Films have far better adhesion to the substrate surface compared to other deposition techniques; adhesion quality can be improved by inducing higher kinetic energy to the sputtering ions by varying plasma conditions like pressure, power.

However, there are some drawbacks:

- (a). There are possibilities of the substrate and the deposited film getting damaged by the bombarding ions.
- (b). The target gets damaged due to heat generated during ion bombardment. Thus water cooling set up is necessary for the sputtering system.

Chapter 2

- (c). Too thick coating occurs, due to the high internal steer level.
- (d). Disorders are generated in magnetic targets; A new sputtering gun equipped with modern technology is required to handle magnetic targets.



Fig 2.4: Magnetron sputtering system in our lab, used for depositing TCO layers.

The magnetron system present in our lab is shown in [Fig. 2.4.](#): HindHivac RF magnetron sputtering. The magnetron cathode measures a diameter of 3 inches is attached to the base of the target. Equipped with a movable shutter and a rotatable substrate holder, this system is used to form uniform thin films of TCO layer with controlled thickness and quality, for a work presented in this thesis. A heater, with a maximum temperature of 500 °C, is attached to the substrate holder to maintain the temperature of the substrates. A flow of chilled water underneath the target cools it down, since the target might get damaged and broken due to the heat generated by the energetic bombardment of the target. The vacuum in the chamber is maintained at $\sim 1 \times 10^{-6}$ Torr by diffusion pump backed by a rotary pump. Mass flow controller is used to allow controlled flow of Ar gas into the system at a particular pressure during film deposition.

- **Ion beam deposition (IBD):**

This is a sophisticated PVD process, which involves directing a beam of ions towards a target of source material, thereby ejecting the target molecules or atoms. These sputtered atoms then get deposited on a nearby substrate surface, forming thin films. The main components of this system are (a) ion source, from which ions are generated; (b) ion

Chapter 2

optics, which directs and concentrates the path of the ions within the chamber and (c) the target, towards which the ions are to bombard; (d) the substrate, on which the sputtered atoms from the target gets deposited. The whole process takes place in a vacuum chamber, so as to cut off the interactions with other environmental atoms and reduce contamination risks. Sometimes, a mass analyzer could be an optional addition to the system. Working with highly energetic and concentrated beam of ions, the IBD system, in comparison to the other conventional PVD systems, makes it possible to regulate thickness and produce a dense, superior quality layer of thin films. It also ensures good adhesion of the film to the substrate. However, due to the low efficiency of the ion source, IBD yields a low deposition rate of $\sim 1\text{ \AA/s}$.

- **Pulsed laser deposition (PLD):**

In this deposition technique, a high powered ultra-violet sourced laser is focussed on one or more targets, thereby eroding off the target atoms. These atoms vaporize, forming the plasma within the ultra-high vacuum chamber and get deposited on the substrates as thin films. The distance between the substrate holder and the plane of the targets, positioned parallel to each other, is usually kept in the range of 2-10 cm. Different types of targets are mounted on the plane of the target holder, which is specially designed to rotate such that uniform target ablation and deposition is maintained. The film thickness is controlled by adjusting the counts of laser pulses. [Fig. 2.5](#) shows the schematic diagram of the PLD set-up.

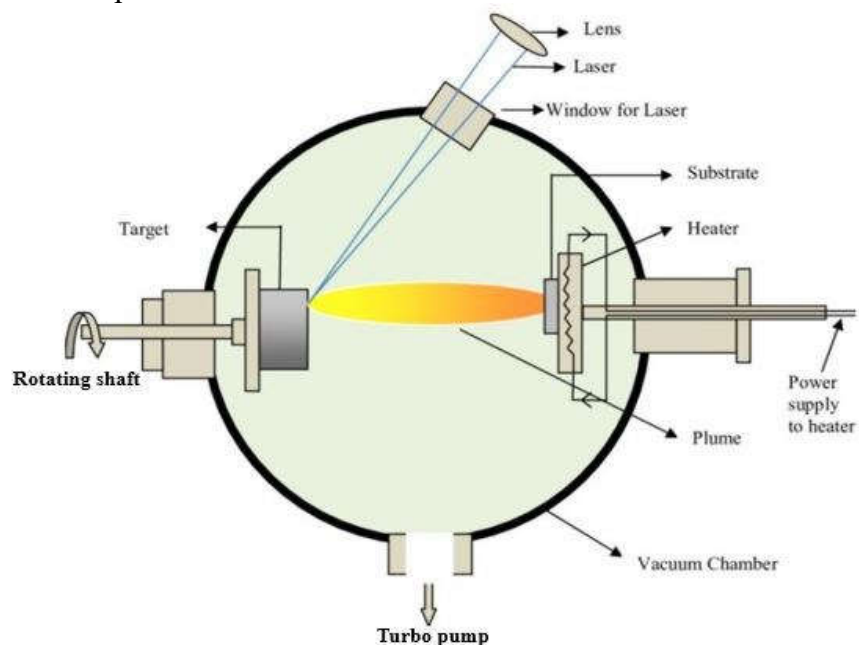


[Fig. 2.5: Schematic diagram of PLD \(adopted from ref \[8\]\)](#)

Chapter 2

Deposition takes place within ultra-high vacuum or in the presence of reactive gases at a specific pressure to form various types of oxide, carbide, or nitride films. Furthermore, a process known as stoichiometry transfer allows for the creation of complex thin films with a stoichiometry that is almost identical to the target [9]. Even Silicon nanoparticles can be prepared using the PLD technique in a contaminant free environment [10]. The versatility of the PLD lies in its ability to change laser parameters like wavelength, pulse etc, as well as the deposition parameters like substrate temperature, pressure and the distance between the substrate and target, as per the desired properties of the thin films.

2.3. Chemical vapour deposition (CVD):

Chemical vapour deposition (CVD) is a commonly used deposition technique, where the thin films of various materials are formed via several chemical reactions between gas phased precursors [11]. Being versatile and unique, the CVD method is widely applicable to form films of desired properties in research laboratories and industries. The total process from gaseous precursors to thin film formation is conducted in a high vacuum deposition chamber.

The source gas precursors are first transferred to the reaction chamber through convection and diffusion; subsequent application of energy (thermal, electric or magnetic) from various sources, results in the formation of a precursor ions and by-products via chemical gas phase reactions. The reactive precursor ions (suitable for film formation) get deposited on the substrates, releasing their energy to reach a stable state forming films. Once they reach the substrate surface, the ions are subjected to surface chemical reactions, prone to attract other reactive precursor ions towards themselves. These are the prime parameters which decide the nature of the film formed [12–14].

The processes of CVD are entirely different from those of PVD. The PVD techniques involve initial evaporation or ion bombardment or sputtering of the source in the solid state followed by condensation of the molecules on the substrate surface. While CVD deals with thermodynamically complex reactions of gas phase molecules as source materials and depends on a lot of parametric conditions of temperature, pressure, power and reaction durations. The reactions occur in the gaseous phase at temperatures far below the melting points of the sources, unlike that in PVD systems. The control of various parameters in the CVD techniques allows one to obtain thin films of excellent purity with desired thicknesses. However, the complex chemical reactions, the thermodynamics and chemical kinetics occurring within are difficult to

Chapter 2

get into. Moreover, the gaseous and solid by-products of the CVD reactions are harmful and toxic to environment. Thus, subsequent techniques are needed to neutralize their toxicity and dispose them off in nature.

There are different types of CVDs, depending on the type of energy source for the initiation of the chemical reactions: (a) Thermal CVD: where the heat energy supplies the necessary kinetic energy to the electrons for chemical reactions; (b) Plasma enhanced CVD : Electric and magnetic fields are responsible for the conversion of the gas molecules into plasma, which initiates the reactions; (c) Photocatalytic CVD : Light source or lasers act as catalysts for the chemical reactions in the CVD.

- **Thermal chemical vapour deposition (Thermal CVD):**

This CVD requires the initiation of the chemical reactions on or near the surface of a heater set at high temperatures, emitting the energy required for the formation of precursor ions from the gas phase molecules. Here, the gases, which are inserted into the reactor chamber, get heated from hot bodies (source of heat/ heater) like hot filaments or hot walls and reaches the excited states, until it decomposes into precursor ions after subsequent chemical reactions. These ions and radicals then diffuse through the reactor chamber, towards the substrates, where it gets deposited as thin films. The reactor chamber is maintained at a pressure by the throttle valves and Turbo pump. Gases are inserted into the chamber in a controlled way by gas lines connected through mass flow controllers. [Fig. 2.6](#) shows the thermal CVD system with mass flow controllers, gas lines, heater source and substrate holder.

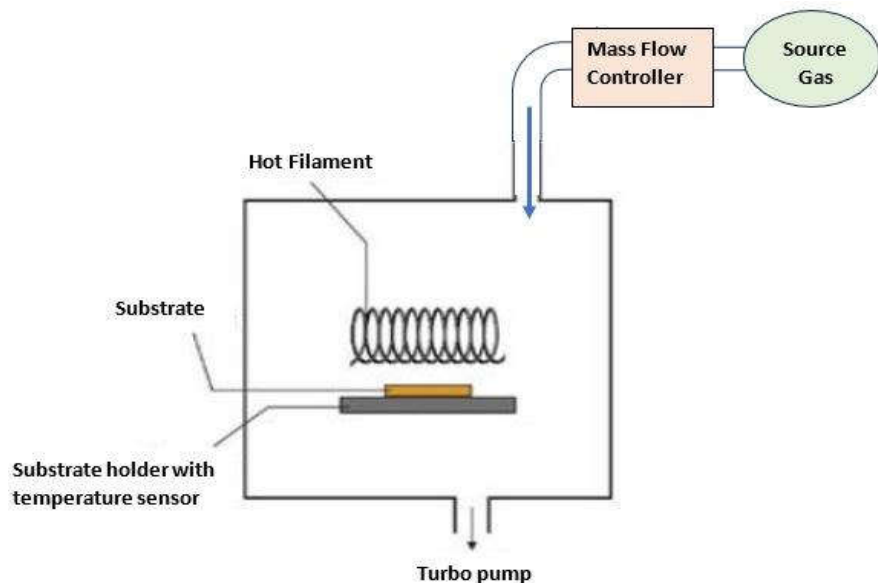


[Fig. 2.6:](#) Schematic diagram of Thermal CVD.

Chapter 2

One of the major challenges of this CVD is that, since it requires a high temperature, the substrates and all the components inside the reactor chamber must withstand the high temperature conditions. Moreover, the gaseous precursors used are extremely toxic and non-volatile, creating hazards to the environment.

- **Plasma enhanced chemical vapour deposition (PECVD):**

The plasma enhanced chemical vapour deposition process (PECVD) is one of the most unique and effective process for the deposition of thin films of high quality, ensuring better adhesion and adjustable properties, from gas sources, utilising the plasma. The gaseous precursors are converted into the plasma state for the initiation of the chemical reactions, necessary for the formation of precursor ions, which in turn actually get deposited as thin films [15]. It is a recognized industrial technique for producing thin layers of micro/nanocrystalline silicon, carbon, germanium along with their oxides, nitrides, carbides, and other essential materials. Even micro/nano crystalline diamond and diamond like carbon, graphene, carbon nanotubes and various nanocrystalline structured thin films can be successfully prepared by PECVD.

For the initiation of the plasma state of the source gases and its inherent sustenance within the deposition chamber for the entire deposition duration, an electric field source is required. As compared to thermal CVD, PECVD requires low temperatures for the formation of films. For instance, diamond and diamond like carbon (DLC) films were grown by hot filament CVD at filament temperatures as high as < 2000 °C [16]. Whereas, DLCs can be grown at temperatures ~ 450 °C using PECVD. This is possible only due to the additional electric source attached with the PECVD system.

One of the major drawbacks of thermal CVD (Hot filament CVD) is that there are high chances of film contamination by the heated filament present within the deposition chamber of the CVD. Diamonds or DLCs are high band gap materials. Metal contamination from the filament can significantly alter the electronic and optical properties as well as chemical composition of the deposits [17]. Thus, films for industrial applications like optical windows and protective coatings for electronic devices, thermal management and semiconductor-based implementations are usually prepared in PECVDs.

Another major advantage of PECVDs over thermal CVDs is that since electronic collisions with the gas molecules inside the plasma chamber are responsible for the formation of precursor ions, there are no kinetic constraints involved, unlike that within the thermal CVD. The plasma emits intense radiations, primarily consisting of electrons, positive ions, neutral and metastable species and photons, which actually determine the

Chapter 2

chemical composition of the film formed layer by layer on the substrate. The bombardment of the ions and plasma species on the substrate surface is essential for the initial nucleation, followed by the growth kinetics and define the structural formations on the surface, as well as the stress within. These mechanisms of the plasma gas phase chemistry facilitate the film formation at a low temperature as compared to thermal CVD. PECVD also ensures high quality adhesion of the films with the substrate that in turn can control the thickness of the films, maintain low defect density and stress.

Various types of PECVD techniques are available for the preparation of carbon thin films (of various characteristics), which have their individual advantages and drawbacks; like radio frequency (RF) operated capacitively coupled (CCP) CVD and inductively coupled (ICP) CVD, PECVDs powered by very high frequency generator like micro-wave plasma CVD, direct current (DC) CVD, and electron cyclotron resonance (ECR) CVD. Among all these, the RF PECVD systems are commonly used in industries and laboratories for their non-hazardous moderate frequency range (13.56 MHz). It enables the formation of gaseous precursors by high energy electronic collisions, thereby creating uniform thin films of a wide variety of materials, without involving high temperatures in a controlled environment.

➤ **Capacitively coupled plasma enhanced CVD (CC PECVD):**

Radio frequency driven RF capacitively coupled plasma enhanced CVD is the most commonly used CVD in industries. It consists of two parallel plate electrodes, which act as capacitors when an electric field supplied by an ac power source at radio frequency is applied. One of the electrodes is grounded and acts as the substrate holder while the other is connected to the RF power. The distance between the two electrodes can be adjusted to get the desired plasma density and the flux of ions which determine the characteristics of the film formed. The entire system is within a high vacuum chamber, the pressure being regulated by the Turbo pump in backing with the rotary pump. Gas sources are inserted within the chamber at controlled flow rates by mass flow controllers. The substrate heater is maintained at a specific temperature by a temperature controller. When the electric field is applied between the electrodes at a particular temperature and pressure, the gas molecules in between them gets dissociated into precursor ions and other metastable species forming the plasma. These ions get attracted towards the substrate and get deposited as the thin films [18]. Fig. 2.7 shows the schematic diagram of the RF driven CCP CVD system.

Chapter 2

The CCP CVD system has been used in a work presented in the thesis for the formation of DLC thin films, where the precursor gases were CH₄ and H₂. A substrate temperature of 450 °C was maintained by the heater and a low RF power was used to supply the electric field in between the electrodes.

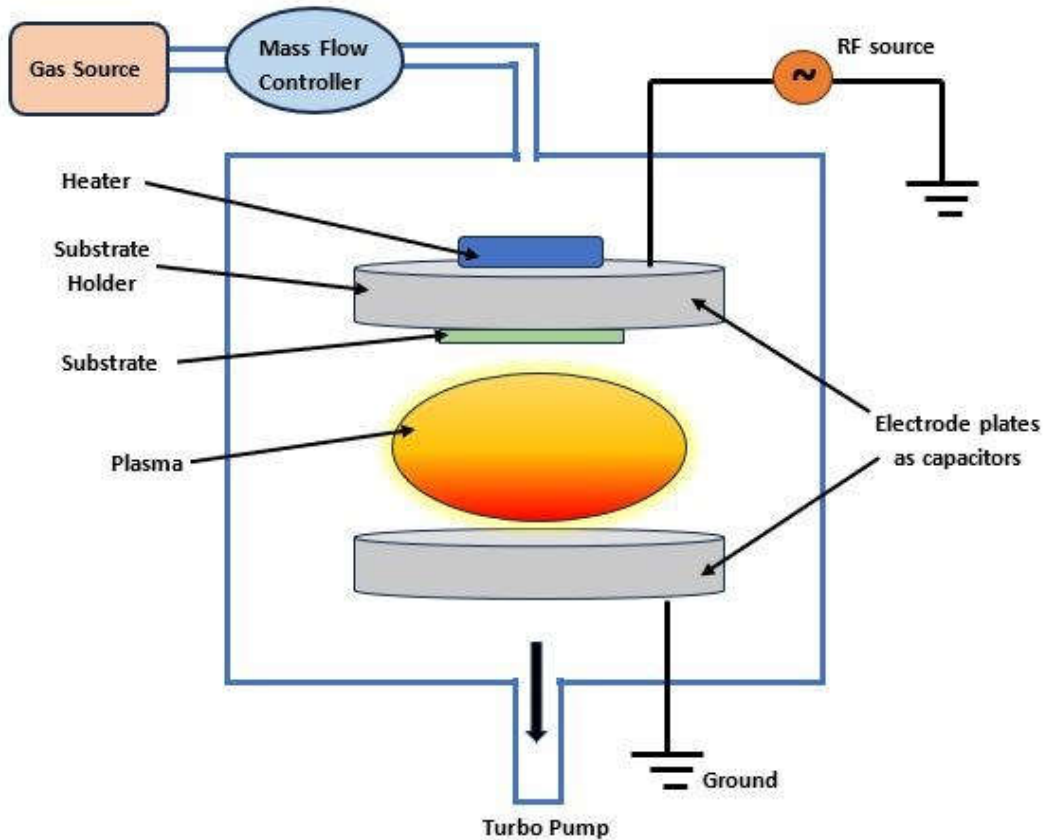


Fig. 2.7: Schematic diagram of RF CCP CVD system.

➤ Inductively coupled plasma enhanced CVD (ICP CVD):

Although CCP PECVD systems are widely in use in the industries for the formation of uniform thin films, there had always been a desire for improvising the growth techniques, which would not only incorporate the advantages of CCP CVD, but also reduce the energy involved in the process, along with the production of high-quality films. The advantage of the plasma growth process lies in the high energy of the electrons within the plasma, which facilitates the excitation and ionization of precursor gas molecules. Plasma maintained at high deposition pressure results in higher growth rates of crystalline diamond thin films. However, achieving uniformity of films over large areas is challenging at high deposition pressures [19]. Low pressure ensures uniform deposition over large areas, but the growth rate is reduced due to the formation of low-

Chapter 2

density plasma. The inductively coupled plasma (ICP) CVD system is a promising high-density plasma source (electron density $\sim 10^{12} \text{ cm}^{-3}$) that provides a high deposition rate due to its high dissociation efficiency even at low pressures. Its low plasma sheath potential near the chamber walls minimizes ion bombardment on the substrates, enhancing uniformity. It also ensures excellent uniformity of plasma parameters both axially and radially, facilitating easier crystallization in the film network. [20,21]. These are the properties which elevates it from the conventional CCP CVD system.

The system consists of an inductive coil, arranged in planar, spiral or helical shaped and coupled with the RF power source. RF power, generated at 13.56 MHz frequency is applied across this inductively coupled arrangement in order to produce the magnetic flux. A matching network is connected in series with the RF power to minimize the reflected power. The RF current produces a magnetic flux that enters the discharge zone and creates a solenoidal RF electric field. This electric field accelerates the free electrons in the discharge region and keeps the plasma alive. A schematic diagram of the ICP CVD system in our laboratory is demonstrated in [Fig. 2.8](#).

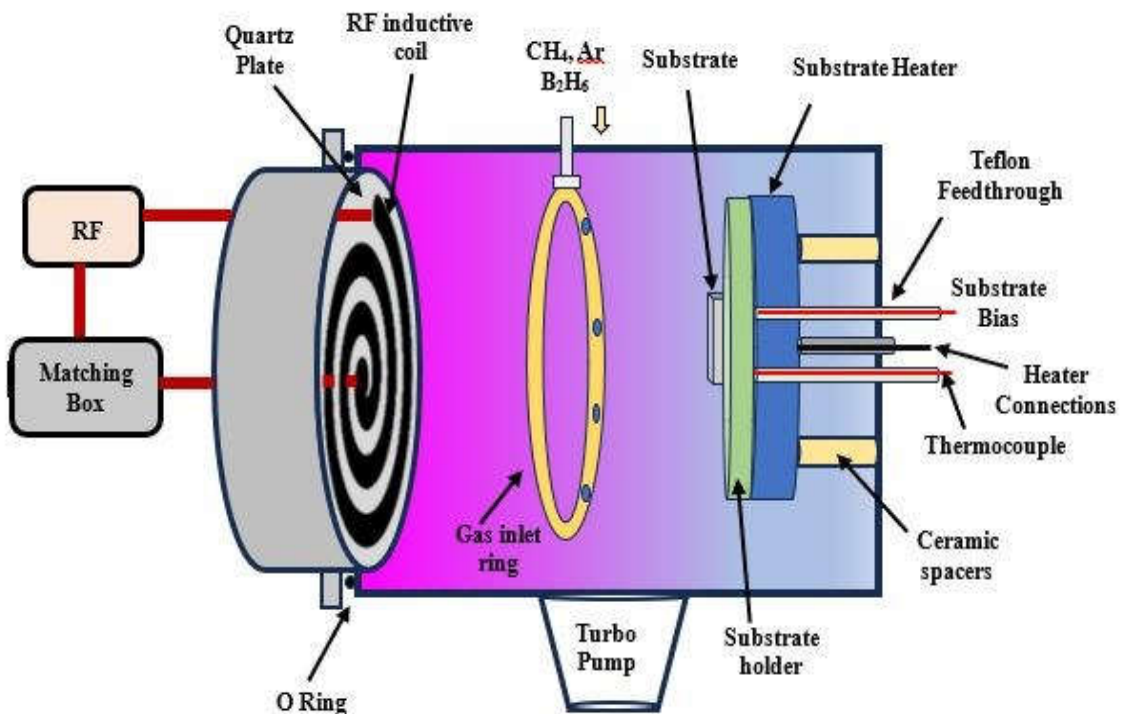


[Fig. 2.8: Schematic diagram of ICP CVD system used in our laboratory.](#)

Intrinsic and B doped DLC films, which were elaborately studied and presented as a part of this thesis had been prepared by the RF power driven ICP-CVD system present in our laboratory. A photograph of the system is shown in [Fig. 2.9](#). The main components which constitute the ICP CVD include the deposition chamber, the pumping

Chapter 2

systems, the gas flow controllers, and the source gas cylinders. The byproducts are intoxicated by a series of water pump and scrubber, before being flushed out into the environment. The deposition chamber or the reactor is a cube with each side measuring 30 cm and is composed of stainless steel of grade 316. This is maintained at high vacuum of $\sim 1 \times 10^{-6}$ Torr by a turbo molecular pump aided by a rotary pump prior to deposition. The pressure during the deposition is regulated by an automated throttle valve attached to the base of the reactor. The electric field is produced when an RF power (of maximum magnitude 1000 W) is applied across the coplanar four antennae spiral inductive coil, via the matching box. The temperature of the substrate can be regulated in the range from 0 to 500 °C via the temperature controller and a thermocouple attached to the back side of the substrate holder. Provision for an external negative DC bias voltage application is also present at the back side of the substrate. Gas flow to the reactor is controlled by a set of mass flow controllers. Source gases of CH₄ and Ar were used for the preparation of intrinsic DLC films. An addition of B₂H₆ (1% in He) was used for the fabrication of B doped DLC films.

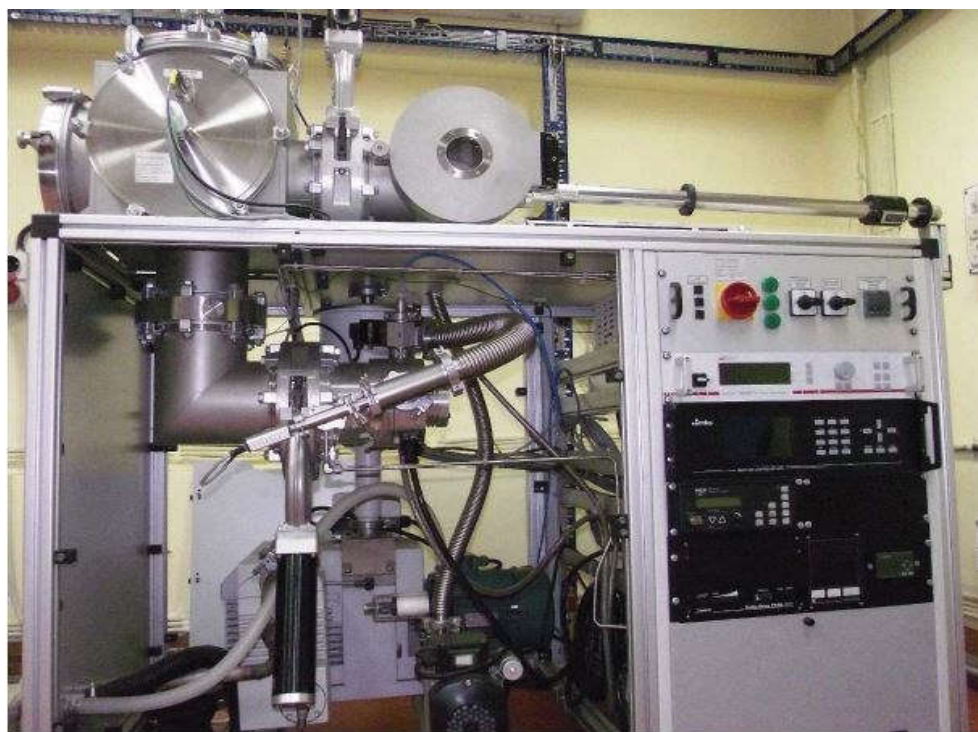


Fig. 2.9: Photograph of the ICP-CVD system used in our laboratory, used for the growth of DLC and B-doped DLC thin films.

➤ Microwave plasma enhanced CVD (MW PECVD):

Among the other PECVDS, the microwave plasma enhanced CVD system is a high-density plasma CVD, operating at a higher frequency of 2.45 GHz. At such a high

Chapter 2

frequency, the electrons and plasma ions within the reactor oscillates, unlike other plasma CVDs. The process involves microwave energy for the dissociations of the gas molecules in the reactor chamber, forming the plasma. The oscillating motion of the plasma ions and electrons collides with themselves as well as other undissociated molecules in a repetitive and systematic manner, creating more and more precursor ions, thereby generating a highly dense plasma state. This helps in uniform film deposition with desirable properties. The MW PECVD method offers some great advantages over other PECVD systems: (a) Since it does not involve any electrodes within the reactor chamber, there is no chance of contamination from the degradation of electrodes; (b) it produces films with good qualities and extreme adhesion to the substrates; (c): It offers higher deposition rates as compared to other PECVDs. However, there are limitations within the technique itself. The use of such a high frequency source is extremely hazardous for any living being. Thus, the system needs to be properly shielded before being used. Another issue is that, the initiation of the microwave plasma and its sustainence is possible at high deposition pressures (~several Torrs) as compared to RF PECVD systems. Fig 2.10 demonstrates the schematic representation of MW PECVD.

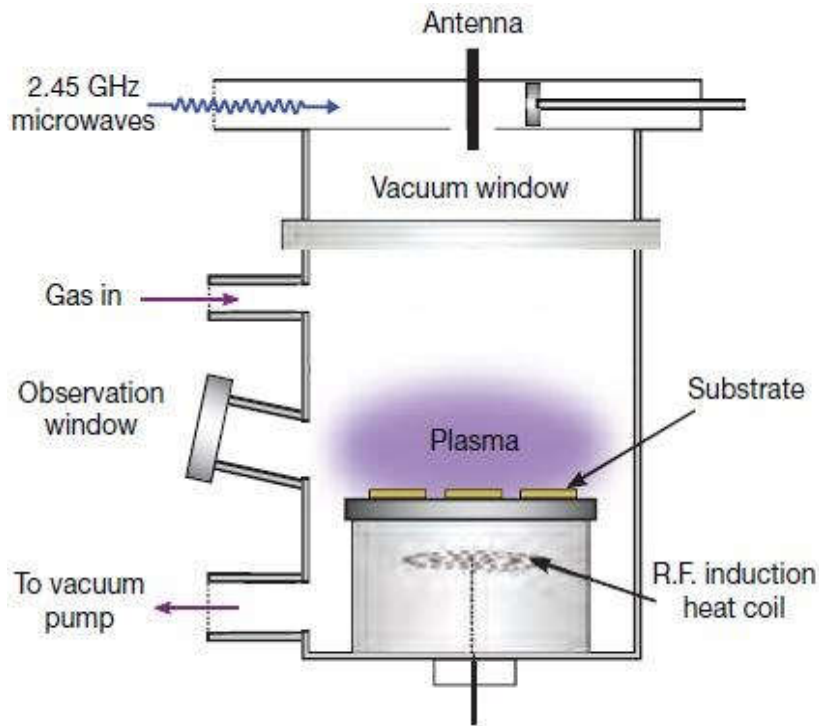


Fig. 2.10: Schematic diagram of microwave CVD (adopted from [22]).

Chapter 2

2.4. Plasma physics and chemistry in PECVD:

There are various ways in which the plasma can be initiated: (a) by the application of high heat energy to the gases; (b) by the application of intense electric and magnetic fields to the source gases. The gas molecules are forced to collide with each other under such extreme conditions, generating ions, electrons and neutral species, which exist in a thermodynamic equilibrium state. In a non-equilibrium or metastable state, the ions and electrons are usually more active compared to the neutral species. This state is referred to as the ‘cold’ plasma.

Generation of plasma in PECVDs takes place due to the application of radio frequency powered electric field to the source gases. The free electrons in the gases are the first to interact with the electric field due to their unbound nature and obviously due to their lower masses. The ions and neutral particles remain undisturbed. Thus, during elastic collisions with the gas species, the energy loss of the accelerated electrons is negligible due to the large mass difference. However, as long as this energy is lower than the threshold energy, this (energy loss) remains insignificant even in inelastic collisions [23]. Electrons with energies higher than threshold energy and above bombard gas species with higher masses to generate reactive ions, which even generate a slight amount of heat energy, increasing the temperature of the plasma. Since the plasma electrons are highly active, moving everywhere around the reactive chamber, the core of the plasma consisting of the precursor ions remain positively charged with respect to the electrodes. In the presence of the electric fields, these precursor ions get attracted towards the electrode which is grounded and bombard on the substrates which are attached on to the grounded electrode. The bulk of the plasma is maintained at a steady potential, where all sorts of ionization and dissociations takes place due to the removal of electrons from the sheaths. The intense radiations emitting from the plasma is due to the excitations of the electrons during dissociation and is observed only in the bulk region of the plasma; the sheaths are comparatively darker, where no dissociation takes place. The positive precursor ions reach the substrates by diffusion, where they are subjected to subsurface interactions. All these phenomena influence the properties of the thin films [24].

2.5. Role of ions:

Ions present within the plasma play a very important role in the thin film formation as well as in shaping up their characteristics. The first step in the approach of plasma ions towards the film formation is bombardment of ions on the substrate surface. Ion bombardment can be beneficial as well as have an adverse effect on the growth of thin films. The bombarding ions

Chapter 2

at the initial stage causes nucleation on the substrate surface, which is the first step for film growth. Subsequent bombardment creates second and third nucleation centres, which is beneficial for the growing film layers. However, excessive bombardment with high energy ions on the already grown film surface causes etching of the grown layers and is detrimental to the crystalline structures already formed. It has been found that the ions in the plasma are responsible for $\sim 70\%$ of the microcrystalline structure formation in thin films grown in PECVD [25]. When the deposition rate is high, it is necessary to suppress the energy of the bombarding ions in order to have a microcrystalline structure of the growing films. Plasma parameters like RF power, excitation frequency, gas pressure, temperature, flow rates of the source gases and the configuration of the electrodes determine the energy of the bombarding plasma ions. The density of the electrons in the plasma determines the ion density. The kinetic energy of the ions is obtained from the temperature of the electrons. According to Maxwell Boltzmann range, the electron average energy (E_{av}) is given by the formula:

$$K_B T = \frac{2E_{av}}{3} \quad \text{eqn (2.1)}$$

Where K_B is Boltzmann constant and T the electron temperature. The peak ion energy of the plasma decreases with the excitation frequency, since higher the frequency, higher is the electron density and lower is the temperature of the electrons [26]. This is the case with RF power described in [27]. The power delivered through the RF source is directly proportional to the amplitude of plasma excitation.

In a PECVD, the presence of effective precursor ions at the surface of the growing films within the same plasma, determines whether the film would be amorphous or microcrystalline or a mixture of both. Here, it is important to emphasize that, even at low substrate temperatures (T_s), the presence of ions in the case of high frequency would increase the surface diffusion of impinging species, which is a prerequisite for the material to acquire good crystallinity [28]. Thus, the crystallinity of the thin films is higher in case of very high frequency (VHF) CVD like MW CVD [27]. The truth of this concept depends on the condition that the energy of the impinging ions on the growing films must be less than the minimum energy required for formation of defects. The peak of the ion energy distribution is dependent on the excitation frequency. For higher frequencies of ~ 70 MHz and above, the peak of the ion energy is ~ 14 eV. However, for RF (13.56 MHz), the peak occurs at ~ 45 eV. A possible way to enhance crystallinity of thin films and reduce the defect density is to introduce deuterium instead of hydrogen as the diluent gas. This is because deuterium, being heavier in mass compared to

Chapter 2

hydrogen, possesses a lower rate of electron loss, lower electron temperature and hence bombards the growing surface with lower energies [29].

Dilution with inert gases within the plasma is a possible method to create high density plasma at low temperatures and low pressures as well as low powers. The inert gases employed for this purpose are Ar, He, Ne, Kr and Xe [30,31]. The use of Ar as a diluent for carbon films causes columnar growth while Xe causes damage to the growing film surface. Introducing He into the PECVD chamber for Carbon film growth has a similar effect as that of radio-active hydrogen or deuterium. He, being light weighted, the energy with which the metastable He bombards on the growing surface is mild as compared to other inert gases. The energy of the growing surface increases optimally with the impingement of the He ions on it, such that it activates the structural relaxation process, enabling the development of a more compact and organized network.

2.6. Growth mechanism of thin film deposition:

Thin films are deposited on the substrates by the arrangement of atoms in the form of clusters or nuclei. When the arrangement of atoms in the lattice of the substrate material matches that of the film which is to be formed on it, the nucleation is typed as homogeneous; alternatively, it is termed as heterogeneous nucleation. Three basic steps are involved in the formation of thin films [32]:

- The formation of precursor ions, molecules or clusters in the plasma state
- The drift or the transport of the precursor species towards the substrates
- The adsorption of these on the substrate surface

Fig. 2.11 shows the steps of thin film deposition. As the precursor species approach the surface of the substrate, a series of surface and subsurface interactions occur, before the thin films take their final state. These are listed as below [33]:

1. The precursor ions approaching the substrate, complete loose their kinetic energy on interaction with the substrate atoms, thereby producing local heat.
2. Since the species are not in thermal equilibrium, they hover on the surface, finding a thermally stable state forming clusters by interacting with other impinging precursor ions.

Chapter 2

3. The clusters coalesce to form bigger clusters until they reach thermodynamic stability and can overcome the nucleation barrier to bond with the substrate lattice atoms. This step is termed as nucleation stage.
4. While forming clusters, the precursor ions can merge in either ways; laterally or columnar (i.e., perpendicular to the substrate). The lateral clustering is thermodynamically favourable, forming islands.
5. After initial nucleation, the smaller islands coalesce to form larger islands on the substrate. At this point, new nuclei are also formed. This stage is called coalescing stage.
6. Clustering continues until all the gaps on the substrate surface are filled to initially form a porous network, and finally a continuous film network is formed.

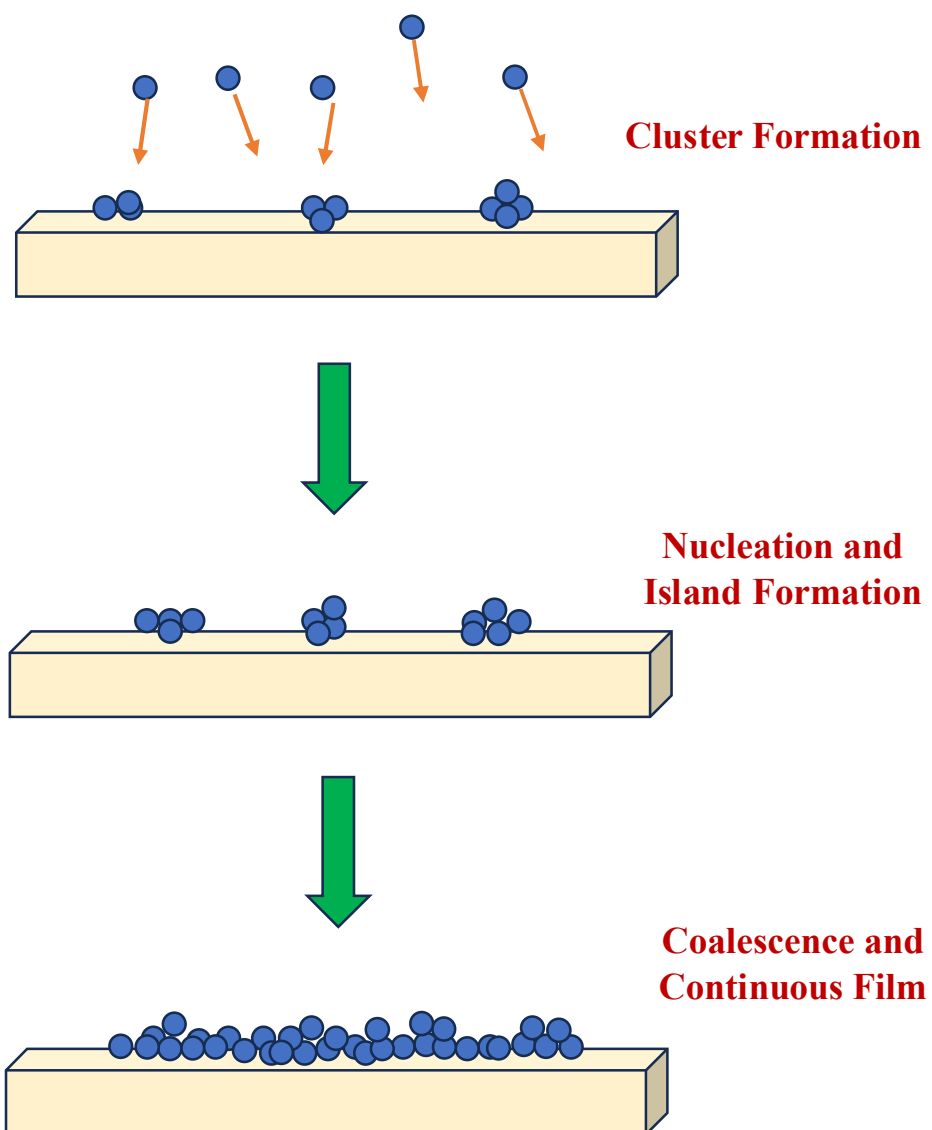


Fig 2.11: Step by step representation of the thin film deposition process.

Chapter 2

2.7. References:

- [1] D.M. Mattox, Handbook of physical vapor deposition (PVD) processing: Film formation, Adhesion, surface preparation and contamination control, Noyes publications (1998) ISBN: 0-8155-1422-0.
- [2] V. Ramakrishna, A.S. Oberai, P.A. Farrar, D.W. Kemmer, P.A. Totta, N.G. Koopman, M.B. Small, Future Requirements for High Speed VLSI Interconnections, Proc. 4th IEEE VLSI Multilevel Interconnec. Conf. (1987) 27.
- [3] N. Abid, A.M. Khan, S. Shujait, K. Chaudhary, M. Ikram, M. Imran, J. Haider, M. Khan, Q. Khan, M. Maqbool, Advances in Colloid and Interface Science 300 (2022) 102597
- [4] B.N. Chapman, S. Mangano, “Thin Film Deposition Processes and Techniques”, Noyes Publication, New Jersey, (1988).
- [5] V. Thaiyalnayaki, M.F. Cerqueira, J.A. Ferreira, J. Tovar, Vacuum 82/12 (2008) 1433.
- [6] R. Saleh, N. Nickel, Thin Solid Films 427 (2003) 266.
- [7] L. Yun, Y.C. Chen, J. Yun, S.Z. Liang, J.C. Hui, Y. Wei, L.X. Wei, Chin. Phys. Lett. 32 (2015) 046802.
- [8] J. Mittra, G.J. Abraham, M. Kesaria, S. Bahl, A. Gupta, S.M. Shivaprasad, C.S. Viswanadham, U.D. Kulkarni, G.K. Dey, MSF 710 (2012) 757–761.
- [9] J.H. Kim, K.A. Jeon, G.H. Kim, S.Y. Lee, Opt. Mater. 27 (2005) 991.
- [10] R. Okada, S. Iijima, Appl. Phys. Lett. 58/15 (1991) 1662.
- [11] L. Sun, G. Yuan, L. Gao, J. Yang, M. Chhowalla, M.H. Gharahcheshmeh, K.K. Gleason, Y.S. Choi, B.H. Hong, Z. Liu, Nat Rev. Methods Primers 1 (2021) 5.
- [12] T. Sato, Jpn. J. Appl. Phys. 6 (1967) 339–347.
- [13] Gemini 2 Product Brochure, Gemini Research, Inc. Fremont. CA.
- [14] D. Richman, RCA Rev. 41 (1997) 613.
- [15] A. Michelmore, J.D. Whittle, R.D. Short, Frontier. Phys. 3 (2015)1.
- [16] N. Dilawar, S. Sah, B.R. Mehta, V.D. Vankar, Bull. Mater. Sci. 19 (1996) 467–473.
- [17] J.-M. Bonard, Thin Solid Films 501 (2006) 8–14.
- [18] Y.X. Liu, Y.R. Zhang, A. Bogaerts, Y.N. wang, J. Vac. Sci. Technol. A 33 (2015) 020801.
- [19] H. Noda, H. Nagai, M. Shimakura, M. Hiramatsu, M. Nawata, J. Vac. Sci. Technol. A 16 (1998) 3170–3174.
- [20] J. Hopwood, Plasma Sources Sci. Technol. 1 (1992) 109–116.
- [21] G. Nogay, Z.M. Saleh, E. Özkol, R. Turan, Mater. Sci. Eng. B 196 (2015) 28–34.
- [22] S. Eaton-Magaña, U.F.S. D’Haenens-Johansson, Gems & Gemology 48 (2012) 124–127.
- [23] M. Rand, J. Vac. Sci. Technol. 16 (1979) 420.

Chapter 2

- [24] E.A.G. Hamers, A. Fontcuberta Morral, C. Niikura, R. Brenot and P. Roca Cabarrocas, *J. Appl. Phys.* 88 (2000) 3674.
- [25] M. Kondo, S. Yamasaki and A. Matsuda, *J. Non-Cryst. Solids*, 266 (2000) 544.
- [26] M. Nisha, K.J. Saji, R.S. Ajimsha, N.V. Joshy and M.K. Jayara, *J. Appl. Phys.* 99 (2006) 033304.
- [27] H. Keppner, U. Kroll, P. Torres, J. Meier, D. Fischer, M. Goetz, T. Tscharner and A. Shah, *Proc. 25th IEEE PV Spec. Conf.* (1996) pp. 669.
- [28] M. Kondo and A. Matsuda, *Thin Solid Films* 1 (2001) 383.
- [29] S. Veprek, F.A. Sarrott and Z. Iqbal, *Phys. Rev. B* 36 (1987) 3344.
- [30] D. Das, M. Jana and A.K. Barua, *J. Appl. Phys.* 89 (2001) 304.
- [31] D. Das and K. Bhattacharya, *Jpn. J. Appl. Phys.* 46 (2007) L1006.
- [32] P. M. Martin, *Handbook of Deposition Technologies for Films and Coatings: Science, application and technology*, *Elsevier Inc.*, (2010), ISBN: 13:978-0- 8155-2931-3.
- [33] K. Seshan, *Handbook of Thin Film Deposition Processes and Techniques: principles, method, equipment and applications*, *Noyes publications*, (2002), ISBN: 0-8155-1442-5.

Chapter 3

Thin film characterization techniques

Chapter 3

3.1. Introduction

In order to study the various properties of the deposited thin films, they are subjected to different types of characterization techniques. Each individual technique has a different and unique role in bringing out a different character of the film. For a complete information about the thin films, a clear concept about its physical nature, structural and morphological properties, optical, electrical characteristics, and compositional elements is desired. In this chapter, the experimental arrangement and the scientific concepts, along with the working principle behind each of the characterizing units, used to study the thin film properties are discussed.

3.2. Optical Properties:

➤ UV-Vis NIR optical spectroscopy

When light is incident on the surface of a thin film, a part of it is transmitted through it, while part of it is absorbed. The rest of the light is reflected from its surface itself. This spectroscopy is obtained when there is an electronic transition from the valence band to the conduction band when light is incident on the material. The wavelength range of the Ultra-Violet region is 200-400 nm, while that of the Visible range is 400-700 nm and that of the NIR region is 700-2600 nm [1].

The band gap E_g of any material can be determined using this spectroscopy [2]. The nature of E_g can be direct or indirect. When the minimum energy level of the conduction band is in the same k space as that of the maximum energy level of the valence band, then electronic transition takes place directly at the same k value. This is the direct band gap. On the other hand, when the minimum energy level of the conduction band is at a different k space than that of the maximum level of the valence band, then electronic transition occurs at a different k value through intermediate steps, transferring momentum. These materials are termed as indirect band gap semiconductors [3].

Considering zero net reflections for transparent materials, when the incident light, consisting of photons with energy E_{ph} is greater than the optical band gap E_g of the material, then it is absorbed by the material. If E_{ph} is less than E_g , the light gets transmitted. The ratio of the intensity of the transmitted light to that of the light incident on it is determined by the thickness of the film, traversed by it and the photon energy (wavelength) of the incident light. If $I(x)$ is the intensity of the light after covering a distance x , then according to Beer-Lambert's law [4],

$$I(x) = I_o \exp(-\alpha x) \quad \text{eqn (3.1)}$$

Chapter 3

Where I_0 is the intensity of the incident light at $x = 0$ and α is the absorption co-efficient of the film. Here, if A denotes the absorbance of the film of thickness d , then α can be expressed as

$$\alpha = \frac{2.303 A}{d} \quad \text{eqn (3.2)}$$

According to Tauc, based on the assumption that the density of states of the amorphous semiconductor material is parabolis near the edges of the band gap, the optical band gap E_g is given by [5-7]:

$$(\alpha h\nu) = B (h\nu - E_g)^n \quad \text{eqn (3.3)}$$

B is the Tauc's constant, depending on the band shapes in the k space and $h\nu$ is the photon energy. The value of n signifies the nature of band gap. The exponent n can have different magnitudes depending on the band edge distribution, e.g., 3, 2, 3/2 and 1/2, which are related to the indirect forbidden, indirect allowed, direct forbidden and direct allowed band distribution, respectively [8]. Extrapolation with the linear portion of the fitted graph on the photon energy axis gives the band gap energy (E_g) of the material. [Fig. 3.1](#) shows the Tauc's plot of a DLC thin film.

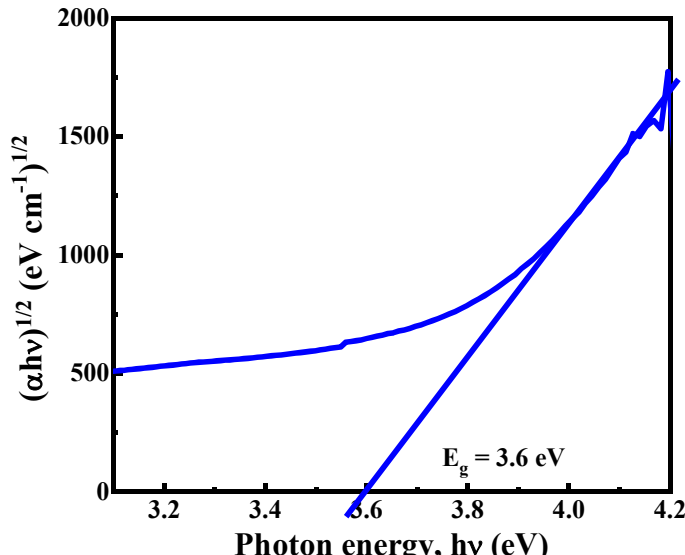


[Fig. 3.1:](#) Tauc's plot of a DLC thin film grown on glass.

The schematic diagram of the UV-Vis NIR spectrophotometer representing the various components is shown in [Fig. 3.2](#) below.

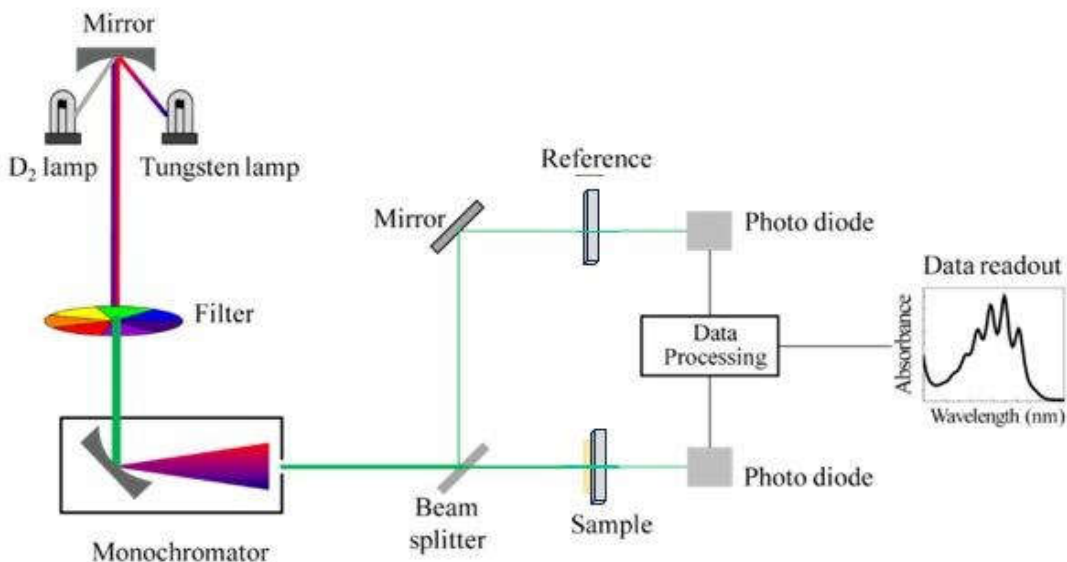


Fig. 3.2: Schematic diagram of UV-Vis NIR spectrophotometer.

The instrument used for the study of optical phenomena is Agilent Cary 5000. The source of light is incident on the filter followed by a monochromator such that a beam of a certain wavelength is projected at a time. The wavelength of the incident ray keeps on changing from 200 nm to 1500 nm. This beam is splitted into two rays by a beam splitter, one of which is directed towards the reference glass substrate and the other is projected on the thin film grown on the glass substrate. The transmitted rays are analyzed by photo diode detectors and the spectra is obtained in the software connected to the computer. Different types of analysis are provided within the software to obtain transmittance, absorbance and reflectance spectra of the films.

- **Determination of optical parameters:**

Two of the most important fundamental optical properties that determine how an incident light interacts with a material are extinction coefficient and refractive index of the material. The extinction coefficient (k) is a measure of the amount of light is absorbed as it traverses unit distance through the material. Refractive index (n) of a material determines the reduction in the speed of incident light as it passes through the material with respect to its speed in vacuum.

Now using the transmittance and reflection data two optical constants i.e., (i) extinction coefficient (k) and (ii) RI (n) of the DLC thin films can be measured [9] from two following equations:

Chapter 3

$$k = \frac{\alpha\lambda}{4\pi} \quad \text{eqn (3.4)}$$

α being the absorption co-efficient (eqn 3.2) and λ is the wavelength of the incident light, and

$$n = \left[\frac{4R}{(1-R)^2} - k^2 \right]^{1/2} - \frac{(R+1)}{(R-1)} \quad \text{eqn (3.5)}$$

R being the surface reflectance of the films.

3.3. Physical properties:

➤ Profilometer

An important tool for the measurement of thickness of the thin films is the stylus profilometer. The vertical depth of the thin films over a given horizontal area along with the surface roughness of the films can be determined by this instrument. In this work, we estimate the thickness of thin films using the Dektak 6M stylus profilometer, a sophisticated surface texture measuring device that uses a step-height measurements method. Thickness ranging from nm to several hundreds of microns can be obtained with accuracy. The stylus, whose tip is made of diamond crystal, is forced to be in contact with the surface of the film and is made to hover on the surface laterally for a pre-specified length contact force through vertical stylus displacement. By changing the position of the stylus, both vertically and horizontally, it can monitor the minor surface variations on the films. The vertical shift of the stylus due to the surface modulations, generates an electrical signal, giving an idea about the step height. However, since the stylus is in direct contact with the surface, films of soft textures (like organic films) are prone to get damaged by the stylus. Thus, this is suitable for relatively films which are hard and stiff.

The schematic of a stylus profilometer (acquired from ref [10]) showing the different parts of operation is shown in Fig. 3.3. While the diamond tip with a radius of ~ 4 mm spans the surface area of the film, a laser beam is focussed on the diamond tip top to monitor its displacement. The thickness of the film is measured by noting the displacement of the laser beam as the diamond tip moves vertically [11]. On the other hand, the lateral movement of the stylus is determined by the voltage of the transducer. The actual thickness of the film is obtained by co-relating the voltage with the displacement of the laser beam, the standard voltage to height calibration being $1 \text{ mV}/\mu\text{m}$ [12].

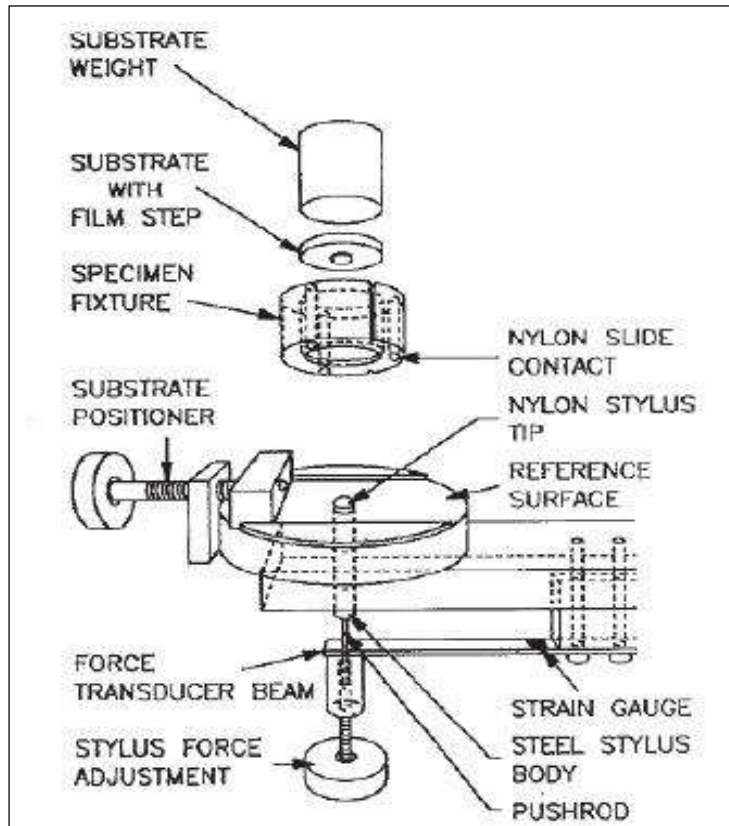


Fig. 3.3: Schematic of the profilometer.

3.4. Structural Properties:

➤ X-ray diffraction (XRD)

This measurement technique helps in analyzing the atomic or molecular orientation and structure of the thin films. X-rays are electromagnetic waves, which like visible light also exhibit interference and diffraction. The wavelength of X-rays is of the order of 0.1nm, so ordinary objects cannot serve the purpose of a grating for the X-ray. In 1912, Laue, a German Physicist, suggested that a crystal which consists of a three-dimensional array of regularly spaced atoms could serve the purpose of a grating for X-rays. This is because the spacings in between the atoms of a crystal is of the order of the wavelength of X-rays. So it is through crystals that we can get diffraction pattern for x-rays.

When x-rays interact with the crystalline sample, one gets a diffraction pattern, which corresponds to the presence of phases in the sample. Every crystalline substance gives a typical pattern, exhibiting the typical characteristics of the sample under test. If a mixture of samples is subjected to X-ray diffraction, then each type of sample will give a different pattern which is a property of that sample only. The X-ray diffraction pattern of

Chapter 3

a pure substance is, therefore, like a fingerprint of the substance. The mechanism of the diffraction of X-rays from crystals was explained by W.L.Bragg.

According to Bragg, the crystals are made of a periodic array of atoms or molecules, which are arranged in parallel planes called crystal planes. X-rays are formed by fast moving electrons. The X-rays are artificially produced by accelerating electrons in an alternating electric field. These electrons are oscillating with the frequency of the field. When these fast-moving electrons are incident on a crystal plane, the atoms of the crystal plane start vibrating with the same frequency as that of the incident electrons and hence of the electric field. The vibrating atoms of the crystal generate waves in different directions. These waves, coming from different atoms of the crystal planes interfere with each other. In most of the directions, destructive interference occurs, whereas in some specific directions, constructive interference occurs, where the waves are in phase with each other. The following figure (Fig. 3.4) illustrates the Bragg's law.

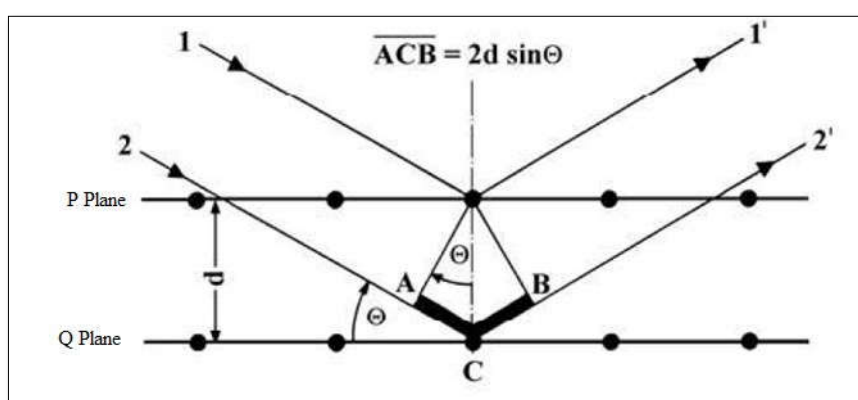


Fig 3.4: Illustrating the Braggs Law.

Planes P and Q are the 2 parallel planes of a crystal. Parallel rays 1 and 2 are incident on the 2 parallel planes P and Q respectively. They get reflected from corresponding atoms on the 2 planes as Rays 1' and 2' respectively. Θ is the angle between the incident ray and the reflected ray. The path difference between the 2 rays is ACB. If d is the interplanar distance, then

$$ACB = 2d \sin \theta \quad \text{eqn (3.6)}$$

If we consider that there is a constructive interference between the 2 rays, so that we can get a diffraction pattern, then the path difference must be an integral multiple of the wavelength of the X-rays (λ). So

$$2d \sin \theta = n\lambda \quad \text{eqn (3.7)}$$

Chapter 3

Where $n = 1, 2, 3, \dots$. This is the famous Bragg's Law [13].

Now, if we know the wavelength of the X-rays (λ) and the angle θ , then we can easily find out the interplanar distance d from the equation,

$$d = \frac{n\lambda}{2\sin\theta} \quad \text{eqn (3.8)}$$

The following Fig 3.5 shows a schematic diagram of the X-Ray Diffractometer. The crystal sample, under study is mounted on the stage. The X-rays coming out of the X-ray tube are collimated by a slit system consisting of Lead sheets, each with a pin hole and are made to fall on the sample in the form of a beam, making an angle of θ with the crystal plane. The diffracted beams from the crystal are made to fall on the Photographic plate which records the diffraction pattern.

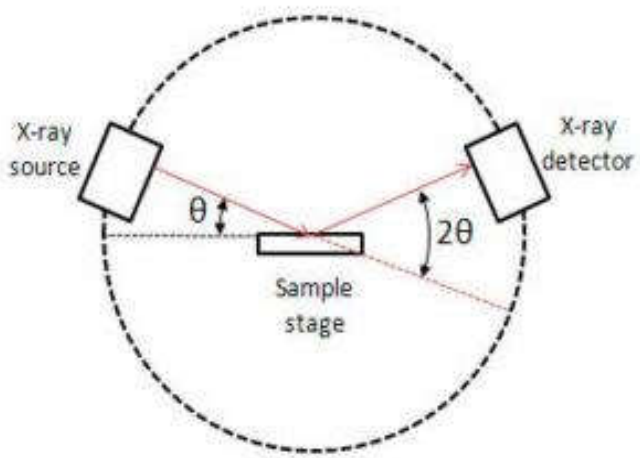


Fig. 3.5: Schematic arrangement of the XRD components.

The size of the crystalline grains D present in the film can be obtained from the peak in the XRD pattern, according to Scherrer equation [13,14], as:

$$D = \frac{k\lambda}{\beta \cos\theta} \quad \text{eqn (3.9)}$$

Where k is the shape factor, proportional to the shape and symmetry of the crystal orientation. It is ~ 0.9 for spherical crystals with cubic symmetry [15]. λ is the wavelength of X-ray source, which equals 1.54\AA . θ is the Bragg angle and β is FWHM (full width at half maxima) of the XRD peak. If $2\theta_1$ and $2\theta_2$ are the consecutive angular positions with zero intensity of the XRD peak, then β is given by the formula:

$$\beta = \frac{1}{2}(2\theta_1 - 2\theta_2) \quad \text{eqn (3.10)}$$

➤ Raman spectroscopy

When electromagnetic waves, in the form of photons are incident on the molecules of a material, the electrons present in the molecular orbitals get excited to higher energy states (i.e. the virtual states) by the absorption of the photons. a state of polarization is produced within the molecules. The absorbed photon gets immediately re-emitted by the electrons, causing their de-excitation. This happens due to the metastable nature of the virtual high energy states. The de-excitation of the electrons is lost as scattered light energy. In most cases, the scattered photon possesses the same energy (E_2) as that of the incident photon energy (E_1). This type of scattering of light or photons is called elastic or Rayleigh scattering. Needless to say, that in Rayleigh scattering, the wavelength of the incident photons (λ_1) is equal to that of the scattered photon (λ_2), e.i. $\lambda_1 = \lambda_2$. This is the most commonly occurring phenomenon. A small portion of the photons suffer inelastic scattering; i.e. the wavelength of the photons before and after excitations are not equal; ($\lambda_1 \neq \lambda_2$). Such type of scattering is called the Raman scattering.

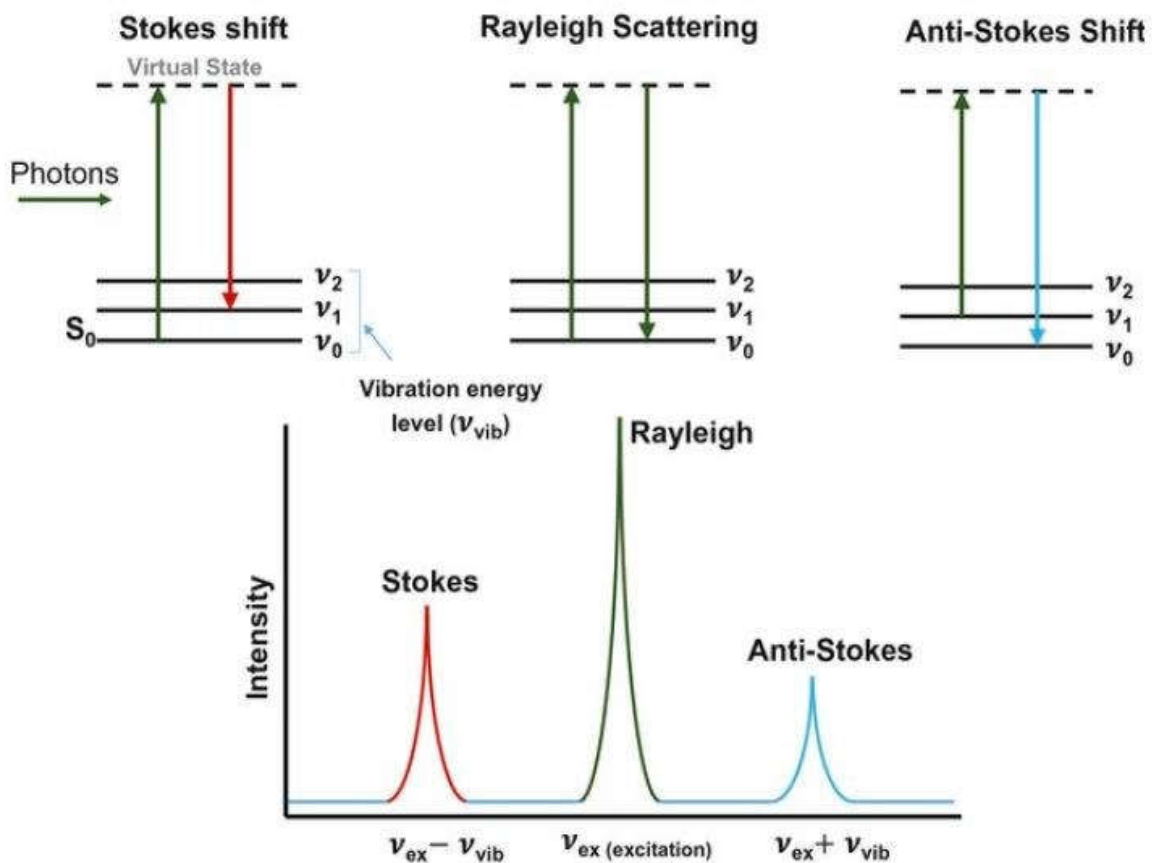


Fig. 3.6: Band diagram showing the fundamentals of Raman Scattering [16].

Chapter 3

When the energy of the scattered photon is less than that of the incident photon, it is called Stokes Raman scattering. The final energy state of the de-excited electron is at a higher level than that of the ground state electron. The difference in energy levels is due to the rotational and vibrational transitions of the electrons. Alternatively, when the scattered photon releases energy higher than that of the incident photon, i.e., the de-excitation of the electrons lands itself to an energy state below its initial energy level, it is called anti-Stokes Raman scattering. The intensity of the anti-Stokes scattering is always less than the Stokes scattering, because the possibility of the electrons to be in an excited state above the ground energy level is very small (which is the criteria for anti-Stokes scattering). Most of the electrons remain in the ground state, which intensifies the Stokes lines [16]. In all the Raman scattering processes, both energy and momentum are conserved. Various Raman signals can be observed based on the vibrational or rotational states of the sample. For a molecule to exhibit Raman activity, there must be a change in its polarizability or deformation of its electron cloud corresponding to the initial vibrational state. In a Raman spectrum, the Raman shift ($\Delta \nu$) is linked with the difference in frequency between the incident laser light (ν_L) and the scattered light (ν_R).

$$\Delta\nu \text{ (cm}^{-1}\text{)} = \nu_L - \nu_R \quad \text{eqn (3.11)}$$

Fig. 3.7 represents the schematic of the Raman instrument used for the characterization of thin films. In the analysis of the work presented in the thesis, the Raman measurements were carried out by Horiba J-Y (T64000) spectrometer at room temperature in a 180° back scattering orientation. A laser source of 532 nm wavelength at a low power of $\sim 2 \text{ mW cm}^{-2}$ was used to focus a sample area with diameter $\sim 30 \mu\text{m}$.

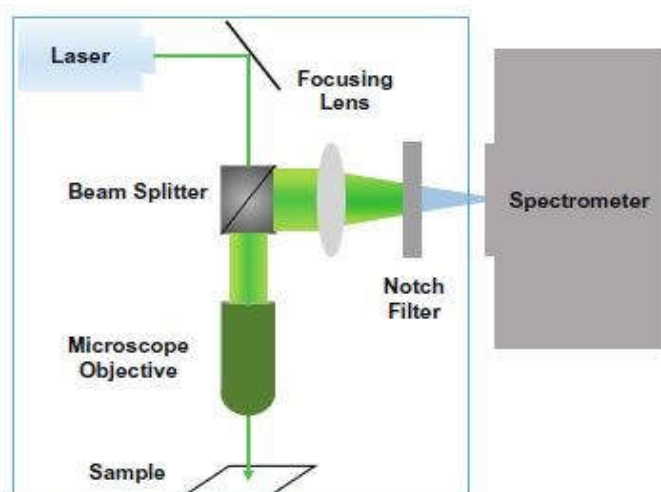


Fig. 3.7: Schematic of the Raman microscope [16].

➤ **Transmission electron microscopy (TEM)**

Transmission electron microscopy (TEM) is a powerful imaging technique to have an insight into the material in its real atomic level. It provides unparalleled view of the microstructure of any material. As the name suggests, TEM involves the transmission of forced electrons through the material to obtain high resolution images of the lattice planes. The transmitted beam is magnified several folds by a series of lenses to generate the image on a fluorescent screen.

One of the main components of the system is the electron gun, which ejects accelerated electrons by applying a specified voltage. The flux of electrons ejecting from the gun is made to focus into a concentrated ray using a set of lenses, which is incident on the specimen to be examined. A part of this array of electrons are transmitted, while the other part is diffracted from the surface of the specimen. The interference of both these transmitted and diffracted electron beams are used to form the TEM image. Magnification of highest order can be achieved by increasing the number of lenses, until the instrumental resolution limit is reached. Resolution of an imaging system is defined as the least distance at which two distinct points can be identified. As per the diffraction theory, the resolution limit (r) is formulated as:

$$r = \frac{0.61\lambda}{n \sin\alpha} \quad \text{eqn (3.12)}$$

here n is the refractive index of the medium, α is the half-angle formed by the aperture at the specimen and λ is the radiation wavelength. Another important parameter is the depth of field (h) is defined as:
$$h = \frac{0.61\lambda}{n \sin\alpha \tan\alpha} \quad \text{eqn (3.13)}$$

For very small value of α , $\sin\alpha \approx \alpha$ and $\tan\alpha \approx \alpha$, while for vacuum system $n = 1$; thus for theoretical calculations, the resolution limit (r) and depth of field (h) of an electron microscope is

$$r = \frac{0.61\lambda}{\alpha} \quad \text{eqn (3.14)}$$

$$h = \frac{0.61\lambda}{\alpha^2} \quad \text{eqn (3.15)}$$

Contrasts in the images are obtained from the absorption and diffraction of electrons and these are used to study the distribution of nanocrystalline phases in the amorphous network of the material. The transmitted and diffracted electrons are

Chapter 3

responsible for the formation of bright and dark field images obtained in the TEM. This image pattern reveals details about the crystal structure and defects of the sample. By the application of Bragg's law in the reciprocal space, the presence and abundance of crystalline planes and its orientation in the network of the material can be distinguished from the selected area diffraction patterns.

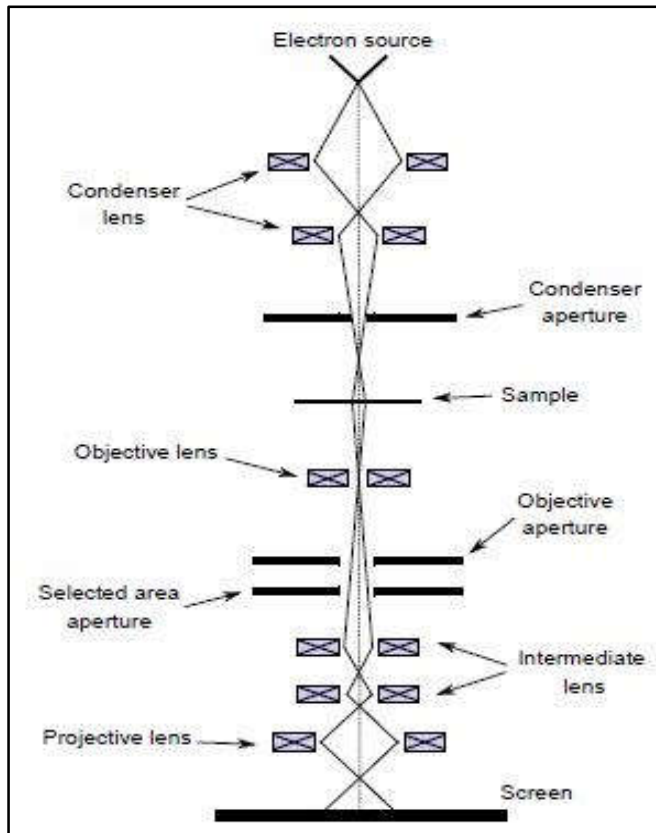


Fig 3.8: The schematic representation of the components of TEM [17].

Fig. 3.8 shows the schematic diagram of the internal components of operation present inside the TEM. The instrument used for the analysis of the DLC films presented here is the JEOL 2010 HRTEM model. This employs energy in the range of 80 keV to 200 keV to accelerate the electrons from the electron gun source. It has a resolution of 0.1940 nm, with a magnifying ability ranging from 50 to 1500000. For TEM measurements, samples of an optimum thickness (\sim 50-60 nm) are prepared on carbon coated copper grids. The thickness of the samples must be low for allowing transmission of electrons.

➤ Field emission scanning electron microscopy (FESEM)

Scanning electron microscopy (SEM) is a fundamental imaging process which is used to obtain the structural morphology of the surface of the material by probing it with a focussed beam of high energy electrons. One of the important aspects of SEM is

Chapter 3

its ability to produce high resolution ($> 1 \text{ nm}$) images of all types of 2-dimensional and 3-dimensional structures at higher magnifications [17]. This instrument employs an electron gun in which a metal filament is heated to such an extent that it releases electrons. The emitted electrons are accelerated by an anode attached within the electron gun. The accelerated high energy electrons are focussed on a set of one or two condenser lenses to align them in one direction. These then are passed through scanning coils to the final lens, which projects the electron beam onto a rectangular scanning area on the sample surface. The electron beam is scanned in a raster pattern to obtain a high resolution image of the sample surface.

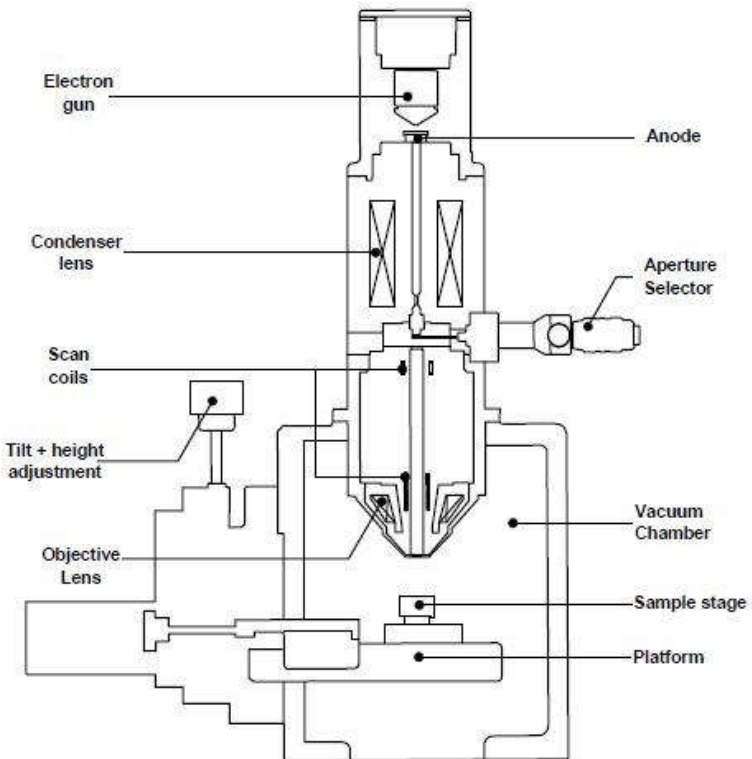


Fig. 3.9: The internal components of FESEM [17].

On the sample surface, the high energy electrons interact with the surface electrons of the sample. This interaction generates secondary electrons and back scattered secondary electrons (BSE), which are collected by the detectors to produce signals. The signals are then analysed to obtain images on screen. The availability of free electrons on the sample surface is thus necessary for the processing of images. Therefore, for insulating samples, a thin layer of metal (Eg. Platinum) is deposited on the sample surface for obtaining images. [Fig. 3.10](#) shows the interaction of the electrons from the SEM gun with the electrons on the sample surface.

Chapter 3

In FESEM, there is an additional attachment of field emission cathode which generates still narrowed beam of electrons with higher spatial resolution and lowers the risk of damage on the sample surface by reducing the charging possibilities.

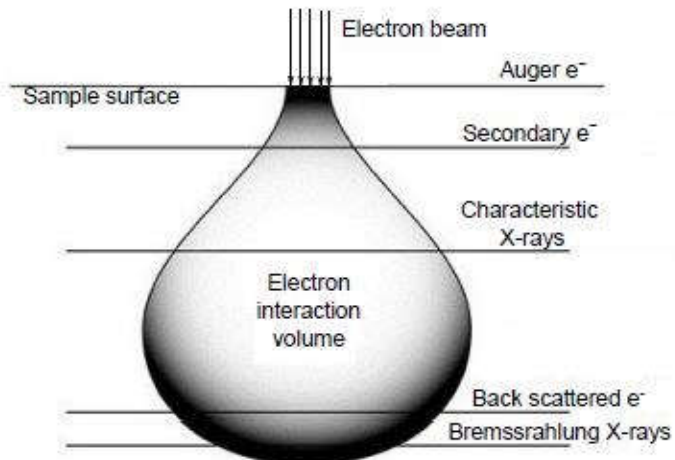


Fig. 3.10: The interaction volume and signal emission.

FESEM can also be used to obtain information about the chemical composition of the surface area scanned, via EDS (energy dispersive X-ray spectroscopy) and elemental mapping. This is the effect of the electronic interactions with the surface electrons. Often the high energy beam electrons eject the electrons from the inner shells of the atoms. In order to fill up the vacancy produced, electrons from higher energy states drop in, emitting energies characteristic of X-rays. These are then characterized to decipher the elements present in the sample.

➤ Atomic force microscopy (AFM)

Atomic force microscopy is one of the microscopes that generates three dimensional images of materials by probing it in three dimensions. It provides a clear concept about the surface roughness of the material as well as the linear profile of the ups and downs of the sample surface. The instrument involves the use of a cantilever with a sharp tip, made of Si_3N_4 (silicon nitride) or Si, which probes near the surface to be scanned. The radius of curvature of the cantilever is $\sim 5\text{-}10\text{ nm}$ and it is of $3\text{-}6\text{ }\mu\text{m}$ in length. The schematic diagram of the AFM operation and working principle is presented in [Fig. 3.11](#). A force is applied in between the probe tip and the sample surface, while maintaining a constant distance between the two, which is given by Hooke's law:

$$F = -kx \quad \text{eqn (3.16)}$$

Chapter 3

k being the spring constant, while x is the shift of the tip of the cantilever. The force deforms the cantilever, making it oscillate both laterally and vertically; whose deflection is regulated by a laser source [17]. Laser light from the source is incident on the cantilever from the top. Any deflection of the cantilever causes a shift or deflection of the laser light which is detected by a motion sensitive photo-diode detector, as shown in Fig. 3.11. The photo-diode detector is piezoelectric in nature, which means it can contract and expand when there is a change in voltage, caused by the reflected laser light. This enables the formation of three-dimensional images of high resolution. By convention, it is the sample surface which is moved in all three directions, while the cantilever tip position is fixed.

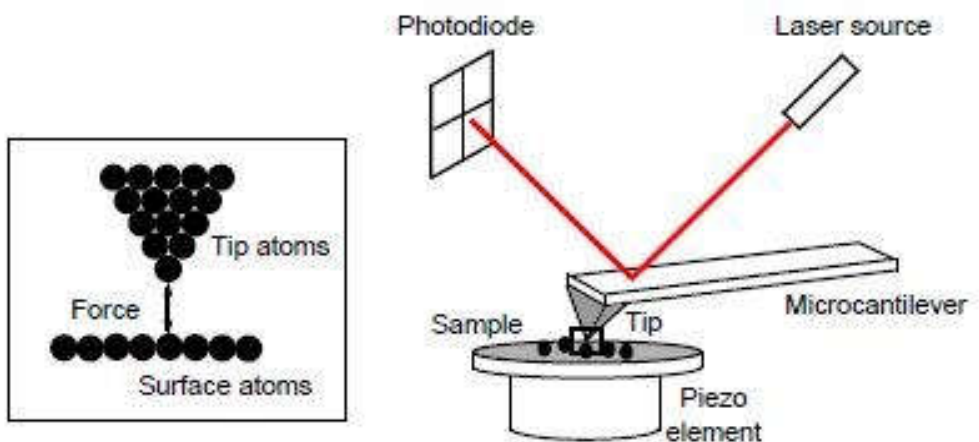


Fig. 3.11: Working principle of Atomic Force Microscope.

Depending on the functioning of the cantilever tip, AFM imaging can be categorized in three imaging modes [18]:

- **Contact mode of AFM:**

Here, the constant distance of separation between the tip and the sample is very small < 0.5 nm. Thus, the tip is almost in contact with the surface and a repulsive force is in action between the tip and the surface. During scanning, a constant force is maintained, which causes the deflection of the cantilever, sending a feedback signal to the detector, generating the 3-D image. This type of probing often damages soft tissues on the sample surface, highlighting its main drawback of this mode of AFM imaging.

- **Tapping mode of AFM:**

Also known as ‘intermediate contact mode’, this imaging method involves a tip to sample surface distance of $0.5 – 2$ nm. The mechanism, being similar to that of the contact mode, the cantilever oscillates with a resonating frequency, different from

Chapter 3

the previous one. During the entire scanning process, the tip continuously taps on the surface to obtain the 3-D image.

- The non-contact mode of AFM:

Here the separation distance between the tip and the surface is 0.1–10 nm. The tip of the AFM is never in contact with the surface during the entire process, and oscillates with a resonating frequency or at a slightly higher note. The resonant frequency is brought down by the van der Waals force which comes into play between the tip and the surface. A stable oscillation is maintained and a three-dimensional topographical representation of the surface is created by the feedback loop system in conjunction with the decrease in the resonant frequency. This tip has a longer lifetime than the other AFM modes since there is a weak force applied between the tip and surface. The different modes of AFM imaging and the interatomic variation of forces with sample to tip distance is presented in [Fig. 3.12](#).

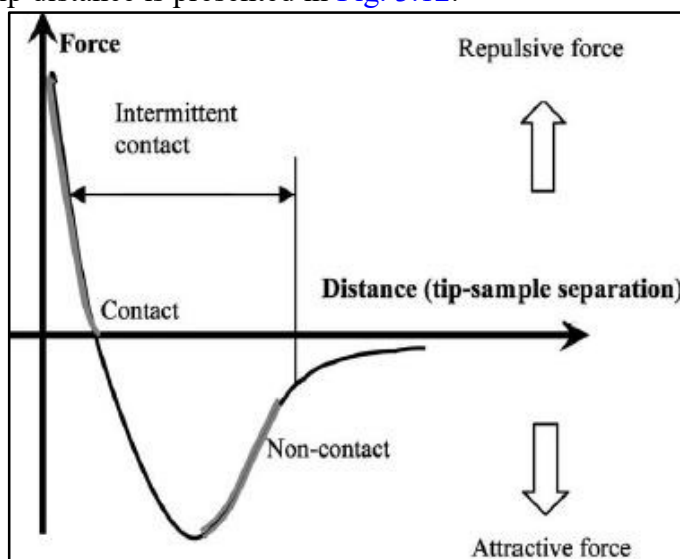


[Fig. 3.12: Interatomic variation of forces with sample to tip distance \[18\].](#)

3.5. Compositional properties:

- **X-ray photoelectron spectroscopy (XPS)**

The X-ray photoelectron spectroscopy (XPS) is a sophisticated technique that determines the compositional properties of the sample. It gives a clear quantitative information about the contents of the functional bonds and chemical states of the different elements present in the sample. The working of the XPS is based on the fundamental phenomenon of photo-electric effect.

X-rays are used as the source, which are incident on the surface of the sample, after being projected through a monochromator. Conventionally, monoenergetic X-ray

Chapter 3

sources like Mg Ka (1253.6 eV), Al Ka (1486.6 eV), or monochromatic Al Ka (1486.7 eV) are used. These photons have their penetrating power up-to 1 to 10 μm , i.e. they can analyze films only close to the surface. The high energy beam of photons (X-rays) after being incident on the sample surface, ejects electrons from the inner core or valance orbitals of the atoms of the elements and bonds present in the films to vacuum or free space. Due to the vacancy created in the inner core shell, electrons from the higher energy states fill in the gap, emitting photons [19]. Fig. 3.13 shows the ejection of electrons from the core level.

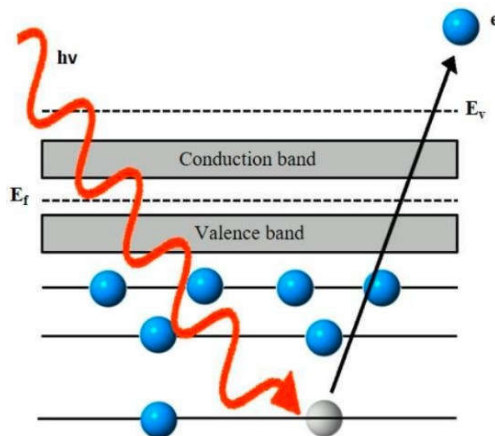


Fig 3.13: Electronic interactions at the core level of atomic orbitals.

The kinetic energy (E_K) of the ejected electrons carries information about the binding energy (E_b) of the atomic orbital and is related as:

$$E_K = h\nu - E_b - \phi \quad \text{eqn (3.17)}$$

where $h\nu$ is the energy of the incident photon, and ϕ is the work function.

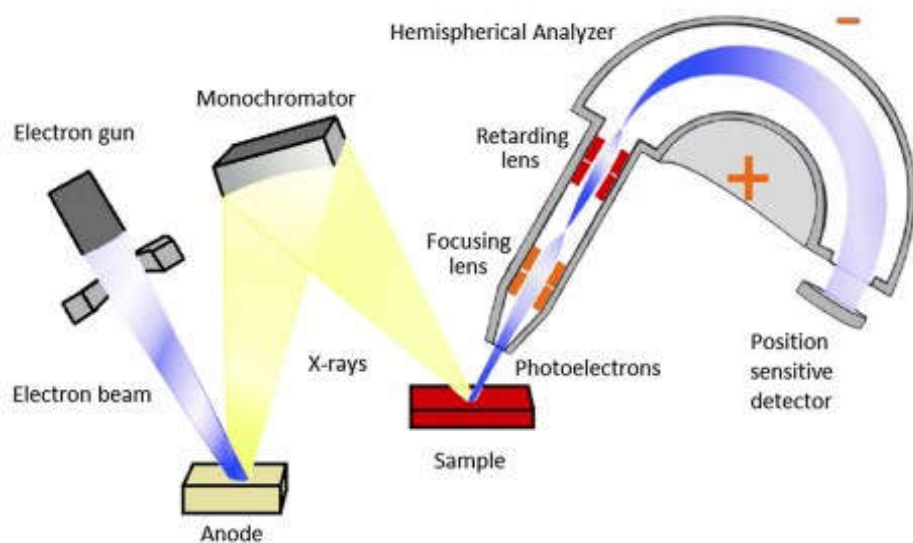


Fig. 3.14: Schematic of the working of an XPS instrument.

Fig. 3.14 demonstrates the working of an XPS instrument. Since the work function of the respective instrument is pre-calibrated and neutralized, the binding energy, characteristic of a specified bond or chemical state of the elements present in the sample can be evaluated. From the prior knowledge of the binding energies of different elemental bonds, the elemental composition of those present in the sample can be determined.

The percentage of the various bonds of carbon present in the sample can be determined from the ratio of the area of the individual deconvoluted peaks with respect to the total area covered by the total peak appearing in the spectra from the element C 1s. If S_i be the area of the i th bonded peak and S is the area covered by the entire peak arising from C 1s, then the percentage P_i is given as [20,21]:

$$P_i = \frac{S_i}{S} \quad \text{eqn (3.18)}$$

3.6. Electrical properties:

➤ Temperature dependent dark conductivity

The conductivity and activation energy of the thin films are measured by applying voltage across the electrodes for lateral conduction of electricity and measuring the current by a 6517A Keithley electrometer. For the measurement, two parallel Aluminium electrodes of pre-defined shapes and dimensions (defined by masks) are deposited on the film by thermal evaporation method at room temperature. The electrodes are of ~ 80 nm thick, are ' ℓ ' (1 cm) long and are separated by a distance w (0.1 cm).

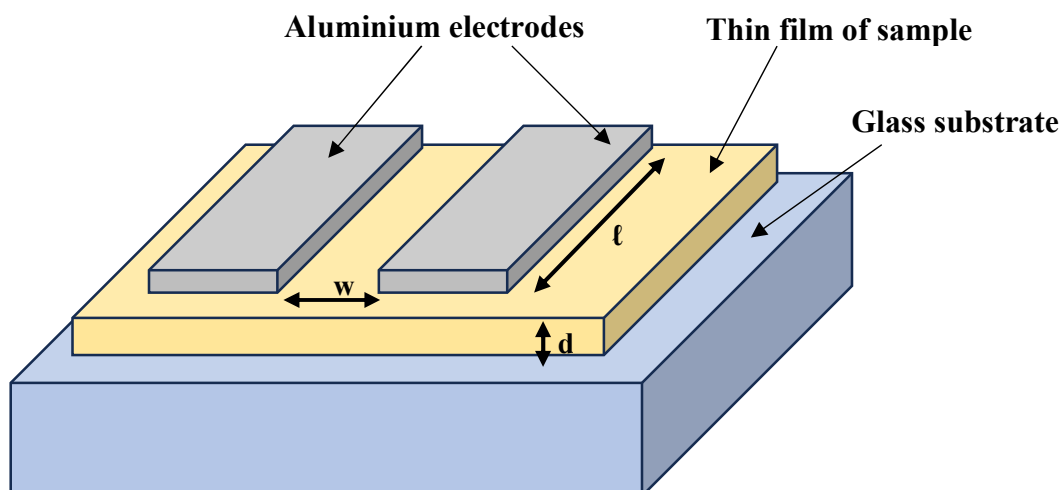


Fig. 3.15: The arrangement of the electrodes on the thin film for electrical measurement.

Chapter 3

The thickness of the electrodes being negligible compared to the separation distance w , the electrical conduction is assumed to occur laterally through the thin film itself. The actual arrangement is shown in [Fig. 3.15](#).

The sample is then placed in a vacuum chamber provided with a cryo-set up, where a range of voltages is applied across the electrodes and the corresponding current passed is measured by the 6517A Keithley electrometer. From the current (I)-Voltage (V) data obtained the conductivity (σ) of the sample of thickness d is measured, as per the equation:

$$\sigma = \frac{Iw}{V\ell d} \quad \text{eqn (3.19)}$$

Conductivity of the sample should be measured in their ohmic area for improved repeatability and reduced measurement error. In order to calculate the activation energy of the sample, the electrical conductivity is to be measured by gradually decreasing the temperature from 450 K to 180 K. This measurement is done to analyse the transport of thermally activated charged carriers within the sample. Initially the temperature of the sample is raised to 450 K and measurement is done while cooling the sample in gradual steps to room temperature and below it by applying a specific voltage (usually a voltage in the middle of the linear region of the I-V graph at room temperature is chosen). The activation energy E_a is evaluated by fitting the conductivity data with temperature (T) according to the following equation:

$$\sigma = \sigma_0 \exp(-E_a/K_B T) \quad \text{eqn (3.20)}$$

where σ_0 is the exponential constant and K_B is the Boltzmann constant.

3.7. Measurement of solar cell I-V characteristics:

In order to understand the characteristics of solar cell, i.e. the conversion of solar energy into electricity, the current density J vs voltage V needs to be measured. The parameters that define the characteristics of a solar cell are short circuit current density (J_{SC}), open circuit voltage (V_{OC}), fill factor (FF) and efficiency (η). The current produced when charge carriers are generated in the presence of light is known as the short circuit current (I_{SC}). This current should ideally equal the load current when there is no bias. In order to remove the reliance on solar cell area (A), the short-circuit current density $J_{SC} = I_{SC}/A$ is used. On the other hand, the open circuit voltage V_{OC} is defined as the voltage across the solar cell when the load resistance

Chapter 3

is infinite. The Fill Factor (FF) gives a measure of the maximum power that can be obtained from a solar cell and is given by

$$FF = \frac{J_{mp}V_{mp}}{J_{sc}V_{OC}} \quad \text{eqn (3.21)}$$

where J_{mp} and V_{mp} are the maximum current density and maximum voltage respectively. The efficiency of the solar cell is defined as:

$$\eta = \frac{P_{out}}{P_{in}} = \frac{J_{sc}V_{OC}FF}{P_{in}} \quad \text{eqn (3.22)}$$

where P_{out} and P_{in} are the output and input power respectively.

The I-V curve of the solar cell is measured under the illumination of AM 1.5 G spectrum i.e. 100 mW/ cm², which is equivalent to the sunlight at room temperature. A standard reference silicon cell is used to calibrate and maintain the intensity of the 1-Sun light throughout the experiment. The basis for this calibration is the presumption that the reference cell's calibration and the sun simulator's light spectrum in Dark-Star are the same. [Fig 3.16](#) gives a presentation of the I-V curve demonstrating all the important parameters of a solar cell.

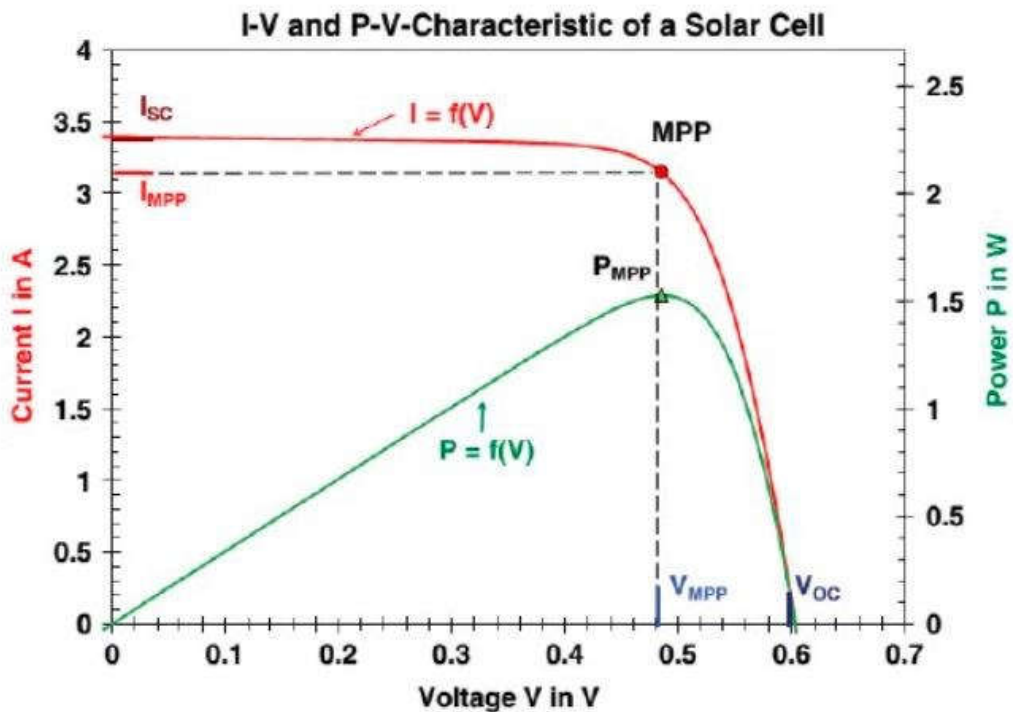


[Fig. 3.16: I-V and P-V curve of a solar cell.](#)

However, there are some precautions needed to be taken before the I-V measurements of a solar cell can be collected. During measurements under the illumination of sunlight, a set of filters must be placed in between the light source and the solar cell to cut off the rest of the spectrum

Chapter 3

other than visible light. During dark I-V measurements, care should be taken that no light can interfere with the data collection process. Thus, a copper shield is used to cover the solar cell. The program menu must specify the measured current range and the substrate type (n-type or p-type) of the cell before the I-V measurement.

3.8. References:

- [1] T. Basche, *J. Luminescn.* 76 & 77 (1998) 263.
- [2] S. V. Gaponenko, Optical properties of semiconductor nanocrystals, *Cambridge University press* (1998) ISBN: 0-521-58241-5.
- [3] B. K. Sharma, Spectroscopy, 14th Ed., *Goel publishing house* (2000).
- [4] K.J. Laidler, J.H. Meiser, Physical Chemistry, 2nd edition (1995).
- [5] J. Tauc, Optical Properties of Solids, edited by F. Abelès (North-Holland, Amsterdam, the Netherlands) p.277 (1972).
- [6] R.H. Klazes, M.H.L.M. van der Broek, J. Bezemer, S. Radelaar, *Philos. Mag. B* 45 (1982) 377–383.
- [7] K.D. Mackenzie, J.R. Eggert, D.J. Leopold, Y.M. Li, S. Lin, W. Paul, *Phys. Rev. B* 31 (1985) 2198.
- [8] S.K. Suram, P.F. Newhouse, J.M. Gregoire, *ACS Comb. Sci.* 18 (2016) 673–681.
- [9] R. Safari, F. Sohbatzadeh, T. Mohsenpour, *Surfaces and Interfaces* 21 (2020) 100795.
- [10] J.W. Wood, R. D. Redin, *Rev. Sci. Instrum.* 64 (1993) 2405.
- [11] T. Kanada, T. Kubota, A. Suzuki, *Meas. Sci. Technol.* 2 (1991) 191–197.
- [12] R.E. Evans, *Rev. Sci. Instrum.* 43 (1972) 806–810.
- [13] P. Scherrer, *Göttinger Nachrichten Gesell.* 2 (1918) 98.
- [14] B.D. Cullity, S.R. Stock, Elements of X-Ray Diffraction, 3rd Ed., Prentice-Hall Inc., p 167–171, ISBN: 0-201-61091-4, (2001).
- [15] J. I. Langford, A. J. C Wilson, *J. Appl. Cryst.* 11 (1978) 102–113.
- [16] Y.C. Cho, S.I. Ahn, *Sci Rep* 10 (2020).
- [17] Naresh Marturi. Vision and visual servoing for nanomanipulation and nanocharacterization in scanning electron microscope, *Micro and nanotechnologies / Microelectronics. Universit_e de Franche-Comt_e*, 2013. English. <tel-01025318>.
- [18] N. Jalili, K. Laxminarayana, *Mechatronics* 14 (2004) 907–945.
- [19] J.T. Kloprogge, B.J. Wood, *Handbook of Mineral Spectroscopy*, Volume 1: X-ray Photoelectron Spectra, Elsevier (2020). ISBN: 978-0-12-804522-0.
- [20] A.F. Azevedo, F.A. Souza, J.T. Matsushima, M.R. Baldan, N.G. Ferreira *J. Electroanal. Chem.* 658 (2011) 38–45.
- [21] A.E. Aleksenski І, V.Yu. Osipov, A.Ya. Vul, B.Ya. Ber, A.B. Smirnov, V.G. Melekhin, G.J. Adriaenssens, K. Iakoubovskii, *Phys. Solid State* 43 (2001) 145–150.

SECTION A

*Carbon nanostructures (DLC): Growth and
Characterisation*

Diamond-like carbon (DLC) is one of the diverse allotropes of carbon that consists of a mixture of crystalline and amorphous phases with C atoms arranged in different coordinations, e.g., tetrahedral sp^3 hybridized C-C bonds of diamond or trigonal sp^2 C=C as in graphite or even some sp hybridized C≡C bonds. The proportional strength of these differently coordinated C bonds present in the matrix determines the physical properties of the DLC material [1]. As the name suggests, DLC films likely contain a significant amount of sp^3 hybridized carbon that determines its diamond-like properties, involving much easier and inexpensive ways of production [2,3]. DLC with a significant amount of hydrogen content (10-50 %) forms a separate class, the hydrogenated DLC (HDLC, a-C:H), wherein the H-content plays an essential role in determining its various properties [4,5]. Transparent DLC films with high nanocrystalline diamond contents find numerous applications in opto-electronics like micro-electromechanical system (MEMS), nano-electromechanical system (NEMS), microelectrode, field emission devices, etc. [6–8]. They are also useful as coatings for moisture-resistant lubricants, water repellent and cathode for lithium batteries, and also as protective anti-reflection coatings for solar cells against action of radiation (solar wind, γ -quanta) which is one of the key factors for efficiency degradation in space [9–12]. With the production cost minimised, DLCs get compromised in terms of the quality (crystalline properties) and hence in ultimate device usability. We are thus interested in evolving a cost-effective quality product of DLC with enhanced crystalline properties by incorporating considerable nanocrystalline diamond phases, making them possess the closest diamond-like properties possible.

DLC films have been predominantly synthesized using methods such as RF magnetron sputtering [5,9,13], ion beam implantation [14], and a range of plasma-enhanced chemical vapor deposition (PECVD) techniques. These include RF capacitively coupled [15] and inductively coupled PECVD and microwave PECVD [16–18], which typically involve high-density and high-pressure (several Torr) plasmas, often generated from gaseous precursors like methane (CH₄) and hydrogen (H₂) [17]. The use of microwave plasma CVD for DLC films has been adequately explored [19–21]. However, there are practical limitations in microwave-operated CVD. Microwaves are hazardous to health and need proper shielding during deposition, incurring expenses; moreover, they suffer from sustaining a stable plasma, particularly at low powers. These challenges can be easily dealt with using harmless RF-operated CVD systems involving inductively coupled or capacitively coupled plasma (ICP and CCP) [22,23]. Considering the advantages of the ICP and CCP systems in terms of lower

frequency operation and uniform deposition, the synthesis of DLC films in these processes is focused.

Mostly Si wafers are used as substrates for the deposition of crystalline DLC films. In certain instances, the preparation of DLC films includes a pre-treatment process involving diamond powders. This pre-treatment is commonly achieved either by subjecting the substrates to ultrasonic agitation in a diamond powder solution or by mechanically polishing the substrate surface using diamond grit [1,24,25]. Silicon wafers, due to their single-crystal structure, facilitate the nucleation and subsequent epitaxial growth of diamond-like carbon (DLC) films. The pre-treatment process enhances the nucleation density and catalyses the oriented growth of crystalline films. The pre-treatment process preceding deposition involves a two-step method that demands precise techniques and meticulous attention during film preparation. Additionally, the incorporation of diamond powders contributes to the overall costliness of the process. Post deposition annealing processes are also reported to enhance the crystalline quality of the DLC films [26,27]. The direct deposition of crystalline DLC films onto glass substrates, without any prior surface treatment, presents a significant challenge in a one-step process.

This study aims to achieve transparent diamond-like carbon (DLC) films incorporating a substantial amount of nanocrystalline diamond on commonly available, cost-effective glass substrates. The films are deposited in a single-step process without requiring traditional diamond powder pre-treatment of the substrate.

A.1:

DLC films by ICP CVD

➤ **Introduction:**

The growth processes in the plasma mainly occur in non-equilibrium conditions, involving dynamic competition of opposite concomitant reaction routes, one involving the film growth process and the other involving the etching of the grown layers. The advantage of the plasma growth process is that the electrons within the plasma have considerably high energy, enabling excitation and ionization of the precursor gas molecules. Plasma maintained at a high deposition pressure ensures higher growth rates in crystalline diamond thin films. However, maintaining the uniformity of films with large areas is quite challenging at high deposition pressures [28]. Low pressure ensures uniform deposition over large areas, but the growth rate is hampered due to the low-density plasma formation. The inductively coupled plasma (ICP) CVD system is a promising high-density plasma source (electron density $\sim 10^{12}$ cm $^{-3}$) that provides a high deposition rate by its high dissociation efficiency even at low pressures. Its low plasma sheath potential near the chamber walls ensures low ion bombardments on the substrates, enhancing uniformity. It also guarantees excellent uniformity of the plasma parameters both in the axial and radial directions and enables easier crystallization in the film network [29–32]. The primary objective of this study is to utilize the beneficial features of the ICP CVD system to fabricate diamond-like carbon (DLC) films exhibiting significant crystallinity. This will be achieved on glass substrates at low pressure without the need for any preliminary substrate pre-treatment with diamond powder.

➤ **Experimental**

DLC films were prepared in an in-house designed planar RF (13.56 MHz) ICP CVD reactor, the schematic diagram of which is presented in [Fig. A.1.1](#). It is made of a stainless-steel cubic chamber with sides 30 cm long. Before deposition, a process turbo pump (LEYBOLD), backed by a two-stage rotary pump, was used to maintain a base vacuum of 1.33×10^{-4} Pa. A set of MKS mass flow meters controlled the gas flow rate into the system, and the pressure during deposition was regulated by an automated throttle valve attached at the end of the reactor. RF power (supplied by Dressler Cesar 1310 RF power generator) was applied to the plasma via a co-planar, 4-antennae spiral inductive coil (0.54 μ H inductance), through a matching box. In this system, four inductive coils, having a common center are arranged in a co-planar spiral configuration such that the diameter of the total spiral is in size with the edge of the cubical deposition chamber. This entire arrangement is attached to the back side of the chamber across a quartz window, through which current is passed at radio frequency. The

quartz window is vacuum-sealed through a set of O-rings on both sides. Since the four coils are electrically parallel, the operation is possible at a low voltage, facilitating a uniform stable plasma within the deposition chamber. The substrates were heated using a resistive type electrically sealed heater connected to a temperature controller via ceramic feedthrough, all attached at the backside of the substrate holder of ~ 15 cm diameter and placed at the chamber wall through ceramic spacers.

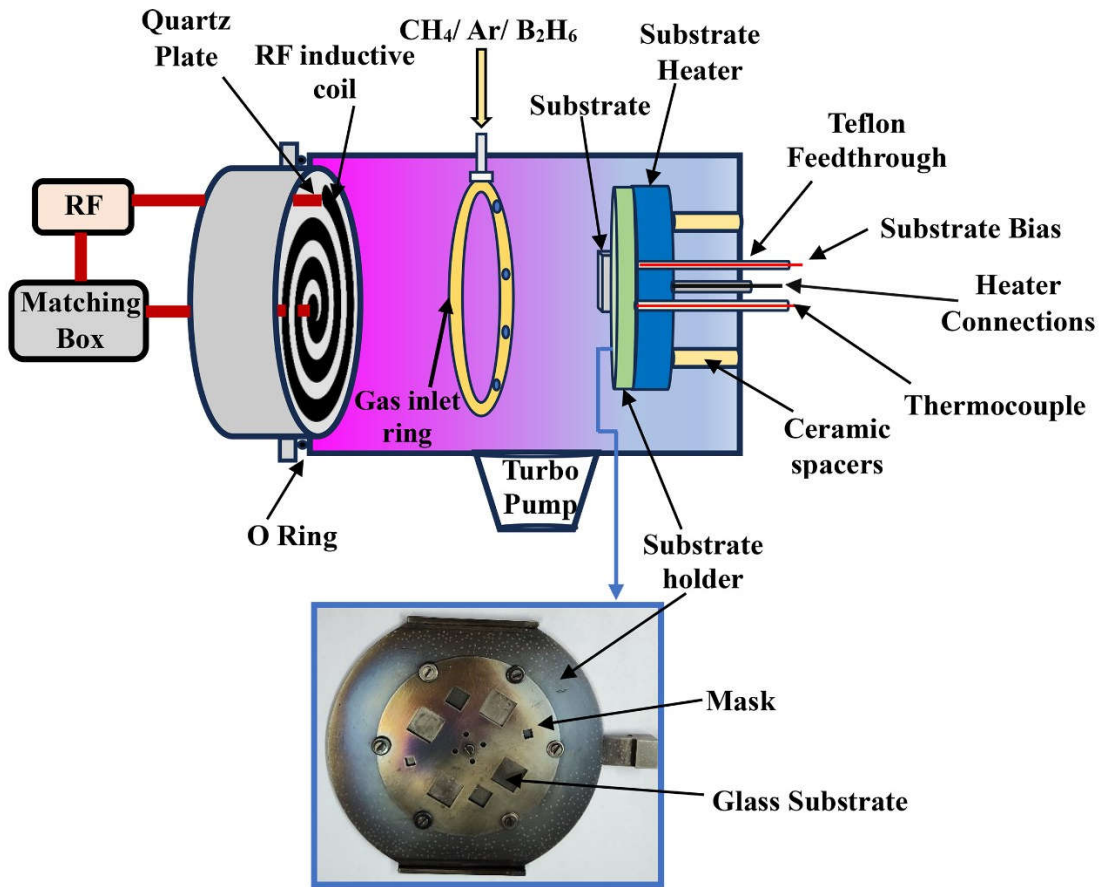


Fig A.1.1. Schematic diagram of the inductively coupled plasma chemical vapour deposition system.

A thermocouple shielded by a teflon feedthrough measured the temperature of the substrate holder on which the glass substrates were held tightly with the help of a stainless-steel mask. The actual temperature on the top surface of the glass substrate was estimated from the calibration curve obtained separately. The stainless-steel circular substrate holder acted as the other electrode, where a desirable negative DC bias voltage (Matsusada REk500-3.2, Japan) was applied. The conducting metal mask, around the periphery of the growth area, attracted the positively charged precursor ions onto the glass substrates (size $1.5 \times 1.5 \text{ cm}^2$), causing film formation [33]. In the CH_4/Ar plasma produced in a CVD, the electron density n_e lies in the range of $\sim(10^8 - 10^{10}) \text{ cm}^{-3}$, and the density of precursor ions CH_n^+ for various combination

ratios of CH₄ and Ar usually varies within (10¹³ – 10¹⁶) cm⁻³ [34]. Due to the application of a negative bias voltage to the substrate, the number of positive precursor ions attracted towards the substrate was much higher than the repelled electrons. Thus, although some of the precursors were lost due to the electron recombination (quenching of the plasma) near the substrate holder, the effective growth of the films was facilitated.

Corning® Eagle 2000™ glasses (thickness ~0.1 cm), cut into squares of size (1.5×1.5 cm²) were used as substrates. The substrates were cleaned with de-ionized water and ultrasonically treated with alcohol (2-Popanol, 99.5% purity) and acetone before being mounted into the deposition chamber. Before deposition, the plasma chamber was maintained at a high vacuum (10⁻⁶ Torr) for 1 h. Further substrate cleaning was done by 10 min of Ar plasma etching immediately before the deposition and using identical plasma parameters.

The Raman studies of the prepared samples were performed using a Jobin-Yvon Horiba (T64000) Raman spectrophotometer with a 532 nm wavelength diode pump solid-state (DPSS) laser (make: Spectra-Physics) at a power density of ~2 mW cm⁻² and a 50× magnification microscope focussing the sample area of ~30 μm diameter. An X-ray photoelectron spectroscopy (XPS) instrument (Omicron Nano Technology 0571), equipped with an Mg K α X-ray source (1253.7 eV), was used to analyze the binding energy and elemental composition. The XPS unit operates at a filament current of 25 mA and beam energy of 1000 V. Ar⁺ ion was used for cleaning the substrate surface. The binding energy scale was calibrated with reference to a pure silver (Ag) sample. Peak fitting of the XPS spectra was done using Origin Pro software, where the peaks were fitted according to voigt functions. Electrical measurements were performed using a KEITHLEY 6517A electrometer and co-planar parallel Al electrodes grown on the sample on glass substrates. Surface morphological studies were done via atomic force microscope (AFM, Veeco dI CP II, Model: 0100) operating in the tapping mode and scanning electron microscope (SEM) (JEOL JSM-6700F FESEM). The SEM images were obtained at an operating voltage of (2-5) kV. The crystalline and structural properties were analyzed using the JEOL JSM 2010 transmission electron microscope (TEM) with 200 kV electronic beams incident on the sample surface. For this study, the samples deposited on glass substrates were scratched out, mixed in ethanol (99.9%), and then drop-casted on carbon-coated Cu microscopic grids. The entire area (1.5 x 1.5 cm²) of the film on glass was scratched using a razor blade, and suspended in 0.5 ml of ethanol. A micro-pipette was used to drop cast the TEM grids with 10 μl of the solution (~3 drops).

A.1.1: Chapter 4

Intrinsic DLC films: influence of negative
substrate bias application

Chapter 4

Diamond-like carbon (DLC) films are comprised of C atoms arranged in different coordinations e.g., sp^3 , sp^2 and sp . DLC films possess high hardness, electrical insulation, low friction coefficient and are highly transparent, which make them useful in opto-electronic devices. DLC films are prepared by magnetron sputtering, capacitively coupled RF plasma CVD and mostly by high-pressure microwave plasma CVD. In the present work we intend to prepare DLC films on inexpensive glass substrates from a low pressure and high-density (CH_4 + Ar) plasma of planar inductively coupled plasma (ICP) CVD.

During deposition, plasma was maintained by varying CH_4 flow rate from 5 to 50 sccm, diluted by 50 sccm of Ar at low pressure (p) of 30 mTorr (~ 4 Pa) and 900 W of rf power (P). Each film was deposited for 5 h with average thickness ~ 30 nm, at a fixed temperature maintained at 450 °C. Furthermore, at otherwise optimized parametric conditions, a set of films were deposited applying negative dc substrate bias varying from 0 to -100 V, to study the evolution of crystallinity in the DLC films.

4.1. Results:

4.1.1 Effect of variation of CH_4 flow rate:

[Fig. 4.1\(a\)](#) and [4.1\(b\)](#) show the deconvoluted Raman spectra of the DLC films prepared at 900 W of rf power, 450 °C substrate temperature, 30 mTorr (~ 4 Pa) deposition pressure and varying CH_4 flow rates from 5 to 50 sccm.

Each Raman spectrum has been deconvoluted into six specific components for the present samples, as in [Fig. 4.1\(a\)](#) and [4.1\(b\)](#). Diamond peaks are identified as those appearing in the wavelength range of (1326-1332) cm^{-1} with full-width at half-maximum (FWHM) of ~ 39 cm^{-1} . The diamond peak is grossly different from that of bulk single-crystal diamond, which is generally characterized at 1332 cm^{-1} with FWHM of 1-2 cm^{-1} , corresponding to the vibrations of cubic sub-lattices of the uniformly oriented sp^3 hybridized C-C bonds [35,36]. The D band appearing at around 1350 cm^{-1} is associated with the vibrations of 6-fold aromatic rings formed by sp^2 hybridized C-C bonds. This band appears when there is a disorder in the sp^2 graphitic lattice, and hence it is called a disorder activated band [37]. Another characteristic peak, the G band, appearing at 1600 cm^{-1} , originates from the in-plane vibrations of all sp^2 hybridized C-C graphitic bonds, irrespective of the aromatic rings [38]. In between the D and G bands, another broad peak at around 1480 cm^{-1} is attributed to the trans-polyacetylene (t-PA) segments present at the grain boundaries. This trans-polyacetylene peak usually evolves with a companion mode at ~ 1150 cm^{-1} , which is again highly dispersive [39]. The peak at 1280 cm^{-1} is a characteristic of diamond-like carbon films [40]. The D' band at 1620 cm^{-1} arises due to

Chapter 4

the disordered graphitic lattice [41,42]. The ratio in the intensity of D band to the G band (I_D/I_G) provides a quantitative assessment of the defects present within the ordered crystalline lattice with the graphitic content, which can be used to investigate structural changes in the film [39]. The intensity ratio of the diamond peak to the D band peak (I_{Dia}/I_D) assesses the proportion of sp^3 hybridized C-C bonds to the network disorder.

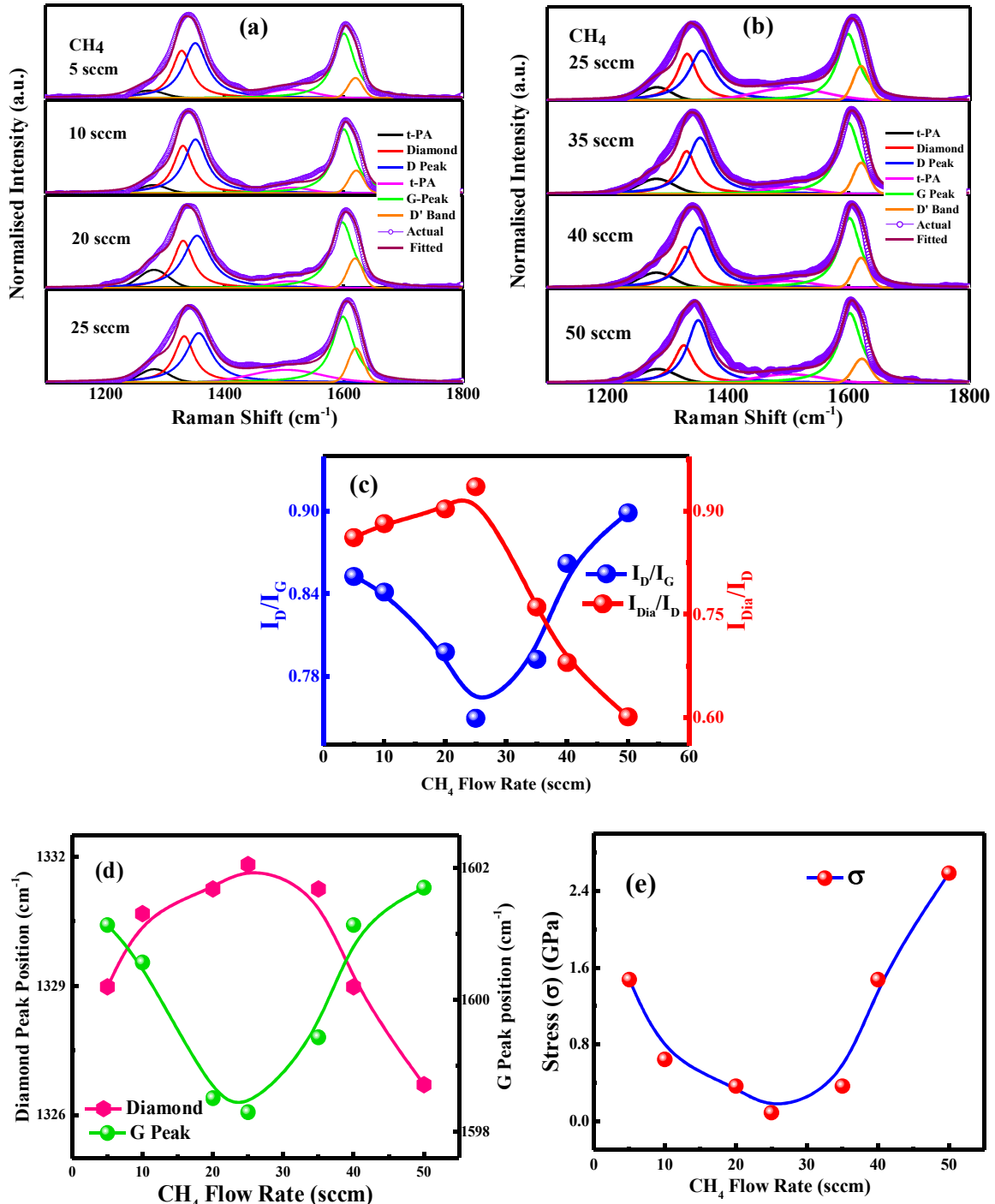


Fig. 4.1. (a) and (b) Deconvoluted Raman spectra of the films prepared at 900 W with varying CH₄ flow rates from 5 to 50 sccm; (c) Variation of the Intensity ratios I_D/I_G and I_{Dia}/I_D with CH₄ flow rate;

Chapter 4

(d) Variation of diamond peak and G peak positions with increasing CH₄ flow rate; (e) Changes in the residual stress developed within the DLC films with increasing CH₄ flow rate.

Fig. 4.1(c) identifies that with the increase in the CH₄ flow rate from 5 to 25 sccm, the I_D/I_G ratio decreases to a minimum of 0.75 and the I_{Dia}/I_D increases to a maximum value of 0.94. However, with a further increase in CH₄ flow rate up to 50 sccm, there is a reversal in the nature of variation of both I_D/I_G and I_{Dia}/I_D. Fig. 4.1(d) shows the shift of the diamond peak and G peak positions with the increase in the CH₄ flow rate. It is observed that the diamond peak initially shifts from \sim 1329 to 1331.8 cm⁻¹ for an increase in CH₄ flow rate from 5 to 25 sccm, while for further increase in CH₄ flow up to 50 sccm, it shifts to a lower wavenumber of \sim 1326.7 cm⁻¹. On the other hand, the G peak position shifts from 1601.2 to 1598.3 cm⁻¹ with increasing CH₄ flow rate up to 25 sccm, then it gradually moves to a higher wavenumber of \sim 1601.7 cm⁻¹ for 50 sccm of CH₄ flow. The decreasing I_D/I_G ratio, along with the red-shift of the G peak, signifies the reduced number and size of the *sp*² graphitic clusters [43–46].

In the diamond network, some internal stress develops due to growth defects, and that causes a shift in the diamond peak position from 1332 cm⁻¹ [47,48]. This residual stress (σ) in the network could be estimated using the following relation:

$$\sigma = -0.488 \text{ GPa cm}^{-1} \Delta\nu \quad \text{eqn (4.1)}$$

where $\Delta\nu$ is the relative difference of the observed diamond peak to the un-stressed natural diamond appearing at 1332 cm⁻¹. The stress could be tensile or compressive as determined by the positive or negative sign of σ , respectively [49]. Tensile stress is generated due to the presence of a large number of voids and dislocations in the lattice. In contrast, compressive stress results from the hydrogen clusters and impurity phases in the film network [47,49]. Fig. 4.1(e) shows the variation of the residual stress (σ) with the increase in CH₄ flow rate. It exhibits a gradual decrease in σ , as the CH₄ flow rate increases from 5 sccm; σ attains its minimum magnitude at CH₄= 25 sccm and again increases at a further increase in CH₄ flow beyond 25 sccm. So, for the current set of films, the stress is tensile, which identifies the presence of voids and dislocations in its network.

The X-ray photoelectron spectroscopy (XPS) was performed to explore the chemical stoichiometry and the bonding configurations of the optimized sample. It also provided an estimate of the relative strength of various *s-p* hybridized carbon atoms bonded within the material [50]. Fig. 4.2 shows the XPS C 1s spectra of the sample grown with 25 sccm CH₄. Each C 1s spectrum was deconvoluted into five components using Voigt functions [51,52]. The peak at 284.1 eV appeared due to the excitations of the *sp*² hybridized C=C bonds. The *sp*³

hybridized C-C bonds were related to the peak at around 284.6 eV [53,54]. The other deconvoluted peaks at around 285.3, 286.2 and 289 eV were attributed to the excitations from C—OH, C=O and O—C=O bonds, respectively [50,51,53]. Percentages of the sp^2 and sp^3 contents were determined from the integrated areas ratios of the deconvoluted components in the spectrum [51,52]. The sp^2 hybridized C=C bonds were estimated as ~19.7%, and the sp^3 bonded C—C bonds as ~44% for the sample prepared with 25 sccm CH₄. As observed from the spectral deconvolution, along with the significant bonds between C atoms, a non-trivial fraction of O and OH bonding with C remains within the network, which are estimated to be ~12.59 % for C—OH, ~8.67% for C=O, ~15.05 % for the O—C=O bonds.

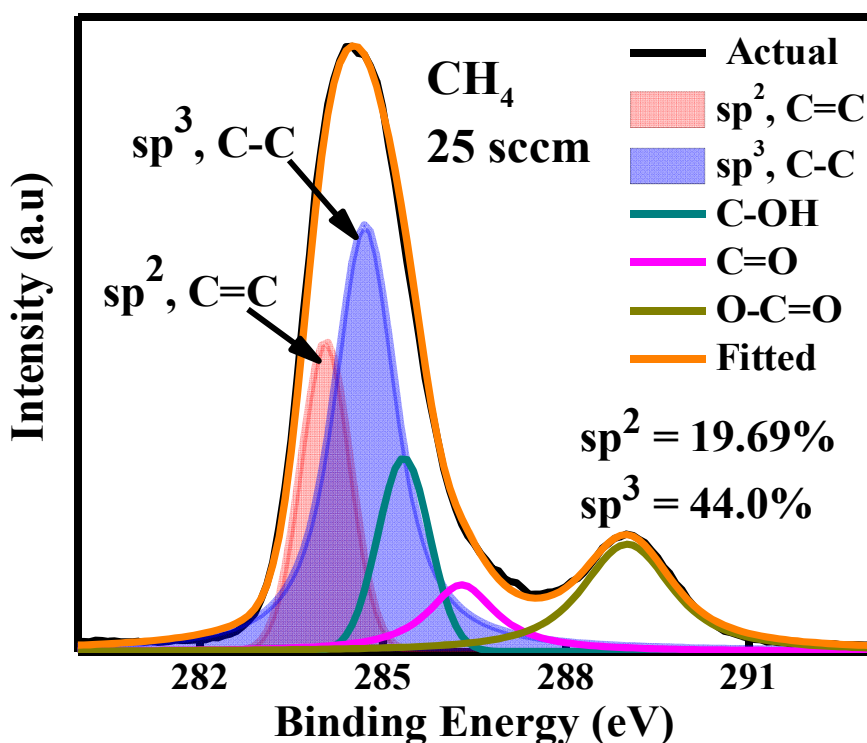


Fig. 4.2. C 1s XPS spectrum of the sample grown with 25 sccm CH₄.

Fig. 4.3(a) presents the transmission spectra of the DLC films prepared with varying the flow rate of CH₄ from 20 to 40 sccm, as obtained from the UV-Vis spectroscopy. All the films were highly transparent in the visible region, with average transparency of more than 80%. The corresponding optical band gaps of the films were calculated using Tauc's plot analysis, as demonstrated in **Fig. 4.3(b)**.

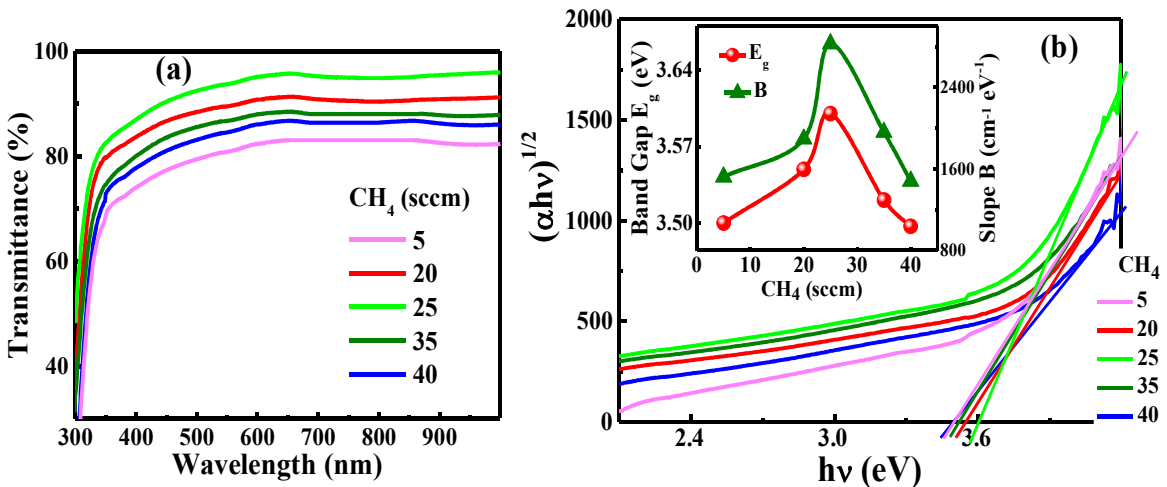


Fig. 4.3. (a) Transmission spectra of the samples prepared with varying the CH_4 flow rate from 5 to 40 sccm, (b) corresponding Tauc's plot showing the optical band gaps of the samples; inset shows the variation of the optical band gaps (E_g) and the corresponding slopes of the tangents to the Tauc's plot.

In this method, the absorption spectra of the samples are fitted with the power-law function, given by Tauc's equation [55]:

$$\alpha h\nu = B (h\nu - E_g)^n \quad \text{eqn (4.2)}$$

where α is the absorption coefficient, $h\nu$ is the energy, and E_g is the optical band gap. B is the slope of the straight line extrapolated on the energy axis. The exponent n can have different magnitudes depending on the band edge distribution, e.g., 3, 2, 3/2 and $1/2$, which are related to the indirect forbidden, indirect allowed, direct forbidden and direct allowed band distribution, respectively [56]. Extrapolation with the linear portion of the fitted graph on the photon energy axis gives the band gap energy (E_g) of the material. The slope B is called the edge width parameter, which measures the sharpness of the band edge. It gives an idea about the width of the band tails, which in turn is related to the disorder or defects in bond lengths or bond angles present in the film, and is inversely proportional to the width of the tail states [57–59]. The inset of Fig. 4.3(b) shows the variation of the optical band gap E_g and slope B of the Tauc's plot with the CH_4 flow rate. It is noted that with the increase in CH_4 flow rate from 20 to 25 sccm, the slope B increased, identifying reduced disorder in the network; while on further increase in the CH_4 flow rate to 35 and 40 sccm, B gradually decreased. Raman results also demonstrate similar gradual increase of disorder in the film network at a flow rate of CH_4 above 25 sccm. The optical band gaps (E_g) of the films showed similar nature of changes to the slopes in the Tauc's plot, with increase in CH_4 flow rate. The sample prepared with 25 sccm of CH_4 exhibited the highest optical band gap of ~ 3.6 eV.

Fig. 4.4 shows the variation of RMS surface roughness obtained from the AFM images of the samples with varying CH_4 flow rates from 20 to 40 sccm. The inset presents the AFM image with the highest surface roughness of 14.06 nm, for the sample prepared with 25 sccm of CH_4 flow rate; its corresponding low I_D/I_G value (Fig. 4.1(c)) and high sp^3 content (Fig. 4.2(a)) may indicate significant crystalline content in the network. Reduced surface roughness at elevated CH_4 flow rate beyond 25 sccm indicates the formation of amorphous prone structures from the available higher hydride CH_n precursors produced via insufficient dissociation of source gas at the applied rf power of 900 W [60]. Accordingly, the film prepared at 25 sccm of CH_4 flow rate corresponds to the optimised sample in this series, as perceived from various analyses.

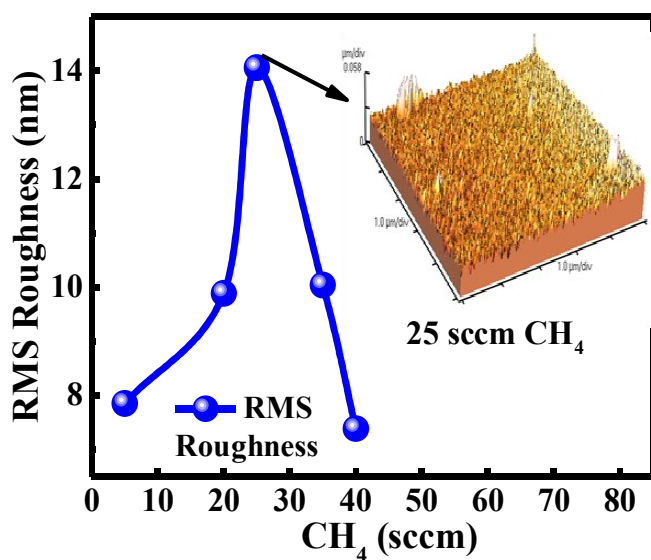


Fig. 4.4. The variation of RMS roughness of the samples prepared with CH_4 flow rates changed from 5 to 40 sccm, and the inset shows the AFM image of the sample prepared with 25 sccm CH_4 .

4.1.2. Effect of negative substrate bias:

In order to further improve the sp^3 content of the DLC films, the substrates were maintained at varied dc negative bias from 0 to -100 V, keeping the otherwise optimum deposition conditions unchanged, e.g., at $P= 900$ W, $T_S= 450$ $^{\circ}\text{C}$ and $p= 30$ mTorr (~ 4 Pa) and the flow rate of CH_4 fixed at 25 sccm. However, due to the associated etching of the growing surface in substrate bias enhanced growth, the deposition time was increased at elevated bias so as to maintain nearly equal thickness of the films around 40 nm.

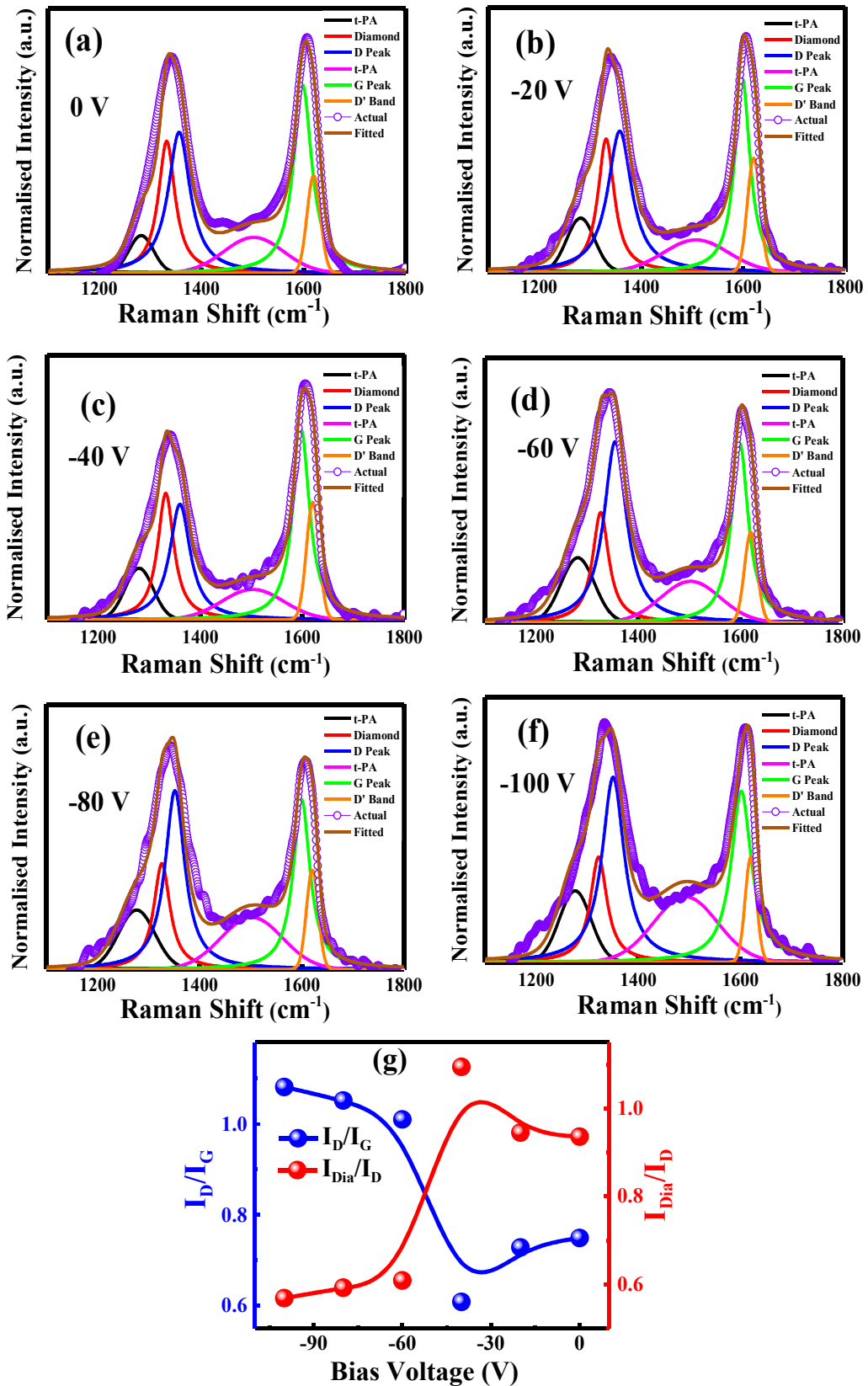


Fig. 4.5. (a–f) Deconvoluted spectra of films prepared with 25 sccm CH₄ at varying negative bias; (g) The variation of the intensity ratios I_D/I_G and I_{Dia}/I_D with the increase in negative substrate bias voltage.

Chapter 4

Figs. 4.5(a–f) show the deconvoluted Raman spectra of the as-prepared films at varying dc negative bias voltages, and Fig. 4.5(g) shows the corresponding I_D/I_G and I_{Dia}/I_D values of the films. Each spectrum is deconvoluted into 6 components, as earlier above. A systematic reduction in I_D/I_G and the concomitant increase in I_{Dia}/I_D ratios are evident from Fig. 4.5(g), with an initial increase in negative substrate bias. However, at applied bias voltage (V_B) above -40 V and its increasing magnitude up to -100 V, the sp^3 content of the DLC films gradually deteriorated in terms of related increasing I_D/I_G and reducing I_{Dia}/I_D values. The DLC film grown at -40 V dc bias demonstrated the minimum $I_D/I_G \sim 0.61$ corresponding to the maximum $I_{Dia}/I_D \sim 1.09$, which are superior to the corresponding values: ~ 0.75 and ~ 0.94 , respectively, for the film produced without the application of an additional electrical bias to the substrate, at a similar CH_4 flow rate of 25 sccm. Accordingly, the involvement of an optimum negative dc substrate bias applied on the substrate during film growth seems to be effective in maintaining superior sp^3 content in the DLC network.

Table 4.1: The variation of the different components of the films grown at 25 sccm CH_4 with increasing negative substrate bias voltage from 0 to -100 V.

Bias (V)	I_D/I_G	I_{Dia}/I_D	Diamond Peak Position (cm^{-1})	G Peak Position (cm^{-1})	Residual Stress (GPa)	E_g (UV-Vis) (eV)
0	0.75	0.94	1331.82	1598.30	0.09	3.60
-20	0.73	0.94	1332.25	1598.20	-0.12	3.64
-40	0.61	1.09	1332.39	1597.73	-0.19	3.71
-60	1.01	0.61	1326.14	1598.86	2.86	3.36
-80	1.05	0.59	1325.57	1599.43	3.14	3.02
-100	1.08	0.57	1322.16	1601.70	4.80	2.64

Table. 4.1 shows the variation of different characteristic parameters of the films grown at increasing substrate negative bias. The diamond peak position blue-shifts from 1331.8 to 1332.4 cm^{-1} with an increase in substrate bias to -40 V, along with the corresponding minimization of residual stress within the film network, beyond which, however, it red-shifts to 1322.2 cm^{-1} at a substrate bias of -60 V. The improved quality of the DLC film prepared with

Chapter 4

25 sccm CH₄ at -40 V is indicated by the minimum of I_D/I_G (0.61), maximum of I_{Dia}/I_D (1.09) and low compressive stress (-0.19).

With the application of negative bias up to 40 V, the impinging ions interact on the growing film surface, induces cross-linking within C-C network with *sp*³ hybridization. Compressive stress is generated due to the formation of *sp*³ C-C clusters within the matrix. However, as the negative bias rises further beyond 40 V, higher energy of the impinging ions onto the film surface is dissipated as heat, initiate etching from the growth zone and create disorder in the dense *sp*³ C-C clusters. Tensile stress is generated due to the formation of defects and voids in the lattice [47–49,61].

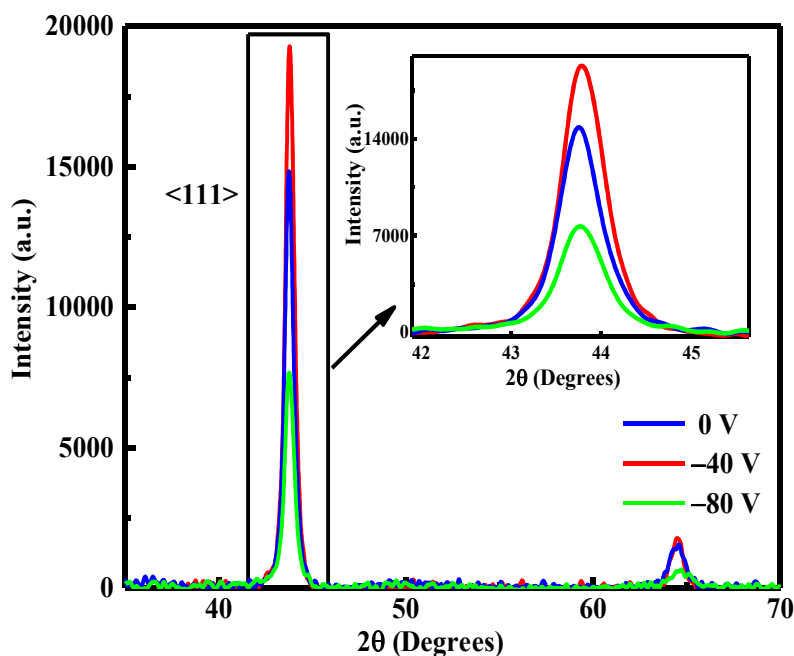


Fig 4.6. The XRD spectra of films prepared at 0 V, -40 V and -80 V dc substrate bias; Inset: Magnified portion of the peak appearing at $2\theta = 43.8^\circ$.

The structural characteristics and grain size of the DLC films were studied by X-ray diffraction. Fig 4.6. shows the XRD spectrum of the samples prepared at 0, -40 and -80 V substrate bias. The inset shows the enlarged portion of the most intense peak at $2\theta \sim 43.8^\circ$. Each spectrum exhibits a sharp peak at $2\theta \sim 43.8^\circ$, which corresponds to the <111> plane of the cubic diamond lattice [62]. The other peak at $\sim 64.55^\circ$ originates from the SiO₂ components present in the glass substrate. The inter-planar spacing (*d*) for a lattice plane can be calculated from Bragg's equation:

$$2 d \sin \theta = n\lambda \quad \text{eqn (4.3)}$$

Chapter 4

where 2θ is the diffraction angle (i.e., the angle between the incident X-ray beam and the diffracted ray), n is an integer, and λ is the X-ray wavelength ~ 1.54 Å. The value of d for the $<111>$ plane is calculated to be ~ 0.2065 nm. Using Debye-Scherrer's equation (4), the average grain size (D) of the nanocrystals is evaluated as [57]:

$$D = \frac{\kappa\lambda}{\beta \cos \theta} \quad \text{eqn (4.4)}$$

where β is the full-width-at-half-maximum (FWHM) of the diffraction peaks. The average grain size (D) has been estimated to be almost identical ~ 14.8 nm for all the above said samples. The XRD peak at $2\theta \sim 43.8^\circ$, as observed from Fig. 4.6 (inset), exhibits a variation in intensities for the films prepared at different substrate bias voltages. The intensity increases as the bias voltage increase from 0 to -40 V and then decreases at -80 V, which indicates that the -40 V sample has a higher concentration of phases with $<111>$ orientated planes.

The XPS C 1s spectrum of the DLC film prepared at -40 V ($\text{CH}_4 = 25$ sccm) is shown in Fig. 4.7, with the corresponding deconvolution into 5 components, as earlier. With the application of negative dc substrate bias of -40 V, the content of sp^3 C-C bonds in the sample increased from 44% (Fig. 4.2(a)) to $\sim 64.28\%$ (Fig. 4.7) while that of sp^2 hybridized C=C bonds reduced from 19.7% to $\sim 9.04\%$. At -40 V dc substrate bias, the increase of the sp^3 content identifies a gross reduction in the structural disorder and better crystalline orientation in the film network, which appears consistent with the results obtained from the Raman data revealing much lower I_D/I_G ratio and other parameters (as given in Table. 4.1). In the matrix the percentage composition of the other bonds like C-OH, C=O, O-C=O are $\sim 9.83\%$, $\sim 8.55\%$ and $\sim 8.29\%$, respectively, which are individually lower than the identical film grown without applying the substrate bias.

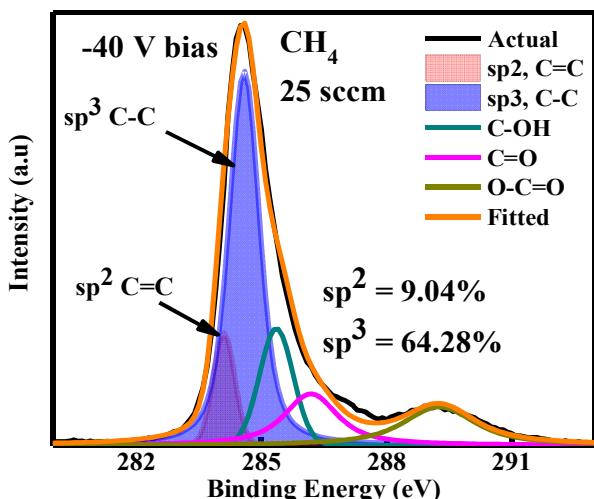


Fig. 4.7. Deconvoluted C 1s XPS spectrum of the film prepared at -40 V bias.

Chapter 4

The transmission spectra of the DLC films prepared at various negative substrate bias 0 to -100 V and the optical band gap obtained from the corresponding Tauc's plot are presented in Fig. 4.8. The transmission of the samples over the entire visible region gradually increased on increasing the magnitude of the applied substrate bias up to -40 V above which, however, the films systematically became less transparent. The optical band gap E_g and the slope of the Tauc's plot B, shown at the inset of Fig. 4.8(b), initially increased with the applied negative bias voltage up to -40.0 V, beyond which, however, both the parameters systematically decreased in magnitude. The highest $E_g \sim 3.71$ eV corresponds to high transparency, and the increased slope B indicates the reduced disorder in the film prepared at -40 V of dc substrate bias.

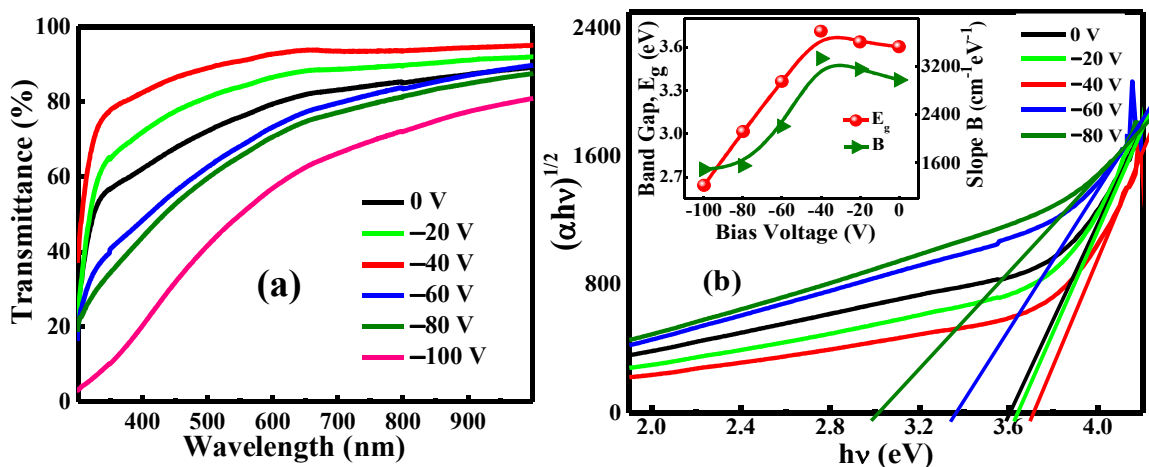


Fig. 4.8. (a): Transmission spectra of the samples prepared with different bias voltages varying from 0 to -100 V dc, (b) Corresponding Tauc's plot of the samples with the inset showing the variation of the band gap and slope of the Tauc's plot with the variation of the bias voltage.

The surface roughness variations estimated from the AFM data of the DLC films, shown in Fig. 4.9, identify the highest RMS roughness of ~ 17.54 nm at an applied substrate bias voltage of -40 V, above and below of which the surface roughness reduces systematically. With the increase in bias voltage, the precursor ions were attracted towards the substrate with increased number density and momentum, which facilitated the formation of an increased number of nucleation sites and the growth of the improved nanocrystalline structures from elevated energy transfer. However, on further increase in the bias voltage above -40 V, an enormous rise in the flux of precursors to the nucleation sites hindered the favorable growth of nanocrystals. A subsequent increase in the amorphous fraction led to the observed reduction in surface roughness.

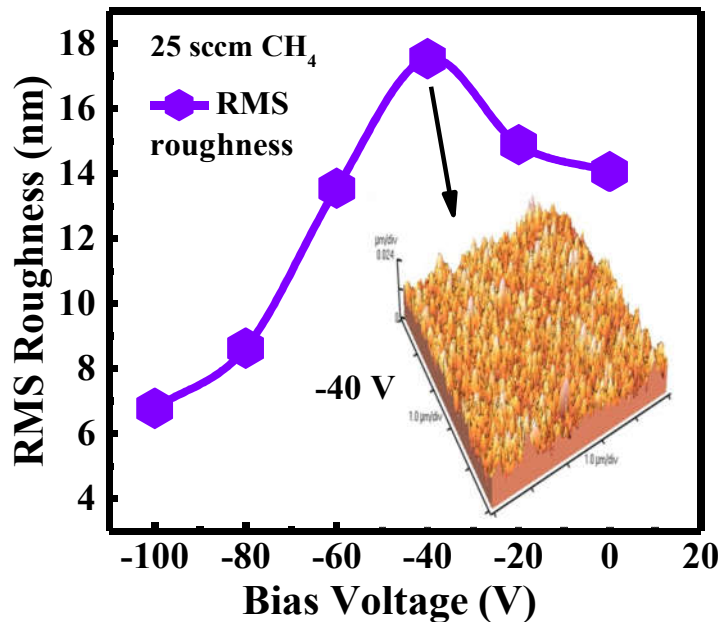


Fig. 4.9. The variation of RMS roughness of the samples prepared with 25 sccm CH_4 flow rate at varied substrate bias from 0 to -100 V, and the inset shows the AFM image of the sample prepared at -40 V dc bias.

Fig. 4.10(a) and 4.10(b) show the surface morphologies of the DLC films prepared at 25 sccm and 40 sccm of CH_4 , respectively, without any application of substrate bias. The surface of the film in Fig. 4.10(a) demonstrates smooth amorphous tissue like patches connected with a net-shaped crystalline-like network randomly distributed within the matrix; however, those patches coalesce together, at a higher flow rate of CH_4 to form larger chunks of smooth irregular islands separated by non-uniform voids, in Fig. 4.10(b). The average surface roughness reduces, with amorphous tissue-like patches being the dominant fraction in the form of chunks, as shown in Fig. 4.4. However, the amorphous tissue-like smooth section of the matrix is eliminated by applying -40.0 V of bias to the substrate during growth (Fig. 4.10(c)). Uniformly distributed and mostly nanocrystalline-like diamond grains seem to form a range of interconnected helical shapes. Thus, the overall surface roughness increases in the bias enhanced growth of the DLC thin films (Fig. 4.9). Similar formation of the interconnected helical shapes within the larger chunks of smooth irregular islands forming nanocrystalline-like diamond grains of lesser density is evident on application of -40 V of substrate bias during growth of DLC thin film from 40 sccm of CH_4 flow rate in the plasma, as shown in Fig. 4.10(d).

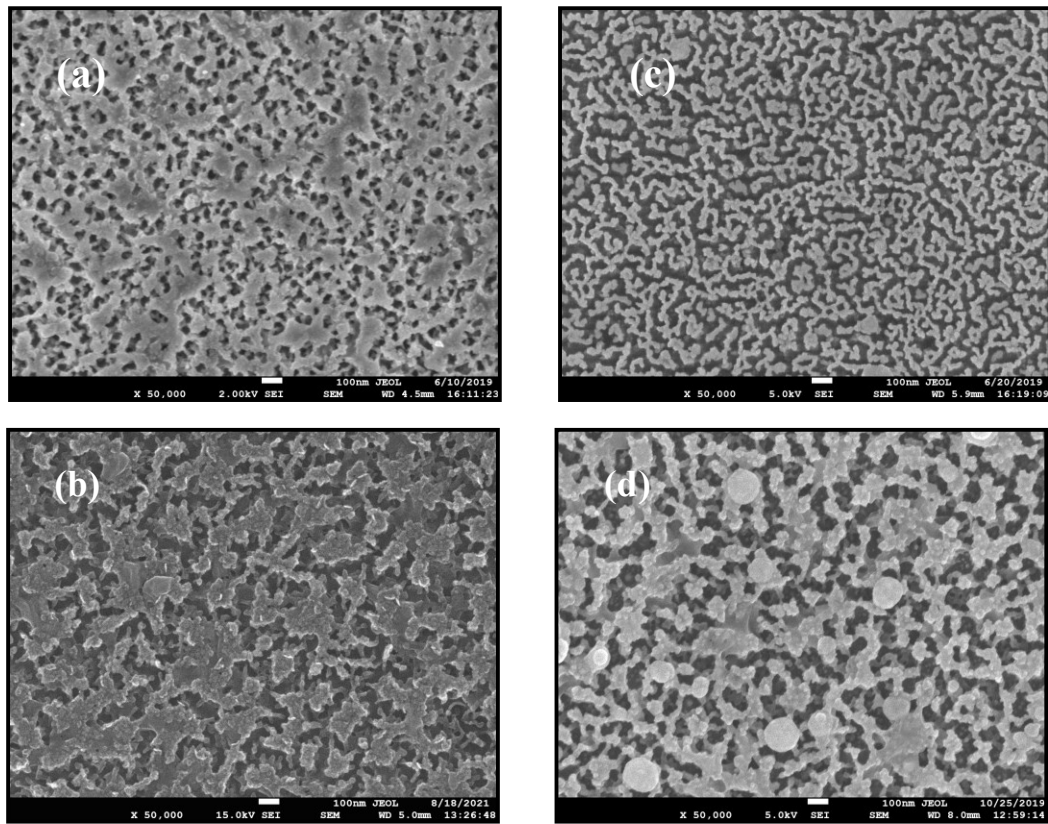


Fig. 4.10. SEM micrographs of the DLC films prepared with (a) 25 sccm CH₄, without bias, (b) 40 sccm CH₄, without bias, (c) 25 sccm CH₄, with a substrate bias of -40 V dc, and (d) 25 sccm CH₄, with a substrate bias of -80 V dc.

The crystalline configuration of the grown network in the optimized DLC film was studied by transmission electron microscopy. The TEM micrograph in Fig. 4.11(a) demonstrates an amorphous matrix with well-identified nanocrystallites uniformly distributed within it. The high-resolution image in Fig. 4.11(b) shows distinct <111> planes in circular patches distributed all over the matrix [63–65]. Crystalline-like configuration of the network was confirmed by the presence of a spotted diffraction pattern corresponding to definite <111> crystallographic planes, shown in Fig. 4.11(c). A 3-dimensional shaped structure possessing elevated ridges was obtained within the matrix, as shown in Fig. 4.11(d). Fig. 4.11(e) shows the distinct crystal planes of <111> orientation (0.204 nm lattice spacing) with sharp discontinuities, showing the different facets of crystalline planes. This lattice spacing D matches with that obtained from the XRD analysis (~0.206 nm). However, each of these facets has the same <111> crystalline orientation. The hexagonal shape of truly diamond structure within the amorphous matrix is evident in Fig. 4.11(f).

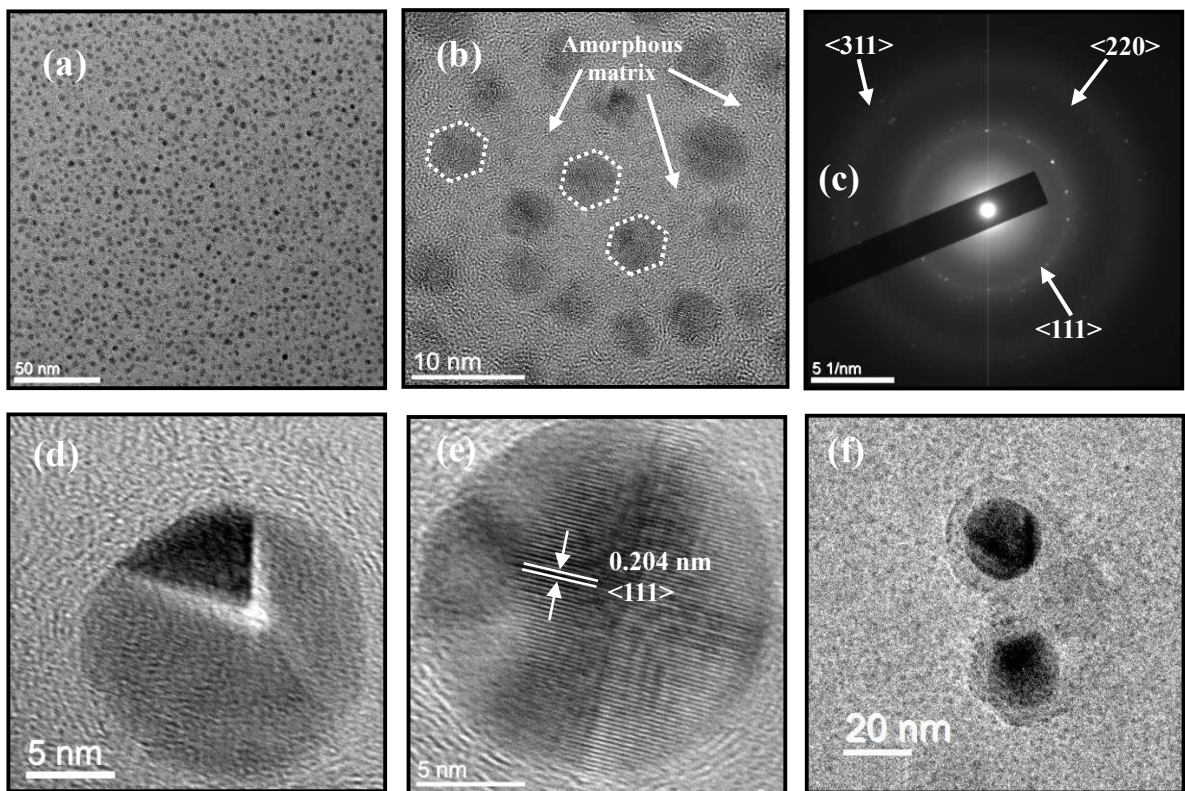


Fig. 4.11. (a) TEM micrographs of the optimized nanodiamond films prepared with -40.0 V dc substrate bias; (b) High-resolution image, showing the distinct $<111>$ crystalline planes present in circular patches distributed all over; (c) inset shows the SAED image with the planes; (d) A 3D-shape of nanodiamond obtained in the matrix; (e) Distinct $<111>$ crystal planes observed with sharp 3 D ridges; (f) Crystal lattice and hexagonal shape with almost equal sides.

4.2. Discussion:

The present work mainly focuses on developing diamond-like carbon (DLC) films from CH_4 and Ar plasma without substrate pre-treatment and its subsequent improvement in terms of crystalline quality via systematic optimization of the plasma parameters. Films have been characterized by several spectroscopic and microscopic studies. It has been identified that the crystallinity of DLC films increases with an increasing flow rate of the precursor gas up to a particular scale and also on the application of a certain magnitude of applied negative dc substrate bias.

The pre-treatment of glass substrates prior to the deposition with nanodiamond powders facilitates high nucleation density, thereby enhancing the quality of DLC growth [1,25]. Since the present work does not involve any pre-nucleation of the glass (non-diamond) substrates or any pre-treatment via mechanical scratching, the initial nucleation on the substrate surface in

Chapter 4

the plasma is very important for the growth of the DLC films. The substrates were subjected to Ar plasma etching to remove any dirt particles on the glass substrate.

It is observed that at 900 W rf power, 450°C and 30 mTorr (~4 Pa) of pressure, with the increase in CH₄ flow rate from 5 to 25 sccm, the crystalline quality and the *sp*³ C-C content of the films increases. The main precursors in forming diamond-like carbon films in CH₄/Ar plasma are the CH₃ radicals formed by the dissociation of CH₄ molecules by the Ar ions in the plasma via chemical reactions [66–69]. Thus, higher CH₄ flow rates lead to a higher density of CH₃ radicals. Within the low CH₄ flow rate regime (≤ 25 sccm), increased CH₄ flow rate enhances the formation of the precursor ions (CH₃), promoting the growth of diamond phases. The CH₃ radicals get nucleated onto a radical site on the surface by hydrogen abstraction reactions, which automatically creates another radical site on the nucleated one for the next CH₃ radical and continue the cycle [70]. However, the presence of excess CH₃ radicals leads to the CH₃-CH₃ recombination, forming a large molecule of C₂H₆ [71]. Therefore, at higher CH₄ flow rates (> 25 sccm), the growth of the non-diamond components from larger hydrocarbon particles dominates, hampering the ordered crystalline orientation of the diamond phases. This is reflected in the variation of the residual stress generated, during growth, within the films.

Application of negative dc bias to the substrate, in general, increases the nucleation density and facilitates nanostructured growth in thin films, including the DLC or nanodiamond films. [33,66,72,73]. The active precursor ions in the plasma e.g., (CH₃), H⁺ and Ar⁺ are drawn towards the substrate under the negative bias. The energetic H⁺ and Ar⁺ ions bombard the substrate surface causing defects or creating dangling bonds by H abstraction. These serve as nucleation sites for the diamond phases [74–77].

Thus, when the negative bias is increased initially from 0 to -40 V, the nucleation density increases and the precursor ions have sufficient energy to nucleate and get deposited in an ordered orientation of *sp*³ C-C bonds. The bombarding H⁺ and Ar⁺ ions, on the other hand, continuously etched both the *sp*³ and *sp*² C-C bonds during the process. Because *sp*² C=C bonds are made up of weaker π -bonds, etching of non-diamond *sp*² C=C bonds is more dominant than *sp*³ C-C bonds (diamond phase) at lower bias voltages (≤ -40 V). Hence, the simultaneous increase in the nucleation densities and the etching of the non-diamond components enhance the crystalline nature of the films during application of 0 to -40 V bias voltage. On applying bias voltages > -40 V, etching of the *sp*² and *sp*³ C-C bonds occurs, incorporating disorder within the matrix, thereby reducing the crystalline quality of the DLC films [78].

Chapter 4

Fig. 4.12 presents the histogram comparing the I_D/I_G ratios of DLC and a-C films prepared by others with those obtained in the present case. The lowest I_D/I_G ratio value obtained in each experiment is plotted in the histogram. L. Yu *et al.* prepared the DLC films by magnetron sputtering involving nanodiamond powder pre-treatment of the substrate. They reported an I_D/I_G value of 0.77 for the 40 nm thick seeded sample [25]. The a-C films, prepared by J. Filik *et al.*, in an rf CCP at -50 V dc bias has an I_D/I_G value of 0.82 [79]. The minimum I_D/I_G ratio of Ti containing DLC films prepared by rf capacitively coupled PECVD varies from 0.95 to 2.4 at different substrate temperatures [68]. The DLC films prepared by a closed field unbalanced magnetron sputtering ion plating system, along with an application of -30 V substrate bias, exhibited an I_D/I_G ratio of 0.7 [13]. The lowest I_D/I_G ratio obtained for DLC films by rf (13.56 MHz) magnetron sputtering was ~ 0.46 [5]. DLC films prepared by others in rf PECVD [80], magnetron sputtering [9] and ion beam deposition techniques [14] exhibit I_D/I_G ratios of 0.56, 0.61 and 1.73, respectively. The DLC prepared in the present work possesses an I_D/I_G value of 0.61 with a dc negative bias voltage application of -40 V. Using high pressure plasma in MW-PECVD, spherical nanodiamond, and additionally employing diffuse plasma under the shadow mask, even microcrystalline diamond, have been reported; however, using a low-pressure plasma in ICP-CVD, the present growth of diamond-like carbon films with substantial nanocrystalline phases revealing well defined lattice planes is a significant achievement [81,82].

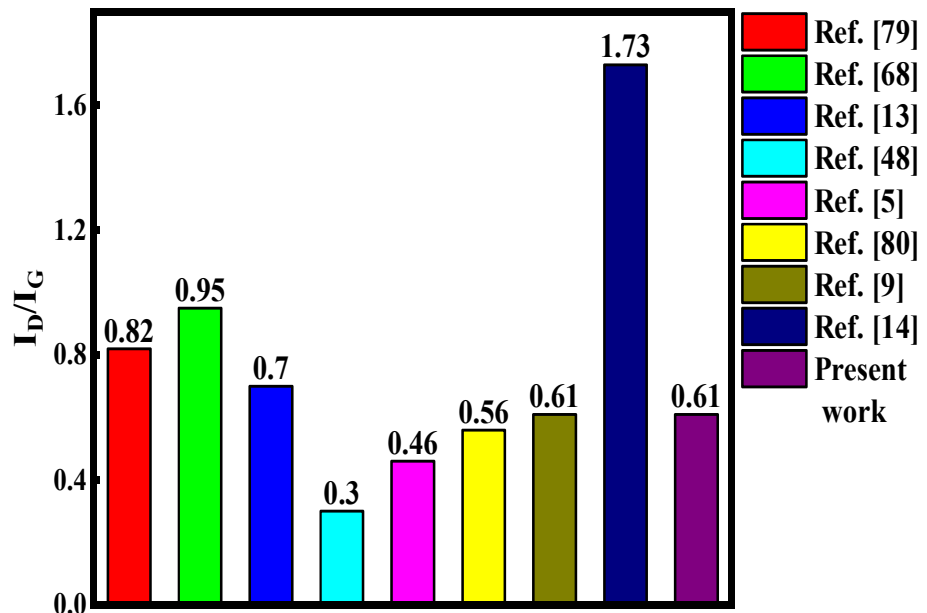


Fig. 4.12. Comparison of I_D/I_G values of DLC obtained in different works reported in the literature.

Chapter 4

4.3. Summary and conclusion:

The present manuscript involves the single-step growth of diamond-like carbon thin films with nanodiamond components in a planar inductively coupled rf plasma (ICP) CVD system, without any initial substrate pre-treatment by expensive diamond powder. The film with improved crystalline quality was obtained by optimizing the parameters like CH₄ flow rate and dc negative substrate bias at a high rf power of 900 W, substrate temperature of 450 °C and a low deposition pressure of 30 mTorr (~4 Pa). A signature of good quality DLC films, with considerable *sp*³ content, was obtained with a characteristic minimum $I_D/I_G = 0.75$ and maximum of $I_{Dia}/I_D = 0.94$ from Raman studies at an optimum deposition condition of 25 sccm of CH₄ flow rate. A systematic variation of the diamond peak shift gives an idea of the residual stress generated within the films; the sample grown at 25 sccm CH₄ exhibits low tensile stress of 0.09 GPa. However, the XPS results shows that the *sp*³ content of the sample with 25 sccm CH₄ flow rate is about 44 %. This optimized film (25 sccm CH₄) shows the highest roughness of 14.06 nm, due to a higher crystalline diamond fraction in the film. The quality of DLC films improve further by applying negative dc bias to the substrates. At a dc bias of -40 V, DLC films are produced with better crystallinity corresponding to a lower $I_D/I_G \sim 0.61$ and higher $I_{Dia}/I_D \sim 1.09$ in the Raman spectrum. The *sp*³ content of the DLC film prepared with -40 V negative dc bias is found to be ~64.28%, which is about 20.28%, higher than the film prepared without substrate bias. The optimized DLC films are highly transparent with an optical band gap of ~3.71 eV. The XRD peaks and TEM images confirm its high crystalline quality with well-identified <111> crystallographic facets of hexagonal structure, featuring fractions of diamond-like components in an amorphous matrix.

A.1.2: Chapter 5

Boron doped DLC films

Chapter 5

➤ Introduction:

Intrinsic diamond-like carbon (DLC), characterized by its carbon-carbon (C-C) bonds, functions as an insulator due to its wide energy band gap of 5.47 eV [83]. The high electrical resistivity of DLCs hinders their usage in many electronic and industrial applications [84]. Enhancing the conductivity of diamond-like carbon (DLC) films can be effectively achieved through doping. Introducing dopants into the carbon-carbon (C-C) matrix generates defect states within the energy bands. These defect states enable the efficient transport of charge carriers between adjacent bands, thereby improving the material's conductivity. Electrically conductive DLC films are widely utilized in various applications, particularly in high-speed microelectronics and optoelectronics, such as field emission flat panel displays [85,86].

DLC films can be doped with N and P to form *n*-type semiconductors, and *p*-type DLCs are grown by incorporating B into the diamond lattice, the atomic radius of B matches that of C [87,88]. Doping alters the electrical, optical, and tribological properties of diamond-like carbon (DLC) films [89,90]. In boron-doped diamond-like carbon (DLC) films, electrical conduction typically occurs through electron hopping between localized defect states situated within the energy gap between the conduction and valence bands [91,92].

Electrically conducting DLC thin films with superior properties like high hardness, high transparency, low friction coefficient, and super corrosion stability are extremely useful in many applications [93]. Besides, intrinsic DLC films have poor adhesion with substrates triggered by their high internal stress [94], which could be reduced by B doping, and, in turn, improved adhesion to the substrate is possible [89,95]. B-doped DLCs possessing ~10 at.% B are reported to exhibit 65% less stress relating to undoped DLC films [89]. Doped DLC films are used in carrier injection enhancement [96], room temperature electroluminescence [97], as cold-cathode material [98], in metal-semiconductor-metal detectors [99], electrochemical applications [100], piezoelectric applications [101], thin film transistor [102], and DLC/Si solar cells [103–106].

The B-doped DLC films are grown by numerous techniques, e.g., microwave plasma chemical vapour deposition (CVD) [107,108], electron cyclotron resonance (ECR) plasma CVD [109], hot filament CVD [110], plasma enhanced CVD (PECVD) [111,112], pulsed laser deposition [113,114], plasma immersion ion processing [89], etc. In PECVD, the B doping is employed *in situ*, at low deposition temperature, using gaseous sources, e.g., diborane (B₂H₆), tri-methyl boron (TMB), and di-boron trioxide (B₂O₃) into the precursor gas mixture containing

Chapter 5

H₂/Ar/hydro-carbon [115]. One of the prime advantages of PECVD techniques is that thin films with a wide range of properties are grown by varying the growth parameters [116]. The growth of diamond thin films with controlled grain sizes and properties desirable for specific applications is possible uniquely by this process [117]. Although the growth of undoped DLC films on low-temperature substrates is popular [118,119], relatively less attention has been paid to producing B-doped DLC films at low growth temperatures [120,121].

Amongst the various PECVD systems, the inductively coupled plasma (ICP) CVD, possessing a high density of electrons ($\sim 10^{12} \text{ cm}^{-3}$), yields a dense plasma yet at a low pressure and offers a higher growth rate [22,30–32]. In addition, the inherent high atomic H density in the hydrocarbon plasma in ICP-CVD induces efficient etching of the amorphous component of the newly grown matrix, facilitating its fruitful crosslinking with the existing network underneath. The power generated through the inductively coupled coils also enables uniform film deposition at relatively low temperatures [22].

The prime motivation of this present work is to obtain electrically conducting and adequately transparent B-doped DLC films in a radio frequency (RF) inductively coupled plasma (ICP) CVD unit at a low pressure and relatively low temperature. The plasma gases consist of CH₄ as the precursor and Ar as the diluent gas, while the source of B is gaseous diborane (B₂H₆) (1% in He). The use of glass as substrate in this work satisfies the requirement in two ways: possessing a thermal expansion coefficient similar to that of diamond ($7 \times 10^{-7} \text{ K}^{-1}$), and being readily available and cost-effective. The ICP-CVD technique ensures a uniform B-DLC film deposition over a wide area at a low plasma pressure and low substrate temperature of $\sim 450 \text{ }^{\circ}\text{C}$, following a one-step growth sequence without using diamond powder.

➤ Experimental

The experimental details have been elaborately described in the preliminary part of Section A (for the development of Carbon nanostructures (DLC)). Apart from CH₄ and Ar as the precursor gases, B₂H₆ (1 % in He) was used as the dopant gas for the preparation of B-doped DLC films.

5.1:

**Effect of changing B_2H_6/CH_4 ratio on the
properties of B-doped DLC**

Chapter 5

The present work deals with the efforts to obtain electrically conducting and adequately transparent B-doped DLC films in a radio frequency (RF) inductively coupled plasma (ICP) CVD unit by adjusting the dopant and precursor gas flow rates at a low substrate temperature of 450 °C and pressure of 40 mTorr.

The substrates were treated in Ar plasma for 10 mins at an RF power of 800 W and chamber pressure of 40 mTorr before the film growth. With the deposition parameters fixed at 450 °C, 800 W RF power, 40 mTorr gas pressure, and -40 V substrate bias, a set of DLC films was grown by varying the flow rate of B₂H₆ (1% in He) within (0–25) sccm and Ar within (50–25) sccm and keeping the CH₄ flow fixed at 25 sccm; maintaining 5 h. of deposition for each sample. The substrate bias of -40 V was previously optimized for growing the intrinsic DLC films with significant nanocrystalline phases (as in **section A.1**). The average thickness of each sample was ~70 nm, as measured by the Dektak 6M stylus profilometer.

A set of samples was prepared by varying the flow rate ratio $r = (B_2H_6/CH_4)$ in % while maintaining the constant CH₄ flow rate of 25 sccm and keeping the total flow of all gases fixed at 75 sccm, as given in [Table 5.1.1](#).

Table 5.1.1: Set of samples prepared by varying $r = (B_2H_6/CH_4)$ in %.

CH ₄ flow rate (sccm)	Ar flow rate (sccm)	B ₂ H ₆ (1% in He) flow rate (sccm)	$r = (B_2H_6/CH_4)$ (%)
25	50	0	0
25	48	2	0.08
25	45	5	0.2
25	40	10	0.4
25	35	15	0.6
25	30	20	0.8
25	25	25	1

5.1.1. Results and discussion:

The Raman spectrum of each sample of the set is deconvoluted into 6 satellite components, as shown in [Fig. 5.1.1\(a\)](#). The two broad peaks are observed in each spectrum. The broad peak, centered at about 1345 cm⁻¹ comprises two components; the diamond peak and the D band. As a symmetric peak fitted with a Lorentzian function [\[122\]](#), the diamond peak at 1332 cm⁻¹, shows the exact tetrahedral orientation of the diamond's sp^3 hybridized C-C bonds [\[123,124\]](#). However, the FWHM of the diamond peak is ~45 cm⁻¹, which is much broader

Chapter 5

compared to the perfect diamond peak. The broadening effect is due to the reduced size of the diamond grains and an increase in the non-diamond content within the sample [125]. The irregularity in the crystalline sp^2 hybridized C=C bonds causes the D band, which emerges at 1360 cm^{-1} [116,126]. The G peak, at about 1600 cm^{-1} , is the second broad peak that results from the bond stretching vibrations of the sp^2 hybridized C=C bonds found in both rings and chains. Both the D and G peaks are related to the graphitic phase and are fitted with Lorentzian distributions [116]. The G peak depicts the presence of crystalline orientation of graphitic sp^2 hybridized C=C bonds [88]. The G peak is broadened and shifted to 1600 cm^{-1} due to the presence of disordered C layers [126,127]. The appearance of the peak at around 1275 cm^{-1} is indicative of the vibrations caused due to the formation of B-C bonds [128] and signifies the incorporation of B atoms within the diamond lattice.

Two companion peaks, v_1 , and v_2 appear at 1150 cm^{-1} and 1490 cm^{-1} due to the trans polyacetylene segments, present at the grain boundaries [129–131]. Here the v_1 mode gets completely covered by the 1275 cm^{-1} peak. Another small peak is detected at 1620 cm^{-1} , out of vibrations occurring from the disordered graphitic lattices [132].

An estimate of the amount of disorder, in comparison with the crystalline orientation of the graphitic phase of the films, can be accounted for from the intensity ratio of the D peak concerning the G peak (I_D/I_G) [14,133]. Fig. 5.1.1(b) shows that the I_D/I_G ratio increases with the rise in r value from 0 to 1% and reaches its maximum of ~ 0.819 at $r = 1\%$, i.e., the disorder content in the sample network approaches the maximum when the working plasma holds the highest dopant (B_2H_6) content. The increasing value of I_D/I_G is associated with the increased size and number of the graphitic micro-domains and a reduction in the number of four-fold coordinated C atoms [46,134,135].

Comparison of the different phases of sp^3 and sp^2 hybridized C-C bonds present in the B-doped DLC matrix is made based on the intensity ratios of the diamond peak (I_{Dia}) to the G peak (I_G), as I_{Dia}/I_G . In Fig. 5.1.1(b), the I_{Dia}/I_D value decreases with the increase in the r -value, reaching the minimum of ~ 0.83 at $r = 1\%$. This indicates that the extent of sp^3 C-C bonds in the DLC film continuously reduced at the cost of increasing sp^2 C=C bonds with the increase in dopant dilution of the carbonaceous precursors, r (%), in the plasma [136].

The crystalline content of the films, on account of the disorder associated with the sp^2 C=C structural distribution, is further assessed by comparing the intensity ratios of the diamond peak concerning the D peak, as (I_{Dia}/I_D) [14,131,137]. Fig. 5.1.1(b) exhibits the decreasing

Chapter 5

nature of I_{Dia}/I_D with the increase in r from 0 to 1%. The lowest value of $I_{\text{Dia}}/I_D \sim 1.01$ identifies the lowest crystalline content of the DLC film at the maximum dopant dilution of the plasma at $r = 1\%$.

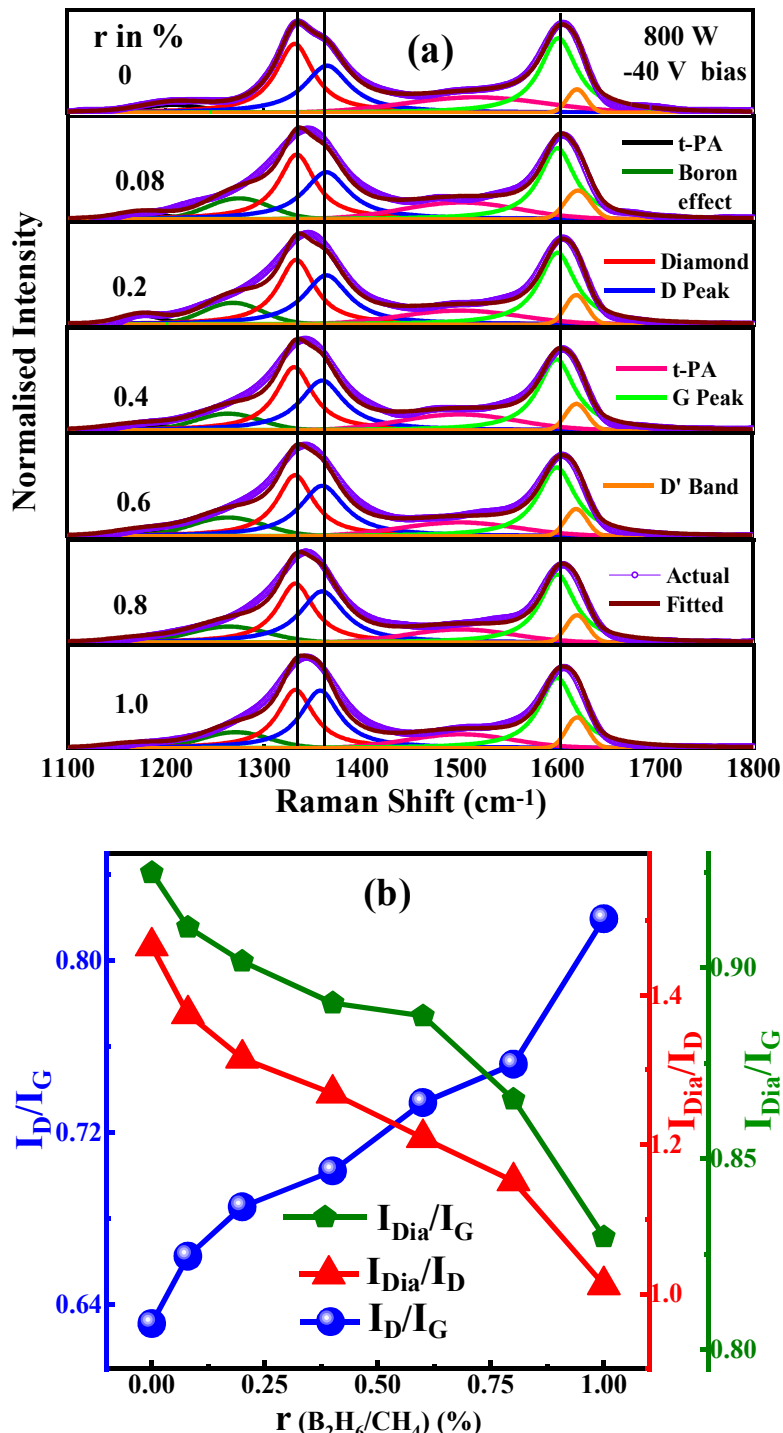


Fig. 5.1.1: (a) Deconvoluted Raman spectra of the samples with r (=B₂H₆/CH₄) varying from 0 to 1% (Black vertical lines are to guide the eyes corresponding to the nearest deconvoluted satellite peaks);
(b) Variation of the intensity ratios: I_D/I_G , I_{Dia}/I_D , and I_{Dia}/I_G with the changes in r (=B₂H₆/CH₄).

Chapter 5

Fig. 5.1.2 shows the XRD patterns over a span of $2\theta \sim 30^\circ$ – 60° for the samples prepared with r varying from 0 to 1%. It is observed that for the undoped DLC film prepared at $r = 0\%$, a sharp diffraction peak appears at around $2\theta = 43.49^\circ$, which corresponds to the $\langle 111 \rangle$ crystalline planes of diamond [62]. With the introduction of a minute amount of dopant corresponding to $r = 0.08\%$, the peak at $2\theta = 43.49^\circ$ becomes significantly sharper, identifying substantial improvement in the dopant-induced crystallization in the DLC network. However, with the increase in $r = 0.4\%$, the peak reduces abruptly both in intensity and sharpness, rather it turned into a hump with a broad full width at half maximum (FWHM). With the further increase in r , the hump gradually reduces in intensity and virtually disappears for $r = 1\%$. This indicates that the very initial phase of B atoms' incorporation in the network facilitates the expansion of the tetrahedral orientation of C-C bonds. This could happen if the primary C-C network remains electronically slightly *n*-type, and a minute amount of dopant incorporation turns it intrinsic with a corresponding better crystallographic orientation. However, at increasing r (%) the doped C-C network transforms *p*-type gradually, with a corresponding loss of crystallinity.

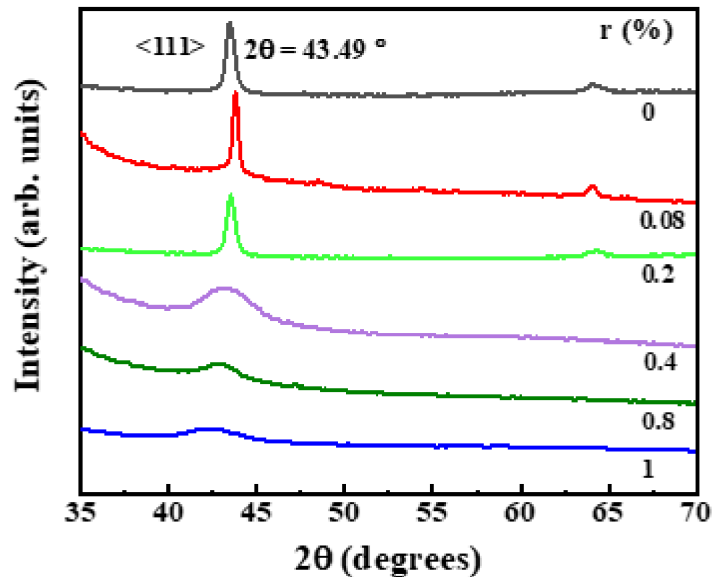


Fig. 5.1.2: XRD patterns of the samples prepared with r varying from 0 to 1%.

The chemical composition of the as-prepared B-doped DLC films was investigated via X-ray photoelectron spectroscopy (XPS) studies in both wide-range and high-resolution analyses of the different elements. It gives a quantitative estimate of the atomic concentrations of the elements C, O, and B, present in the films. Fig 5.1.3(a) shows the XPS spectrum (full scan) of the sample prepared with $r = 0.8\%$, showing two sharp peaks at 285.3 eV and 533.3 eV, which correspond to C 1s and O 1s orbitals, respectively. A small peak of N 1s appears at

Chapter 5

~400 eV. [Fig. 5.1.3\(b–c\)](#) shows the high-resolution spectra of C 1s and B 1s electronic states of the sample prepared at $r = 0.8\%$, respectively. The C 1s spectrum is deconvoluted into 5 component peaks using Voigt functions (comprising 80% Gaussian and 20% Lorentzian character) [\[138,139\]](#).

The peak appearing at 284.2 eV arises due to the vibrations from the sp^2 C=C bonds and the one centred at 284.6 eV comes from the vibrations of the sp^3 C-C bonds [\[42,53,140\]](#). The smaller peaks at 285.5, 286.2, and 289.8 eV are assigned to alcoholic C-OH, carbonyl C=O, and carboxyl O-C=O groups, respectively [\[51,53\]](#). The C 1s spectrum of the film prepared at $r = 0\%$ remains virtually similar to that for $r = 1\%$. However, the presence of B atoms as dopants in the DLC network for $r = 1\%$ makes the difference, as identified by the high-resolution spectral analysis and subsequent deconvolution of the corresponding peak appearing at around 190 eV, shown in [Fig. 5.1.3\(c\)](#). The B 1s spectrum is deconvoluted into 3 peaks: the first one, at 185 eV originates from the de-excitation of the electrons within the B₄-C bonds; the second one, centred at 188 eV, arises due to the B-C_{3.4} bonds and the third one corresponds to the binding energy of B-O bonds present in the film (at 192 eV) [\[141,142\]](#).

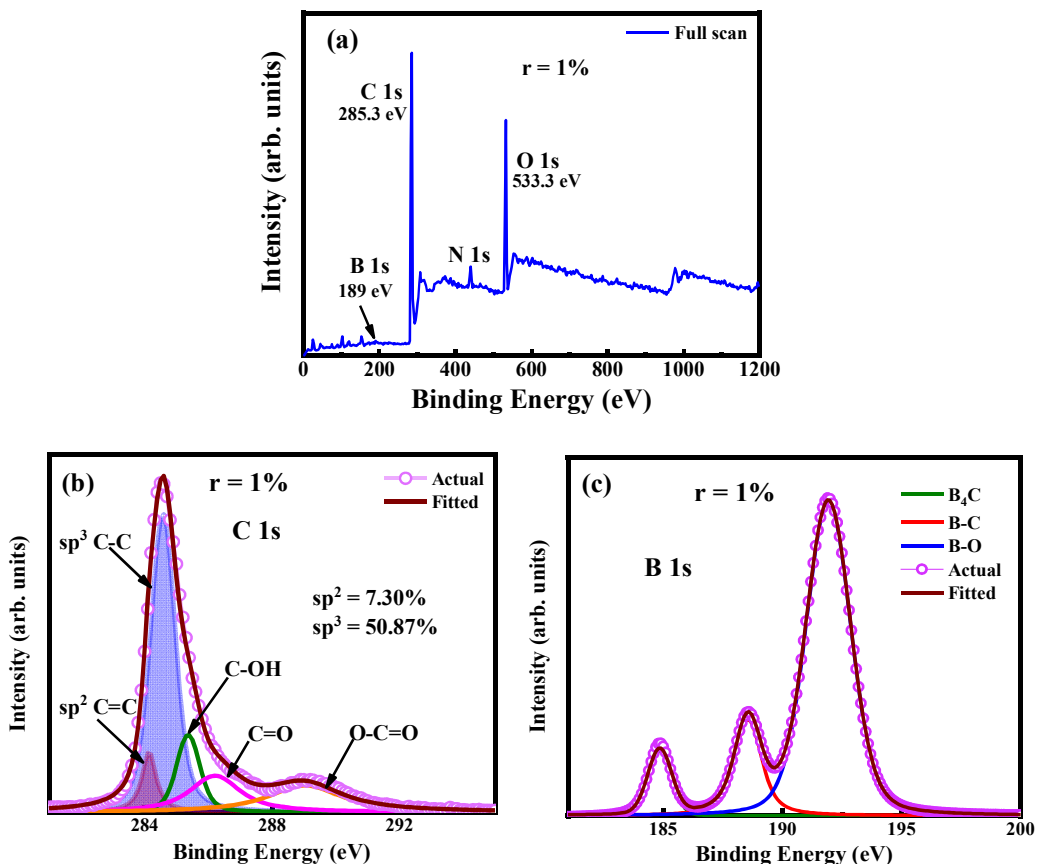


Fig. 5.1.3: (a) XPS wide range spectrum of the sample prepared at $r = 1\%$; High resolution (b) C 1s spectrum, and (c): B 1s spectrum of the sample.

Chapter 5

The percentage composition (P_i) of different elemental bonds constituting the film is evaluated from the relative peak areas of the individual deconvoluted peaks of the XPS spectra, in terms of the equation [51,143]:

$$P_i = S_i / S \quad \text{eqn (5.1.1)}$$

where S_i is the integrated area under each deconvoluted peak corresponding to the chemical bonds i and S is the total area under the spectrum [141]. From Fig. 5.1.3(b), the sp^3 C-C and the sp^2 C=C contents are estimated as 50.87% and 7.30%, respectively. The estimated contents of B₄-C, B-C_{3.4} and B-O bonds are ~7.96%, 16.11% and 75.92% respectively (Fig. 5.1.4(b)).

To study the thermally activated electronic transport in B-doped DLC films, the dark conductivity was measured by gradually decreasing the temperature of the films from 450 K to 180 K. Fig. 5.1.4(a) shows the dark conductivity (σ) vs 1/T plots of the samples prepared at varied flow rate ratio r (B₂H₆/CH₄) in %. The data points of the σ vs 1/T plots are fitted into two segments, using least square linear fits and following Arrhenius-like temperature dependence as [144]:

$$\sigma = \sigma_0 \exp\left(-\frac{\Delta E}{kT}\right) \quad \text{eqn (5.1.2)}$$

where ΔE is the activation energy, σ_0 is the pre-exponential factor and K is the Boltzmann constant. From the fitted graphs (Fig. 5.1.4(a)), two different slopes across the room temperature identify two different activation energies: ΔE_H , correlating the high-temperature range, and ΔE_L , in the low-temperature section. Notably, this implies that there are two modes of transport of the electrons through the DLC films, which are dominant at two different temperature ranges.

The room temperature conductivity (σ_{RT}) and the corresponding high-temperature activation energy (ΔE_H) are plotted against varying r in Fig. 5.1.4(b). As observed, there is a sharp transition in both the values with the change in r from 0 to 0.08%. With the increase in r from 0 to 0.08%, the RT dark conductivity (σ_{RT}) increases sharply from 2.12×10^{-7} S cm⁻¹ to 5.17×10^{-6} S cm⁻¹; however, for further increase in r , the σ_{RT} increases gradually to $\sim 3.02 \times 10^{-5}$ S cm⁻¹ at $r = 1\%$. This is accompanied by a sharp decrease in ΔE_H value from ~ 305 meV at $r = 0\%$ to 191 meV at $r = 0.08\%$, and attaining its gradual minimum magnitude of ~ 170 meV at $r = 1\%$. The increase in conductivity corresponds to two factors: i) the change in the film network from amorphous to crystalline and ii) the incorporation of B dopants into the matrix. This in turn is related to the decrease in ΔE_H . The enhanced σ_{RT} is indicative of the incorporation of B dopant atoms along with an improvement in the DLC network ordering. The

Chapter 5

conduction in the above room-temperature regime is mainly due to the thermionic transition of the acceptors from the defect states of the valence band to the empty states in the conduction band [145].

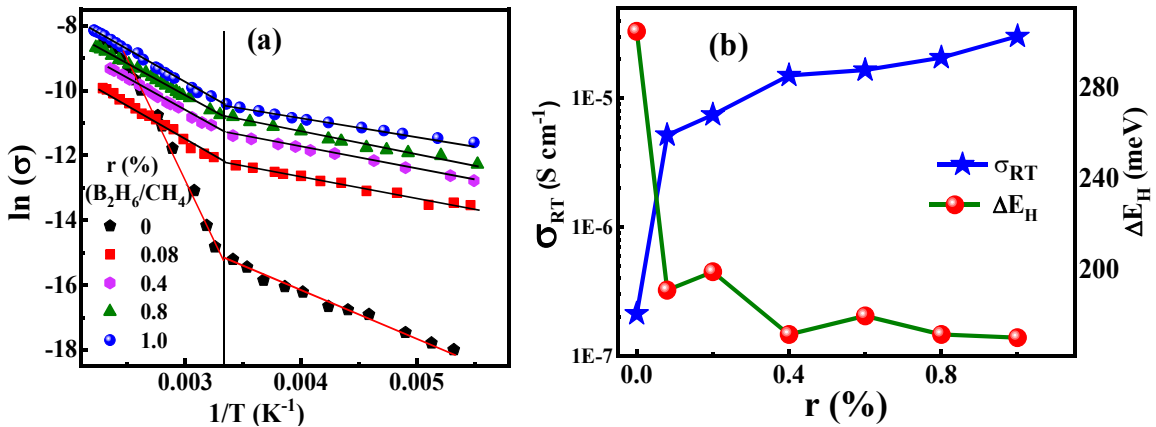


Fig. 5.1.4: (a) $\ln(\sigma)$ vs $1/T$ graph of the samples prepared with varying r , and (b) variation of room temperature conductivity (σ_{RT}) and the corresponding high-temperature activation energy (ΔE_H) with the increase in r from 0 to 1%.

In the low-temperature range (below 300 K), the $\ln(\sigma)$ vs $1/T$ tends to deviate from the Arrhenius-type relation. Instead, a linear square fit can be attained for the $\ln(\sigma)$ vs $(T)^{-1/4}$ plot much more efficiently in this regime. This is shown in Fig. 5.1.5(a) for the samples prepared at r varying from 0 to 1%. In the absence of electron-electron interactions, the transport of charge carriers takes place by hopping from the occupied states below the Fermi level to some empty states above the Fermi level, which may not be the nearest energy states. This mode of transport of charge carriers is the main cause of conductivity in the low-temperature regime, named Mott's variable range hopping (VRH), given by the following equation [146]:

$$\sigma = \sigma_{OM} e^{[-(\frac{T_{OM}}{T})^{1/4}]} \quad \text{eqn (5.1.3)}$$

where σ_{OM} is the hopping conductivity pre-factor and T_{OM} is the characteristic temperature, (collectively called the Mott parameters) both of which are dependent on the material of the film [55,147]. These parameters, σ_{OM} and T_{OM} were calculated from the intercept and slope of the least square fitting of the data in Fig. 5.1.5(a), respectively. Fig. 5.1.5(b) shows a drastic decrease in the magnitude of T_{OM} from $\sim 8.2 \times 10^7$ K at $r = 0\%$ to $\sim 5.7 \times 10^6$ K at $r = 0.08\%$, however, for further increase in r the decrease in T_{OM} is less prominent, reaching $\sim 1.8 \times 10^6$ K at $r = 1\%$.

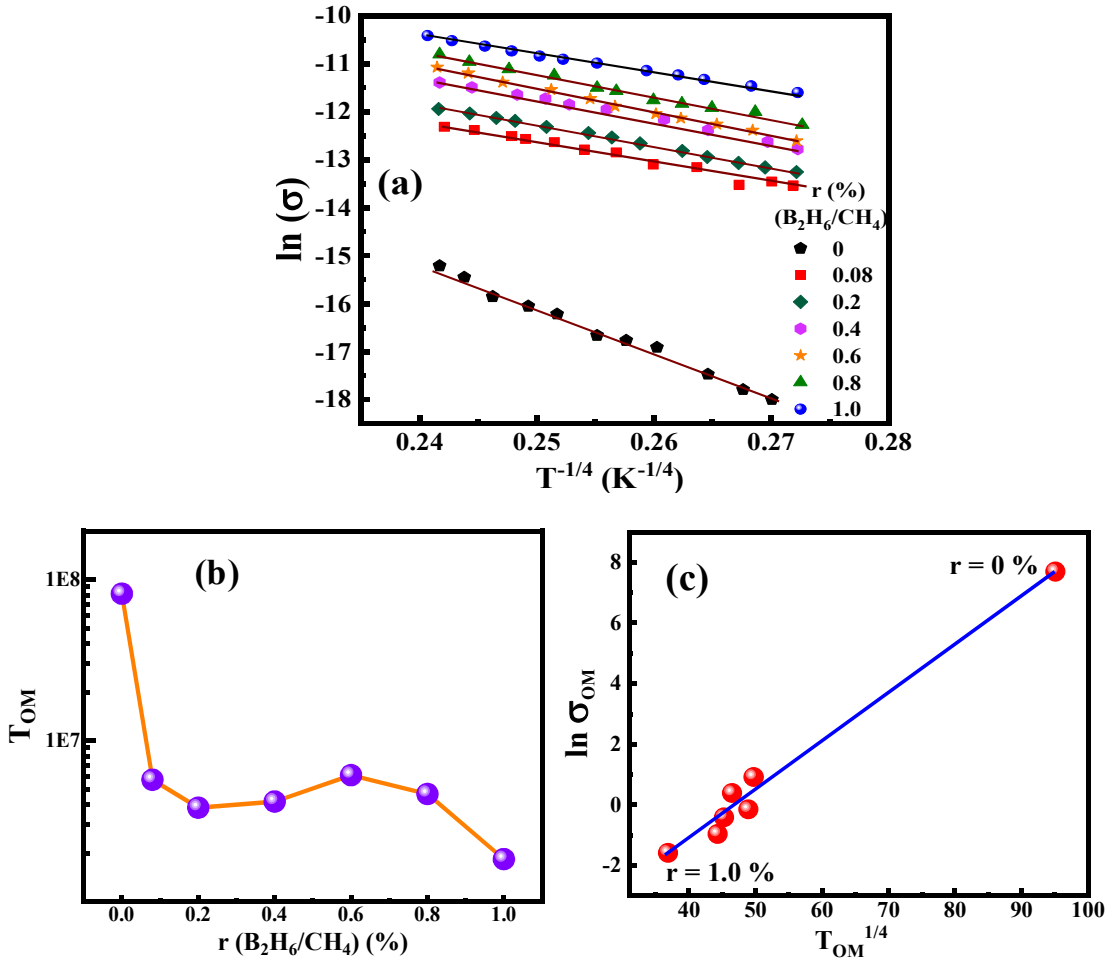


Fig. 5.1.5: (a) Variation of $\ln(\sigma)$ vs $(T)^{-1/4}$ with change in r ; (b) Variation of Mott parameter T_{OM} with r ; (c) Plot of $\ln(\sigma_{OM})$ vs $T_{OM}^{1/4}$, showing a linear relationship.

The Mott parameters, when plotted as $\ln(\sigma_{OM})$ vs $T_{OM}^{-1/4}$, exhibit a good linear relationship as shown in Fig. 5.1.5(c), and thus follow Godet's model. According to this model, at low temperatures when the transport of the charge carriers takes place via VRH and the density of states (DOS) is an exponential function of energy, the Mott parameters are linearly related to each other [148].

Fig. 5.1.6(a) shows the UV-Vis transmission spectra of the samples prepared at varying r (from 0 to 1%). The films have a high degree of transparency (> 70%) in the wavelength range above 700 nm. Transmission in the UV-visible region in these films occurs due to the transitions from the sp^2 related π states to the anti-bonding distorted σ states or due to band-to-band transitions [149]. To calculate the optical band gap (E_g) of the films, the absorption spectra of the samples are fitted using a power law equation, called Tauc's Equation:

$$\alpha h\nu = B (h\nu - E_g)^n \quad \text{eqn (5.1.4)}$$

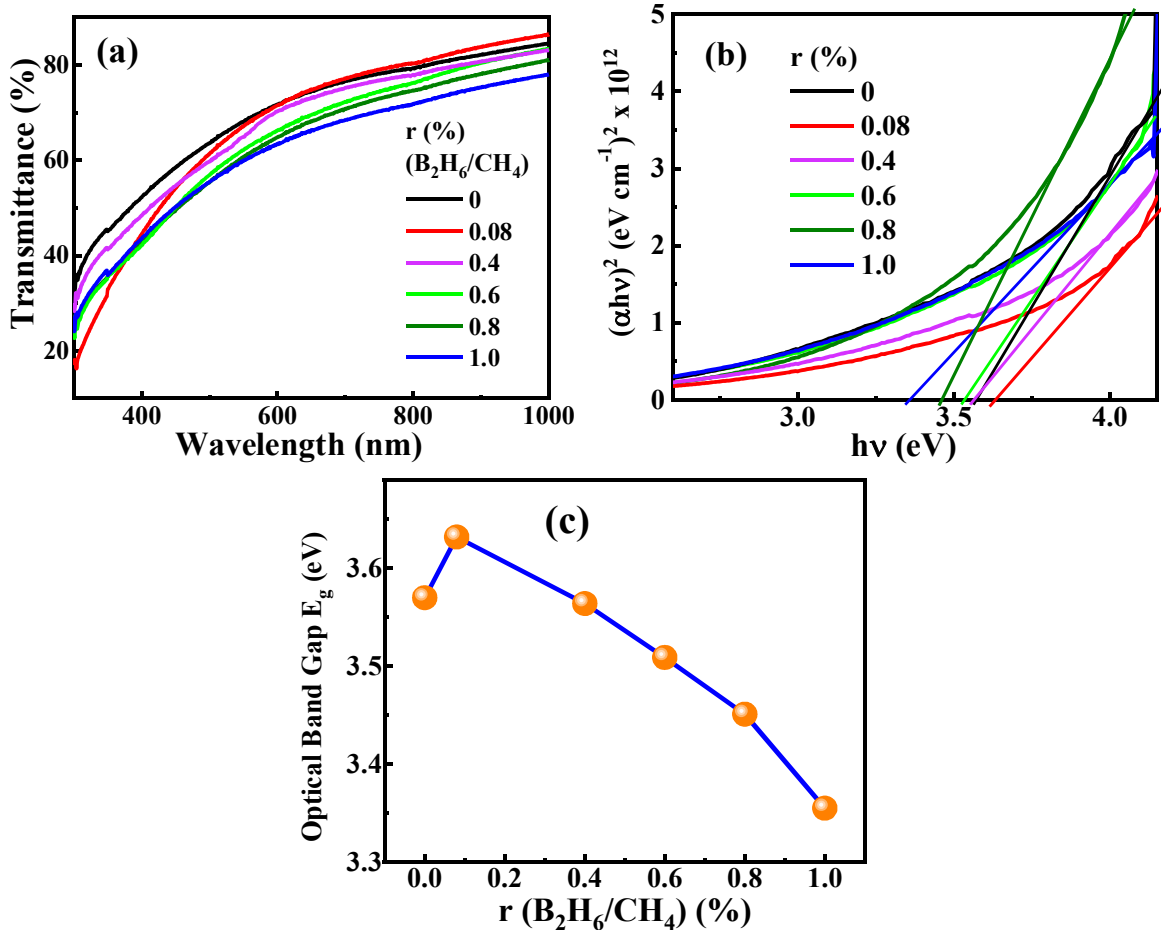


Fig. 5.1.6: (a) Transmission spectra of the samples prepared by varying r from 0 to 1%, (b) corresponding Tauc's plots; and (c) variation of the optical band gaps concerning r (%).

where α is the absorption coefficient of the sample, E_g is the optical band gap, and ν is the frequency of the incident light. B is the slope of the tangent to Tauc's plot. The electronic character of the band gap is related to the exponent n , which has values of 3, 2, 3/2, and 1/2. The electronic transitions in the band gaps are indirectly forbidden and indirectly allowed for $n = 3$ and 2, while the n values of 3/2 and 1/2 correspond to directly forbidden and directly allowed transitions [56]. The appropriate n value is determined by finding the best fit of the $(\alpha h\nu)^{1/n}$ vs. $h\nu$ plot (Tauc's plot) such that a linear trend is obtained, thus expressing the correct nature of the transition. The tangent is drawn from this linear portion of Tauc's plot to the energy axis, where $(\alpha h\nu)^{1/n} = 0$. The intercept on the energy axis gives the E_g of the film [150]. In the case of B-doped DLC films, the n value is found to be = 1/2, indicating a direct band-to-band transition nature. The optical band gaps (E_g) of the films are obtained employing Tauc's plot, shown in Fig. 5.1.6(b), and their variation with the increase in r is shown in Fig. 5.1.6(c).

The absence of sharp band edges in Tauc's plot (Fig. 5.1.6(b)) indicates that the B-doped DLC films have extended band-tails i.e., sub-bandgap states. These are related to the

Chapter 5

defects and disorders present in the lattice. The optical band gap of the undoped DLC film ($r = 0\%$) is estimated at 3.57 eV. It is interesting to observe that at the minor doping level corresponding to $r = 0.08\%$, the E_g increases to 3.63 eV; however, for further increase in r , E_g reduces monotonically to 3.35 eV at $r = 1\%$. The content of sp^2 -bonded C=C bonds and their cluster sizes determine the E_g values of B-doped DLC films [151]. Since the π states lie closer to the Fermi level, the E_g is the separation between the filled π -states of the valance band and the empty π -states of the conduction band. Thus, the higher the cluster size and the content of sp^2 C=C bonds in the films, the band-to-band separation decreases, lowering the E_g values [152,153]. In this series of samples, increased $r(\%)$ signifies increased effective B incorporation within the DLC matrix. B doping plays an important role in enhancing the nucleation density of the DLC films. The B atoms act as catalysts in the dissociation of the CH_4 molecules and enhance the formation of the nucleation species within the plasma. Thus, large numbers of smaller-sized crystalline grains with increased grain boundaries are formed. This increases the formation of sp^2 hybridized C-C clusters, which are present in the amorphous part in between the grains [116]. Thus, with the increase in $r (\%)$, increasing sp^2 C=C bonds and defects reduces the transmission of light and hence the optical band gap.

[Fig. 5.1.7\(a–c\)](#) shows the AFM micrographs of the samples prepared at $r = 0$, 0.6, and 1%, the corresponding variations in root mean square (RMS) roughness of the sample surface are presented in [Fig. 5.1.7\(d\)](#). The RMS roughness is observed to increase with the increase in $r (\%)$, the B_2H_6 to CH_4 flow rate ratio in the plasma, i.e., with the increasing B incorporation within the DLC films. These catalyse the surface mobility and effective inclusion of carbon precursor ions onto the growing surface at their proper lattice positions [154], thereby favouring improved nano structural growth. Thus, the enhanced formation of dense nanostructures on the surface of the B-doped DLC films accounts for the increased roughness with the increase in $r (\%)$. The sample prepared at $r = 1\%$, possesses the maximum RMS roughness of 48.12 nm.

The SEM micrographs of the samples are shown in [Fig. 5.1.8](#). A gross change in the surface structure has been observed on increasing the doping corresponding to changes in r from 0.08 to 1.0% under -40 V negative substrate bias. The undoped sample possesses a smooth surface (not shown in Figure), while B doping induces the formation of clusters, which coalesce together and grow larger, and produce a rough surface as also identified by the AFM analysis.

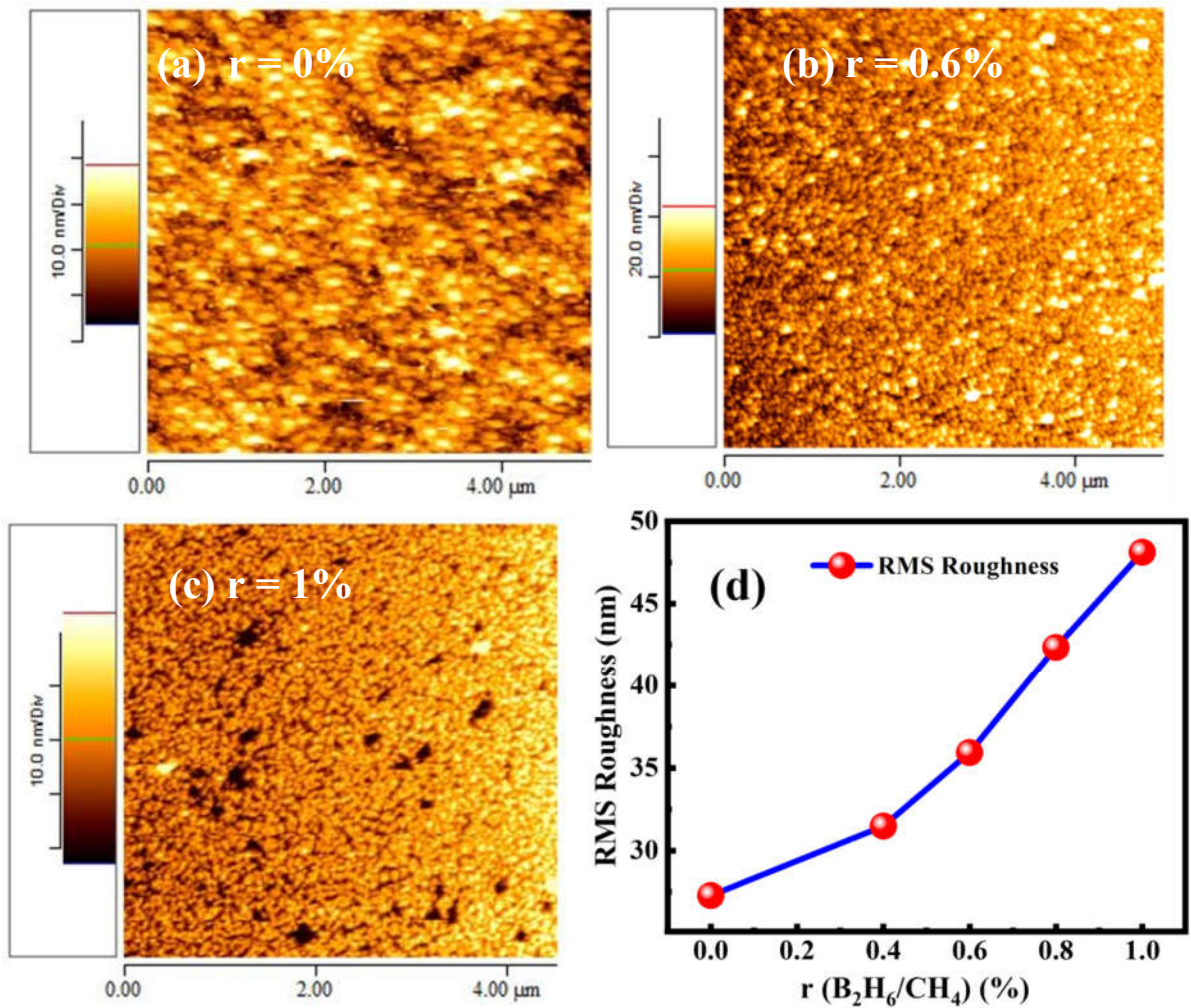


Fig. 5.1.7: AFM images of the samples prepared at (a) $r = 0\%$, (b) 0.6% , and (c) 1% . (d) Changes of RMS roughness with r varying from 0 to 1%

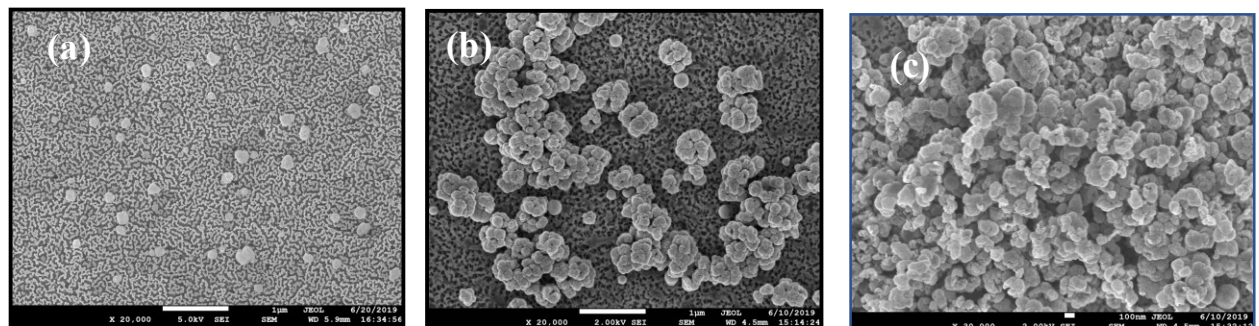


Fig. 5.1.8: SEM micrographs of the samples prepared at $r = 0.08$, 0.6 , and 1% .

The TEM micrographs of the films prepared at $r = 0\%$, 0.08% and 1% at -40 V negative DC substrate bias are shown in Fig. 5.1.9(a-c), respectively. The high-resolution images evidence the film matrices exhibiting $\langle 111 \rangle$ crystalline planes of diamond with lattice

Chapter 5

spacings of 0.211 nm, in nanocrystalline hexagonal patches spread over the amorphous network. The SAED images in Fig. 5.1.9(d–f) give clear views of the diffraction patterns corresponding to the $<111>$, $<220>$, and $<311>$ oriented crystalline planes.

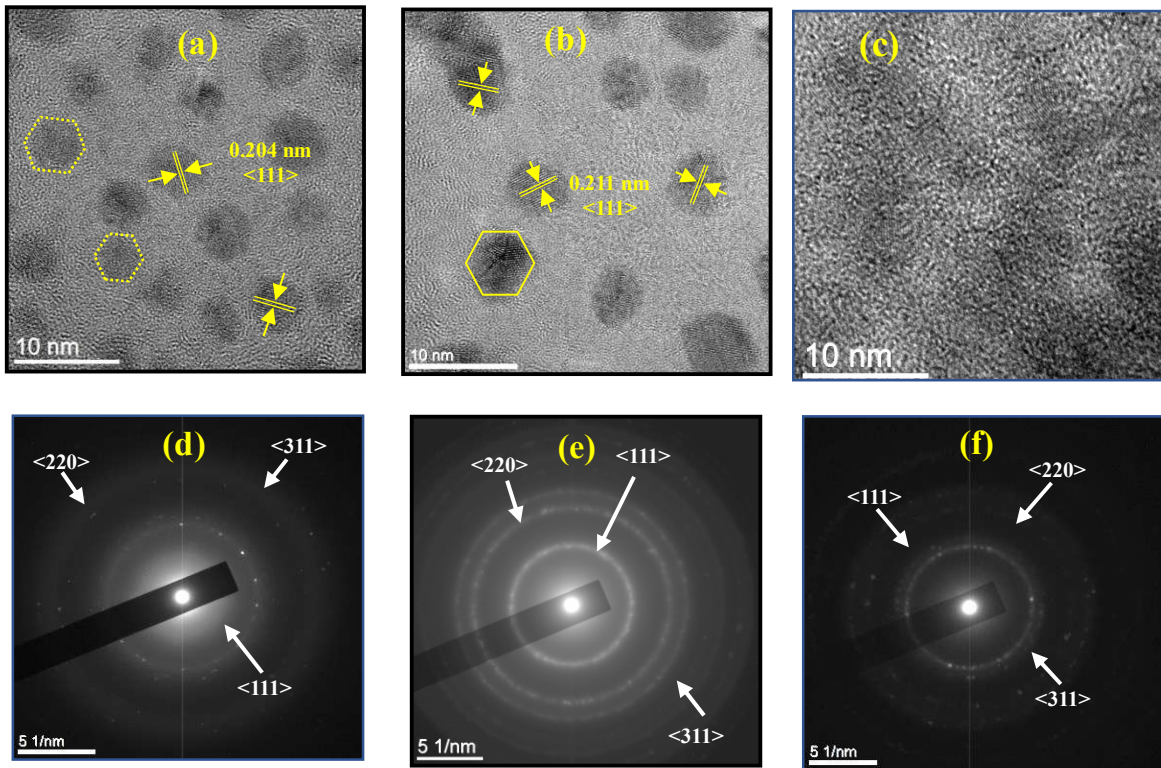


Fig. 5.1.9: High-resolution TEM images of the films prepared at $r =$ (a) 0%, (b) 0.08%, and (c) 1%, and (d–f) show the SAED patterns of the corresponding samples. The doped film prepared at $r = 0.08\%$ shows very prominent $<111>$, $<220>$, and $<311>$ planes of a diamond.

Fig. 5.1.10 shows the energy dispersive X-ray spectroscopy data of the sample prepared at $r = 1\%$. The elemental composition of C and B of 96.97% and 3.03% is indicated from this observation.

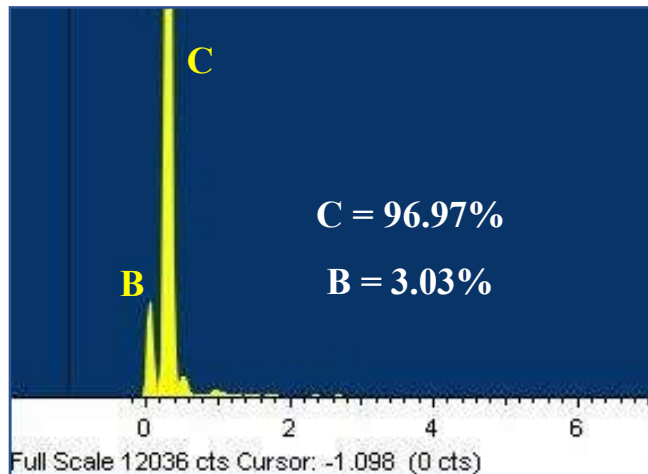


Fig. 5.1.10: EDX spectra of the sample prepared at $r = 1\%$ showing the absolute elemental contents of C and B (obtained from the TEM)

Chapter 5

Along with the precursor gases (CH_4 and B_2H_6) present in the plasma, there is an additional effect of the presence of the diluent gases: Ar and He. Since the ionization energies of Ar (15.76 eV) and He (24.59 eV) are not much different, both have a virtually similar effect on the formation of the B-DLC films [155] via producing the CH_n^+ ions (the principal products being CH_3^+ and CH_4^+), which are the prime film-forming precursors, and also by creating active nucleation sites on the substrate surface [156,157]. Moreover, when excited states of these inert gas molecules (Ar^* and He^*) collide with the film-growing surface, the energy transfer helps increase the effective temperature of the growth zone, as well as the mobility of the ions. All of these facilitate improving the structural order of the film network [158]. However, in preparing the series of samples with the increase in $\text{B}_2\text{H}_6/\text{CH}_4$ flow ratio (r , in Table 1), the increasing He content in the plasma as the diluent of B_2H_6 is compensated by an almost equivalent amount of decreasing flow rate of Ar, to keep a constant total gas flow rate of the gases in the ensemble. Thus, the changes in the structural, optical, and electrical characteristics of the films hardly depend on changing the diluent gases, however, those amply vary on the B_2H_6 to CH_4 flow ratio (r) in the plasma.

5.1.2. Conclusion:

Plasma-enhanced chemical vapour deposition technique was used to investigate the boron-doped DLC films via studies on the structural, electrical, and optical properties. The samples were prepared at a previously optimized negative DC substrate-bias voltage of -40 V, $\text{B}_2\text{H}_6/\text{CH}_4$ flow rate ratio (r) varying within (0–1) %, substrate temperature of 450 °C, at a very low plasma pressure of 5.33 Pa, and RF power of 800 W. With increased B doping, in general, an increase in I_D/I_G , and a decrease in both I_{Dia}/I_D and I_{Dia}/I_G was identified in the Raman data. The doped sample prepared at $r = 1\%$ possessed a minimum I_D/I_G ratio of ~0.819, a maximum I_{Dia}/I_G of ~0.83, and an I_{Dia}/I_D of ~1.012. XPS analysis identified the sp^3 content of ~50% along with good B incorporation. This was supported by the enhanced electrical conductivity of $\sigma_{\text{RT}} \sim 3.02 \times 10^{-5} \text{ S cm}^{-1}$, a corresponding minimum of $\Delta E_H \sim 170 \text{ meV}$, a reduced optical band gap of $E_g \sim 3.35 \text{ eV}$, and the maximum RMS roughness of 48.12 nm. From Tauc's plot, it was evident that the B-DLC possessed extended band tails with sub-bandgap absorptions, due to the presence of defects in the doped films. The crystalline qualities of the DLC films were exhibited by the very prominent $\langle 111 \rangle$, $\langle 220 \rangle$, and $\langle 311 \rangle$ crystallographic planes of diamond in the TEM image. At a very low doping level corresponding to $r = 0.08\%$, a significantly sharp X-ray diffraction peak appeared at around $2\theta = 43.49^\circ$, corresponding to the $\langle 111 \rangle$ crystalline planes of diamond, a concomitant minor widening in the optical band gap was evident.

5.2:

Effect of substrate bias variation on B
doping of DLC films

Chapter 5

To improve the crystalline properties of boron-doped diamond-like carbon films, researchers have frequently employed substrate pre-treatment techniques such as mechanical scratching and ultrasonic abrasion using diamond powders [90,159]. Substrate pre-treatment, however, involves multiple steps to take care of before the deposition process e.g., treating the substrate surfaces with abrasive powders (mainly nanodiamond powders) either by mechanical scratching or by ultrasonication or spin coating of solutes containing nanodiamond grains on the substrate surface [160]. Incorporating diamond powders contributes to an increase in production costs. Alternatively, by applying a negative bias voltage to the substrate, crystallinity in boron-doped diamond-like carbon (DLC) films can be enhanced through a single-step process, eliminating the need for diamond powders. Biasing facilitates the initial nucleation process of the substrates and aids in the etching of amorphous layers within the developing films by drawing precursor ions toward the substrates [137].

The objective of this study is to improve the effective electrical conduction of the B-doped DLC films, maintaining good crystallinity with adequate optical transparency in a one-step deposition process employing the unique ICP-CVD unit. This is achieved by increasing the substrate (-ve) dc bias voltage application.

A set of samples of thickness ~50 nm was prepared maintaining the plasma at ~40 mTorr and 800 W, the substrate temperature at ~450 °C and varying its dc bias from -40 to -120 V. Flow rates of the precursor gas CH₄, the dopant gas B₂H₆ (1% in He) and the diluent gas Ar was maintained each at 25 sccm, keeping the B₂H₆/CH₄ ratio secured at 1.0%.

5.2.1. Results and discussion:

Fig. 5.2.1(a) presents the Raman response from a series of DLC samples, prepared at B₂H₆ to CH₄ flow rate ratio (F) = 1.0% and varying the substrate dc bias from -40 to -120 V. The deconvoluted Raman spectra of an intrinsic DLC film deposited at -80 V substrate bias are inserted below the B-DLC film (grown at -80 V) for comparison. Each Raman peak is associated with a specific bond vibration frequency exploiting which the film's structure, quality, and composition are estimated. Raman spectra help identify the *sp*³ C-C and *sp*² C=C bonds of the DLC matrix, apart from differentiating the nature of carbonaceous materials within the film like NCD, CNT, or DLCs [46]. Since the Raman bands arising from various components are broad and overlapping, a proper deconvolution of the spectra is required to identify their contributions. Each Raman spectrum of the samples has been deconvoluted into six components using combinations of Gaussian and Lorentzian functions. The first broad peak

Chapter 5

appearing between 1200 to 1450 cm^{-1} is deconvoluted into two segments; the diamond peak at 1326–1334 cm^{-1} emerges from vibrations of the crystal-like alignment of C-C bonds with sp^3 hybridization, and the D-peak at $\sim 1350 \text{ cm}^{-1}$ appears on account of disorders formed in the matrix by the C=C bonds in sp^2 hybridization [161].

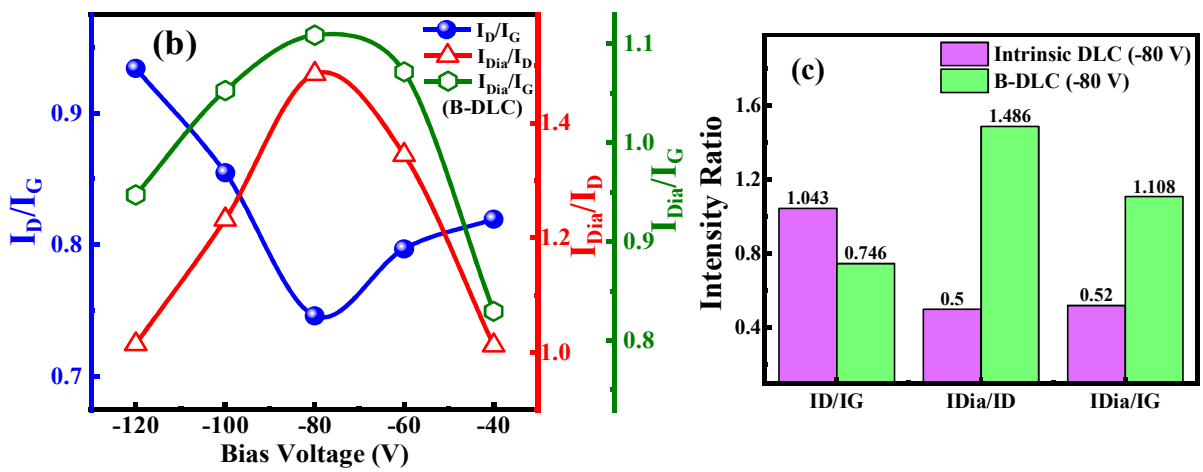
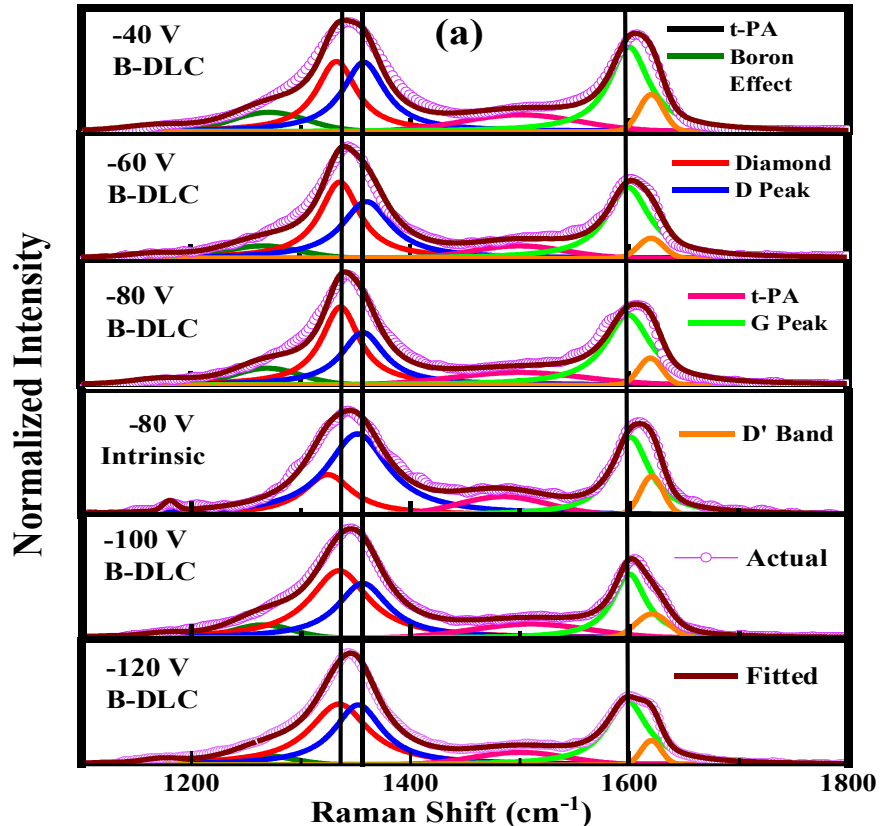


Fig. 5.2.1. (a) Deconvolution in the Raman bands of several B-DLC films grown at several negative substrate bias voltages; The deconvoluted spectra of an intrinsic DLC film prepared at -80 V is given for comparison; (b) variations in the B-DLC films' corresponding intensity ratios: I_D/I_G , $I_{D\text{ia}}/I_D$ and $I_{D\text{ia}}/I_G$; (c) comparison of the different intensity ratios of the doped and intrinsic DLC film grown at -80 V dc bias.

Chapter 5

The bulk single crystal diamond originates the 1332 cm^{-1} peak having an FWHM of $\sim 2\text{ cm}^{-1}$, typically representing the complete tetrahedrally orientated sp^3 hybridized C-C bonds, arranged in cubic sublattices with uniform distribution around all directions [35]. In the current scenario, the diamond peak shifts from ideally at 1332 cm^{-1} to $1326\text{--}1334\text{ cm}^{-1}$, and the corresponding FWHM appears too broad, about 40 cm^{-1} . Shift in the diamond peak identifies the defects and structural disorder in the lattice. Sometimes, local heating due to the incident Raman laser beam may cause the peak shift to some extent [39,162]. The grain boundaries, the amorphous matrix in the DLC network, and even the tiny size of the diamond crystallites may cause the diamond peak to broaden and overlap with the D peak [163].

The other broad peak centered at $\sim 1605\text{ cm}^{-1}$ is further deconvoluted into the G peak near 1600 cm^{-1} besides a smaller D' -band at $\sim 1620\text{ cm}^{-1}$. G peak appears owing to in-plane vibration of the C=C bond with sp^2 hybridization [38]. This peak proves the existence of the graphitic components within the B-doped DLC matrix. The D'band also portrays the vibrations due to the interaction of impurities or disorders with the extended modes of graphene [164]. The smaller peak at $\sim 1275\text{ cm}^{-1}$ arises from the vibrations in the B-C bonds formed within the lattice [130]. Two neighbouring peaks at 1140 and 1490 cm^{-1} indicate the trans-polyacetylene component in the grain boundaries [130]. The 1140 cm^{-1} peak sometimes gets overlapped by the 1275 cm^{-1} peak, which occurs due to B-doping. All the identified Raman peaks are noted in Table 5.2.1.

Table 5.2.1: Table of the Raman component peaks.

Peak position	Peak name	Origin
1140 cm^{-1}	trans polyacetylene peak	Trans-polyacetylene components in grain boundaries
1275 cm^{-1}	B-C bonds	Boron in C-C matrix
$1326\text{--}1334\text{ cm}^{-1}$	Diamond peak	Crystalline alignment of sp^3 C-C bonds
1350 cm^{-1}	D peak	Disorders in the matrix due to sp^2 C=C bonds
1490 cm^{-1}	trans-polyacetylene peak	Trans-polyacetylene components in grain boundaries
1600 cm^{-1}	G peak	In-plane vibration of sp^2 C=C bond
1620 cm^{-1}	D' band	Impurities and disorders in sp^2 C=C matrix

Chapter 5

[Fig. 5.2.1\(b\)](#) shows the variations of different intensity ratios I_D/I_G , I_{Dia}/I_D , and I_{Dia}/I_G , arising from the change in dc bias from -40 to -120 V. The D peak to G peak intensity ratio (I_D/I_G) evaluates the disorder concerning the sp^2 hybridized C=C bonds. It initially decreases from 0.82 at -40 V to 0.75 at -80 V; subsequently, it increases to 0.93 at -120 V. Decreasing I_D/I_G indicates the reduced defect density in the graphitic regions and increased C-C bond [42,134].

The diamond peak intensity ratio relative to the D peak, I_{Dia}/I_D , evaluates the perfectly ordered sp^3 C-C tetrahedral bond content concerning disorders in B-DLC matrix. The I_{Dia}/I_D maximizes at ~ 1.49 for the sample prepared at -80 V, which signifies the highest degree of the tetrahedral (sp^3) orientation of C-C bonds. In addition, the diamond peak to G peak intensity ratio (I_{Dia}/I_G) signifies the effective fraction of tetrahedrally oriented diamond sp^3 C-C bond concerning the graphitic C=C bond of sp^2 hybridization [165]. The highest $I_{Dia}/I_G \sim 1.11$ arises for the sample deposited at -80 V substrate bias. Both the ratios I_{Dia}/I_D and I_{Dia}/I_G diminish on changing the bias beyond -80 V, demonstrating that the most diamond-like properties, including the lowest disorder content concerning both the tetrahedrally oriented diamond sp^3 C-C bond and the sp^2 C=C bond of amorphous and graphitic carbon, arise in the sample grown at -80 V substrate bias.

The Raman analysis identifies a reduction in I_D/I_G value with the initial rise in dc bias from -40 to -80 V. The reduction of I_D/I_G ratio may indicate (1) an increasing quantity in the fourfold co-ordinated C-C bonds, (2) a decrease in the number and size of crystalline graphitic grains, and (3) a reduction in the amorphous carbon contents [166,167]. An increased negative bias voltage causes an enhanced flow of B atoms along with other plasma ions towards the substrate surface, which facilitates the easy and effective incorporation of B atoms and, in turn, helps increase the number of nucleation centers. B atoms also promote the formation of suitable carbon precursor ions by dissociating the CH_4 molecules [154]. B atom can easily break the potential barrier of the C-H bonds in the CH_4 molecule since it possesses the perfect symmetry and comparable orbital size to that of C for interacting with the lowest unoccupied antibonding states of carbon. The plausible reaction of the B atom interacting with CH_4 follows as [168]: $B + CH_4 \rightarrow CH_3 + BH$. Thus, the implicit inclusion of the B atoms improves the crystalline orientation, making them more diamond-like, thereby reducing the graphitic clusters and amorphous C. This is confirmed by the deconvoluted Raman spectra of the intrinsic DLC film grown at -80 V ([Fig. 5.2.1\(a\)](#)), and the comparison between the intensity ratios of the concerned peaks for the intrinsic DLC and B-DLC films, prepared under identical conditions ([Fig.](#)

Chapter 5

5.2.1(c)). It is inferred that the I_D/I_G ratio of the B-DLC film (0.75) is lower than that of the intrinsic film (1.04). The elevated I_{Dia}/I_D (1.49) and I_{Dia}/I_G (1.11) ratios of the B-DLC film, compared to their respective values of 0.5 and 0.52 for the intrinsic DLC film grown at an identical dc bias of -80 V, confirms an elevated crystallinity evolving within the B-doped DLC network. However, on further elevation of the negative bias to -120 V, the I_D/I_G ratio gradually rises, signifying an increased amorphous component in the DLC matrix. Too high a bias voltage does not favor the formation of sp^3 -hybridized C atoms [134,169]. Only a specified ion energy window, typically 20–200 eV, is suitable for producing the diamond-like C-C bonds [170]. For effective diamond deposition, the C ions must be energetically capable of penetrating the subsurface atomic sites and reaching the proper lattice positions. Robertson [171] evaluated this energy as \sim 100 eV. The C precursors with excess energy inevitably disrupt the crystalline order. The B atoms at higher voltages catalyze the effect by dissociating the CH_4 molecules and forming highly energized more C precursor ions. Besides, at higher bias voltages, the plasma ions bombardment on the substrate etches out the bonded C-C, C-B, and C=C bonds of the growing film network [137]. The variations of I_{Dia}/I_D and I_{Dia}/I_G with the bias voltage demonstrate that diamond-like C structures become most prominent in the sample prepared at -80 V concerning the graphitic and amorphous C contents [82].

The elemental compositions of various chemical bonds in the B-DLCs network are estimated from the X-ray photo-electronic spectroscopic analysis. Fig. 5.2.2(a–c) represents the wide-scan spectra of the B-DLC films deposited at -40, -80, and -120 V dc bias, respectively, which identify the most intense C 1s peak near 284.5 eV along with the smaller intensity O 1s peak at 532 eV. At increased bias voltage (-80 V), the O 1s peak reduces drastically. However, at a higher bias of -120 V, the intensity of the O 1s peak rises. The high-resolution C 1s XPS spectra of samples grown at -40, -80, and -120 V dc bias, presented in Fig. 5.2.2(d–f), respectively, are deconvoluted into five satellite peaks, fitted through Voigt functions. The satellite component at \sim 284 eV emerges due to the de-excitation of electrons from the K shell of the C=C bonds in sp^2 hybridization. The sp^3 C-C bonds initiate relatively higher intensity peaks at 284.6 eV [139,140]. The other smaller intensity peaks are assigned to C-OH, C=O, and O-C=O groups at 285.5, 286.2, and 289.9 eV, respectively [140]. The B-C bonds appear with a tiny peak within the C 1s spectra at 283 eV binding energy [172]. The XPS instrument being six times less sensitive to B than C, the B-C peak is overlapped by the broadness of the sp^2 (284 eV) and sp^3 (284.6 eV) hybridized C-C bonds [173].

Chapter 5

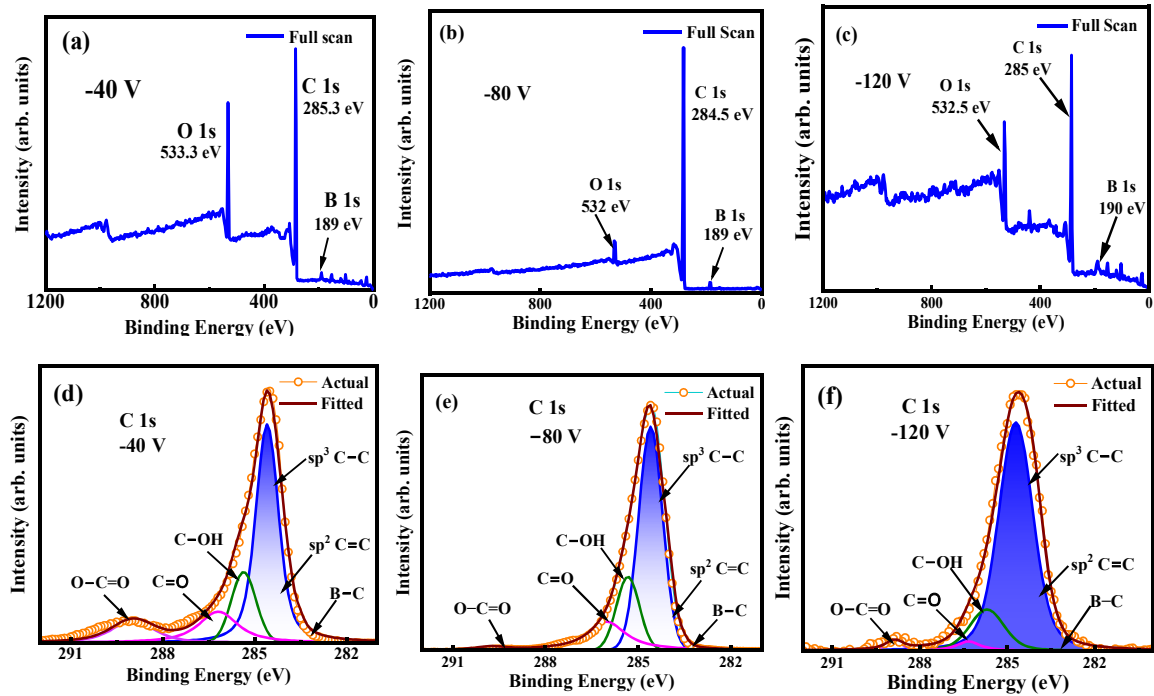


Fig. 5.2.2. Wide scan XPS response of DLC network grown at (a) -40 V, (b) -80 V, and (c) -120 V substrate dc bias. Deconvolution of C 1s peaks of films at (d) -40 V, (e) -80 V, and (f) -120 V.

Fig. 5.2.3(a–c) represents the narrow-scan B 1s response of the DLC films grown at -40, -80, and -120 V substrate bias, identifying the B incorporation within the DLC matrix. After deconvolution, the satellite peaks, arising from the B₄-C bonds appear at 185 eV, and those originating from the B-B bond appear at 188 eV. The peak at 192 eV arises from the B-O bond [172,174].

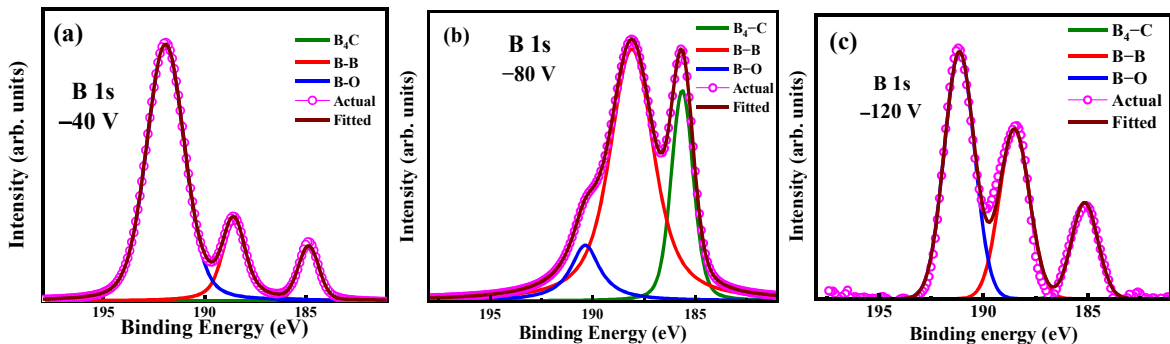


Fig. 5.2.3. The high-resolution XPS B 1s spectrum of each film grown at dc bias: (a) -40 V, (b) -80 V, and (c) -120 V.

If S_i represents the integrated area of the i^{th} component peak of the XPS spectrum corresponding to a particular chemical bond present in the sample, and S is the entire spectral

Chapter 5

area, then the percentage composition P_i of that bond within the sample has been estimated from the empirical relation [51]:

$$P_i = \frac{S_i}{S} \times 100 \quad \text{eqn (5.2.1)}$$

Thus, the percentage composition of the sp^2 and sp^3 bonded components present in the sample are evaluated from the C 1s spectra and various B-related constituents are estimated from the B 1s spectra. The elemental percentage of the different component bonds of the DLC films prepared at -40, -80, and -120 V is shown in [Table 5.2.2](#).

From [Table 5.2.2](#) it is observed that, with the bias increasing from -40 to -80 V, the sp^2 hybridized C=C bonds decrease from 7.30% to 5.01%, and sp^3 C-C bonds enhance from 50.87% to 57.29%. At a higher bias of -120 V, the sp^2 content increases to 6.11%, accompanied by a decrease in the sp^3 content (52.47 %). Thus, the diamond-like carbon

Table 5.2.2. Elemental percentage of the different bonds, present in the DLC films prepared at different dc bias voltages.

Bias Voltage at which the sample is prepared	sp^2 C=C content (%)	sp^3 C-C content (%)	sp^3/sp^2	B4-C content (%)	B-B (%)	B-O (%)
-40 V	7.03	50.87	7.24	7.96	16.11	75.92
-80 V	5.07	57.29	11.30	24.25	64.66	11.08
-120 V	6.11	52.47	8.59	16.82	33.91	49.27

bonding orientations increase along with a subsequent decrease in the non-diamond components (including graphene and amorphous carbon) at the optimum substrate bias of -80 V. The intensity ratios, I_{Dia}/I_D and I_{Dia}/I_G , extracted from the Raman data, can be correlated with the sp^2 C=C and sp^3 C-C bond ratios in B-DLCs obtained from the XPS study [37]. Simultaneously, there is a rise in the percentage composition of B4-C bonds from 7.96% to 24.25%, along with an increase in the B-B bonds (188 eV peak) from 16.11% to 64.66% at bias elevated from -40 to -80 V. Simultaneously, a sharp reduction in the content of B-O (192 eV peak) from 75.92% (at -40 V) to 11.08% (at -80 V) arises. At -120 V, the percentage of B4-C and B-B bonds lowers to 16.82 % and 33.91 %, along with a rise in B-O bonds to 49.27 %. Thus, an optimum increase of the negative bias voltage helps eliminate the O-related components from the B-doped DLC matrix and enhances the extent of bonding between B and C. However, similar evidence is not discernible from the Raman analyses, probably because of

Chapter 5

the relatively weak Raman response of the B-O bonds. In Raman spectra, the B-O bonds in BO_3 (boroxol) rings appear at $\sim 808 \text{ cm}^{-1}$ and 1260 cm^{-1} , and the B-O stretching vibrations occur in the range $(1500\text{--}1550) \text{ cm}^{-1}$ [130,175]. In the Raman spectra of the present set of samples, the $\sim 808 \text{ cm}^{-1}$ component was not detectable being comparable with other background fluctuations. Furthermore, other responses around the $(1250\text{--}1550) \text{ cm}^{-1}$ region are not separately detectable, being overshadowed by the strong intensities of the D-band, G-band, D'band, and the associated others.

The temperature-dependent conductivity measurements were performed by slowly varying the temperature from 450 to 180 K, to study the thermally activated electrical behavior of the B-DLC films. Fig. 5.2.4(a) represents the film conductivity (σ) corresponding to substrate biases varying from -40 to -120 V. The $\ln(\sigma)$ vs $1/T$ plot follows an Arrhenius-type relation [176,177]:

$$\sigma = \sigma_0 \exp\left(-\frac{\Delta E}{kT}\right) \quad \text{eqn (5.2.2)}$$

σ_0 is called the conductivity pre-factor, ΔE is its activation energy, K is the Boltzmann constant, and T is the temperature. The ΔE was evaluated from the least-square-linear fitted slope of the $\ln(\sigma)$ vs. $1/T$ curve. From Fig. 5.2.4(a) the least square fitting of the curve identifies two different slopes above and below the room temperature ($\sim 27^\circ\text{C}$). Thus, two different activation energies, ΔE_H (activation energy in the above room temperature region) and ΔE_L (activation energy for the below room temperature zone), indicate two different modes of electronic conduction during the high-temperature and the low-temperature regimes.

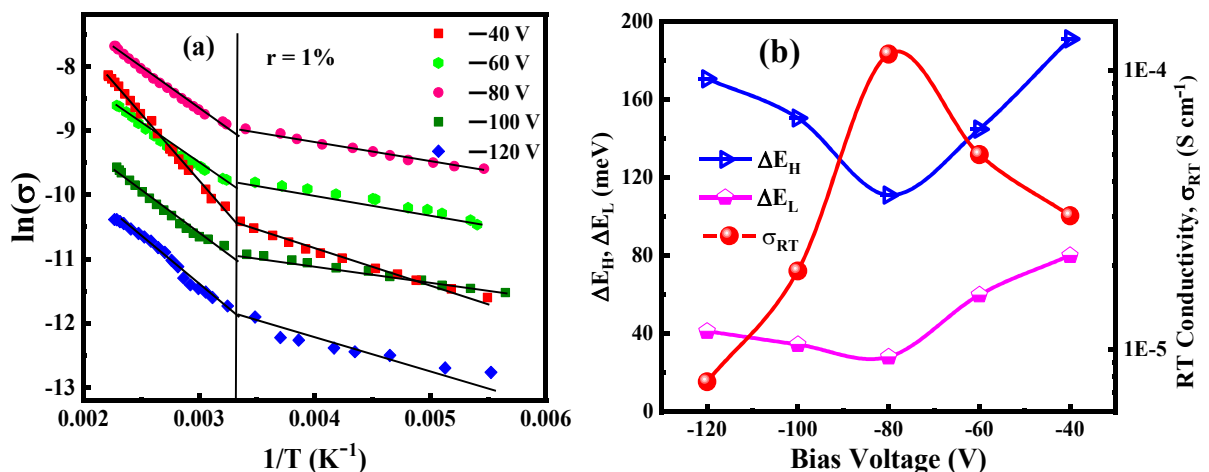


Fig. 5.2.4. (a) $\ln(\sigma)$ vs $1/T$ plots for the DLC films grown at various substrate biases, (b) The RT conductivity (σ) and activation energy (ΔE_H , ΔE_L) of the samples varying with substrate bias.

Fig. 5.2.4(b) presents the variations in the samples' RT-conductivity and the corresponding activation energy. At substrate bias elevated from -40 V to -80 V, the

Chapter 5

conductivity rises to its highest magnitude of $\sim 1.15 \times 10^{-4} \text{ S cm}^{-1}$, and the related ΔE_H and ΔE_L attain their lowest magnitudes of 111 meV and 28 meV, respectively, at -80 V. However, above -80 V bias, the conductivity reduces and approaches $\sim 7.68 \times 10^{-6} \text{ S cm}^{-1}$ at -120 V, and the corresponding activation energy increases for both ΔE_H and ΔE_L [33].

Interestingly, it is evident that the logarithm of the pre-exponential factor $\ln(\sigma_0)$ changes linearly with the above room temperature activation energy (ΔE_H). This behavior follows the Meyer-Neldel (MN) Rule [178]:

$$\sigma_0 = \sigma_{00} e^{\frac{\Delta E_H}{E_{MN}}} \quad \text{eqn (5.2.3)}$$

where σ_{00} is a material-dependent constant, and E_{MN} is the MN characteristic energy. The E_{MN} has been evaluated using the slope of $\ln(\sigma_0)$ vs. ΔE_H plot, as shown in Fig. 5.2.5. It is noted that the E_{MN} shows a reversal of sign during increasing the bias; E_{MN} belongs to its positive value during a change in bias from -40 to -80 V and a negative value for its further variation from -80 V to -120 V. This signifies a transition from the non-degenerate to a degenerate semiconductor-like characteristic while changing the substrate bias to a more negative voltage beyond -80 V.

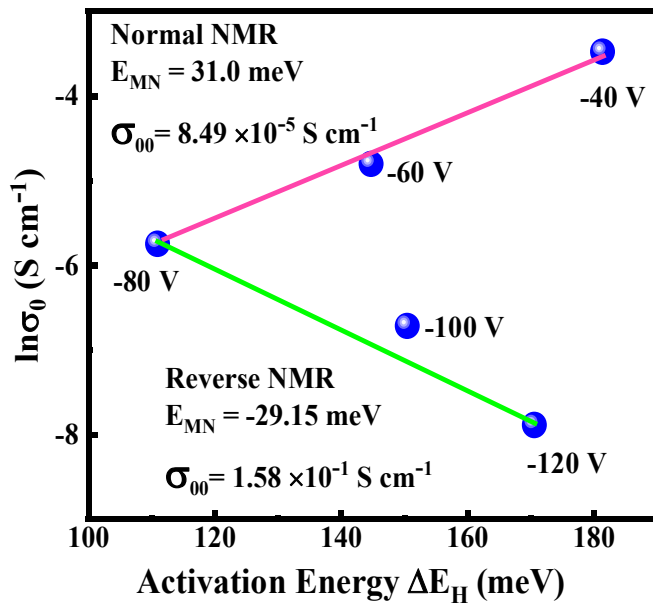


Fig. 5.2.5. Variation of $\ln \sigma_0$ vs ΔE_H for the DLC films grown at different substrate biases varying from -40 to -120 V, where MNR is followed during -40 to -80 V and reverse MNR is obeyed beyond -80 V.

Initially, when increasing the bias between -40 V and -80 V, there is an improvement in crystallinity via an increased sp^3 C-C bonding and an elevated B-doping of the network. The conduction pathway of the holes (charge carriers) is governed by the doped crystalline grains

Chapter 5

and their doped amorphous counterpart in the matrix. In this regime, the major carriers are stimulated by thermal energy from the Fermi-level to the valence band through crystalline grains across the amorphous matrix, and with the characteristic positive energy $E_{MN} \sim +31$ meV, following the conventional MNR [179].

Interestingly, as the bias voltage is varied beyond -80 V, a negative correlation between σ_0 and ΔE is observed, causing a negative E_{MN} of ~ -29 meV. A transition from non-degenerate to degenerate semiconductor-like behavior is revealed, where a relatively different mode of electronic transport is followed, signifying reverse MNR [144,176,180]. At bias voltages beyond -80 V, the B atom incorporation suddenly increases. An impurity band is created close to the valence band consequent to intimate interactions among the dopant atoms. This band gets broadened with the enhanced inclusion of B atoms at bias voltages of increased magnitude and subsequently, merges with the valence band, giving rise to an uninterrupted band tail for the amorphous matrix. Subsequently, the Fermi level shifts into the valence band of crystalline grains and within the extended band tails of the amorphous network, thereby introducing the degenerate semiconductors type behavior when the pre-exponential factor σ_0 is activated following the reverse NM rule [132]. Thus, in the above room temperature regime, switching in the electronic band characteristics of the material occurs during the elevation of negative bias beyond a threshold of -80 V under the present parametric condition of the ICP-CVD plasma.

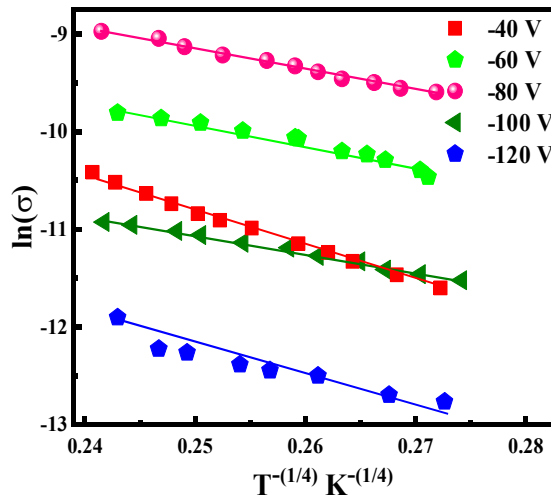


Fig. 5.2.6. $\ln(\sigma)$ vs $1/T^{1/4}$ plot showing Mott's conductivity at the low-temperature region for the B-DLC samples grown at varying dc bias.

Chapter 5

Besides, in the below room temperature regime, it is observed that the $\ln(\sigma)$ obeys Mott's variable range hopping phenomena more precisely than the Arrhenius equation (Eqn. 2), following [181]:

$$\sigma = \sigma_m \exp\left(-\frac{T_m}{T}\right)^{1/4} \quad \text{eqn (5.2.4)}$$

where σ_m is the pre-factor of conductivity, and T_m is a material-dependent constant. Fig. 5.2.6 shows the Mott's plots in the low-temperature regime for all the DLC films. The dominant transport of the charge carriers occurs from the Fermi level to an arbitrary unoccupied energy state in the corresponding band beyond the Fermi level. These energy states may or may not be the nearest ones, following the variable range hopping mechanism (VRH) [55,146].

Changes in the optical properties due to substrate bias variation were studied from the transmission spectra procured from the UV-Vis spectroscopic measurement. Generally, B-doped DLC films have a low scattering loss, with high transmission ability due to the small-sized crystalline grains and a dominant amorphous matrix [182]. Fig. 5.2.7(a) shows that most of the sample in the series exhibits above 80% transparency at wavelengths above 700 nm, implying that most of the visible light is transmitted through the films. Initially, the transmittance increases for the entire wavelength range on raising the bias from -40 to -80 V and then decreases on its further rise to -100 and -120 V. The optical gap (E_g) of B-doped DLC samples was evaluated from the Tauc's plot following Tauc's equation,

$$\alpha h\nu = B(h\nu - E_g)^n \quad \text{eqn (5.2.5)}$$

here α presents the absorption coefficient, $h\nu$ the photon energy, and B the characteristic constant [183]. The nature of transitions of electrons within the energy bands of the sample determines the exponential value n , which can have values of 3, 2, 3/2, and 1/2. The first two values correspond to the indirect forbidden and indirect allowed transition, and the last two to the direct forbidden and direct allowed electronic transitions [56]. For the DLC films, the n value equals 1/2, considering the direct electronic transition occurring in it.

Fig. 5.2.7(b) shows the Tauc's plot $[(\alpha h\nu)^2$ vs. $h\nu$] of the B-DLC films. Extrapolation of the straight-line section of the plot on the $h\nu$ axis at $\alpha = 0$ evaluates the sample's E_g . The variation of E_g with different bias voltages is shown in Fig. 5.2.7(c). The E_g value enhances from 3.60 eV to 3.70 eV at a bias elevated from -40 V to -80 V and then decreases to 3.64 eV as the bias voltage is further raised to -120 V. The B-doped DLC matrix consists of sp^2 C=C, sp^3 C-C, and C-H, B-B and B₄-C bonds, as estimated from the XPS measurements. These bonds control the optical gap of the material. At the initial phase of increasing the bias voltage up to

Chapter 5

-80 V, B incorporation within the DLC matrix could be very efficient due to the accelerated momentum of the plasma ions (precursor and dopant) towards the substrates. B atoms boost the nucleation and easy bonding of the sp^3 -hybridized C atoms at suitable lattice positions to form tetrahedral orientation all over, thereby inhibiting the formation of sp^2 -hybridized C=C clusters and structural defects (amorphous parts) [154]. The cluster model of Robertson states that the DLC films' optical band gap depends on the sp^2 bonds and the size of their clusters [76,151]. The π -states of sp^2 C=C bonds lie nearer to Fermi level than σ -states of sp^3 C-C bonds. The optical gap (E_g) between filled π -states of VB and empty π -states of CB is reduced when more π -states (of large clusters of sp^2 C=C) are present [76]. Thus, the optical band gap values increase with effective B doping. However, with a further increase in bias voltage, the energized plasma ions bombard the film-growing surface, causing disorder and amorphization; the dominance of sp^2 -hybridized C=C bonds gradually instigates forming larger clusters. Thus, the E_g value decreases with the rise in substrate bias voltage above -80 V.

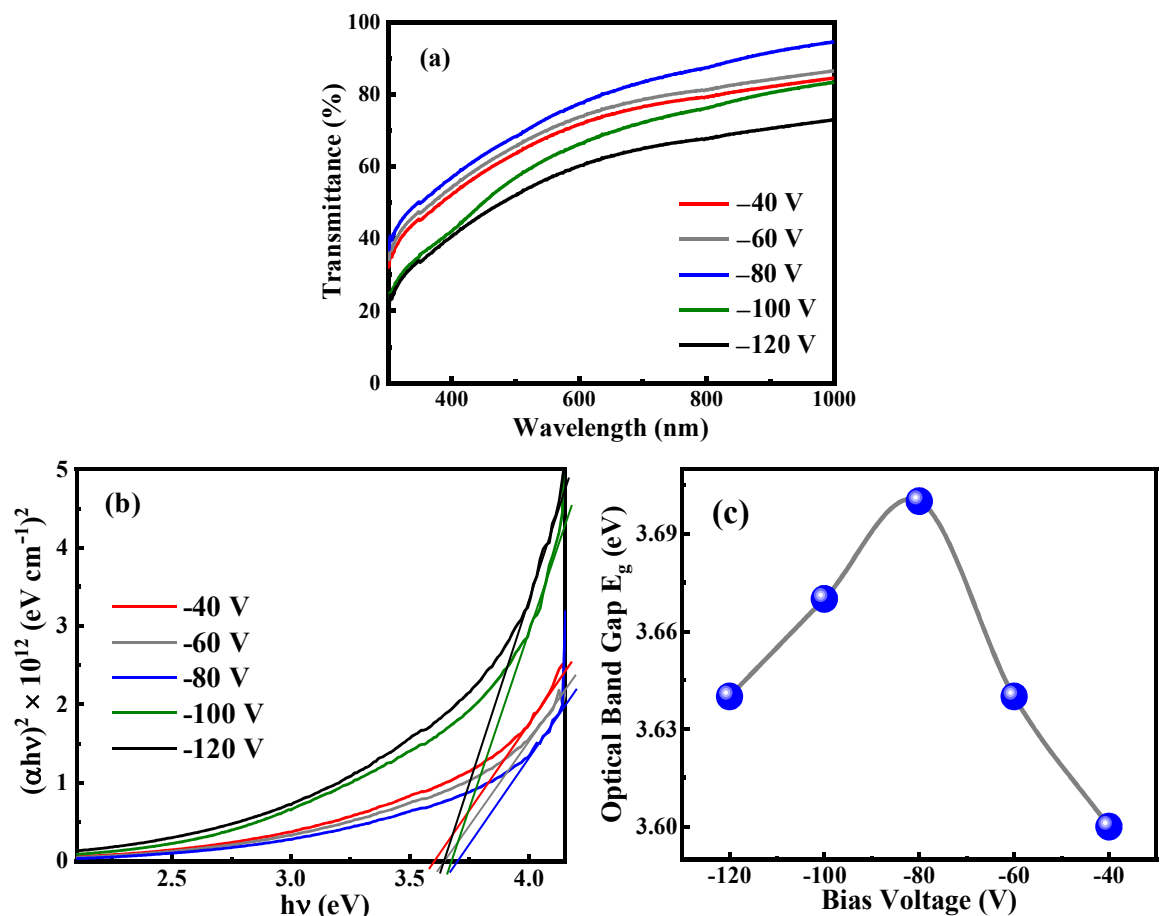


Fig. 5.2.7. (a) Transmission profile of the B-DLC films deposited at different substrate biases; (b) Tauc's plot of the samples; and (c) changes in optical band gap with applied bias.

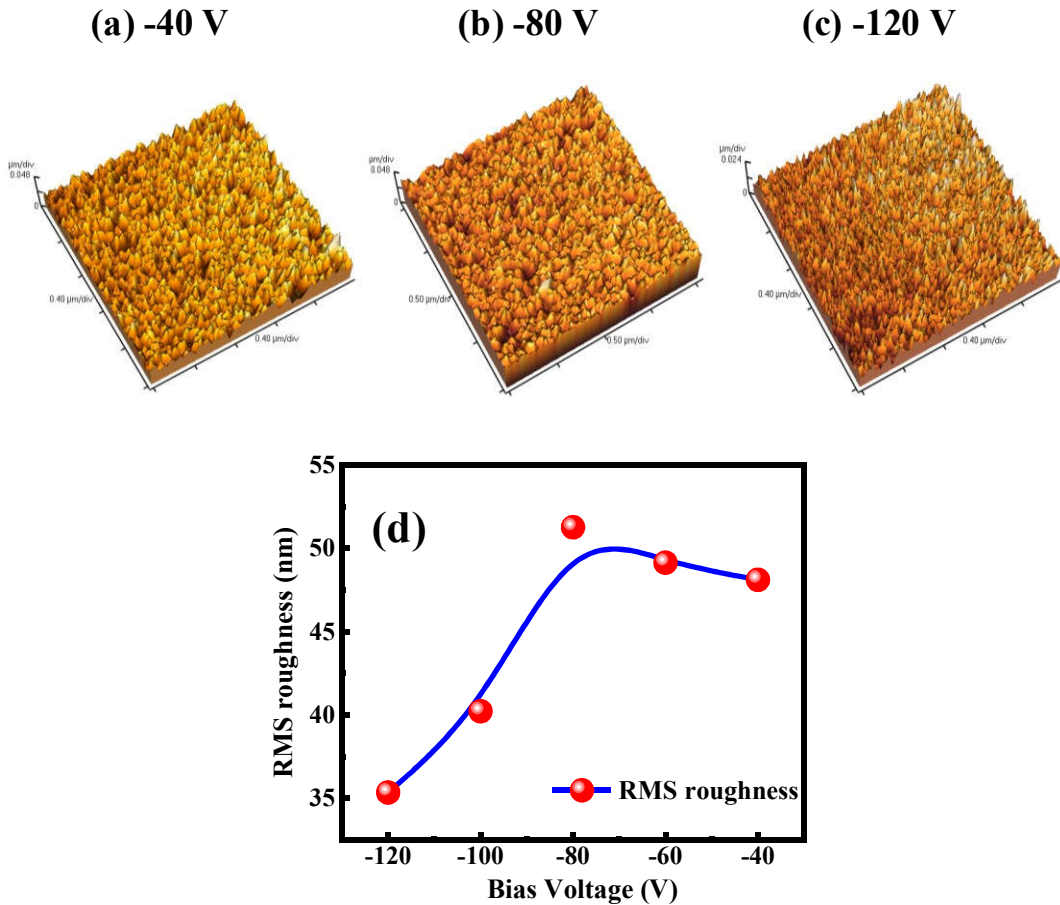


Fig. 5.2.8. The AFM micrograph of B-DLC samples grown at different biases: (a) -40 V, (b) -80 V, (c) -120 V; and (d) changes in the films' RMS roughness with applied bias voltage.

Fig. 5.2.8(a–c) shows the AFM micrographs and Fig. 5.2.8(d) the variations in films' RMS surface roughness, with changing bias voltages [184]. The RMS roughness values increase from 48.12 nm to 51.27 nm on raising the bias from -40 to -80 V. At increasing bias within -40 to -80 V, the nucleation density is enhanced due to the accelerated motion of the precursor ions onto the substrate surface, causing the formation of dense nanostructures and increasing surface roughness [185]. Besides the impact of precursor ions, increased ionic bombardment by Ar^+ and H^+ promotes the etching of the loosely bound amorphous fraction of the growing network, further fostering surface roughness [137]. However, on increasing the bias voltage beyond -80 V and up to -120 V, the incoming flux of the precursor ions onto the substrate surface becomes so intense that those already landed on the substrate are very rapidly covered by the incoming ones before being stabilized at the low-energy configurational position. Accordingly, despite significant etching, the overall matrix turns toward an amorphous configuration, as supported by the Raman data (Fig. 5.2.1(b)) and the electrical

Chapter 5

conductivity characteristics (Fig. 5.2.4(b)). The rapid amorphization of the network leads to gradual smoothening in the surface morphology, as recorded by a lowering in the RMS roughness to ~ 35.36 nm at an applied bias voltage of -120 V (Fig. 5.2.8(d)).

Fig. 5.2.9 (a–c) represents the SEM images of the films prepared at -40 V, -80 V, and -120 V respectively. The film prepared at -40 V exhibits a granular surface with no clusters. The interlinked matrix connecting the grains is separated by deep gorges at certain places. The evolution of cluster-like structures is evident from the SEM image (Fig. 5.2.9(b)) of the -80 V DLC film. Large clusters are formed one over the other, thereby developing deep pores in between. In the case of the film grown at a very high substrate bias of -120 V, the SEM image (Fig. 5.2.9(c)) reveals that the underlying matrix possesses dense helical-shaped structures connected like a mesh on which spherical ball-like assemblies are produced in place of the clusters. Vigorous ion etching on the growing surface leads to a discontinuity in the upper spherical balls. The helical-shaped underlying structure also suffers from a loss in mutual connectivity within its mesh-like network, as evident in Fig. 5.2.9(c), which results in a significantly low room-temperature electrical conductivity of the sample (Fig. 5.2.4(b)).

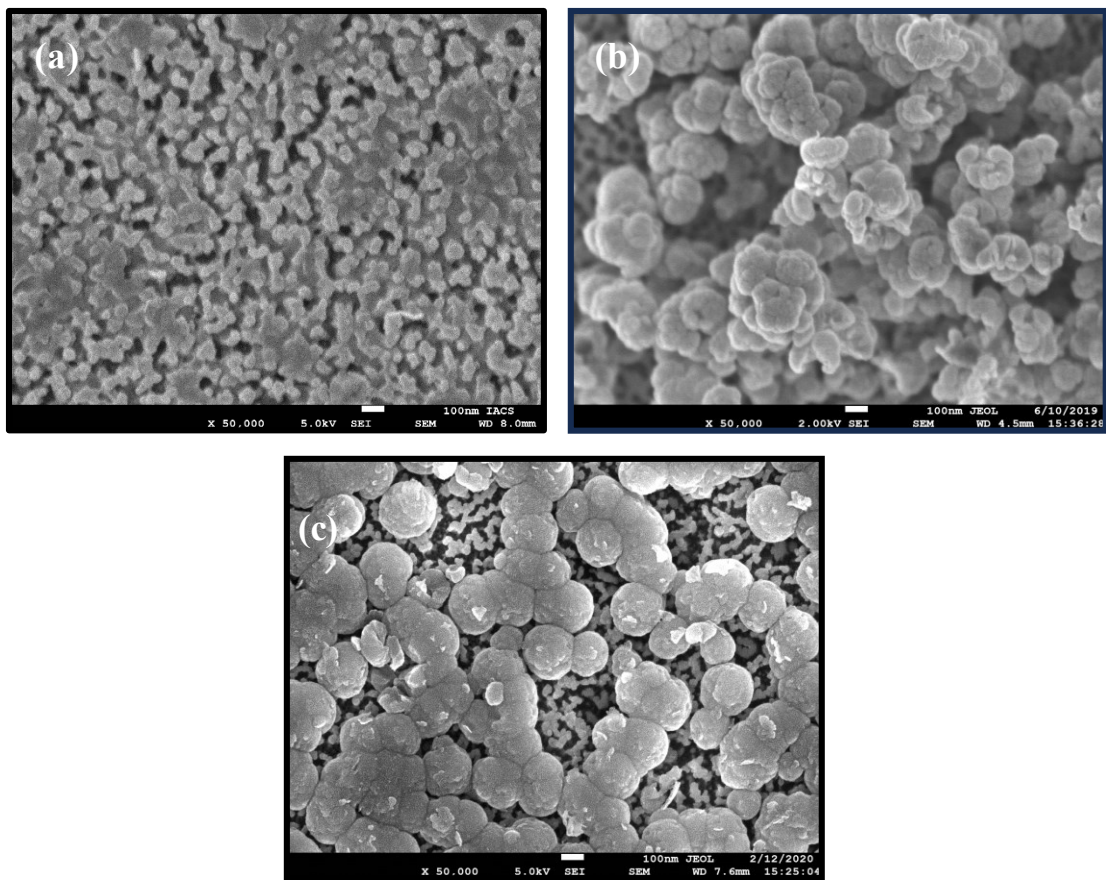


Fig. 5.2.9. The SEM micrographs of B-DLC films grown at a different bias: (a) -40 V, (b) -80 V and (c) -120 V.

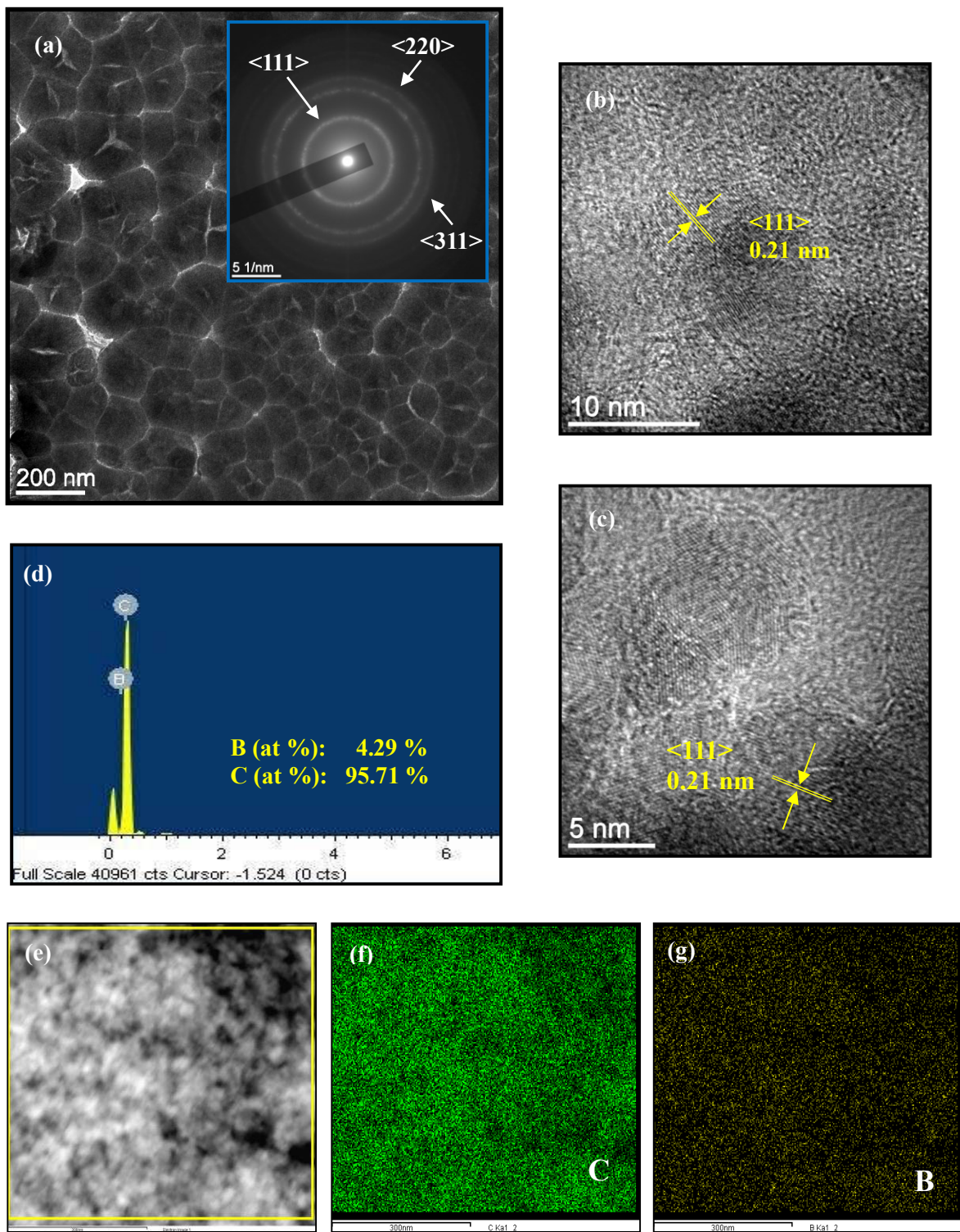


Fig. 5.2.10. (a) TEM micrograph of the B-DLC film corresponding to -80 V dc substrate bias; inset shows the SAED pattern with $<111>$, $<220>$ and $<311>$ planes, (b–c) high-resolution images of the sample showing the prominent $<111>$ crystalline planes of diamond; (d) EDX spectrum presenting the contents of B and C in the sample; (e) dark field HRTEM image; (f–g) elemental mapping signifying the presence of C and B.

Chapter 5

[Fig. 5.2.10\(a\)](#) shows the TEM micrograph of B-DLC films grown at -80 V of substrate bias. The SAED pattern in the inset shows the distinct circular rings related to crystalline planes of $<111>$, $<220>$, and $<311>$ orientations of C. The high-resolution images in [Fig. 5.2.10\(b\)](#) and [5.2.10\(c\)](#) reveal patches with prominent parallel crystalline planes whose inter-planar spacing of ~ 0.21 nm resembles the $<111>$ orientations of a diamond. The EDX spectrum ([Fig. 5.2.10\(d\)](#)) shows the atomic content of B and C to be 4.29% and 95.71%, respectively. The dark field STEM image is displayed in [Fig. 5.2.10\(e\)](#), and the corresponding color mapping of C and B components are presented in [Fig. 5.2.10\(f\)](#) and [5.2.10\(g\)](#), respectively.

Table 5.2.3: Comparative study of similar works reported in the literature.

References	Material	I_D/I_G	Optical band gap (eV)	sp^3 content	Conductivity ($\Omega^{-1} \text{ cm}^{-1}$)
[186]	B-doped DLC film by rf PE-CVD	0.52	–	–	1×10^{-6}
[92]	B-doped DLC-like a-C film by dc GD-CVD	–	1.8	77%	2.52×10^{-9}
[187]	B-doped diamond thin films by hot filament CVD	–	–	–	3.16×10^{-4}
[85]	B-doped DLC film by rf sputtering	1.06	–	$\sim 20\%$	7.1×10^{-2}
[189]	Ni/B co-doped DLCs by Electrodeposition	0.71	–	$\sim 59\%$	–
[188]	B-doped DLC films by pulsed laser deposition	0.99	1.88	$\sim 40\%$	$\sim 5 \times 10^{-3}$
[113]	B-doped C films by pulsed laser deposition	–	0.9	–	$\sim 1 \times 10^{-2}$
[190]	B-C coatings by pulsed laser irradiation	0.6	–	$\sim 58\%$	–
Present work	B-doped DLC by rf ICP CVD	0.75	3.7	57.29%	1.15×10^{-4}

[Table 5.2.3](#) compares various works reported in the literature related to the quality of B-doped DLC films. Li *et al.* [186] and Chan *et al.* [92] reported a very low conductivity ($\sim 10^{-6}$ to $10^{-9} \Omega^{-1} \text{ cm}^{-1}$). Additionally, the B-DLC films prepared by Chan *et al.* [92] exhibited a low optical band gap of 1.8 eV. Mort *et al.* [187] reported an electrical conductivity (σ_D) of $\sim 3.16 \times 10^{-4} \Omega^{-1} \text{ cm}^{-1}$ of the B-DLC film prepared by hot-filament CVD. Pu *et al.* [85] reported B-DLC films grown by rf sputtering, possessing a high I_D/I_G value of ~ 1.06 with a low sp^3 C-C content of $\sim 20\%$ and σ_D of $\sim 10^{-2} \Omega^{-1} \text{ cm}^{-1}$. B-doped DLC films having a higher I_D/I_G ratio of ~ 0.99 , a low sp^3 C-C of $\sim 40\%$, an E_g of 1.88 eV, and $\sigma_D \sim 5 \times 10^{-3} \Omega^{-1} \text{ cm}^{-1}$ were grown by

Chapter 5

Dey *et al.* [188], using pulsed laser deposition system. Rusop *et al.* [113] reported the B-doped C films deposited using a pulsed laser, where films possessed a relatively high σ_D of $\sim 10^{-2} \Omega^{-1} \text{ cm}^{-1}$, with a low E_g of ~ 0.9 eV. The present work manifests the B-DLC films whose I_D/I_G values (0.75) and the corresponding sp^3 C-C bond content ($\sim 57\%$) are comparable to those conveyed by Zhang *et al.* [189], and Kulesh *et al.* [190]. The B-DLC film in this work possesses σ_D of $\sim 1.15 \times 10^{-4} \Omega^{-1} \text{ cm}^{-1}$ and an E_g of ~ 3.7 eV. Thus, the current work deals with developing B-DLC films of reasonably superior qualities possessing good crystallinity, lower I_D/I_G values, high sp^3 C-C content, and good conductivity, including the highest optical band gap.

5.2.2. Conclusion:

The motive of the current work is to improve the B-doping of the DLC matrix while maintaining optimum crystallinity, by controlling the negative substrate bias and following a single-step growth technique, without employing any substrate pre-treatment or post-deposition thermal annealing. As the substrate bias is elevated within -40 to -80 V, the crystallinity improves to a considerable extent, involving an increase in the sp^3 C-C content from 50.87% to 57.29%, besides significant B₄-C bonds in the DLC matrix. However, at higher bias of -120 V, the sp^3 C-C content decreases to 52.47 %, along with a lowered B₄-C content. The $(I_D/I_G)_{\min}$ of ~ 0.75 , along with the $(I_{D\text{ia}}/I_D)_{\max} \sim 1.49$ and $(I_{D\text{ia}}/I_G)_{\max} \sim 1.11$ ratios in the Raman band, indicates good crystallinity of the B-DLC network grown at -80 V substrate bias. At increased bias, an efficient substitution of B atoms into the lattice positions containing sp^3 -hybridized C-C bonds and sp^2 -hybridized C=C bonds generates the acceptor states, facilitating increased electrical conductivity (σ_D), typically $\sim 1.15 \times 10^{-4} \text{ S cm}^{-1}$ at an applied dc substrate bias of -80 V. Interestingly, while gradually increasing the bias voltage across -80 V, the pre-exponential factor (σ_0) corresponding to the above room temperature conduction modifies significantly, with its characteristic energy (E_{MN}) changing from $\sim +31$ meV to ~ -29 meV. This signifies a change from the conventional MNR to the reverse MNR attribute and a transition from the non-degenerate to degenerate semiconductor-like characteristics of the B-DLC network at increased negative dc substrate bias. However, in the below room temperature conduction, the dominant transport of charges occurs obeying Mott's variable range hopping mechanism (VRH), independent of the substrate bias.

The highest optical transparency of $\sim 80\%$ (at 700 nm wavelength) and the corresponding maximum optical band gap (E_g) of ~ 3.70 eV, with a moderately smooth surface (RMS roughness 51.27 nm), are the characteristics of the B-DLCs grown at -80 V substrate bias. TEM images show prominent crystallographic planes corresponding to the <111> orientation of the

Chapter 5

diamond. Excessive negative bias above -80 V causes amorphization of the network and formation of carbonaceous soot layers, which causes light absorption and a decrease in E_g , simultaneously reducing the σ_D . Realizing the growth of B-doped DLC films with increased electrical conductivity and transparency while maintaining good crystallinity could not have been possible simply by optimizing the negative substrate bias; instead, simultaneous utilization of the compelling hydrocarbon dissociation efficiency and the corresponding high atomic H density in the inductively coupled low-pressure high-density plasma has rendered it feasible. Apart from the popular tribological applications to reduce friction and improve wear resistance in automotive systems, these B-DLC films can be used as protective coating on optoelectronic devices, using their high transparency and especially the good conductivity enabling transport of electrical current to generate heat for removing water-vapor to maintain superior window effect.

A.2:
DLC films by CCP CVD

➤ **Introduction:**

Diamond-like carbon (DLC) comprises a family of amorphous carbon materials, with a fusion of diamond-like (sp^3 bonded C) and graphite-like (sp^2 bonded C) hybridizations [191]. Because of its outstanding combination of properties close to those of natural diamond, e.g., a high degree of hardness (as high as up to 80 GPa) [192], thermal conductivity, low friction coefficient and a series of adjustable range of optical characteristics like band gap (1–4 eV) [193] and refractive index (1.6–2.2) [5,194], DLC finds potential optical and optoelectronic applications in optical lens, micro and nano-electromechanical devices, nanotribology, etc. [2,82,195,196].

Different physical and chemical vapor deposition (CVD) techniques, including radio frequency plasma-aided deposition, pulsed laser deposition, magnetron sputtering, etc could be used to create the DLC films [197]. Among those, CVD has shown to be the most promising technology due to its ability to regulate the quality of diamond-like properties more precisely than other methods. CVD, or precisely the radio frequency plasma-enhanced chemical vapor deposition (RF-PECVD) technique, ensures the growth of DLC films of desired characteristics by properly optimizing the plasma conditions. Highly energetic radicals are produced from gaseous precursors due to the alternating currents of the electric field at a particular frequency, generating the plasma [198]. The energy barriers for nucleation and growth processes are significantly lowered by the presence of these radicals, which also reduce the total thermal budget by minimizing the growth temperature and growth time [199,200].

PECVD systems employed for DLC growth include microwave (MW) plasma, direct current plasma, inductively coupled plasma (ICP), and capacitively coupled plasma (CCP) [201]. The use of microwave plasma CVD for DLC films has been adequately explored [19–21]. However, there are practical limitations in microwave-operated CVD. Microwaves are hazardous to health and need proper shielding during deposition, incurring expenses; moreover, they suffer from sustaining a stable plasma, particularly at low powers. These challenges can be easily dealt with using harmless RF-operated CVD systems involving inductively coupled or capacitively coupled plasma (ICP and CCP) [22,23]. Considering the advantages of the ICP and CCP systems in terms of lower frequency operation and uniform deposition, the synthesis of DLC films in these processes is focused. However, CCP has a built-in benefit because of easier apparatus setup, lower energy usage, and the formation of a more homogeneous plasma that facilitates scaling up [202].

The preparation of DLC films by CVD often requires high electrical power (≥ 500 W) for the plasma initiation [20,137,203]. In a radio frequency-driven CCP CVD, the higher the power employed, the higher the potential drop across the electrode plates [23]. However, by obtaining a higher capacitance, via adjusting the distance between the two electrode plates within the plasma chamber, a strong electric field can also be generated even at a low power in CCP CVD.

In PECVD, plasma processing mostly involves diluent gases like Ar, He, and H₂ for facilitating nano-crystallization in film growth [59,204]. Due to its high diffusivity, H₂ benefits not only in precursor formation and maintaining film homogeneity, but also regulates the spontaneous structural development toward crystallinity by preserving a balance between surface reactivity and passivation at desired deposition conditions [77,205]. However, an excess flow rate of H₂ lowers the deposition rate by etching the growing film surface. For further enhancing the crystalline quality of DLC films, substrate pre-treatments involving ultrasonication or mechanical scratching of the substrate surface with nanodiamond powder are employed [206]. These incur expertise and care for multi-step deposition techniques, involving expenses. Nevertheless, substrate bias has also been applied to improve the crystalline properties of DLC films [137].

In this work, efforts have been made to prepare intrinsic DLC films with considerable crystallinity and high transparency in a single step deposition method. Notably, this process was achieved without applying any substrate bias or performing pre-treatment with diamond powders. The deposition was carried out utilizing a capacitively coupled plasma chemical vapor deposition (CCP CVD) system, operating at a low radio frequency (RF) power of 250 W and a moderate temperature of 450 °C.

➤ Experimental

DLC films were obtained from a (CH₄ + H₂) plasma ignited at a low power of 250 W and relatively low temperature of 450 °C in RF (13.56 MHz) driven CCP CVD technique. The stainless-steel plasma reactor chamber consists of a circular plate that acts as one of the electrodes. The substrate holder acts as the other electrode, on which deposition occurs. A vacuum of $\sim 1 \times 10^{-6}$ Torr, was attained within the reactor using a processed turbo pump, backed by a rotary pump. Plasma pressure during the deposition was controlled by the booster pump along with a throttle valve attached at the bottom of the chamber. CH₄ and H₂ precursor gases were used with their flow rates maintained by transducers and mass flow controllers (MKS-

make). A steady temperature was maintained by a temperature controller, connected to a resistive heater, placed in contact with the substrate holder.

Corning® Eagle 2000™ glasses were used as substrates, after being cleaned by sequential ultrasonication with de-ionized water, acetone, and alcohol, respectively, and mounted on the substrate holder within the deposition chamber. An initial vacuum of 1×10^{-6} Torr at a temperature of 450 °C was maintained for 1 h before the actual deposition commenced.

The characterization techniques for analyzing the structural, optical and morphological properties of the DLC films are discussed in preliminary parts of Section A.

A.2.1: Chapter 6

Optimization of intrinsic DLC films

Chapter 6

Two sets of DLC films were prepared. For the first set, the deposition pressure was varied from 1 to 7 Torr, maintaining the flow rates of both CH₄ and H₂ at 25 sccm each, and RF power at 250 W. With the optimized pressure procured from the first set of samples, the second set was prepared by varying the flow rate of H₂ from 12.5 to 100 sccm, keeping CH₄ flow fixed at 25 sccm (H₂/CH₄ ratio changing from 0.5 to 4), keeping other parameters unchanged.

6.1. Results and discussion:

6.1.1. Optimization of pressure:

To investigate the microstructure of the DLC films Raman spectroscopy is used as a unique non-destructive characterization technique. The deconvolution of each Raman spectrum of the samples prepared at different deposition pressures (ranging from 1 to 7 Torr) identifies seven individual components, as shown in [Fig. 6.1\(a\)](#) and [\(b\)](#). The components appearing at 1160 and 1500 cm⁻¹, are related to the vibrational modes of *trans*-polyacetylene chains at the grain boundaries [\[207\]](#). The diamond peak is another component centered at positions within (1319–1331) cm⁻¹. In single-crystal diamonds, this peak appears at 1332 cm⁻¹, which is the characteristic of the vibrations of *sp*³ hybridized C–C bonds comprising the perfect crystalline structure of cubic diamond lattice [\[208\]](#). The observed shift in the peak position from 1332 cm⁻¹ is due to mechanical stress generated at the lattice-substrate interface or within the lattice, or due to the impurities and defects developed during the film's growth. Stress and defects generated within the lattice can modify bond lengths and angles, which slightly alter the vibrational modes causing shifts in the Raman line [\[19,162,209\]](#). The D band at ~1360 cm⁻¹ is called the defect peak since it is associated with the disorders caused by the *sp*² C=C bonds (residing in aromatic rings) within a crystalline *sp*³ C–C network [\[42,210\]](#). The 1600 cm⁻¹ peak, identified as the G band, originates due to the in-plane stretching and contractions of the *sp*² C=C bonds [\[211\]](#). The last component in the series, appearing at 1620 cm⁻¹, is the D' band, which is linked with the disorder and defects (like vacancies or functional groups) in the graphitic network [\[212\]](#).

[Fig. 6.1\(c\)](#) presents the variation of the 3 different intensity ratios (I_D/I_G, I_{Di_a}/I_D, and I_{Di_a}/I_G) with the increase in deposition pressures (1 to 7 Torr). These ratios give valuable information about the structural features of diamond-like materials. The relative intensity of the D band to that of the G band, recognized as the I_D/I_G ratio, expresses the extent of the disorder concerning the graphitic network. As can be perceived from [Fig. 6.1\(c\)](#), it decreases

Chapter 6

(0.79 to 0.63) with the rise in the deposition pressure from 1 to 4 Torr, signifying increasing sp^3 C–C bonds and hence higher crystalline diamond-like nature at lower I_D/I_G values [213].

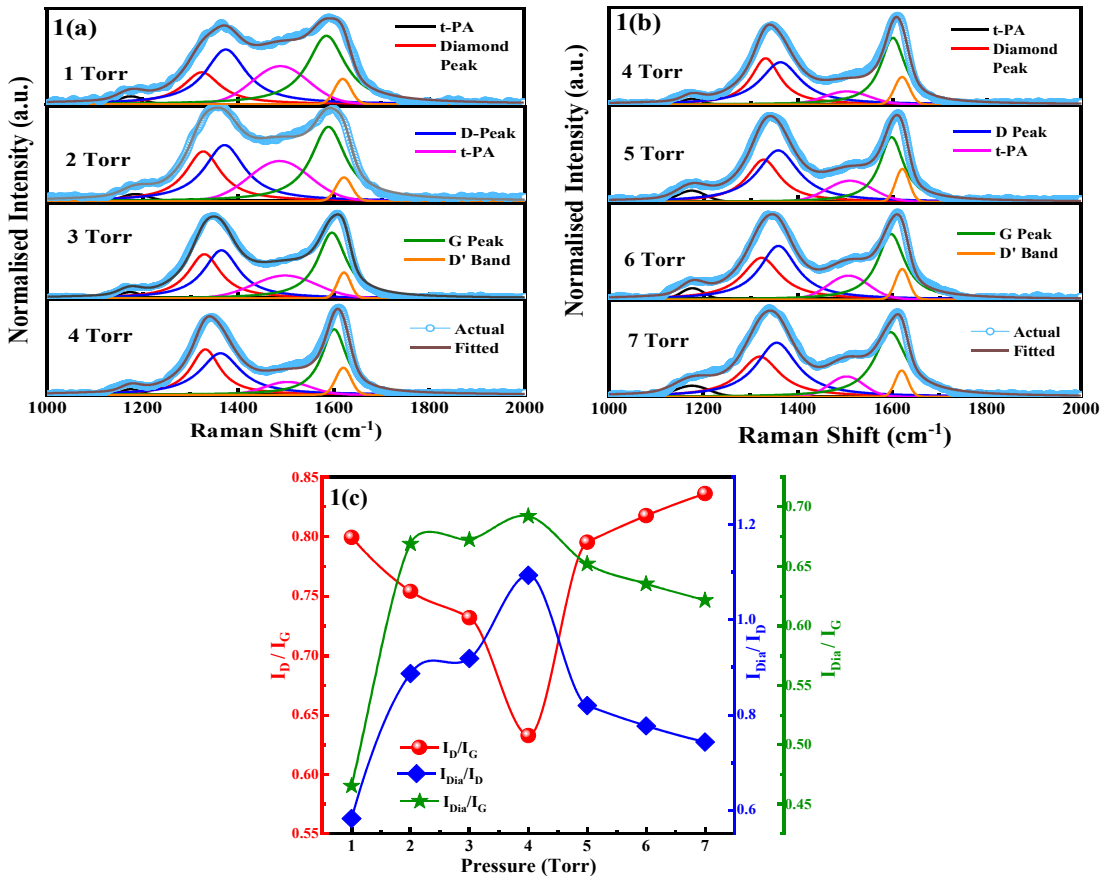


Fig. 6.1: Deconvoluted Raman spectra of the samples prepared at different deposition pressures varying from (a) 1 to 4 Torr and (b) 4 to 7 Torr; and (c) Variation of intensity ratios with the changes in pressure.

On increasing the deposition pressure to above 4 Torr, up to 7 Torr, the I_D/I_G value rises, suggesting lower sp^3 C–C content, filled with defects. The relative intensity of the diamond peak to the D band, I_{Dia}/I_D , attains a maximum value of 1.09 at 4 Torr of pressure. It signifies the proportional content of diamond-like crystalline sp^3 C–C structure from the perspective of the disorder and defects. Likewise, the relative intensity ratio of the diamond peak to the G band (I_{Dia}/I_G), shows its highest value at a deposition pressure of 4 Torr (0.69), indicating that the sample possesses a high content of crystalline diamond-like structures concerning the C=C bonds of sp^2 (graphitic) bonds at 4 Torr.

Fig. 6.2(a) shows the changes in the positions of D and G bands on increasing the deposition pressure. The D band position decreases monotonously from 1375 to 1355 cm^{-1} with the increase in deposition pressure from 1 to 7 Torr. This shift of the D band towards the

Chapter 6

lower wavenumber signifies the decreasing disorder within the graphitic network [14]. A redshift in the G band position from 1600 to 1586 cm^{-1} is observed with the rise in pressure from 1 to 4 Torr. For a further rise in pressure to 7 Torr, the G band shifts to $\sim 1596\text{ cm}^{-1}$. The redshift is associated with the reduced quantity and size of the sp^2 C=C component clusters [44,210]. It is also accompanied by a reduction in the I_D/I_G ratio (shown in Fig. 1(c)), indicative of the decreased disorder [137].

The shift in the diamond peak is shown in Fig. 6.2(b), which is used to evaluate the residual stress (σ) within the lattice, following the formula [47,137]:

$$\sigma = -\Delta\nu \times 0.488 \text{ GPa/cm}^{-1} \quad \text{eqn (6.1)}$$

with $\Delta\nu$ representing the relative peak shift of the observed diamond peak from its characteristic position of unstressed single crystal diamond at 1332 cm^{-1} .

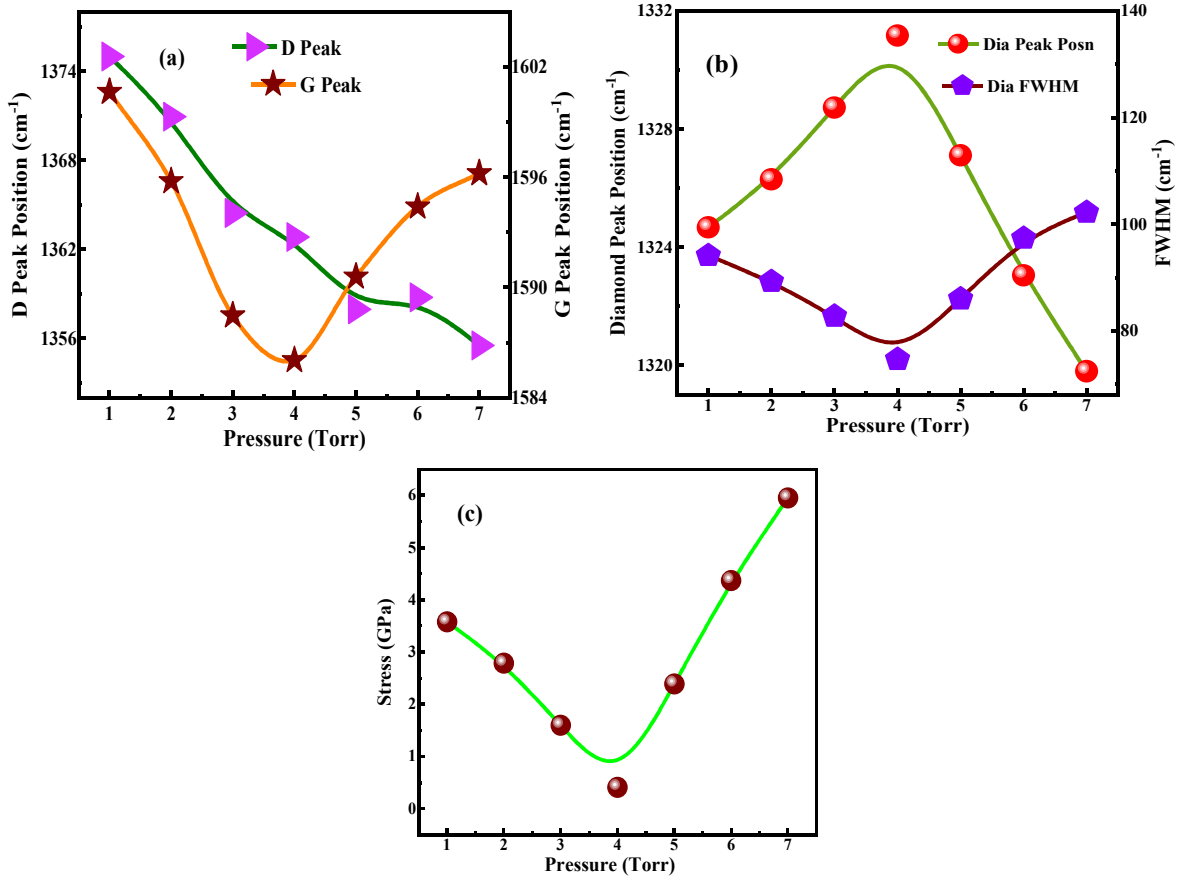


Fig. 6.2: (a) Variation of D and G band positions, (b) variation of diamond peak position and its corresponding FWHM, and (c) the change in the stress generated within the DLC network with changes in deposition pressure from 1 to 7 Torr.

Depending on how the observed diamond peak is altered, the network may experience positive or negative stress, manifested as tensile and compressive stress, respectively. The

Chapter 6

tensile stress is generated due to differences in thermal expansion coefficients between the substrate and the DLC film. Development of tensile stress also occurs from voids and dislocations within the network, during the film growth. On the other hand, compressive stress arises as an intrinsic property, mainly due to coalesced impurity components and hydrogen clusters in a dense matrix [137,214].

As is shown in [Fig. 6.2\(c\)](#), the stress is tensile, sharply decreasing from 3.57 GPa (at 1 Torr) to 0.4 GPa (at 4 Torr), after which it again increases to 5.95 GPa (at 7 Torr). With the least disorders and voids in the film network, the DLC film prepared at 4 Torr appears more diamond-like.

[Fig. 6.3\(a–c\)](#) represents the C 1s XPS spectra of the samples prepared at 1, 4, and 7 Torr of the deposition pressure, respectively. XPS provides analytical information regarding the elemental composition and chemical bonding states within the DLC films, by measuring energy from the emitted photo-electrons obtained after irradiation of the sample surface with X-rays.

The peak, centered at \sim 285 eV, is characteristic of the electrons ejected from the 1s core orbital of the C atoms in the DLC films. This spectrum is deconvoluted into 5 satellite peaks, using the voigt function, positioned at 284.2, 284.9, 285.6, 286.5, and 289 eV, characteristic of the different chemical states and bonds of C: like sp^2 C=C, sp^3 C–C, C–OH, C=O, and O–C=O, respectively [213]. Important information abstracted from the XPS data is the percentage content of the different bonds within the film surface, which is evaluated from the relative ratio of the individual peak areas to the total area under the curve. If p_i is the percentage composition of a certain bond in the XPS spectrum, evaluated as [208],

$$p_i(\%) = \frac{A_i}{A} \times 100 \quad \text{eqn (6.2)}$$

where A_i is the area of the deconvoluted peak corresponding to the chemical state and A is the area covered by the total spectrum.

As deduced from [Fig. 6.3\(a\)](#), utilizing the [eqn \(6.2\)](#), the percentage compositions of sp^3 C–C and sp^2 C=C bonds are 48.95% and 27.56% respectively, for the sample prepared at 1 Torr. While increasing the pressure to 4 Torr, an escalation in the sp^3 content to 66.75% occurs, along with a corresponding decrease in the sp^2 content to 19.4% ([Fig. 6.3\(b\)](#)). With a still higher deposition pressure of 7 Torr, the sp^3 content decreases to 44.78%, and the sp^2 C–C increases to 31.9% ([Fig. 6.3\(c\)](#)). The increment of sp^3 C–C bonds for increasing pressure from 1 to 4 Torr is followed by its decrement at higher deposition pressures (to 7 Torr), which supports the analysis deduced from the Raman data.

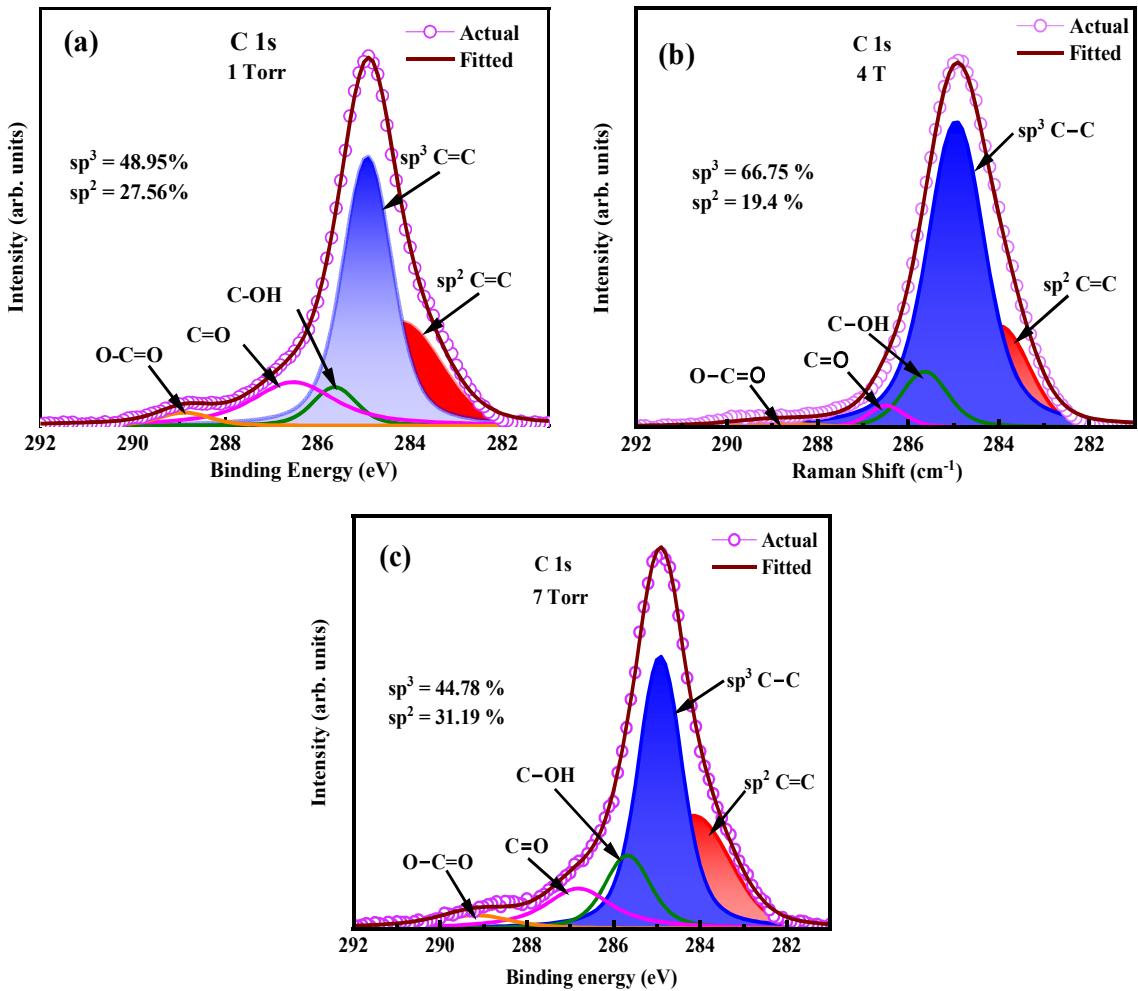


Fig. 6.3: C 1s XPS spectra of the samples grown at (a) 1 Torr, (b) 4 Torr, and (c) 7 Torr.

The transmittance spectra of the samples on glass substrates are shown in Fig. 6.4(a). All the samples maintain high transmission values of above 80% in the wavelength range above 600 nm, with insignificant scattering loss. The sample prepared at 4 Torr pressure remains the most transparent, with ~85% transparency at 400 nm and above. Transmittance of the DLC films escalates as the pressure increases from 1 to 4 Torr, beyond that it gradually decreases, which is related to the films' structural properties including their crystalline orientations.

The optical band gap (E_g) of each of the individual films was estimated from the Tauc's plot, following the equation [215,216]:

$$\alpha h\nu = B(h\nu - E_g)^n \quad \text{eqn (6.3)}$$

where α and $h\nu$ stand for the absorption coefficient and photon energy respectively. B is the characteristic proportionality constant of the material, related to the density of states near the band edge and the transition probability. The variable n is the Tauc's exponent, which depends on the optical transition in the film. For direct and allowed band transitions, the value of n is

Chapter 6

$\frac{1}{2}$, while it is 2 for indirect allowed transitions [217]. With the Tauc's plot being drawn with $(\alpha h\nu)^n$ vs $h\nu$ as the y and x-axis respectively, a sharp band edge (following a linear region) is obtained when $n = 2$, indicating the occurrence of indirectly allowed transitions within the DLC films [216], as shown in Fig. 6.4(b). The energy band gap E_g is then measured as the intercept on the energy axis ($h\nu$) by the extrapolated tangent drawn to the linear region of the Tauc's plot [217]. The variation of E_g values with the change in deposition pressure is shown in the inset of Fig. 6.4(b). It is observed that the highest E_g (~ 3.65 eV) is obtained for the sample at 4 Torr. The E_g values reduce to lower magnitudes (3.36 eV (at 1 Torr) and 3.29 eV (at 7 Torr)) at either side as the deposition pressure varied from 4 Torr.

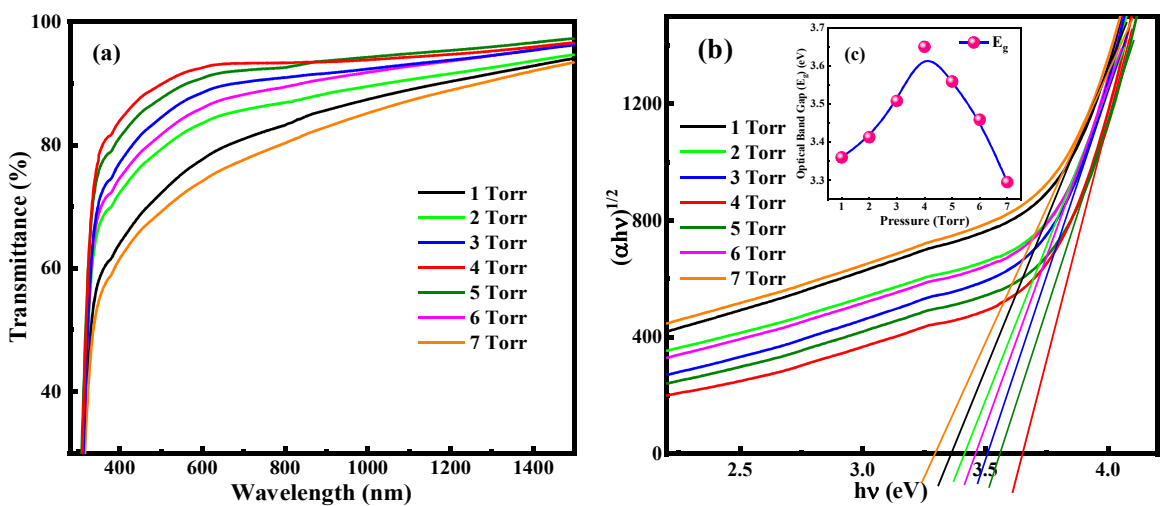


Fig. 6.4: (a) Transmittance spectra of the samples prepared at different pressures (1 to 7 Torr); (b) corresponding Tauc's plots and variation of optical band gap vs deposition pressure in the inset.

The optical band gap of the DLC films decreased with the increase in the quantity and size of the sp^2 C=C clusters. The abundance of π - π^* states of graphitic clusters facilitates easy electronic transition reducing the band gap [195,218]. Thus, the maximum $I_{D\alpha}/I_G$ and $I_{D\alpha}/I_G$ ratios for the sample prepared at 4 Torr (obtained from Raman analysis) indicate a higher crystalline sp^3 C-C orientation concerning the graphitic clusters and correspond to the highest optical band gap. This is also supported by the low sp^2 C=C content ($\sim 19.4\%$) and a high sp^3 content ($\sim 66.75\%$) of the DLC film grown at 4 Torr (as analyzed from XPS).

Fig. 6.5(a-c) shows the AFM micrographs of the samples prepared at 2, 4, and 6 Torr. The variation of the root mean square (RMS) roughness of the sample surface, exhibited at different deposition pressures (1 to 7 Torr) in Fig. 6.5(d), identifies the maximum RMS roughness of ~ 16.45 nm for the sample prepared at 4 Torr. It increases from 2.087 nm at 1 Torr,

until it reaches the highest value at 4 Torr, followed by a decreasing trend at further higher deposition pressures (up to 7 Torr).

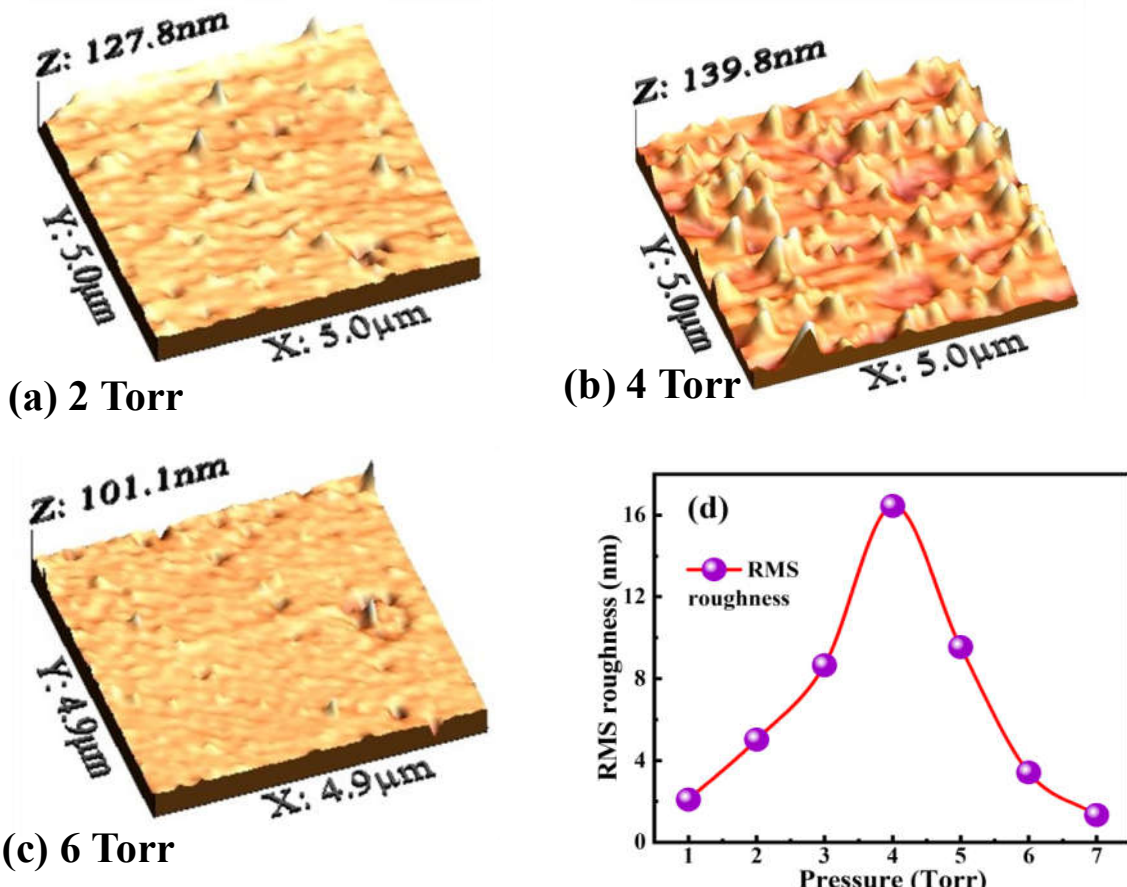


Fig. 6.5: AFM micrographs of the films prepared at (a) 2 Torr; (b) 4 Torr; (c) 6 Torr; (d) The change of RMS roughness of the samples at different pressures.

With the increase in pressure (up to 4 Torr), the flux of the precursor ions within the plasma increases, leading to the formation of more and more nucleation centers on the growing surface, the accumulation of which with time causes the formation of larger-sized nanostructures and subsequently increased surface roughening [5]. Moreover, the increased bombardment of the higher density of atomic H eliminates the amorphous component on the growing matrix and leads to additional surface roughening. On further increase in pressure (above 4 Torr) the mean free path of the plasma ions is reduced by too many collisions, which lowers the energy of the plasma ions and thereby, the reactivity of the plasma. However, the production of the higher density of precursor ions leads to the formation of amorphous components in the growth zone, leading to a smoother surface of the DLC films [5]. The formation of increasing amorphous component in the DLC matrix at pressures above 4 Torr is also reflected in the previous analysis from the Raman spectroscopy, XPS, and optical data.

6.1.2. Optimization of H₂/CH₄ flow rate ratio:

From the earlier optimization, the sample prepared at 4 Torr with H₂/CH₄ flow rate ratio (25/25) = 1, was inferred as the DLC film with good-quality properties closest to diamond. For further optimization, another set of samples was prepared by varying the flow rates of H₂ from 12.5 sccm to 100 sccm, with the CH₄ flow rate fixed at 25 sccm, thereby changing the H₂/CH₄ ratio from 0.5 to 4. The Raman spectra of these samples are shown in Fig. 6.6(a), and the variation of the corresponding intensity ratios (I_D/I_G, I_{Dia}/I_D, and I_{Dia}/I_G) with H₂/CH₄ flow ratio are presented in Fig. 6.6(b). Deconvolution of each Raman spectrum (not shown in Fig. 6) produces 6 satellite peaks as described in the previous section (Fig. 6.1(a) and (b)). Analysis of the different combinations of intensity ratios with diamond peak, D band, and G band conveys an idea about the microstructural quality of the DLC film network, in terms of crystallinity, disorder, and structural rigidity. Fig. 6.6(b) identifies an initial decrease in the I_D/I_G values with the increase in H₂/CH₄ ratio from 0.5 to 1, above which it increased significantly and attained an almost saturation with a magnitude of ~1 for a higher flow rate ratio above 2. This nature of variation seems identically opposite to that of I_{Dia}/I_D, while for I_{Dia}/I_G no such saturation is attained for the H₂/CH₄ ratio increasing up to a magnitude of 4.

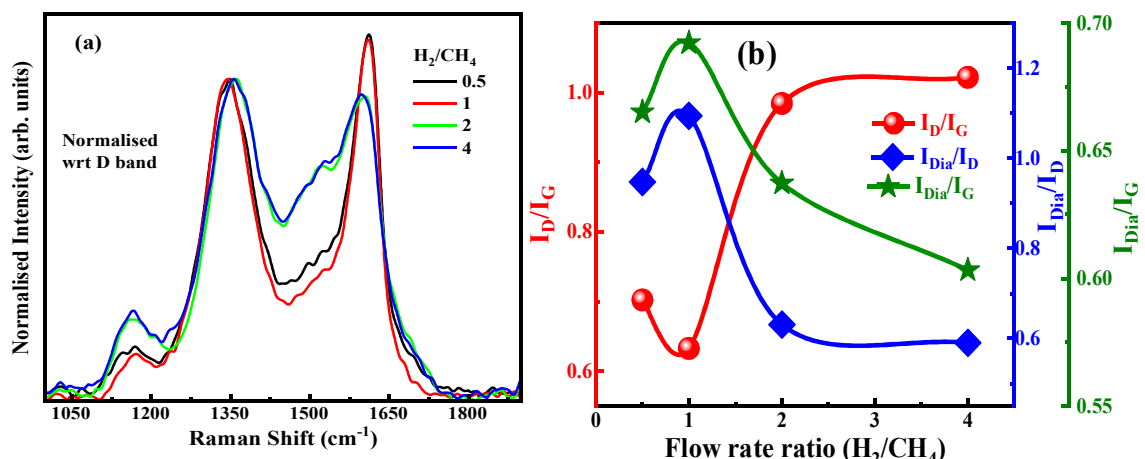


Fig. 6.6: (a) Deconvoluted Raman spectra of the samples prepared at different flow rate ratios of H₂/CH₄; (b) The changing intensity ratios (I_D/I_G, I_{Dia}/I_D, and I_{Dia}/I_G) with H₂/CH₄.

The Raman data of the present set of DLC films are shown in Table 6.1. The D band shifts to a lower wavenumber at H₂/CH₄ = 1, then moves to higher wavenumbers as the H₂/CH₄ ratio increases to 4. The nature of variation in the G band position changes similarly with the increasing H₂/CH₄ flow ratios from 0.5 to 4. The lowest wavenumber positions of the D band and G band at H₂/CH₄ = 1, indicate the lowest disorder with the least fraction of sp² C=C groups in the DLC matrix. The diamond peak position (~1331.17 cm⁻¹) of the DLC film prepared at H₂/CH₄ = 1 appears the closest to the crystalline bulk diamond (1332 cm⁻¹), indicating the

Chapter 6

lowest impurities remaining in this film. Corresponding to this small shift, the stress is minimum (~ 0.4 GPa), as derived from eqn. (6.1), indicating the film resembles the most diamond-like in the series.

Table 6.1. Variation of different components from analysis of Raman spectra with the change in the flow rate ratio H_2/CH_4 from 0.5 to 4.

H_2/CH_4 flow rate ratio	D band position (cm^{-1})	G band position (cm^{-1})	Diamond peak position (cm^{-1})	FWHM of diamond peak (cm^{-1})	Stress (GPa)
0.5	1367.9545	1603.0844	1330.3571	84.41558	0.80174
1	1362.8247	1600.6494	1331.1688	74.67532	0.40563
2	1370.9416	1603.0844	1328.7338	94.67532	1.59391
4	1371.7532	1603.8961	1328.7338	99.02597	1.59391

The XPS measurement of the DLC films grown at $H_2/CH_4 = 0.5$, 1, and 4 was performed; the corresponding analysis of the C 1s spectra of the samples helped evaluate the respective contents of sp^3 C–C and sp^2 C=C bonds, using eqn (6.2), and their comparative presentation is given in Fig. 6.7. The sp^3 C–C content initially increases from 54.93% (at $H_2/CH_4 = 0.5$) to 66.75% (at $H_2/CH_4 = 1$) and then decreases to 48.6% at a higher flow rate ratio of 4. The sp^2 C=C bond content exhibits a minimum value at $H_2/CH_4 = 1$, among the three films analyzed by XPS.

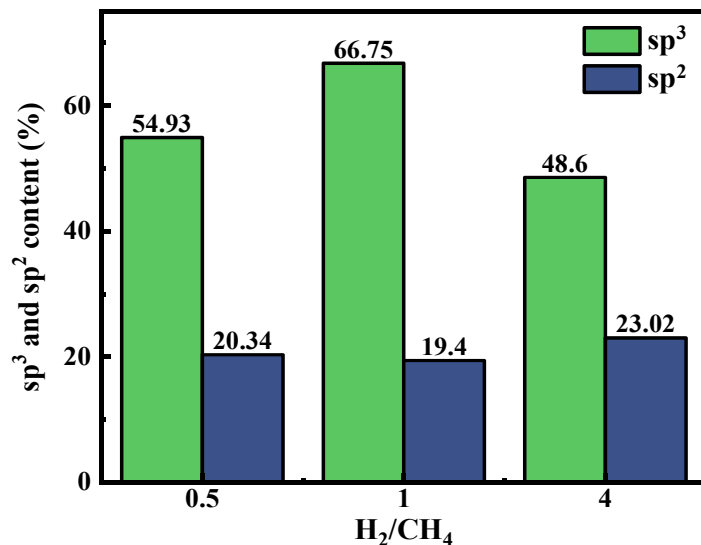


Fig. 6.7: Contents of sp^3 C–C and sp^2 C=C bonds at different H_2/CH_4 ratios, derived from XPS analysis.

Chapter 6

The transmittance spectra of the DLC films are presented in Fig. 6.8(a). The magnitude of transmittance of the films with $H_2/CH_4 = 0.5$ and 1 are higher than 80% and 90%, respectively, for the wavelength range above 600 nm. At an increased flow rate ratio the transmittance decreases to $\sim 70\%$ for 600 nm and above. Fig. 6.8(b) shows the corresponding Tauc plots for the DLC films grown at varying flow rate ratios. The varying E_g values are plotted as a function of the H_2/CH_4 flow rate ratios in the inset of Fig. 6.8(b). The decrease of E_g values for H_2/CH_4 ratios increasing > 1 indicates the elevated size and quantity of the sp^2 C=C clusters in the DLC films, as supported by the previous Raman, XRD, and XPS analyses. The highest transparency and the corresponding high optical band gap ($E_g = 3.64$ eV) are manifested by the DLC film grown at H_2/CH_4 ratio = 1.

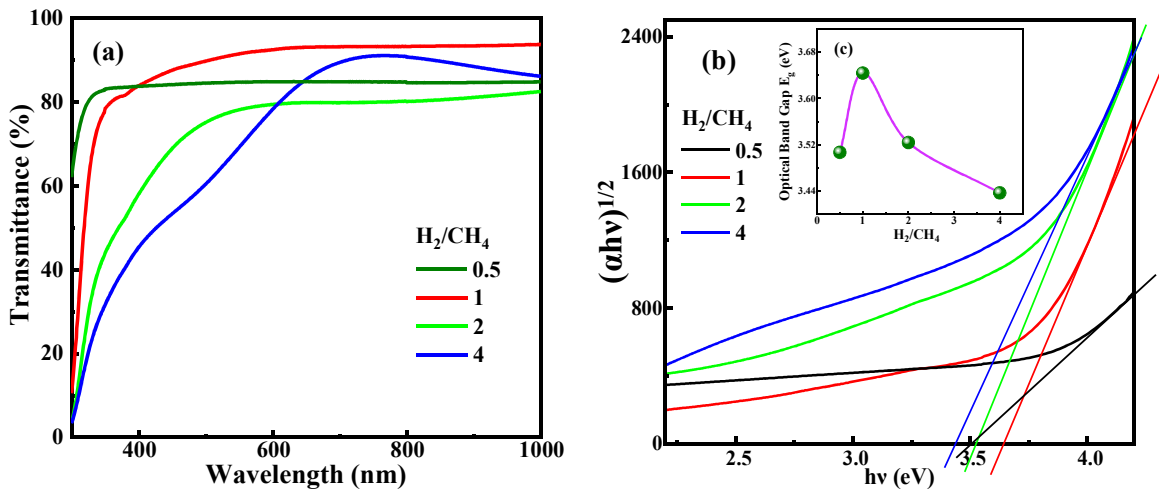


Fig. 6.8: (a) Transmittance of the DLC films at varying H_2/CH_4 ratios; (b) The corresponding Tauc plots and the change of the optical band gaps with the varying H_2/CH_4 flow ratios are shown in the inset.

The X-ray diffraction (XRD) pattern of DLC films grown at changing H_2/CH_4 ratios from 0.5 to 4 is shown in Fig. 6.9. The peak at $2\theta \sim 43.5^\circ$ identifies the (111) crystalline planes of the diamond [189]. The broad hump arising at $2\theta \sim 55^\circ$ corresponds to the (004) plane of graphite [219]. Thus, with the initial increase in the H_2/CH_4 ratio from 0.5 to 1, the diamond (111) plane peak intensity remains the same, beyond which, a drastic reduction in peak intensity arises. The peak at 55° is related to graphitic (004) oriented planes that appear for the films prepared with the lowest (0.5) and highest (4) H_2/CH_4 flow ratios. The disappearance of this peak for films with intermediate H_2/CH_4 flow ratios (1 and 2) indicates minimum graphitic components in corresponding film networks. For the sample with H_2/CH_4 ratio = 1, another small peak appears at 64.23° , which is identified as due to (311) planes of diamond [189]. The decreasing intensity of the peak for the (111) crystalline plane of diamond with a rising H_2/CH_4 ratio announces the reducing concentration of the diamond planes. The grain size of the nanocrystals,

Chapter 6

corresponding to the $<111>$ orientation, present in the DLC (prepared at $H_2/CH_4 = 1$) film, as calculated using the Debye Scherrer equation [137], was found to be ~ 14.6 nm.

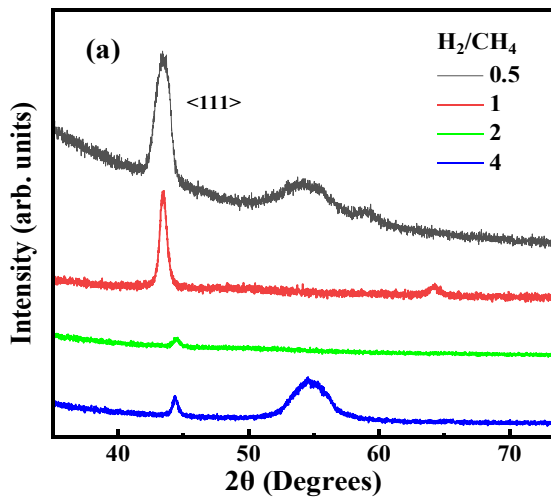


Fig. 6.9: XRD pattern of DLC films grown at different H_2/CH_4 ratios.

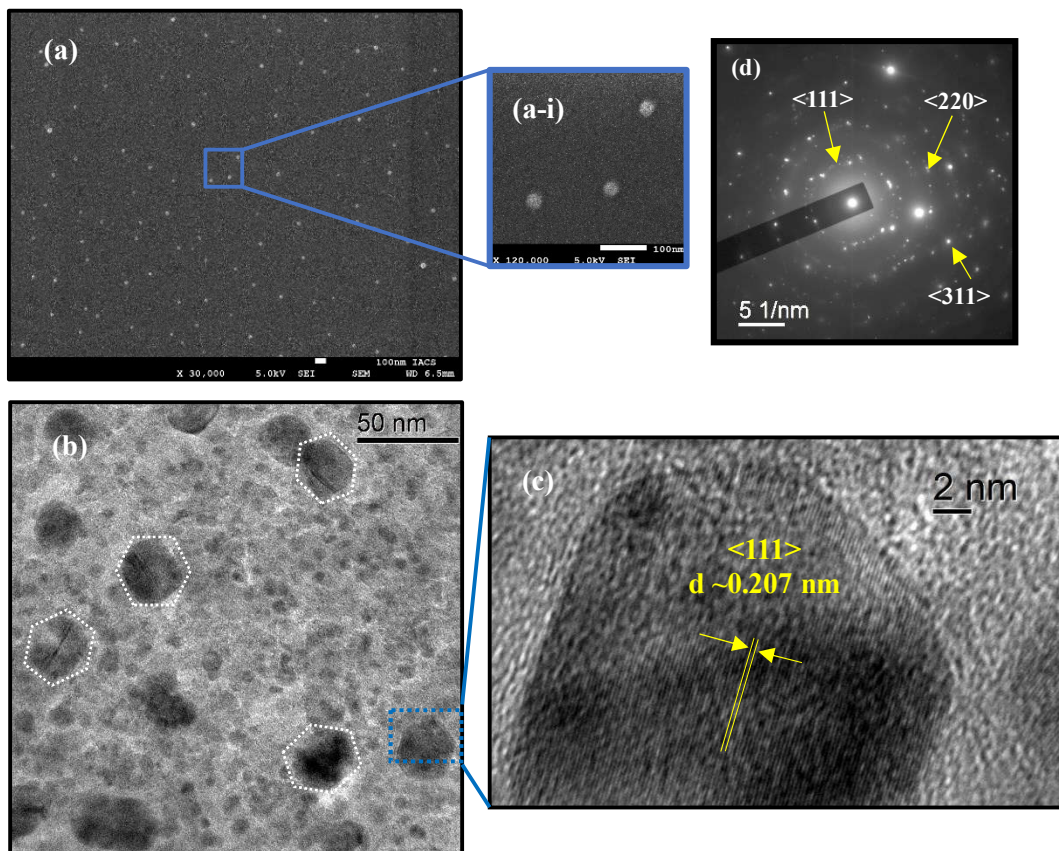


Fig. 6.10: (a) SEM image of the DLC film grown at 4 Torr and H_2/CH_4 ratio = 1; (a-i) enlarged image showing the nanocrystals; (b) TEM image showing the distribution of the nanocrystals in the network; (c) high-resolution image the marked hexagonal nanocrystal with distinct $<111>$ crystalline planes and (d) SAED image of the film showing different crystalline planes of diamond.

Chapter 6

The SEM image of the optimized DLC film (prepared at 4 Torr and $H_2/CH_4 = 1$), as in [Fig. 6.10 \(a\)](#), shows a uniform and continuous base matrix, on which nanocrystals of ~ 20 nm size are evenly distributed. The hexagonal shape of the nanocrystals is observed in the high-resolution image at the inset [Fig. 6.10\(a-i\)](#). The film exhibits nanocrystalline planes as shown in the corresponding TEM micrographs [Fig. 6.10 \(b\)](#), and [\(c\)](#). [Fig. 6.10\(b\)](#) shows the distribution of the nanocrystals within the film network. HR-TEM image in [Fig. 6.10\(c\)](#) demonstrates the distinct interplanar spacings $d \sim 0.207$ nm corresponds to the $\langle 111 \rangle$ orientation of the diamond crystal. Other than $\langle 111 \rangle$, there are few other planes i.e., $\langle 220 \rangle$, $\langle 311 \rangle$, etc. as evident from the corresponding selected area electron diffraction (SAED) pattern in [Fig. 6.10\(d\)](#). The size of the hexagonal nanocrystals marked in [Fig. 6.10 \(b\)](#) is ~ 20 nm, comparable with that obtained from the XRD analysis.

6.2. Conclusion:

In this study, we have successfully established the appropriate parametric conditions for developing DLC films with superior optical characteristics, like high band gap and antireflective properties, maintaining good crystallinity in the CCP CVD system. Two sets of DLC films have been prepared via one-step deposition, without pre-treatment e.g., seeding with nanodiamond powder, or post-deposition annealing. The optimized DLC film was grown at a substrate temperature of 450 °C, RF power of 250 W, and pressure of 4 Torr, while the flow rate ratio of the precursor gases was maintained at $H_2/CH_4 = 1$. This film possessed the minimum $I_D/I_G \sim 0.63$ and maxima of $I_{Dia}/I_D \sim 1.09$ and $I_{Dia}/I_G \sim 0.69$ with low stress ~ 0.4 GPa, indicating minimum defect states in the film network, closest to diamond, which identifies the usability of DLC thin films as a protecting layer for various nano-electronics devices including solar cells. The XPS findings infer that the DLC films possess a high sp^3 C bond content of $\sim 66.75\%$ and the least sp^2 C=C bond content (19.4%). A high optical band gap of ~ 3.65 eV is evaluated from Tauc's plot of this film, with a corresponding high transparency above $\sim 85\%$ in the wavelength range beyond 400 nm.

SECTION B

Carbon Silicon Heterostructures: Application of DLC Films in Silicon-Based Devices

Silicon serves as the base material in the world of microelectronics. The most significant application of silicon is in semiconductor solar power engineering, where it is utilized in the production of photovoltaic devices, specifically solar cells (SCs), which convert solar energy into electricity [220–223]. Currently, over 90% of the global production of solar modules (SMs) and solar batteries is based on silicon, which includes both monocrystalline and polycrystalline forms [223].

One effective method to enhance the performance of silicon solar cells is by reducing light reflection losses, which are primarily due to silicon's high refractive index [224]. A promising method for minimizing light reflection losses in silicon solar cells involves creating nano- and submicron-scale structures on their surfaces. To mitigate this issue, one-dimensional nanostructured silicon, such as silicon nanowires, nanopillars, and nanocones, is employed as antireflective coatings (ARCs) on the top layer of the solar cells [225]. These nanostructures enhance light trapping through multiple reflections within the one-dimensional structures, thereby increasing absorption due to the enlarged surface area [226]. Other options include porous Si layers [227,228], SiO_x films [228] and coatings of nanorods of SiO_2 , ITO [229] and ZnO [230,231]. However, such structures have low mechanical characters and require extra protection layers [229]. In these cases, DLCs are of particular interest, thanks to their optimal combination of optical and mechanical properties [232]. These can be effectively utilized to address challenges related to antireflection and protection in silicon solar cells (SCs) as well as silicon-based optical components in the infrared (IR) spectral region.

Diamond-like carbon (DLC) thin films, even in their thin film form, can exhibit many superior properties akin to bulk diamond. These properties include high hardness, low friction coefficient, high transparency, thermal conductivity, and electrical resistivity. Additionally, DLC films possess tunable characteristics, such as an optical band gap ranging from 1 to 4 eV [193], a refractive index between 1.6 and 2.2 [194], and variable crystalline content within their structure [195].

The prime focus in this work remains on developing DLC films with considerable nanocrystalline phase, superior optical properties e.g., high transparency and optical band gap, and minimal reflectance, such that they can be utilized as anti-reflective layers in Si solar cells. The fabrication of DLC is done via the capacitively coupled plasma chemical vapour deposition (CCP CVD) at a low RF power and a relatively low temperature.

B.1: Chapter 7

Application of DLC films as ARC in silicon
solar cells

7.1. Introduction:

Reflection loss of the incident light seriously affects the light-harvesting efficiency of the solar cells. Bare crystalline silicon (c-Si) has a high surface reflectance of over 30%, which harshly restricts the c-Si-base solar cell efficiency [32]. The Si thin-film solar cells are a cost-effective alternative to bulk c-Si wafer-based solar cells. To improve the photovoltaic (PV) performance by increasing the photo-generated charge carriers there are several measures like, (i) increasing the optical path length of the incident solar light by introducing a combination of surface texturing and light trapping, and (ii) employing effective anti-reflecting coating (ARC) layers on the top surface of the cell toward reducing the optical losses. Given the difficulties involved in surface texturing, ARC is a more straightforward and affordable way to improve the device performance [195]. To increase photo absorption, ARC may also help create light-trapping properties through refractive index (RI) engineering, by altering the incoming light's angle of incidence so that light undergoes multiple internal reflections and bounces back and forth within the cell material [226]. Theoretically, it is possible to achieve zero net reflected energy only if the light waves reflected from the semiconductor surface and the ARC top surface are out of phase and cause destructive interference with each other. ARCs on solar cells are typically formed by one thin layer with a particular RI and thickness, or multiple thin layers with varying RIs and thicknesses. Amongst various other ARC materials available in the literature, DLC films are gaining importance because of their high band gap (up to \sim 4 eV), tunable transmittance, and reflectance, while keeping the index of refraction and the extinction coefficient of the material low [233,234]. When deposited on c-Si wafers, the DLC films demonstrate high adhesion strength and superior stability against irradiations and damp heat exposure. Hence, DLC films should enhance the performance of Si-based solar cells by acting as both an AR coating and a protective encapsulant [235,236]. However, for device applications, multi-step processes of DLC growth, involving substrate pre-treatment like seeding with nanodiamond powder or metal nanoparticles, or post-treatment by high-temperature thermal annealing, etc., introduce additional inconveniences in the fabrication sequence [26,27].

The prime focus in this work remains on developing DLC films with nanocrystalline phase, superior optical properties e.g., high transparency and optical band gap, and minimal reflectance, such that they can be utilized as anti-reflective layers in Si solar cells. DLC films have already been fabricated employing capacitively coupled plasma (CCP) CVD, as discussed in **Section A.2.1: Chapter 6**. Finally, single junction *p-i-n* nc-Si based thin film solar cells with

Chapter 7

a simple ‘Glass/DLC/FZO/*p*-nc-SiO_x:H/*i*-nc-Si:H/*n*-a-Si:H/Al’ structure has been fabricated, using the optimized DLC film in an appropriate thickness as the effective ARC layer.

7.2. Experimental

The optimized DLC films (as prepared in **A.2.1: Chapter 6**) were used as ARC layers in single junction silicon *p-i-n* thin film solar cells having a simple structure of Glass/DLC/FZO/*p*-nc-SiO_x:H/*i*-nc-Si:H/*n*-a-Si:H/Al. In the cell configuration, fluorine-doped zinc oxide (FZO) film was employed as the front-electrode transparent conducting oxide (TCO) layer, Al as rear-electrode back reflector layer and three Si layers, in sequence, as the B-doped *p*-type nanocrystalline Si oxide (nc-SiO_x) window layer, intrinsic (*i*-type) nc-Si absorber layer, and P-doped *n*-type amorphous Si layer. All these layers were optimized in several previous publications [226,247,238] of this laboratory, using growth conditions listed below in **Table 7.1**.

Table 7.1. Growth conditions of the individual layers of the single junction *p-i-n* Si solar cell.

	DLC ARC	FZO TCO	<i>p</i> -nc-SiO _x :H	<i>i</i> -nc-Si:H	<i>n</i> -a-Si:H	Al
Deposition method used	RF-PECVD	RF magnetron sputtering	RF-PECVD	RF-PECVD	RF-PECVD	thermal evaporation
Ar gas flow (sccm)	–	3.3	–	–	–	–
H ₂ gas flow (sccm)	25	–	190	98.6	65	–
CH ₄ gas flow (sccm)	25	–	–	–	–	–
SiH ₄ gas flow (sccm)	–	–	1.4	1.4	–	–
CO ₂ gas flow (sccm)	–	–	0.1	–	–	–
B ₂ H ₆ in He gas flow (sccm)	–	–	0.7	–	–	–
PH ₃ in SiH ₄ gas flow (sccm)	–	–	–	–	13	–
Chamber pressure (Torr)	4	0.02	2.5	4	1	4 x 10 ⁻⁶
Substrate temp. (°C)	450	230	180	180	166	–
RF frequency (MHz)	13.56	13.56	13.56	40.68	13.56	–
RF power (W)	250	50	30	80	10	–
Deposition rate (nm/min)	~1	~2.5	~2	~30	~2.5	~360

Reflection measurements of the DLC films prepared at different deposition pressures (1 to 7 Torr) and at different flow ratio of H₂/CH₄ (0.5 to 4) were carried out utilizing a dual-beam spectrophotometer (Agilent Cary 5000). An illumination of AM 1.5 (100 mW cm⁻²) over a (1

Chapter 7

x 1) cm² active irradiation area from a solar simulator (Model: WACOM) was used to test the performance of the single junction *p-i-n* thin film nc-Si:H-based solar cells at RT and the I-V characteristics of the cells were acquired in a Keithley 2400 source meter. The other characterization units are detailed in previous section.

7.3. Results and Discussions

7.3.1. Antireflection properties:

7.3.1.1. ARC theory.

As discussed earlier, ARCs significantly improve the PV conversion efficiency of solar cells by reducing the surface reflectivity along the path of the incident solar spectrum and thus increasing the number of photo-generated charge carriers, which contributes to the increased short-circuit density of the cells [235,239]. Considering just a single layer of ARC, to fulfill the prerequisite of destructive interference and attain minimal reflection of a particular wavelength (λ) at normal incidence, (i) the geometric mean of the refractive indices (RIs) of the materials on both sides must match the RI of the ARC and (ii) the product of RI and the ARC thickness must be equal to one-quarter of λ [194,240], following:

$$n_2 = \sqrt{n_1 n_3} \quad \text{eqn (7.1)}$$

$$\text{and } n_2 t = \frac{\lambda}{4} \quad \text{eqn (7.2)}$$

where, n_2 is the RI of the ARC layer and n_1, n_3 are the RIs of the materials on either side of ARC; t is the thickness of the ARC and λ is the incident wavelength. Now, for the present case of ‘Glass/DLC/FZO/*p*-nc-SiO_x:H/*i*-nc-Si:H/*n*-a-Si:H/Al’ *p-i-n* single junction Si solar cell, the two media on both sides of the DLC layer are glass and FZO, which have $n_{\text{glass}} \sim 1.5$ and $n_{\text{FZO}} \sim 1.85$, respectively at a wavelength $\lambda \sim 550$ nm considering the peak of the solar spectrum [240–242]. So, at $\lambda \sim 550$ nm, using eqn (7.1) and (7.2), the ideal RI and thickness of the intermediate single layer of DLC ARC are calculated to be $n_{\text{DLC}} \sim 1.66$ and $t_{\text{DLC}} \sim 82$ nm, respectively.

7.3.1.2. Surface reflectivity and optical constants.

The reflectance spectra from the surface of all the prepared DLC films (preparation and other characterizations have already been discussed in **Section A.2.1: Chapter 6**) were measured in a UV-vis-NIR spectrometer in the range $\lambda \sim (350–1000)$ nm and presented in Fig. 7.1(a) and (b). From Fresnel’s law for normal incidence, the surface reflectivity (R%) of a

Chapter 7

single layer of DLC ARC (having $n_{DLC} \sim 1.66$) may have a theoretical reflectance, $R_{550} \sim 6.15\%$ [5]. From Fig. 7.1(a) it is evident that, when the pressure increases from 1 to 4 Torr, the overall reflectance gradually decreases, and for the 4 Torr sample R_{550} reaches its lowest value of $\sim 5.20\%$, which remains closer to the theoretical value. At higher pressure above 4 Torr, the surface reflectivity again goes upwards to $R_{550} \sim 10.51\%$ for the sample grown at 7 Torr. Lowering of the R% values with the corresponding changes in the deposition pressure (from 1 to 4 Torr) is attributed to the reduction in the disorder and cluster size of the sp^2 C=C graphitic chains and enhancement in the crystalline sp^3 C–C orientation [195], which is also reflected in the transmittance curve in Fig. 6.4(a) (as in Section A.2.1: Chapter 6). At higher deposition pressure beyond 4 Torr, the clustering of the sp^2 C=C bonds increases, thus reducing transmission and enhancing the surface reflectance. While changing the flow rate ratio, the R% for the sample prepared at $H_2/CH_4 = 1$ gives the overall lowest reflection, as shown in Fig. 7.1(b).

Now using the transmittance and reflection data two optical constants i.e., (i) extinction coefficient (k) and (ii) RI (n) of the DLC thin films can be measured [218] from two following equations:

$$k = \frac{\alpha\lambda}{4\pi} \quad \text{eqn (7.3)}$$

α being the absorption co-efficient, λ is the wavelength of the incident light, and

$$n = \left[\frac{4R}{(1-R)^2} - k^2 \right]^{1/2} - \frac{(R+1)}{(R-1)} \quad \text{eqn (7.4)}$$

R is the surface reflectance of the films.

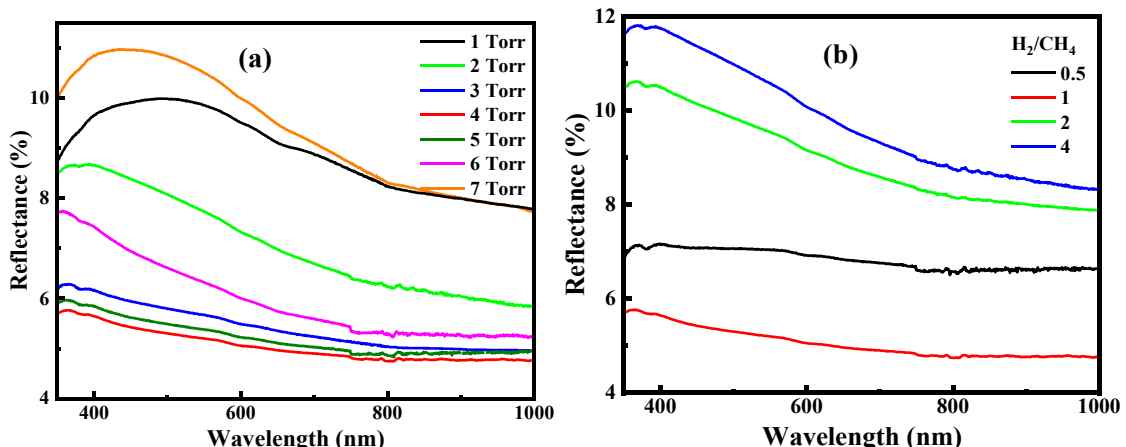


Fig. 7.1: Reflectance spectra of the DLC films grown at (a) different pressures, and (b) different H_2/CH_4 flow rate ratios.

Chapter 7

The RI (n) is quite familiar and discussed in the earlier section; whereas, the optical constant k , measures the quantity of the incident light that is attenuated in the thin film layer, as it passes through the medium. For all the prepared DLC films, the R%, n , and k values at $\lambda \sim 550$ nm are tabulated in [Table 7.2](#), which demonstrates that all these DLC films have a low reflectance of $\leq 10\%$, low RI, $n \sim 1.57$ – 1.83 and low k values $\sim 10^{-2}$ – 10^{-1} , which make them superior to other anti-reflecting materials available in the literature [\[218\]](#). DLC film prepared at a chamber pressure of 4 Torr with an H_2/CH_4 flow rate ratio =1, gives the lowest $R_{550} \sim 5.20\%$, lowest $n_{550} \sim 1.57$, and lowest $k_{550} \sim 0.084$, which are in good agreement with theoretical ideal values and beneficial for the implication as an effective ARC layer in a single junction Si solar cell.

Table 7.2. R, n , and k values at $\lambda \sim 550$ nm of DLC films prepared at different growth conditions.

DLC films (with growth condition)		R_{550} (%)	n_{550}	k_{550}
H_2/CH_4 flow rate ratio	Deposition pressure (Torr)			
1.0	1	9.86	1.81	0.363
1.0	2	7.74	1.71	0.258
1.0	3	5.67	1.60	0.154
1.0	4	5.20	1.57	0.084
1.0	5	5.38	1.59	0.123
1.0	6	6.32	1.62	0.225
1.0	7	10.51	1.83	0.411
0.5	4	7.04	1.67	0.241
2.0	4	9.54	1.79	0.359
4.0	4	10.57	1.73	0.536

7.3.1.3. Application in *p-i-n* single junction nc-Si:H-based solar cells.

The performance of the optimized DLC films grown at 4 Torr with $\text{H}_2/\text{CH}_4 = 1$ has been studied as an ARC layer of the single junction nc-Si:H-based solar cells having a simple configuration of ‘Glass/DLC/FZO/*p*-nc-SiO_x:H/*i*-nc-Si:H/*n*-a-Si:H/Al’ as mentioned earlier in the experimental section, with deposition conditions stated in [Table 7.1](#). The schematic diagram of the solar cell is outlined in [Fig. 7.2\(a\)](#) and the general properties of each layer are presented in [Table 7.3](#).

Chapter 7

Table 7.3. General characteristics of each layer of the *p-i-n* single junction nc-Si:H solar cell.

Cell Layers	Optimized thickness used in the solar cell (nm)	Optical energy band gap E_g (eV)		
		Optical energy band gap E_g (eV)	Dark conductivity σ_D ($S\ cm^{-1}$)	Crystallinity X_C (%)
DLC ARC	80	3.65	—	sp^3 C–C content ~66.75
FZO TCO	200	3.28	$\sim 10^2$	Highly Crystalline
<i>p</i> -nc-SiO _x :H	20	1.89	$\sim 10^1$	~70
<i>i</i> -nc-Si:H	2000	1.75	$\sim 10^{-3}$	~75
<i>n</i> -a-Si:H	30	1.8	$\sim 10^{-2}$	<20
Al rear electrode	1000	—	$\sim 10^4$	—

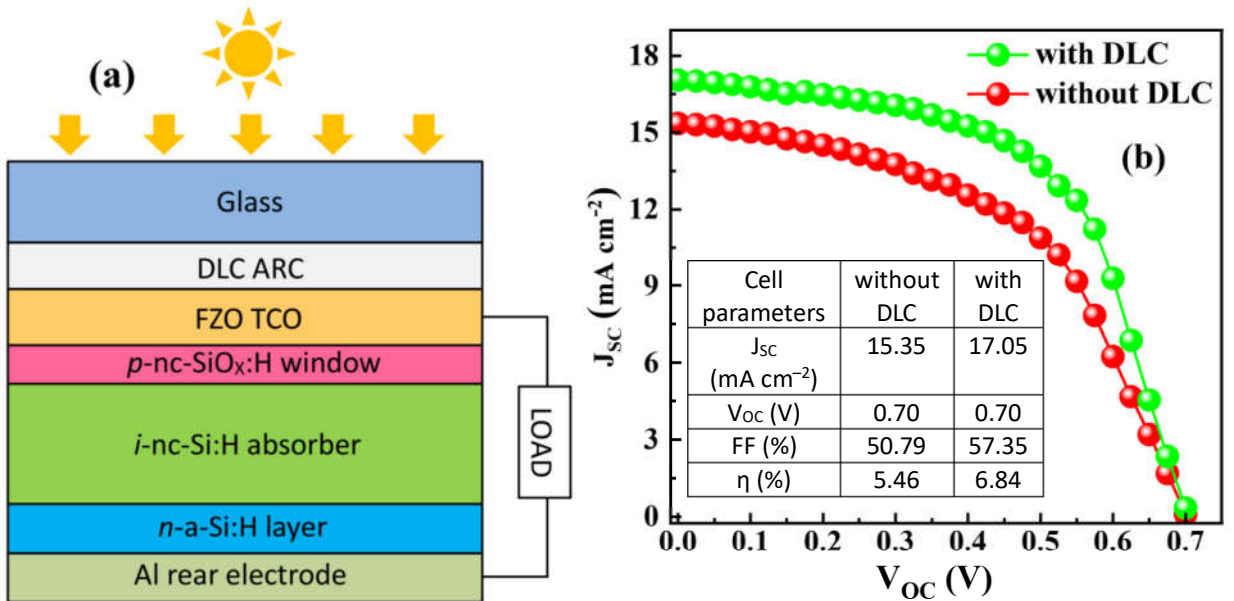


Fig. 7.2: (a) A schematic diagram of *p-i-n* single junction nc-Si:H-based solar cell, with DLC as an ARC layer, (b) J–V characteristics of the cells, one without DLC layer and another with DLC layer, and inset is the tabulated cell parameters for both the case.

Fig. 7.2(b) shows the short-circuit current density (J_{SC}) vs. open-circuit voltage (V_{OC}) characteristics of two cells, one without the DLC layer and another with the DLC ARC layer, and the corresponding cell parameters are tabulated in the inset. Without DLC coating the *p-i-n* single junction Si solar cell attains an efficiency $\eta \sim 5.46\%$ along with a $J_{SC} \sim 15.35\ mA\ cm^{-2}$, fill-factor (FF) $\sim 50.79\%$ and $V_{OC} \sim 0.7\ V$, while with a DLC ARC coating η goes to $\sim 6.84\%$ with same $V_{OC} \sim 0.7\ V$ but an increased $J_{SC} \sim 17.05\ mA\ cm^{-2}$ and FF $\sim 57.35\%$. This significant increment in J_{SC} and FF is mainly attributed to the increased photon absorption by reducing the

Chapter 7

optical losses in the cell (via suppressing the surface reflectance from the underneath Si cell layers and light trapping within the DLC material) [235,236]. Therefore, the outcome validates the potential of DLC films as a superior anti-reflective coating for silicon solar cells.

7.4. Conclusion:

DLC films prepared at parametric conditions (4 Torr, $H_2/CH_4 = 1$) exhibit the lowest $R_{550} \sim 5.20\%$, lowest $n_{550} \sim 1.57$, and lowest $k_{550} \sim 0.084$, which, altogether makes them ideally usable as anti-reflecting coating (ARC) materials in Si solar cells. Finally, the optimized DLC film has been used as an ARC layer of the single junction nc-Si:H-based solar cell, having a simple configuration of ‘Glass/DLC/FZO/*p*-nc-SiO_x:H/*i*-nc-Si:H/*n*-a-Si:H/Al’. With DLC coating the *p-i-n* single junction Si solar cell attains an increment in J_{SC} from $\sim 15.35 \text{ mA cm}^{-2}$ to 17.05 mA cm^{-2} , FF from $\sim 50.79\%$ to 57.35% and η from $\sim 5.46\%$ to $\sim 6.84\%$. This significant increment ($>25\%$) in PV efficiency is mainly attributed to the increased photon absorption by reducing the optical losses in the cell (via suppressing the surface reflectance from the underneath Si cell layers and light trapping within the DLC material), therefore validates the potential of DLC films as a superior anti-reflective coating for Si solar cells.

References

References

- [1] A.P. Mousinho, R.D. Mansano, M.C. Salvadori, *Surf. Coat. Technol.* 203 (2009) 1193–1198.
- [2] D. Das, “Nanocrystalline Diamond: A High-Impact Carbon Nanomaterial for Multifunctional Applications Including as Nanofiller”, *Carbon-Based Nanofillers and their Rubber Nanocomposites*, (edited by Yaragalla, Mishra, Thomas, Kalarikkal and Maria), Elsevier: Amsterdam, The Netherlands, (2019) 123–181.
- [3] A.C. Ferrari, J. Robertson, *Philos. Trans. R. Soc. Lond. A* 362(2004) 2477–2512.
- [4] S. Flege, R. Hatada, W. Ensinger, K. Baba, *J. Mater. Res.* 27 (2012) 845–849.
- [5] D. Das, A. Banerjee, *Appl. Surf. Sci.* 345 (2015) 204–215.
- [6] H. Zanin, P.W. May, M.H.M.O. Hamanaka, E.J. Corat, *ACS Appl. Mater. Interfaces.* 5 (2013) 12238–12243.
- [7] R. Paul, S. Dalui, A.K. Pal, *Surf. Coat. Technol.* 204 (2010) 4025–4033.
- [8] H. Sheng, W. Xiong, S. Zheng, C. Chen, S. He, Q. Cheng, *Carbon Lett.* (2020) 1976–4251.
- [9] R. Paul, S.N. Das, S. Dalui, R.N. Gayen, R.K. Roy, R. Bhar, A.K. Pal, *J. Phys. D: Appl. Phys.* 41(2008) 055309.
- [10] A. Singha, A. Ghosh, A. Roy, N.R. Ray, Quantitative analysis of hydrogenated diamond like carbon films by visible Raman spectroscopy, *J. Appl. Phys.* 100 (2006) 44910–44914.
- [11] A.A. Voevodin, J.S. Zabinski, Nanocomposite and nanostructured tribological materials for space applications, *Compos. Sci. Technol.* 65 (2005) 741–748.
- [12] K.I. Nickolai, L.N. Anatoliy, M.V. Anatoliy, L.B. Volodymyr, K.S. Gennadiy, K.N. Andriy, Improvement of solar cells efficiency and radiation stability by deposition of diamond-like carbon films, World Renewable Energy Congress (8–13May, 2011) Linkoping Sweden, Issue 57 Volume 11 Article No. 13, 2011, pp.2787–2794.
- [13] M. Lubwama, B. Corcoran, K.V. Rajani, C.S. Wong, J.B. Kirabira, A. Sebbit, K.A. McDonnell, D. Dowling, K. Sayers, *Surf. Coat. Technol.* 232 (2013) 521–527.
- [14] F.C. Tai, S.C. Lee, C.H. Wei, S.L. Tyan, *Mater. Trans.* 47 (2006) 1847–1852.
- [15] D. Caschera, F. Federici, S. Kaciulis, L. Pandolfi, A. Cusmà, G. Padeletti, *Mater. Sci. Eng. C.* 27 (2007) 1328–1330.
- [16] S. Kumar, C.M.S. Rauthan, M.K.M. Srivatsa, P.N. Dixit, R. Bhattacharyya, *Appl. Surf. Sci.* 182 (2001) 326–332.
- [17] C. Rattanasatien, N. Tonanon, W. Bhanthumnavin, B. Paosawatyanyong, *J. Nanosci. Nanotechnol.* 12 (2012) 642–647.

References

- [18] J. Xu, H. Fan, H. Kousaka, N. Umehara, D. Diao, W. Liu, *Diam. Relat. Mater.* 16 (2007) 161–166.
- [19] D. Das, B. Paramanik, *Diam. Relat. Mater.* 145 (2024) 111071.
- [20] W. Zhu, Z. Su, J. Guo, K. Li, K. Chen, W. Li, A. Yi, Z. Liao, Y. Luo, Y. Hu, Y. Xu, Q. Lin, X. Meng, *Diam. Relat. Mater.* 122 (2022) 108820.
- [21] Z. Seker, H. Ozdamar, M. Esen, R. Esen, H. Kavak, *Appl. Surf. Sci.* 314 (2014) 46–51.
- [22] D. Raha, D. Das, *Appl. Surf. Sci.* 276 (2013) 249–257.
- [23] J. Beckman, R. B. Jackman, J. S. Foord, *Diam. Relat. Mater.* 3 (1994) 602–607.
- [24] A.P. Mousinho, R.D. Mansano, M.C. Salvadori, *J. Alloys Compd.* 495 (2010) 620–624.
- [25] L. Yu, C.Q. Yun, Y. Huan, X. Ming, H.S. Long, *Appl. Mech. Mater.* 723 (2015) 502–506.
- [26] H. Li, T. Xu, C. Wang, J. Chen, H. Zhou, H. Liu, *Thin Solid Films* 515 (2006) 2153–2160.
- [27] Š. Meškinis, A. Čieglis, A. Vasiliauskas, K. Šlapikas, R. Gudaitis, I. Yaremcuk, V. Fitio, Y. Bobitski, S. Tamulevičius, *Nanoscale Res. Lett.* 11 (2016) 146.
- [28] H. Noda, H. Nagai, M. Shimakura, M. Hiramatsu, M. Nawata, *J. Vac. Sci. Technol. A* 16 (1998) 3170–3174.
- [29] J. Hopwood, *Plasma Sources Sci. Technol.* 1 (1992) 109–116.
- [30] D. Das, D. Kar, *J. Phys. Chem. Solids* 111 (2017) 115–122.
- [31] G. Nogay, Z.M. Saleh, E. Özkol, R. Turan, *Mater. Sci. Eng. B* 196 (2015) 28–34.
- [32] D. Das, L. Karmakar, *Nanoscale* 12 (2020) 15371–15382.
- [33] D. Raha, D. Das, *Sol. Energy Mater. Sol. Cells* 95 (2011) 3181–3188.
- [34] C. Riccardi, R. Barni, M. Fontanesi, P. Tosi, *Chem. Phys. Let.* 329 (2000) 66–70.
- [35] F. Inzoli, D. Dellasega, V. Russo, R. Caniello, C. Conti, F. Ghezzi, M. Passoni, *Diam. Relat. Mater.* 74 (2017) 212–221.
- [36] S. Osswald, V.N. Mochalin, M. Havel, G. Yushin, Y. Gogotsi, *Phys. Rev. B* 80 (2009) 075419.
- [37] A.C. Ferrari, J. Robertson, *Phys. Rev. B* 61 (2000) 14095–14107.
- [38] A. Roy, D. Das, *J. Phys. Chem. Solids* 160 (2022) 110307.
- [39] A. Roy, D. Das, *Diam. Relat. Mater.* 88 (2018) 204–214.
- [40] F.C. Tai, S.C. Lee, J. Chen, C. Wei, S.H. Chang, J. Raman. *Spectrosc.* 40 (2009) 1055–1059.
- [41] A. Sadezky, H. Muckenhuber, H. Grothe, R. Niessner, U. Poschl, *Carbon.* 43 (2005) 1731–1742.
- [42] D. Das, A. Roy, *Appl. Surf. Sci.* 515 (2020) 146043.

References

- [43] R.K.Y. Fu, Y.F. Mei, M.Y. Fu, X.Y. Liu, P.K. Chu, *Diam. Relat. Mater.* 14 (2005) 1489–1493.
- [44] J. Choi, K. Ishii, T. Kato, M. Kawaguchi, W. Lee, *Diam. Relat. Mater.* 20 (2011) 845–848.
- [45] J. Robertson, *Mater. Sci. Eng. R.* 37 (2002) 129–281.
- [46] A. Roy, D. Das, *J. Phys. Chem. Solids* 152 (2021) 109971.
- [47] J.J. Wei, C.M. Li, X.H. Gao, L.F. Hei, F.X. Lvun, *Appl. Surf. Sci.* 258 (2012) 6909–6913.
- [48] N.G. Ferreira, E. Abramof, E.J. Corat, V.J. Trava-Airoldi, *Carbon* 41 (2003) 1301–1308.
- [49] K.H. Chen, Y.L. Lai, J.C. Lin, K.J. Song, L.C. Chen, C.Y. Huang, *Diam. Relat. Mater.* 4(1995) 460–463.
- [50] D. Das, A. Banerjee, *Surf. Coat. Technol.* 272 (2015) 357–365.
- [51] A.F. Azevedo, F.A. Souza, J.T. Matsushima, M.R. Baldan, N.G. Ferreira, *J. Electroanal. Chem.* 658 (2011) 38–45.
- [52] P. Philipp, L. Bischoff, U. Treske, B. Schmidt, J. Fiedler, R. Hußner, F. Klein, A. Koitzsch, T. Mühl, *Carbon*. 80 (2014) 677–690.
- [53] C. Popov, W. Kulisch, P.N. Gibson, G. Ceccone, M. Jelinek, *Diam. Relat. Mater.* 13 (2004) 1371–1376.
- [54] J.I.B. Wilson, J.S. Walton, G. Beamson, *J. Electron. Spectros. Relat. Phenomena*. 121 (2001) 183–201.
- [55] D. Das, B. Sain, *J. Appl. Phys.* 114 (2013) 073708.
- [56] S.K. Suram, P.F. Newhouse, J.M. Gregoire, *ACS Comb. Sci.* 18 (2016) 673–681.
- [57] P. Mondal, D. Das, *Appl. Surf. Sci.* 286 (2013) 397–404.
- [58] J.B. Coulter, D.P. Birnie III, *Phys. Status Solidi (B)* 255(2017) 1700393.
- [59] D. Das, *J. Phys. D: Appl. Phys.* **36** (2003) 2335–2346.
- [60] A. Williams, M. Nesladek, M. Daenen, S. Michaelson, A. Hoffman, E. Osawa, K. Haenen, R.B. Jackman, *Diam. Relat. Mater.* 17 (2008) 1080–1088.
- [61] P. Wang, X. Wang, T. Xu, W. Liu, J. Zhang, *Thin Solid Films* 515 (2007) 6899–6903.
- [62] H. Pang, X. Wang, G. Zhang, H. Chen, G. Lv, S. Yang, *Appl. Surf. Sci.* 256 (2010) 6403–6407.
- [63] B. Paramanik, D. Das, *Appl. Surf. Sci.* 579 (2022) 152132.
- [64] D. Das, M. Jana, *Sol. Energy Mater. Sol. Cells* 81 (2004) 169–181.
- [65] D. Das, *Solid State Commun.* 108 (1998) 983–987.
- [66] P.W. May, *Phil. Trans. R. Soc. Lond. A* 358 (2000) 473–495.
- [67] W.A. Yarbrough, R. Messier, *Science* 247 (1990) 688.

References

- [68] W.J. Yang, T. Sekino, K.B. Shim, K. Niihara, K.H. Auh, *Thin Solid Films* 473 (2005) 252–258.
- [69] C. Riccardi, R. Barni, M. Fontanesi, P. Tosi, *Chem. Phys. Lett.* 329(2000) 66–70.
- [70] S. Skokov, B. Weiner, M. Frenklach, *J. Phys. Chem.* 98 (1994) 7073–7082.
- [71] N. Mutsukura, K. Yoshida, *Diam. Relat. Mater.* 5 (1996) 919–922.
- [72] D. Das, D. Raha, W.C. Chen, K.H. Chen, C.T. Wu, L.C. Chen, *J. Mater. Res.* 27 (2012) 1303–1313.
- [73] X.T. Zhou, X.M. Meng, F.Y. Meng, Q. Li, I. Bello, W.J. Zhang, C.S. Lee, S.T. Lee, Y. Lifshitz, *Diam. Relat. Mater.* 12 (2003) 1640–1646.
- [74] T.S. Yang, J.Y. Lai, M.S. Wong, C.L. Cheng, *J. Appl. Phys.* 92 (2002) 2133–2138.
- [75] C.Z. Gu, X. Jiang, *J. Appl. Phys.* 88 (2000) 1788–1793.
- [76] M. Jana, D. Das, A.K. Barua, *Sol. Energy Mater. Sol. Cells* 74 (2002) 407–413.
- [77] M. Jana, D. Das, A.K. Barua, *J. Appl. Phys.* 91 (2002) 5442–5448.
- [78] S. Mandal, *RSC Adv.* 11 (2021) 10159.
- [79] J. Filik, P.W. May, S.R.J. Pearce, R.K. Wild, K.R. Hallam, *Diam. Relat. Mater.* 12 (2003) 974–978.
- [80] M.H. Ahmed, J.A. Byrne, *Appl. Surf. Sci.* 258 (2012) 5166–5174.
- [81] A. Banerjee, D. Das, *J. Exp. Nanosci.* 9 (2014) 818–824.
- [82] D. Das, A. Roy, *ACS Appl. Nano Mater.* 5 (2022) 3558–3571.
- [83] C.J.H. Wort, R.S. Balmer, *Mater. Today* 11 (2008) 1–2.
- [84] J. Robertson, *Phys. Status Solidi (a)* 205 (2008) 2233–2244.
- [85] J.C. Pu, S.F. Wang, C.L. Lin, J.C. Sung, *Thin Solid Films* 519 (2010) 521–526.
- [86] P. Avouris, Z.H. Chen, V. Perebeinos, *Nat. Nanotechnol.* 2 (2007) 605–612.
- [87] L. Wang, B. Shen, F. Sun, Z. Zhang, *Surf. Interface Anal.* 47 (2015) 572–586.
- [88] A.A. Ahmad, *J Mater Sci: Mater Electron* 28 (2017) 1695–1705.
- [89] X.M. He, K.C. Walter, M. Nastasi, *J. Phys. Condens. Matter.* 12 (2000) L183–L189.
- [90] Z. Ren, H. Qin, Y. Dong, G.L. Doll, C. Ye, *Wear* 203031 (2019) 436–437.
- [91] C.M. Lin, S.J. Chang, M. Yokoyama, F.Y. Chuang, C.H. Tasi, W.C. Wang, I.N. Lin, *Jpn. J. Appl. Phys.* 38 (1999) 890–893.
- [92] W.C.W. Chan, F. Gaspari, T. Allen, P.K. Lim, E. Moreno, E. Sagnes, D. Manage, J. Szumak, S. Zukotynski, *J. Vac. Sci. Technol. A* 16 (1998) 889–892.
- [93] P. Ashcheulov, A. Taylor, Z. Vlčková Živcová, P. Hubík, J. Honolka, M. Vondráček, M. Remzová, J. Kopeček, L. Klimša, J. Lorinčík, M. Davydova, Z. Remeš, M. Kohout, A.M. Beltran, V. Mortet, *Appl. Mater. Today* 19 (2020) 100633.

References

- [94] T. Takeno, H. Shiota, T. Sugawara, H. Miki, T. Takagi, *Diam. Relat. Mater.* 18 (2009) 403–406.
- [95] M. Tan, J. Zhu, J. Han, X. Han, L. Niu, W. Chen, *Scr Mater.* 57 (2007) 141–144.
- [96] B.J. Chen, X.W. Sun, Y. Divayana, B.K. Tay, *J. Appl. Phys.* 98 (2005) 046107.
- [97] R. Reyes, C. Legnani, P.M.R. Pinto, M. Cremona, P.J.G. de Araujo, C.A. Achete, *Appl. Phys. Lett.* 82 (2003) 4017–4019.
- [98] S.R.P. Silva, J.D. Carey, X. Guo, W.M. Tsang, C.H.P. Poa, *Thin Solid Films.* 482 (2005) 79–85.
- [99] X. Cheng, M. Zhang, X. Chen, C. Chen, *Solid State Electron.* 51 (2007) 423–427.
- [100] A. Zeng, Y. Yin, M. Bilek, D. McKenzie, *Surf. Coat. Technol.* 198 (2005) 202–205.
- [101] S. Meskinis, R. Gudaitis, V. Kopustinskas, S. Tamulevicius, *Appl. Surf. Sci.* 254 (2008) 5252–5256.
- [102] Y. Hayashi, N. Kamada, T. Soga, T. Jimbo, *Diam. Relat. Mater.* 15 (2006) 1015–1018.
- [103] D. Kar, D. Das, *J. Appl. Phys.* 120 (2016) 025102.
- [104] M. Rusop, T. Soga, T. Jimbo, *Sol. Energy Mater. Sol. Cells* 90 (2006) 3214–3222.
- [105] D. Das, S. Samanta, *ACS Appl. Electron. Mater.* 3 (2021) 1634–1647.
- [106] T. Soga, T. Jimbo, K.M. Krishna, M. Umeno, *Int. J. Mod. Phys. B* 14 (2000) 206–217.
- [107] C.L. Tsai, C.F. Chen, C.L. Lin, *J. Appl. Phys.* 90 (2001) 4847–4851.
- [108] M. Benabdesselam, P. Iacconi, F. Wrobel, A. Petitfils, J.E. Butler, *Diam. Relat. Mater.* 16 (2007) 805–808.
- [109] G. Sepold, A. Stephen, S. Metev, *Diam. Relat. Mater.* 8 (1999) 1677–1681.
- [110] A.F. Azevedo, R.C. Mendes de Barros, S.H.P. Serrano, N.G. Ferreira *Surf. Coat. Technol.* 200 (2006) 5973–5977.
- [111] M. Nesladek, J.J. Mares, D. Tromson, C. Mer, P. Bergonzo, P. Hubik, J. Kristofik, *Sci. Technol. Adv. Mater.* 7 (2006) S41–S44.
- [112] Y. Hayashi, S. Ishikawa, T. Soga, M. Umeno, T. Jimbo, *Diam. Relat. Mater.* 12 (2003) 687–690.
- [113] M. Rusop, X.M. Tian, S.M. Mominuzzaman, T. Soga, T. Jimbo, M. Umeno, *Sol. Energy.* 78 (2005) 406–415.
- [114] W. Kautek, S. Pentzien, A. Conradi, J. Krüger, K.W. Brzezinka, *Appl. Surf. Sci.* 106 (1996) 158–165.
- [115] W. Mei, W. Weichen, H. Yujie, L. Musen, *Rare Metals.* 31 (2012) 189–192.
- [116] J. Podder, M. Rusop, T. Soga, T. Jimbo, *Diam. Relat. Mater.* 14 (2005) 1799–1804.
- [117] M. Amaral, A.J.S. Fernandes, M. Vila, F.J. Oliveira, R.F. Silva, *Diam. Relat. Mater.* 15 (2006) 1822–1827.

References

- [118] K. Tsugawa, M. Ishihara, J. Kim, M. Hasegawa, Y. Koga, *New Diam. Front. Carbon Technol.* 16 (2006) 337–346.
- [119] K. Tsugawa, M. Ishihara, J. Kim, Y. Koga, M. Hasegawa, *Phys. Rev. B.* 82 (2010) 125460.
- [120] X.J. Li, L.L. He, Y.S. Li, Q. Yang, A. Hirose, *Appl. Surf. Sci.* 357 (2015) 2141–2146.
- [121] A.A. Ahmad, *J Mater Sci: Mater Electron* 28 (2016) 1695–1705.
- [122] P.W. May, W.J. Ludlow, M. Hannaway, P.J. Heard, J.A. Smith, K.N. Rosser, *Chem. Phys. Lett.* 446 (2007) 103–108.
- [123] N. Ohtake, M. Hiratsuka, K. Kanda, H. Akasaka, M. Tsujioka, K. Hirakuri, A. Hirata, T. Ohana, H. Inaba, M. Kano, H. Saitoh, *Materials* 14 (2021) 315.
- [124] P. Bou, L. Vandenbulcke, *J. Electrochem. Soc.* 138 (1991) 2991–3000.
- [125] G.N. Yushin, S. Osswald, V.I. Padalko, G.P. Bogatyreva, Y. Gogotsi, *Diam. Relat. Mater.* 14 (2005) 1721–1729.
- [126] J.H.T. Luong, K.B. Male, J.D. Glennon, *Analyst* 134 (2009) 1965–1979.
- [127] S. Meškinis, A. Vasiliauskas, M. Andrulevicius, D. Peckus, S. Tamulevicius, K. Viskontas, *Materials* 13 (2020) 1003.
- [128] R.J. Zhang, S.T. Lee, Y.W. Lam, *Diam. Relat. Mater.* 5 (1996) 1288–1294.
- [129] A.C. Ferrari, J. Robertson, *Phys. Rev. B* 63 (2001) 2–5.
- [130] P.W. May, W.J. Ludlow, M. Hannaway, J.A. Smith, K.N. Rosser, P.J. Heard, *Mater. Res. Soc. Symp. Proc.* 1039 (2008) P17-03.
- [131] A.C. Ferrari, J. Robertson, *Philos. Trans. Royal Soc. A* 362 (2004) 2477–2512.
- [132] A. Sadezky, H. Muckenhuber, H. Grothe, R. Niessner, U. Poschl, *Carbon* 43 (2005) 1731–1742.
- [133] M.J. Matthews, M.A. Pimenta, G. Dresselhaus, M.S. Dresselhaus, M. Endo, *Phys. Rev. B* 59 (1999) R6585–R6588.
- [134] S. Zhang, X.T. Zeng, H. Xie, P. Hing, *Surf. Coat. Technol.* 123 (2000) 256–260.
- [135] B. Dong, X. Guo, K. Zhang, Y. Zhang, Z. Li, W. Wang, C. Cai, *Surf. Coat. Technol.* 429 (2022) 127951.
- [136] S.C. Halliwell, P.W. May, N.A. Fox, M.Z. Othman, *Diam. Relat. Mater.* 76 (2017) 115–122.
- [137] S. Saha, D. Das, *Appl. Surf. Sci.* 596 (2022) 153638.
- [138] A. Ganguly, S. Sharma, P. Papakonstantinou, J. Hamilton, *J. Phys. Chem. C* 115 (2011) 17009–17019.
- [139] P. Philipp, L. Bischoff, U. Treske, B. Schmidt, J. Fiedler, R. Hubner, F. Klein, A. Koitzsch, T. Muhl, *Carbon* 80 (2014) 677–690.

References

- [140] S. Ferro, M.D. Colle, A.D. Battisti, *Carbon* 43 (2005) 1191–1203.
- [141] F. Jia, Y. Bai, F. Qu, J. Zhao, C. Zhuang, X. Jiang, *Vacuum* 84 (2010) 930–934.
- [142] T. Kondo, N. Okada, Y. Yamaguchi, J. Urai, T. Aikawa, M. Yuasa, *Chem. Lett.* 44 (2015) 627–629.
- [143] A.E. Aleksenski Ī, V.Yu. Osipov, A.Ya. Vul, B.Ya. Ber, A.B. Smirnov, V.G. Melekhin, G.J. Adriaenssens, K. Iakoubovskii, *Phys. Solid State* 43 (2001) 145–150.
- [144] D. Das, S. Samanta, *Physica E* 128 (2021) 114615.
- [145] E.P. Visser, G.J. Bauhuis, G. Janssen, W. Vollenberg, W.J.P. van Enckevort, L.J. Giling, *J. Phys.: Condens. Matter* 4 (1992) 7365–7376.
- [146] S. De, S. Niranajana, B.S. Satyanarayana, M. Rao, *Optoelectron. Adv. Mater. Rapid. Commun* 3 (2009) 1365–1367.
- [147] Y. Katamune, S. Takeichi, S. Ohmagari, H. Setoyama T. Yoshitake, *Trans. Mat. Res. Soc. Japan* 40 (2015) 243–246.
- [148] C. Godet, *J. Non-Cryst. Solids* 299–302 (2002) 333–338.
- [149] W. Gajewski, P. Achatz, O.A. Williams, K. Haenen, E. Bustarret, M. Stutzmann, J.A. Garrido, *Phys. Rev. B* 79 (2009) 045206.
- [150] J.B. Coulter, D.P. Birnie III, *Phys. Status Solidi B* 255 (2017) 1700393.
- [151] J. Robertson, *Mater. Sci. Eng R.* 34 (2002) 129–281.
- [152] Sk.F. Ahmeda, D. Banerjee, K.K. Chattopadhyay, *Vacuum* 84 (2010) 837–842.
- [153] R. Zhu, Q. Tao, M. Lian, X. Feng, J. Liu, M. Ye, X. Wang, S. Dong, T. Cui, P. Zhu, *Materials* 12 (2019) 1780.
- [154] X.H. Wang, G.H.M. Ma, W. Zhu, J.T. Glass, L. Bergman, K.F. Turner, R.J. Nemanich, *Diam. Relat. Mater.* 1 (1992) 828–835.
- [155] M. Stano, S. Matejcik, J. D. Skalny, T. D. Mark, *J. Phys. B: At. Mol. Opt. Phys.* 36 (2003) 261–271.
- [156] D. Das, *J. Appl. Phys.* 93 (2003) 2528–2535.
- [157] K. Ebihara, T. Nakamiya, T. Ohshima, T. Ikegami, S. Aoqui, *Diam. Relat. Mater.* 10 (2001) 900–904.
- [158] K. Bhattacharya D. Das, *J. Phys. D: Appl. Phys.* 41 (2008) 155420.
- [159] Z.Q. Ma, B.X. Liu, *Sol. Energy Mater. Sol. Cells* 69 (2001) 339–344.
- [160] H. Kovacı, A.F. Yetim, Ö. Baran, A. Çelik, *Ceram. Int.* 44 (2018) 7151–7158.
- [161] H. Zeng, A.R. Konicek, N. Moldovan, F. Mangolini, T. Jacobs, I. Wylie, P.U. Arumugam, S. Siddiqui, R.W. Carpick, J.A. Carlisle, *Carbon* 84 (2015) 103–117.
- [162] N.D. Sharma, J. Singh, A. Vijay, *J. Appl. Phys.* 123 (2018) 155101.
- [163] Z. Sun, J.R. Shi, B.K. Tay, S.P. Lau, *Diam. Relat. Mater.* 9 (2000) 1979–1983.

References

- [164] J. Douda, C.R. González Vargas, E.V. Basiuk, A.I. Díaz Cano, J.A. Fuentes García, X.A. Hernández Contreras, *Appl. Nanosci.* 9 (2019) 567–578.
- [165] J.W. Park, K.H. Kim, N.M. Hwang, *Adv. Mater. Lett.* 9 (2018) 638–642.
- [166] J.W. Ager III, *IEEE Trans. Magnet.* 29 (1993) 259–263.
- [167] C.F. Chen, C.L. Tsai, C.L. Lin, *Diam. Relat. Mater.* 12 (2003) 1500–1504.
- [168] W.H. Fang, S.D. Peyerimhoff, *Mol. Phys.* 93 (1998) 329–339.
- [169] D. Das, K.H. Chen, S. Chattopadhyay, L.C. Chen, *J. Appl. Phys.*, 91 (2002) 4944–4955.
- [170] D.R. McKenzie, Y. Yin, N.A. Marks et al., *Diam. Relat. Mater.* 3 (1994) 353–360.
- [171] J. Robertson, *Diam. Relat. Mater.* 3 (1994) 361–368.
- [172] H. Nakazawa, R. Osozawa, Y. Mohnai, Y. Nara, *Jpn. J. Appl. Phys.* 56 (2017) 105501.
- [173] Y. Liu, S. Chen, X. Quan, H. Yu, H. Zhao, Y. Zhang, G. Chen, *J. Phys. Chem. C* 117 (2013) 14992–14998.
- [174] B.J. Matsoso, K. Ranganathan, B.K. Mutuma, T. Lerotholi, G. Jones, N.J. Coville, *New J. Chem.* 41 (2017) 9497–9504.
- [175] M.H. Manghnani, A. Hushur, T. Sekine, J. Wu, J.F. Stebbins, Q. Williams, *J. Appl. Phys.* 109 (2011) 113509.
- [176] C. Patra, D. Das, *J. Appl. Phys.* 126 (2019) 155305.
- [177] S.W. Choi, J. Yanga, J.H. Park, S.J. Han, P. Song, D.W. Kang, J.D. Kwon, *Curr. Appl. Phys.* 19 (2019) 1120–1126.
- [178] A. Dalvi, N.P. Reddy, S.C. Agarwal, *Solid State Communications* 152 (2012) 612–615.
- [179] T.A. Abtew, M.L. Zhang, Y. Pan, D.A. Drabold, *J. Non-Cryst. Solids* 354 (2008) 2909–2913.
- [180] H. Meiling, R.E.I. Schropp, *Appl. Phys. Lett.* 74 (1999) 1012–1014.
- [181] S.Y. Myong, K.S. Lim, M. Konagai, *Appl. Phys. Lett.* 88 (2006) 103120.
- [182] M.S. You, F.N. Hong, Y.R. Jeng, S.M. Huang, *Diam. Relat. Mater.* 18 (2009) 155–159.
- [183] J. Tauc, R. Grigorovici, A. Vancu, *Phys. Status Solidi* 15 (1966) 627–637.
- [184] D. Das, A. Dey, *Physica E* 111 (2019) 20–28.
- [185] H. Kovacı, Ö. Baran, A.F. Yetim, Y.B. Bozkurt, L. Kara, A. Çelik, *Surf. Coat. Technol.* 349 (2018) 969–979.
- [186] W. Li, X.Y. Tan, Y.M. Park, D.C. Shin, D.W. Kim, T.G. Kim, *Front. Mater.* 7 (2020) 201.
- [187] J. Mort, D. Kuhman, M. Machonkin, M. Morgan, F. Jansen, K. Okumura, Y.M. LeGrice, R.J. Nemanich, *Appl. Phys. Lett.* 55 (1989) 1121–1123.
- [188] R. Dey, S. Hussain, A.K. Pal, *Thin Solid Films* 763 (2022) 139566.
- [189] Y. Zhang, W. Sun, Y. Dong, M. Ma, Y. Liu, S. Tian, Y. Xiao, Y. Jia, *Surf. Coat. Technol.* 405 (2021) 126713.

References

- [190] E.A. Kulesh, D.G. Pilipetsou, A.V. Rogachev, J.X. Hong, N.N. Fedosenko, V. Kolesnyk, *J. Eng. Sci.* 7 (2020) C1–C9.
- [191] J. Peng, J. Liao, Y. Peng, Y. Xiao, J. Huang, L. Li, *Coatings* 12 (2021) 42.
- [192] E. Vaghri, Z. Khalaj, M. Ghoranneviss, M. Borghei, *J Fusion Energy* 30 (2011) 447–452.
- [193] A. Grill, *Diam. Relat. Mater.* 8 (1999) 428–434.
- [194] Q. Yang, S. He, R. Huang, M. Yu, C. Chen, S. Zheng, D. Yun, L. Zheng, Q. Cheng, *Diam. Relat. Mater.* 111 (2021) 108184.
- [195] W. S. Choi, B. Hong, *Renew. Energy* 33 (2008) 226–231.
- [196] Š. Meškinis, S. Tamulevičius, *Physics, Chemistry and Applications of Nanostructures* (2015) 319–325.
- [197] C. H. Su, C. R. Lin, C. Y. Chang, H. C. Hung, T. Y. Lin, *Thin Solid Films* 498 (2006) 220–223.
- [198] D. Das, Plasma kinetics, surface phenomena and growth mechanism in hydrogenated amorphous silicon: transition from amorphous to micro- and nanocrystalline Si:H, in: *Solid State Phenomena (Special Volume on Hydrogenated Amorphous Silicon)*, 44–46, Scitec Publication, Switzerland, 1995, pp. 227–258.
- [199] A. Mohanta, B. Lanfant, M. Asfaha, M. Leparoux, *J. Phys.: Conf. Ser.* 825 (2017) 012010.
- [200] L. Han, J. Liu, Z. Zhao, S. Chen, Z. Ma, L. Zhao, *Physica E: Low-Dimensional Systems and Nanostructures* 84 (2016) 249–257.
- [201] Z. F. Zhou, K. Y. Li, I. Bello, C. S. Lee, S. T. Lee, *Wear* 258 (2005) 1589–1599.
- [202] C. C. Yen, Y. C. Chang, H. C. Tsai, W. Y. Woon, *Carbon* 154 (2019) 420–427.
- [203] B. Paosawatyanyong, A. Muakngam, S. Thitianan, *AMR* 93–94 (2010) 699–702.
- [204] S. Tchakarov, D. Das, O. Saadane, A. V. Kharchenko, V. Suendo, F. Kail, P. Roca i Cabarrocas, *J. Non-Cyst. Solids* 338 (2004) 668–672.
- [205] B. S. Swain, B. P. Swain, N. M. Hwang, *J. Phys. Chem. C* 114 (2010) 15274–15279.
- [206] J. G. Buijnsters, L. Vázquez, J. J. ter Meulen, *Diam. Relat. Mater.* 18 (2009) 1239–1246.
- [207] T. Oshiro, M. Yamazato, A. Higa, M. Toguchi, *Jpn. J. Appl. Phys.* 46 (2007) 756.
- [208] D. Das, S. Saha, *Diam. Relat. Mater.* 146 (2024) 111219.
- [209] S. Prawer, R. J. Nemanich, *Philosophical Transactions of the Royal Society of London. Series A: Mathematical, Physical and Engineering Sciences* 362 (2004) 2537–2565.
- [210] R. K. Ghadai, S. Das, K. Kalita, I. Shivakoti, S. C. Mondal, B. P. Swain, *Mater. Chem. Phys.* 260 (2021) 124082.
- [211] H. Fukue, T. Nakatani, S. Takabayashi, T. Okano, M. Kuroiwa, S. Kunitsugu, H. Oota, K. Yonezawa, *Diam. Relat. Mater.* 142 (2024) 110768.

References

- [212] S. Saha, D. Das, *Thin Solid Films* 797 (2024) 140362.
- [213] F. Shahsavari, M. Ehteshamzadeh, M. H. Amin, A. J. Barlow, *Ceram. Int.* 46 (2020) 5077–5085.
- [214] Z. Nibennanoune, D. George, F. Antoni, S. Ahzi, D. Ruch, J. Gracio, Y. Remond, *Diam. Relat. Mater.* 22 (2012) 105–112.
- [215] S. K. Najaf Abadi, S. I. Hosseini, M. Momeni, H. Khaksaran, *Mater. Chem. Phys.* 229 (2019) 348–354.
- [216] R. Z. Moghadam, H. R. Dizaji, M. H. Ehsani, *J. Mater. Sci.: Mater. Electron.* 30 (22) (2019) 19770–19781.
- [217] Y. Lu, S. Wang, G. Huang, L. Xi, G. Qin, M. Zhu, H. Chu, *J Mater. Sci.* 57 (2022) 3971–3992.
- [218] R. Safari, F. Sohbatzadeh, T. Mohsenpour, *Surf. Interf.* 21 (2020) 100795.
- [219] F. Y. Ban, S. R. Majid, N. M. Huang, H. N. Lim, *Int. J. Electrochem. Sci.* 7 (2012) 4345–4351.
- [220] R.B. Bergmann, *Applied Physics A: Materials Science & Processing* 69 (1999) 187–194.
- [221] W.A. Badawy, *J. Adv. Res.* 6 (2015) 123–132.
- [222] S. Sharma, K.K. Jain, A. Sharma, *Mater. Sci. Appl.* 6 (2015) 1145–1155.
- [223] J. Liu, Y. Yao, S. Xiao, X. Gu, *J. Phys. D: Appl. Phys.* 51 (2018) 123001.
- [224] B. Sha, A.N. Lukianov, M.G. Dusheiko, V.B. Lozinskii, A.N. Klyui, D.V. Korbutyak, S.E. Pritchin, N. Klyui, *Opt. Mater.* 106 (2020) 109959.
- [225] J.-Y. Jung, H.-D. Um, S.-W. Jee, K.-T. Park, J.H. Bang, J.-H. Lee, *Sol. Energy Mater. Sol. Cells.* 112 (2013) 84–90.
- [226] K. Sarkar, D. Das, *Energy Fuels* 37 (2023) 16880–16892.
- [227] V. Yerokhov, O. Ierokhova, 2016 International Conference on Electronics and Information Technology (EIT) (2016).
- [228] L. Remache, A. Mahdjoub, E. Fourmond, J. Dupuis, L. Lemiti, *REPQJ* 1 (2010) 191–195.
- [229] A.K. Sood, A.W. Sood, R.E. Welser, G.G. Pethuraja, Y.R. Puri, X. Yan, D.J. Poxson, J. Cho, E.F. Schubert, N.K. Dhar, D.L. Polla, P. Haldar, J.L. Harvey, *MSA* 03 (2012) 633–639.
- [230] N.P. Klochko, K.S. Klepikova, I.I. Tyukhov, Y.O. Myagchenko, E.E. Melnychuk, V.R. Kopach, G.S. Khrypunov, V.M. Lyubov, A.V. Kopach, *Sol. Energy* 120 (2015) 330–336.
- [231] N.P. Klochko, V.R. Kopach, I.I. Tyukhov, D.O. Zhadan, K.S. Klepikova, G.S. Khrypunov, S.I. Petrushenko, V.M. Lyubov, M.V. Kirichenko, S.V. Dukarov, A.L. Khrypunova, *Sol. Energy* 164 (2018) 149–159.

References

- [232] A. K., A. Varade, N.R. K., S. Dhan, C. M., B. N., P. Krishna, *Diam. Relat. Mater.* 78 (2017) 39–43.
- [233] J. S. Song, Y. S. Park, N. H. Kim, *Appl. Sci.* 11 (2021) 358.
- [234] M. A. Aldeeb, N. Morgan, A. Abouelsayed, K. M. Amin, S. Hassaballa, *Diam. Relat. Mater.* 96 (2019) 74–84.
- [235] W. S. Choi, K. Kim, J. Yi, B. Hong, *Mat. Lett.* 62 (2008) 577–580.
- [236] N. I. Klyui, O. B. Korneta, V. P. Kostylyov, V. G. Litovchenko, A. V. Makarov, V. N. Dikusha, L. V. Neselevska, V. I. Gorbulik, *Semicond. Phys. Quant. Electron. & Optoelectron.* 6 (2003) 197–201.
- [237] B. Paramanik, S. Samanta, D. Das, *Optical Mater.* 133 (2022) 112961.
- [238] D. Das, P. Mondal, *Appl. Surf. Sci.* 416 (2017) 980–987.
- [239] J. Schneider, M. Turek, M. Dyrba, I. Baumann, B. Koll, T. Booz, *Prog. Photovolt: Res. Appl.* 22 (2014) 830–837.
- [240] R. Sagar, A. Rao, *Opt. Mater.* 150 (2024) 115276.
- [241] S.M. Rozati, S. Moradi, S. Golshahi, R. Martins, E. Fortunato, *Thin Solid Films* 518 (2009) 1279–1282.
- [242] F. Yakuphanoglu, Y. Caglar, S. Ilican, M. Caglar, *Physica B: Condensed Matter* 394 (2007) 86–92.

Chapter 8

Summary, Conclusion and Future Work

Chapter 8

8.1. Summary:

This work mainly deals with the optimization of Diamond like carbon thin films with high transparency and considerable nanocrystalline phases at a low pressure, low radio frequency (RF) power and relatively low temperature, in a one-step deposition process, without any initial substrate pre-treatment by expensive diamond powder. The growth process of the DLC films employs the advantages of the unique plasma enhanced chemical vapour deposition techniques operated at radio frequencies RF (13.56 MHz) using CH₄ as the precursor gas and Ar as the diluent. After initial optimization of the intrinsic DLC films by varying the flow rates employing Inductively coupled CVD (ICP CVD) system at a low pressure (30-40 mTorr), the effect of varying the negative bias voltage applied to the substrates, on the properties of the DLC films was studied in detail. In the next phase, boron was incorporated into the DLC matrix by introducing B₂H₆ (1 % in He) along with CH₄ and Ar. Investigations on the effect of negative dc bias voltage variation on the substrates was focussed in the next phase of work. Later a series of sample optimization for crystalline DLC thin films was carried out involving the Capacitively coupled plasma CVD (CCP CVD) at a low RF power (250 W). The optimized DLC, was then utilized as an anti-reflective coating for glass-based Si solar cells to investigate its effect on the efficiency of the solar cell. The final work, presented here, deals with another attractive application of DLC films as an enhancer of field emission properties of silicon nanowires. The details of each work are summarized below.

This initial work details the one-step growth of diamond-like carbon (DLC) thin films containing nanodiamond components using a planar inductively coupled RF plasma chemical vapor deposition (ICP-CVD) system, without the need for expensive diamond powder for initial substrate pre-treatment. By optimizing parameters such as the CH₄ flow rate and DC negative substrate bias at a high RF power of 900 W, a substrate temperature of 450 °C, and a low deposition pressure of 30 mTorr (~4 Pa), films with improved crystalline quality were obtained. Raman spectroscopy indicated high-quality DLC films with significant *sp*³ content, characterized by a minimum I_D/I_G ratio of 0.75 and a maximum I_{Di_a}/I_D ratio of 0.94 under optimal deposition conditions of a 25 sccm CH₄ flow rate. The diamond peak shift analysis indicated low tensile stress (0.09 GPa) in films grown at this CH₄ flow rate. However, XPS results showed that the *sp*³ content for the 25 sccm CH₄ sample was about 44%. This optimized film exhibited a surface roughness of 14.06 nm due to a higher crystalline diamond fraction. The application of a negative DC bias further improved the quality of the DLC films. At a DC bias of -40 V, films with enhanced crystallinity were produced, as indicated by a lower I_D/I_G

Chapter 8

ratio of ~ 0.61 and a higher I_{Dia}/I_D ratio of ~ 1.09 in the Raman spectrum. The sp^3 content of the film prepared with a -40 V negative DC bias was found to be $\sim 64.28\%$, approximately 20.28% higher than that of the film prepared without substrate bias. These optimized DLC films are highly transparent with an optical band gap of ~ 3.71 eV. XRD peaks and TEM images confirmed their high crystalline quality, with well-defined $\langle 111 \rangle$ crystallographic facets of a hexagonal structure, indicating the presence of diamond-like components within an amorphous matrix.

The effect of boron doping on the as optimized intrinsic DLC films, via studies on the structural, electrical, and optical properties is considered as the next part of the work. The deposition conditions involve a negative DC substrate-bias voltage of -40 V, a $\text{B}_2\text{H}_6/\text{CH}_4$ flow rate ratio (r) varying between $0\text{--}1\%$, a substrate temperature of 450 $^{\circ}\text{C}$, a low plasma pressure of 5.33 Pa (40 mTorr), and an RF power of 800 W. Raman spectroscopy revealed that with increased boron doping, the I_D/I_G ratio generally increased, while both I_{Dia}/I_D and I_{Dia}/I_G ratios decreased. The sample with a doping ratio of 1% exhibited an I_D/I_G ratio of approximately 0.819 , an I_{Dia}/I_G ratio of around 0.83 , and an I_{Dia}/I_D ratio of about 1.012 . XPS analysis indicated a sp^3 content of approximately 50% and effective boron incorporation. This was corroborated by the enhanced electrical conductivity (σ_{RT}) of roughly 3.02×10^{-5} S cm^{-1} , a minimum activation energy (ΔE_H) of around 170 meV, a reduced optical band gap (E_g) of approximately 3.35 eV, and a maximum RMS roughness of 48.12 nm. Tauc's plot demonstrated that the boron-doped diamond-like carbon (B-DLC) films had extended band tails with sub-bandgap absorptions due to defects. The TEM images displayed pronounced $\langle 111 \rangle$, $\langle 220 \rangle$, and $\langle 311 \rangle$ crystallographic planes of diamond, indicating high crystalline quality. At a low doping level of 0.08% , a sharp X-ray diffraction peak was observed at around $2\theta = 43.49^{\circ}$, corresponding to the $\langle 111 \rangle$ crystalline planes of diamond, along with a slight increase in the optical band gap.

As a second part of the boron doped DLC films fabrication, an effort has been made to improve the effective B doping into the matrix while maintaining optimum crystallinity, by controlling the negative substrate bias and following a single-step growth technique, without employing any substrate pre-treatment or post-deposition thermal annealing. When the substrate bias is increased within the range of -40 to -80 V, the crystallinity of the material improves significantly, with the sp^3 C-C content rising from 50.87% to 57.29% and a notable presence of $\text{B}_4\text{-C}$ bonds within the DLC matrix. However, at a higher bias of -120 V, the sp^3 C-C content decreases to 52.47% , and the $\text{B}_4\text{-C}$ content also diminishes. The Raman spectral analysis, with $(I_D/I_G)_{\text{min}}$ around 0.75 , $(I_{\text{Dia}}/I_D)_{\text{max}}$ approximately 1.49 , and $(I_{\text{Dia}}/I_G)_{\text{max}}$ about 1.11 ,

Chapter 8

indicates that the B-DLC network grown at -80 V substrate bias exhibits good crystallinity. At higher substrate biases, efficient substitution of boron atoms into lattice sites containing sp^3 hybridized C-C and sp^2 hybridized C=C bonds creates acceptor states, which enhance electrical conductivity (σ_D), typically around 1.15×10^{-4} S cm $^{-1}$ at -80 V. Interestingly, as the bias voltage increases beyond -80 V, the pre-exponential factor (σ_0) for above room temperature conduction changes significantly, with its characteristic energy (E_{MN}) shifting from approximately +31 meV to -29 meV. This shift signifies a change from conventional MNR to reverse MNR attributes and a transition from non-degenerate to degenerate semiconductor-like properties in the B-DLC network with increased negative dc substrate bias. However, below room temperature, charge transport is dominated by Mott's variable range hopping (VRH) mechanism, which remains independent of substrate bias. The B-DLC films grown at a substrate bias of -80 V exhibit an optical transparency of approximately 80% at a wavelength of 700 nm and a maximum optical band gap of about 3.70 eV. These films also possess a relatively smooth surface, with an RMS roughness of 51.27 nm. Transmission electron microscopy (TEM) images reveal distinct crystallographic planes indicative of the <111> orientation of diamond.

The next phase of work deals with the development of DLC films with superior optical characteristics, like high band gap and antireflective properties, maintaining good crystallinity in the CCP CVD system. Two sets of DLC films were prepared using a one-step deposition method, without any pre-treatment such as seeding with nanodiamond powder or post-deposition annealing. The optimal DLC film was grown at a substrate temperature of 450 °C, with an RF power of 250 W, and a pressure of 4 Torr. The flow rate ratio of the precursor gases was maintained at $H_2/CH_4 = 1$. This film exhibited a minimum I_D/I_G ratio of approximately 0.63, a maximum I_{Dia}/I_D ratio of around 1.09, and an I_{Dia}/I_G ratio of about 0.69, with a low stress level of approximately 0.4 GPa. These properties indicate minimal defect states within the film network, closely resembling diamond, making the DLC thin films suitable as protective layers for various nano-electronic devices, including solar cells. XPS analysis revealed that the DLC films have a high sp^3 carbon bond content of approximately 66.75% and a low sp^2 C=C bond content of 19.4%. The optical band gap of the film, determined from Tauc's plot, was found to be around 3.65 eV, with high transparency above 85% in the wavelength range beyond 400 nm. DLC films produced under these specific conditions (4 Torr, $H_2/CH_4 = 1$) demonstrated the lowest (reflectance at 550 nm) R_{550} of approximately 5.20%, the lowest (refractive index at 550 nm) n_{550} of about 1.57, and the lowest (extinction co-efficient at 550 nm) k_{550} of around 0.084.

Chapter 8

These characteristics make them ideal as anti-reflective coating (ARC) materials for silicon solar cells.

The last phase of the work deals with the utilization of the as prepared DLC films with optimum characteristics of crystallinity, optical transparency, and reflectance (fabricated in CCP CVD system) in different silicon-based device applications as an anti-reflectance coating (ARC) on Si solar cells for improvement in the efficiency of the solar cells.

The optimized DLC film was applied as an ARC layer in a single junction nc-Si solar cell with the configuration ' Glass/DLC/FZO/p-nc-SiO_x:H/i-nc-Si:H/n-a-Si:H/Al'. With the DLC coating, the p-i-n single junction Si solar cell showed an increase in JSC from approximately 15.35 mA cm⁻² to 17.05 mA cm⁻², an increase in FF from approximately 50.79% to 57.35%, and an improvement in efficiency (η) from approximately 5.46% to 6.84%. This significant increase (>25%) in photovoltaic efficiency is mainly attributed to enhanced photon absorption due to reduced optical losses in the cell. This reduction is achieved by suppressing surface reflectance from the underlying Si cell layers and improving light trapping within the DLC material. These findings confirm the potential of DLC films as superior anti-reflective coatings for silicon solar cells.

8.2. Conclusion:

In this thesis work, the appropriate parametric conditions for the development of diamond like carbon thin films with optimum crystalline phases, high optical band gap and anti-reflection properties has been successfully established via the use of inductively coupled plasma (ICP) as well as capacitively coupled plasma (CCP) enhanced chemical vapour deposition (PECVD) techniques operating at radio frequencies (13.56 MHz) at a relatively low substrate temperature of 450 °C. The use of these processes has enabled the plasma ignition, its sustenance and subsequent DLC film deposition at remarkably low deposition pressures as well as low RF powers. Intrinsic and boron doped DLC films were prepared at a low pressure (30-40 mTorr) in ICP CVD system. The incorporation of boron into the DLC matrix has successfully enhanced the electrical conductivity of the DLC network, while maintaining adequate crystallinity, thereby making it useful for various electronic applications. Optimized intrinsic DLC films were fabricated at a low RF power of 250 W employing CCP CVD. These were then used in different types silicon-based device applications. Primarily, DLC films have been applied as an antireflective coating for glass-based Si solar cells, thereby enhancing its efficiency.

Chapter 8

8.3. Future Work

Till now, the diamond like carbon thin films and boron doped diamond like carbon films have been developed via ICP CVD and CCP CVD techniques. The main disadvantage of both the processes is that the films grown were all of very low thickness, as has been confirmed by the X-ray diffraction studies and transmittance spectra. Our future plan is to try to improve the thickness of the films, so as to make proper utilization of the films in various application devices via appropriate characterizations. Improvement of the crystalline quality of the films needs also to be looked into. For this, the use of nanodiamond powder for better nucleation on the glass substrates and strengthening the effective bonding of the sp^3 hybridized diamond structure may be employed. Boron doping of the nanodiamond seeded substrates can improve the electrical conductivity of the DLC films many folds thereby making them applicable in electronic and opto-electronic devices. The investigations on the effect of nanodiamond powder seeding of the substrates followed by DLC film deposition on the anti-reflective properties and field emissive properties are also on the list of our future plans. We plan to explore and focus on the n type doping of DLC films with their thorough characterizations.

Chapter 8

8.4. Front pages of published peer-review papers:

Applied Surface Science 596 (2022) 153638



Full Length Article



Growth of diamond-like carbon films with significant nanocrystalline phases in a low-pressure high-density CH₄ plasma in ICP-CVD: Effect of negative dc substrate bias

Sucharita Saha, Debajyoti Das *

Energy Research Unit, School of Materials Sciences, Indian Association for the Cultivation of Science, Jadavpur, Kolkata 700032, India

ARTICLE INFO

Keywords:
DLC films
Low temperature growth
Inexpensive substrate
Low-pressure CH₄ plasma
Dc substrate bias
Planar ICP-CVD

ABSTRACT

Working at relatively low-temperature and low-pressure, the development and optimization of diamond-like carbon (DLC) films with significant nanodiamond components on inexpensive glass substrates, without conventional pre-treatment by diamond powders, is the main objective of the present work. Using the most familiar CH₄-precursors diluted by Ar in a high-density plasma triggered at high rf power (900 W) in a planar inductively-coupled plasma chemical vapour deposition (ICP-CVD) system, DLC thin-films are prepared via optimization in the flow rate of the precursor gas at 30 mTorr (~4 Pa) pressure and 450 °C substrate temperature and, further by applying negative dc-bias to the substrates. The optimized samples obtained with negative substrate-bias possess good crystalline properties. From Raman results, the most crystalline sample is obtained with characteristic minimum I_D/I_G ratio reduced from 0.75 to 0.61, maximum I_{DIA}/I_D enhanced from 0.94 to 1.09, and the sp^3 hybridized C—C bonds increased from 44% to ~64% at a substrate-bias of -40 V. The residual stress, and the optical band gap were calculated from Raman analysis. The optimized DLC film exhibits a high optical band gap (3.71 eV) as calculated from Tauc's plot analysis of the UV-Vis data. The well-identified (1 1 1) crystallographic planes in the TEM micrograph demonstrate a significant fraction of nanocrystalline diamond component in the optimum DLC film.

1. Introduction

Diamond is one of the most versatile materials of extreme scientific interest, due to its profound utility in device fabrication. This is due to its superior properties like extreme hardness, chemical inertness, high optical transparency with selective photon absorption ability [1], electrical resistivity and thermal conductivity. However, diamond manufacture necessitates very advanced procedures that are both costly and energy intensive.

Diamond-like carbon (DLC) is one of the diverse allotropes of carbon that consists of a mixture of crystalline and amorphous phases with C atoms arranged in different co-ordinations, e.g., tetrahedral sp^3 hybridized C—C bonds of diamond or trigonal sp^2 C=C as in graphite or even some sp hybridized C≡C bonds. The proportional strength of these differently coordinated C bonds present in the matrix determines the physical properties of the DLC material [2]. As the name suggests, DLC films likely contain a significant amount of sp^3 hybridized carbon that

determines its diamond-like properties, involving much easier and inexpensive ways of production [3,4]. DLC with a significant amount of hydrogen content (10–50%) forms a separate class, the hydrogenated DLC (HDLC, a-C:H), wherein the H-content plays an essential role in determining its various properties [5,6]. Transparent DLC films with high nanocrystalline diamond contents find numerous applications in opto-electronics like micro-electromechanical system (MEMS), nano-electromechanical system (NEMS), microelectrode, field emission devices, etc. [7–9]. They are also useful as coatings for moisture-resistant lubricants, water repellent and cathode for lithium batteries, and also as protective anti-reflection coatings for solar cells against action of radiation (solar wind, γ -quanta) which is one of the key factors for efficiency degradation in space [10–13]. With the production cost minimised, DLCs get compromised in terms of the quality (crystalline properties) and hence in ultimate device usability. We are thus interested in evolving a cost-effective quality product of DLC with enhanced crystalline properties by incorporating considerable nanocrystalline

Abbreviations: DLC, Diamond-Like Carbon; ICP, Inductively Coupled Plasma; CVD, Chemical Vapour Deposition.

* Corresponding author.

E-mail address: erdd@iacs.res.in (D. Das).

<https://doi.org/10.1016/j.apsusc.2022.153638>

Received 4 March 2022; Received in revised form 8 May 2022; Accepted 9 May 2022

Available online 11 May 2022

0169-4332/© 2022 Elsevier B.V. All rights reserved.

Chapter 8

Thin Solid Films 797 (2024) 140362



Contents lists available at ScienceDirect

Thin Solid Films

journal homepage: www.elsevier.com/locate/tsf



Growth of boron-doped diamond-like carbon films from a low-pressure high-density plasma in inductively coupled chemical vapour deposition

Sucharita Saha, Debajyoti Das *

Energy Research Unit, School of Materials Sciences, Indian Association for the Cultivation of Science, Jadavpur, Kolkata 700 032, India

ARTICLE INFO

Keywords:

Boron doping
Diamond-like carbon
Thin film
Electrical conduction
Optical transparency
Low-pressure high-density plasma
Inductively coupled plasma
Chemical vapour deposition

ABSTRACT

The main objective of this work was the preparation and optimization of boron-doped diamond-like carbon (DLC) films having a good crystalline structure, and electronic and optical properties, at an extremely low deposition pressure and relatively low growth temperature, by varying the flow rates of precursor gases (CH₄, B₂H₆, and Ar) in the plasma controlled at 800 W of RF power. Planar inductively coupled plasma-enhanced chemical vapour deposition technique was used to enable deposition at ~5.33 Pa and 450 °C, at a constant negative substrate bias of -40 V. The flow rate of the dopant gas (B₂H₆) was changed to obtain a set of samples, while the precursor gas (CH₄) flow rate was kept fixed. The doped sample, prepared with B₂H₆/CH₄ ratio (r) = 1 %, was found to possess a maximum I_D/I_G (intensity ratio of the D peak with the G peak) of ~0.819 and a minimum I_{DIA}/I_G ratio (relative intensity of the Diamond peak to the G peak) of ~1.149. A high sp³ content of ~50 % was revealed from the X-ray photoelectron spectroscopy analysis and the transmission electron microscopy images also indicated the presence of prominent (111), (220), and (311) crystallographic planes. The B-doped DLC film possessed enhanced electrical conductivity (σ_{RT}) of ~ 3.02×10^{-5} S cm⁻¹ relative to the intrinsic DLC films, a corresponding minimum of activation energy (ΔE_H) (as calculated in the above room-temperature regime) of ~170 meV, an optical band gap (E_g) of ~3.35 eV, and the root mean square roughness of ~48.12 nm.

1. Introduction

Random networks of varying proportions of sp² and sp³ hybridized C bonds are the prime constituents of diamond-like carbon (DLC) films [1,2]. DLCs with higher sp³ contents possess material properties close to single crystal and polycrystalline diamonds, e.g., high optical transparency, thermal conductivity, and electrical resistance, apart from being extremely hard and chemically inert [3–5]. Intrinsic DLC, consisting of C-C bonds, are insulators, where the energy band gap is high (5.47 eV) [6]. To increase the conductivity, one of the most significant ways is doping of the DLC films. The incorporation of dopants into the C-C matrix creates defect states in between the bands. These defect states facilitate the transport of charge carriers to the corresponding nearest bands, enhancing the conductivity. The electrically conducting DLC films find numerous applications in high-speed microelectronics and optoelectronics like field emission flat panel displays [4,7].

Although diamond is electronically similar to Si, doping in diamond is not as easy as in Si because of the propensity of the C atoms to form graphitic and amorphous carbon (involving sp² hybridized C=C bonds),

besides the sp³ hybridized tetrahedral C-C bonds [8–11]. Thus, the increasing electrical conductivity of the doped diamond films may not be as pronounced and effective as in the case of doped Si films, having the same dopant concentration. DLC films can be doped with N and P to form n-type semiconductors, and p-type DLCs are grown by incorporating B into the diamond lattice, the atomic radius of B matches with that of C [12,13]. Doping modifies the electrical, optical and tribological characteristics of DLCs [14,15]. In B-doped DLC films, generally, conduction appears via the hopping of electrons within the local defect states between the conduction and valence bands [16,17].

The B-doped DLC films are grown by numerous techniques, e.g., microwave plasma chemical vapour deposition (CVD) [18,19], electron cyclotron resonance (ECR) plasma CVD [20], hot filament CVD [21], plasma enhanced CVD (PECVD) [22,23], pulsed laser deposition [24, 25], plasma immersion ion processing [14], etc. In PECVD, the B doping is employed in situ, at low deposition temperature, using gaseous sources, e.g., diborane (B₂H₆), tri-methyl boron (TMB), and di-boron trioxide (B₂O₃) into the precursor gas mixture containing H₂/Ar/hydro-carbon [26]. One of the prime advantages of PECVD techniques is

* Corresponding author.

E-mail address: erdd@iacs.res.in (D. Das).

<https://doi.org/10.1016/j.tsf.2024.140362>

Received 24 March 2023; Received in revised form 10 January 2024; Accepted 24 April 2024

Available online 26 April 2024

0040-6090/© 2024 Elsevier B.V. All rights reserved.

Chapter 8

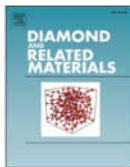
Diamond & Related Materials 146 (2024) 111219



Contents lists available at ScienceDirect

Diamond & Related Materials

journal homepage: www.elsevier.com/locate/diamond



Negative dc substrate bias influencing the low-temperature growth of B-doped DLCs in a low-pressure rf inductive plasma

Debajyoti Das ^{*}, Sucharita Saha

Energy Research Unit, School of Materials Sciences, Indian Association for the Cultivation of Science, Jadavpur, Kolkata 700 032, India

ARTICLE INFO

Keywords:
B-doped DLC films
Electrically conducting
Optically transparent
Low-pressure inductive plasma
Negative substrate bias
Meyer-Neldel characteristics

ABSTRACT

The effects of increasing substrate negative dc bias on growing the boron-doped diamond-like carbon (B-DLC) films are extensively studied, following a single-step and low-pressure plasma processing. With the optimum bias of -80 V, the B-DLC films exhibit good crystalline properties corresponding to accomplishing the $(I_D/I_G)_{\min} \sim 0.75$, $(I_{D\text{ia}}/I_D)_{\max} \sim 1.49$, and $(I_{D\text{ia}}/I_G)_{\max} \sim 1.11$ values in the Raman data. The X-ray photoelectronic spectroscopy results demonstrate attaining $\sim 57.29\%$ of the sp^3 -hybridized C—C bonds and a significant B_4 —C component of $\sim 24.25\%$. A high electrical conductivity ($\sigma_D \sim 1.15 \times 10^{-4}$ S cm $^{-1}$) was attained with coherent low activation energy in the above-room-temperature regime ($\Delta E_H \sim 111$ meV). Microscopic studies reveal a smooth structural surface, distinct $\langle 111 \rangle$ crystalline planes, and a broad optical gap of ~ 3.70 eV. Interestingly, the Meyer-Neldel characteristic energy (E_{MN}), as estimated from the $\ln(\sigma_0)$ vs. ΔE_H plot, demonstrates a positive-to-negative sign-reversal while increasing the bias across -80 V, signifying a transition from the non-degenerate to a degenerate semiconductor-like characteristic at elevated negative substrate bias. Thus, in the above-room-temperature regime, the B-DLC material pursues a switching in its electronic band characteristics when prepared across a threshold in the substrate bias of -80 V under the present plasma conditions. While in the below-room-temperature regime, Mott's variable-range-hopping phenomena prevails arbitrarily at any substrate bias.

1. Introduction

Diamonds are the hardest known materials on earth. They possess excellent mechanical and chemical properties, which are useful in applications. Since diamonds are formed naturally in the environment at extremely high temperatures (~ 1800 °C) and pressure (~ 10 GPa), their artificial manufacturing process involves a lot of technically advanced equipment, incurring high expenses [1]. Diamond-like carbon (DLC) is a material alternative to diamonds. Comprising different proportions of sp^2 and sp^3 C—C bond configurations, DLCs possess properties much closer to diamonds, like high hardness, chemical inertness, high optical band gaps, high electrical resistance, and thermal conductance [2]. They also possess low friction coefficient and wear resistance. Their production mechanisms also involve easy and cheap procedures. DLCs find applications as protective windows and encapsulation layers in solar cells [3,4].

The high electrical resistivity of DLCs hinders their usage in many electronic and industrial applications [5]. Doping of DLCs with acceptors like B and N and donors like I and P could make them electrically

active as *p*-type and *n*-type DLCs, respectively [6]. Electrically conducting DLC thin films with superior properties like high hardness, high transparency, low friction coefficient, and super corrosion stability are extremely useful in many applications [7]. Besides, intrinsic DLC films have poor adhesion with substrates triggered by their high internal stress [8], which could be reduced by B doping, and, in turn, improved adhesion to the substrate is possible [9,10]. B-doped DLCs possessing ~ 10 at.% B are reported to exhibit 65% less stress relating to undoped DLC films [10]. Doped DLC films are used in carrier injection enhancement [11], room temperature electroluminescence [12], as cold-cathode material [13], in metal-semiconductor-metal detectors [14], electrochemical applications [15], piezoelectric applications [16], thin film transistor [17], and DLC/Si solar cells [18–21].

The B-doped DLC films are grown by various deposition techniques like plasma-assisted physical vapor deposition, dc arc-discharge, rf magnetron sputtering, ion beam sputtering, pulsed plasma CVD, and capacitively coupled parallel plate plasma-enhanced CVD (PECVD) [7,22,23]. The CVD systems use gaseous precursors like C_2H_2 and CH_4 in diluent gases like Ar and H_2 , the dopant source gas being B_2O_3 , $B(CH_3)_3$,

^{*} Corresponding author.

E-mail address: erdd@iacs.res.in (D. Das).

<https://doi.org/10.1016/j.diamond.2024.111219>

Received 27 December 2023; Received in revised form 12 May 2024; Accepted 19 May 2024

Available online 21 May 2024

0925-9635/© 2024 Elsevier B.V. All rights are reserved, including those for text and data mining, AI training, and similar technologies.